UNIVERSITY OF SOUTHAMPTON

FACULTY OF ENGINEERING AND THE ENVIRONMENT

Institute of Sound and Vibration Research

Structural health monitoring on a mooring chain using acoustic emission technique

by

Fernando Galván Rivera

Thesis for the degree of Doctor of Philosophy

September, 2019

UNIVERSITY OF SOUTHAMPTON

ABSTRACT

FACULTY OF ENGINEERING AND ENVIRONMENT

Institute of Sound and Vibration Research

Thesis for the degree of Doctor of Philosophy

STRUCTURAL HEALTH MONITORING ON A MOORING CHAIN USING ACOUSTIC EMISSION TECHNIQUE

Fernando Galván Rivera

The aim of this research project is to evaluate the feasibility of Acoustic Emission Technique for the crack growth monitoring on a mooring link. Moreover, this research work focus to do waves decomposition in a bar, bend bar and link to know how the bends in a link have an effect of wave conversion. Therefore, wave modes decomposition in frequency and time domain are done to know how the bends in a link could impact the wave propagation. In addition, AE technique is implemented in a test rig to monitor crack growth generated by Tension-Tension in a studless chain link of large diameter. In first part, a chain tensile test is carried out in artificial seawater using a single grade R5 link of diameter 160 mm, where different tensile loads were applied during almost a period of four months. The AE features are analysed to monitor crack growth, where selected peak amplitude filters are applied to plot the trends of the AE features. In second part, Pochhammer-Chree theory is used to know the dispersive curve and the wave modes in a straight rod. Then, the novel wave mode decomposition method was implemented to identify the wave with higher amplitude in a specific frequency range. Moreover, a study of wave modes decomposition was carried out in time domain in a cylindrical steel bar of small diameter (45 mm diameter). The work was carried out on simulation data and validated with experimental measurements. In last part, the wave decomposition is carried out in time domain for a bar, bend bar and link of large diameter (160 mm diameter). Comparison of wave mode decomposition between bar, bend bar and chain are obtained to know how the bends generate wave mode conversion. The wave decomposition is more complex for bar of large diameter because the number of excited waves increases. Therefore, a Hilbert transformation is applied to the axial component to get that the three components (radial, circumferential and axial) could be in phase to be able to obtain the wave decomposition. The simulations were validated against experimental work in straight bar and link, where good agreements of wave decomposition are obtained.

Table of Contents

List of Tables

List of Figures

DECLARATION OF AUTHORSHIP

I, Fernando Galván Rivera

declare that this thesis and the work presented in it are my own and has been generated by me as the result of my own original research.

Structural health monitoring on a mooring chain using acoustic emission technique

I confirm that:

1. This work was done wholly or mainly while in candidature for a research degree at this University;
2. Where any part of this thesis has previously been submitted for a degree or any other qualification at this University or any other institution, this has been clearly stated;
3. Where I have consulted the published work of others, this is always clearly attributed;
4. Where I have quoted from the work of others, the source is always given. With the exception of such quotations, this thesis is entirely my own work;
5. I have acknowledged all main sources of help;
6. Where the thesis is based on work done by myself jointly with others, I have made clear exactly what was done by others and what I have contributed myself;
7. Parts of this work have been published as:

   F. G. Rivera, G. Edwards, E. Eren, and S. Soua, “Acoustic emission technique to monitor crack growth in a mooring chain,” Applied Acoustics, vol. 139, 156-164, 2018.

Signed: .....

Date: .....

Acknowledgements

I would like to thank to Dr. Maryam Ghandchi Tehrani for giving me the opportunity to study a PhD. I would like to extend thank to Dr. Timothy Waters for teaching me wave propagation and wave decomposition. Without him, I would still be trying to understand what a wave is. I would like to thank both for teaching me what a research is.

I would especially like to thank my parents, my beautiful mother Maria Rivera Garcia and my father Evodio Galván Mata. I would also like to thanks my sisters Maricela, Karla and my brothers Luis, Benito, Manuel, Jorge, Victor and Diego. I would like to thank my pretty wife Gabriela Perez Garcia and my two little princesses Jennifer and Marifer for supporting me and helping me to release the stress during my PhD.

I am grateful to my industrial supervisor Mr. Graham Edwards and Dr. Ruth Sanderson for their invaluable support throughout this PhD.

I am grateful to the Mexican National Council of Science and Technology (CONACYT).

Finally, though definitely not least, I want to mention a special thanks to all Mexicans because thank to their taxes I could get a scholarship to study my PhD.

Nomenclature

A	Are of cross-section of a bar and link
E	Young's modulus
ρ	Density
G	Shear modulus
I	Second moment of area
J	Polar second moment of area
k_l	Longitudinal wavenumber
k_s	Shear wavenumber
k_b	Bending wavenumber
c	Wave speed
ω	Angular frequency
f	Frequency in Hertz
k	Wavenumber
j	$\sqrt{-1}$
t	Time
f_z	Axial distributed force per unit length
u	Axial motion displacement
A_R	Complex axial displacement of a right going propagating wave
A_L	Complex axial displacement of a left going propagating wave
z	Distance along the rod in axial direction
U	Axial displacement of harmonic excitation
F_z	Force amplitude in axial direction
Φ	Torsional motion
T	Torque
f_x	Transverse distributed force per unit length
w	Transversal axial motion
W	Transversal displacement of harmonic excitation
C_R	Wave amplitude of the transverse displacement near-field in right direction
D_R	Wave amplitude of the transverse displacement propagating in right direction
C_L	Wave amplitude of the transverse displacement near-field in left direction
D_L	Wave amplitude of the transverse displacement propagating in left direction
F_x	Spectrum amplitude in transverse direction
f_g	Gaussian modulated sinusoidal function
g_g	Modulated-Gaussian sinusoidal function
F	Fast Fourier Transformation of input excitation
M	Mobility transfer function
V	Fast Fourier Transformation to the output response
v	Time domain of the output response velocity
h_g	Gaussian pulse function
A_f	Amplitude of Gaussian function
t_s	Time shift of the centre of the peak pulse
σ	Standard deviation sometimes called the Gaussian Root Mean Square width
M_u	Axial mobility transfer function
v_u	The output axial response velocity
F_z	Spectrum amplitude in axial direction
V_u	Spectrum of the output response axial velocity
V_w	Spectrum of the output response transversal velocity
$V_\emptyset$	Spectrum of the output response rotational velocity
a_u	Amplitude of the excited wave
c_p	Phase wave speed

M_w Transverse mobility transfer function
$M_\emptyset$ Rotation mobility transfer function
$\emptyset$ Angular motion of harmonic excitation
v_w Output transverse response velocity
v_φ Output axial response velocity
φ Output angular response displacement
r_b Radius of bar
c_g Group velocity of flexural wave
$\mathbf{s}$ Timoshenko displacement vector
ϕ Timoshenko bending rotation of the cross section
ϑ Timoshenko shear deformation
r_g Radius of gyration
c_l Longitudinal wave speed
c_s Shear wave speed
κ Shear coefficient
$\boldsymbol{a}$ Complex amplitude vector of Timoshenko wave motion
k_1 Flexure wave number of Timoshenko
k_2 Shear wave number of Timoshenko
$\widetilde{\omega}$ Non-dimensional circular frequency
$\tilde{k}$ Non-dimensional wavenumber
$\widetilde{\omega}_1$ Non-dimensional circular frequency of flexural wave
$\widetilde{\omega}_2$ Non-dimensional circular frequency of shear wave
$\widetilde{\omega}_c$ Non-dimensional circular cut-off frequency
m_r Ratio of material
γ Non-dimensional of ratio material parameter
c_{p1} Timoshenko phase flexural wave speed
c_{p2} Timoshenko phase shear wave speed
r Non-dimensional radial coordinate
s Non-dimensional coordinate around the neutral axis
R Radius of the curvature
r' Radial coordinate
$\bar{v}$ Non-dimensional axial displacements
$\bar{w}$ Non-dimensional transverse displacements
$\bar{v}'$ Components of displacement in circumferential direction
$\bar{w}'$ Components of displacement in transverse direction
ϵ_s Circumferential strain
γ_{rs} Shearing strain
β Change in slope of the normal to the neutral line
v_c Non-dimensional components of displacement at circumferential direction
w_c Non-dimensional components of displacement at transverse direction
N_E Resultant circumferential force over the cross-section
Q_S Radial shearing force
M_V Resultant moment referred to the neutral axis
q Geometrical constant which defines the curvatures in the rod
W_c Constant amplitude in the curvature rod
K Non-dimensional wavenumber of curvature rod
λ Dimensional wavelength
$\widehat{\mathbf{u}}$ Displacement distribution vector
$\widetilde{\mathbf{u}}$ Wave mode shape vector of cross section
$\mathbf{u}$ Wave mode shape profile displacement vector
u_r Wave mode shape radial displacement profile
u_θ Wave mode shape circumferential displacement profile
u_z Wave mode shape axial displacement profile
$\mathbf{D}^u$ Coefficients of matrix

A_{coeff} Amplitude coefficients vector
c_L Longitudinal speed for Pochhammer-Cheer theory
c_T Transverse speed for Pochhammer-Cheer theory
υ Poisson's ratio
A_c Amplitude coefficient of longitudinal deformation component
B_c Amplitude coefficient of shear vertical deformation component
C_c Amplitude coefficient of shear horizontal deformation component
σ_t Stress tensor
σ_{rr} Radial, radial outer surface stress
$\sigma_{r\theta}$ Radial, circumferential outer surface stress
σ_{rz} Radial, axial outer surface stress
$\mathbf{D}^{\sigma t}$ Stress tensor matrix
n Wave mode shape order
m Variation of wave mode shape in radial direction
$\tilde{u}_r$ Wave mode shape radial component
$\tilde{u}_\theta$ Wave mode shape circumferential component
$\tilde{u}_z$ Wave mode shape axial component
$\tilde{u}_x$ Wave mode shape in x direction in cartesian system
$\tilde{u}_y$ Wave mode shape in y direction in cartesian system
$\mathbf{N}$ Nodal velocity matrix
$\mathbf{Q}$ Wave mode shape matrix
$\mathbf{A}$ Unknown wave amplitude matrix
λ_{min} Minimum wavelength
D Diameter of the ink
$\tilde{z}$ Complex transformation of wave
f_s Complex stretching function
s_f Scaling factor
ξ Dimensionless coordinate of stretching function
u_i Complex displacement for stretching in single direction
Δ_w Original width of the perfectly matched Layer
g Hann-window function
$\hat{R}_{xy}$ Cross correlation coefficient of two random processes (x_i and y_i)
u_x Euler transversal deformation
φ_u Euler rotational deformation
D Complex axial amplitudes of the transverse wave
$\hat{u}_x$ Wave propagating of a displacement in x direction
$\hat{u}_y$ Wave propagating of a displacement in y direction
$\hat{u}_z$ Wave propagating of a displacement in z direction
$\mathbf{Q_R}$ Wave mode shape matrix of real components
$\mathbf{Q_I}$ Wave mode shape matrix of imaginary components
$\mathbf{H}_{(u)}$ Hilbert transform to wave propagating displacement field
$\mathbf{Q_{RI}}$ Wave mode shape matrix real and imaginary components
v_r Velocity response in radial direction
v_θ Velocity response in circumferential direction
v_x Velocity response in x direction
v_y Velocity response in y direction
v_z Velocity response in z direction
Hv_z Axial Hilbert transform in z direction
$\mathbf{N_H}$ Nodal velocity matrix with Hilbert transform in axial direction
$\mathbf{a_R}$ Wave amplitudes using only radial and circumferential wave mode shape $\mathbf{Q_R}$
$\mathbf{a_I}$ Wave amplitudes using only axial wave mode shape $\mathbf{Q_I}$ without Hilbert transform
$\mathbf{Ha_I}$ Wave amplitudes using only axial wave mode shape $\mathbf{Q_I}$ with Hilbert transform
$\mathbf{Ha_{RI}}$ Wave amplitudes using only all wave mode shape $\mathbf{Q_{RI}}$ with Hilbert transform

$\mathbf{A_H}$ Wave amplitude matrix using nodal matrix with Hilbert transform in axial direction

Chapter 1: Introduction

In the last 20 years, the failure of links along the mooring line, has been a problem of floating units. Mooring line systems of floating structures consists of long lengths of links, rope or wire. A common practice is to combine wire rope of steel with heavy links. Links are normally used at the bottom and top of a mooring line. The mooring link is an important component of a mooring line and has a critical role in the integrity of offshore floating units. A failure in a link can be generated by axial, bending and twisting loads [1], [2]. These type of loads excite longitudinal, flexural and torsional waves in cylindrical structures like cylindrical bars [3]. However, the dominant wave mode of loading between links is tensile and bending loading. In the long term, axial loads induced by the waves produce a tension-tension. The tension-tension is due to tension variation loading in the chains, where a crack can initiate and grow until fracture/collapse occurs. The main purpose of inspections is to identify the conditions of the mooring system so that the risk of structural failure can be evaluated and actions can be taken. Mooring breaking can bring to catastrophic events such as production shutdown. Twenty-one mooring accidents were recorded between 2001-2011 and eight of them were considered as multiple breakages [4]. However, during storm in October 1991 and January 1992, there were eight semi-submersible mooring incidents [2]. The number of incidents can increase during storms, therefore more proactive approaches should be considered to cover the demands on the offshore industry to inspect the mooring chain [5]. To tackle this serious industrial challenge, Lloyd's Register and The Welding Institute (TWI) encourage to explore the way of monitoring crack growth in mooring chains using Acoustic Emission Technique (AET).

One powerful monitoring tool for providing information about early warning of flaws is AET, which can be used to detect cracks [6]. Acoustic emissions are the elastic waves that spontaneously released by a material undergoing deformation. Acoustic emission (AE) waves can be generated from a crack but also from other sources, like friction and impact. AE signals are mixed with environmental noise and crack signals, making it difficult to discriminate from crack signals. AET is a passive Non-Destructive Testing (NDT) method that has been implemented by petrochemical industry since early 1980's [5]. This passive technique can be used as an early warning system for the offshore industry. Therefore, in this thesis, a chain tensile test is carried out in artificial seawater, where different tensile loads were applied for almost four months. Then, the AE features are analysed to monitor crack growth. In addition, wave decomposition were carried out in a straight bar, bent bar and link to know how the bends could have an impact in the wave propagation. The wave decomposition work was carried out on simulation and validated with experimental measurements.

1.1 Background

An ordinary marine installation system is composed of an ocean surface vessel, a flexible string cable, mooring lines to be positioned for installation on the ocean floor, as it is shown in Figure 1-1. Mooring systems are used for anchoring a floating structure to the ocean floor (catenary, taut or semi-taut-lines). Mooring lines being made up of steel links and steel wire ropes have a catenary shape with heavy weight, while synthetic fibre ropes are normally straightened in a taut mooring system and used especially for deep water.

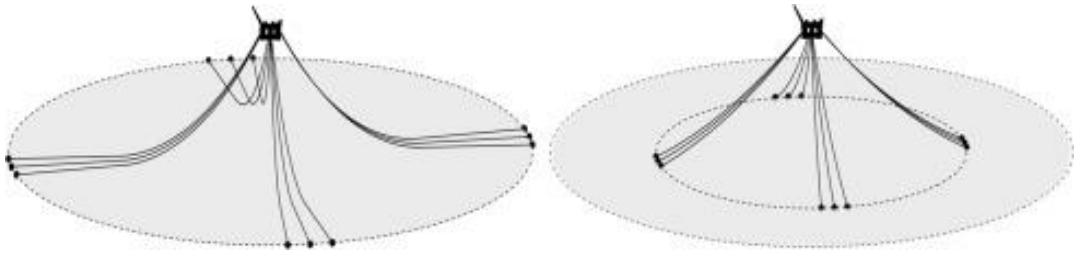

Figure 1-1 (Left) Catenary mooring system. (Right) Taut leg mooring system. [7]

Mooring systems are often used in the offshore oil and gas industry. Two types of mooring system can be found: single point mooring and spread mooring. Single points mooring is often used for ship-shaped such as floating production units. Figure 1-2 shows one example of the turret mooring systems, where some mooring lines are attached to an internal or external turret, and the ship vessel can rotate around this turret. A spread mooring system is formed of multiple lines, which are distributed around the ship avoiding rotation and less heading of the ship. An example of the spread mooring system of a Floating Production Storage and Offloading (FPSO) is shown in Figure 1-1.

Figure 1-2 Single point external turret (left) Submerged turret production (right) [7]

During the high demand of producing oil and gas, Floating Production Units (FPUs) has been experiencing more demand using mooring system. In November 2013, there were 277 FPUs in use around the world, and 62% were FPSO [1]. However, this demand of production, has generated that the number of failures in mooring line increases, where the majority of the failures (54%) is found in the link as shown in Figure 1-3 (left).

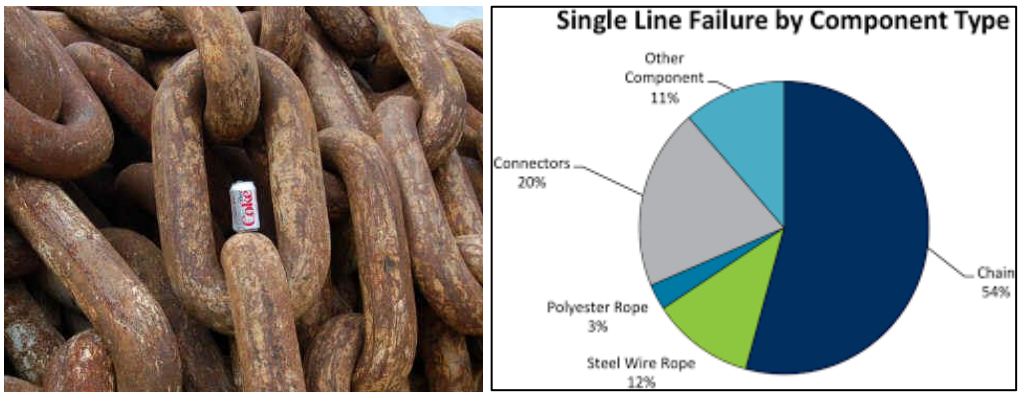

Figure 1-3 Mooring chains (left), Line failure by component type (right) [8]

1.1.1 Mooring chain failures

Links are normally used at the bottom of a mooring line, connected from the anchor to the top of the floating structure, as shown in Figure 1-4. The top and bottom of a mooring line are especially exposed to corrosion, wear, axial load and bending in the links [2]. Mooring lines have to resist large loads. The environmental loads from wind, waves and currents may be strong during extreme weather conditions, reducing the mooring life. Usually, the mooring lines are designed for an operational life of 20 years, but the number of operating years per failure is 8.8 in FPSO [1].

Mooring chain failures on floating unit, which correspond to oil and gas production have been occurring at a rate, where the years of service life is lower than the designed. Failures have happened due to many causes including overload, fatigue, manufacturing defects and excessive wear and corrosion. Mooring systems failures can be of high consequences, potentially resulting in extended production shutdown [1]. The potential cost could be extremely high, for example, an approximation cost of single line failure is in the range of £2-10.5 million. Therefore, predictive maintenance is very important to monitor the performance of a structure during operation. This allows to the engineers to predict the future failures and allowing them to replace just before the structure fails. Predictive maintenance minimises the equipment down time and costs associated with preventative maintenance. Preventative maintenance requires inspecting at predetermined intervals of time, whether or not the maintenance is required [4].

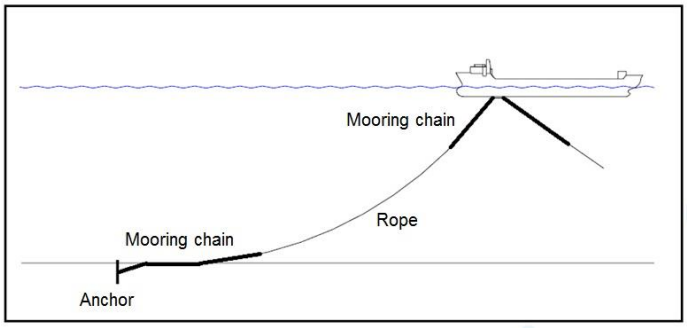

Figure 1-4 Typical mooring line [6]

Figure 1-5 illustrates some of the main causes that affect a mooring system's service life. Bending occurs at abrupt changes of the slope of the mooring line, and the largest line tension happens before this sudden changes of slope. Most of the loading occurs in the bottom zone of the sea, at the end of the catenary line where the chain comes in contact with the seabed. The chain is exposed to abrasion and surface damage due to movements in this thrash zone.

The Noble Denton Phase 1 Mooring Integrity Joint Industry Project (JIP) included a survey of mooring failures. Most of the failure data available was from the North Sea where there are statutory requirements for reporting mooring incidents to the UK Health Safety Executive. Based on data for the period 1980 to 2001, it was reported that, on average, a Floating Production Unit will experience a mooring line failure every 9 years. There are some failures modes, for example, sewered by wear, flexion, tension, corroded tension, fatigue, battered fatigue, corrosion fatigue and plastic wear. However, Failures were most frequent due to high tension and bending on mooring chains [2].

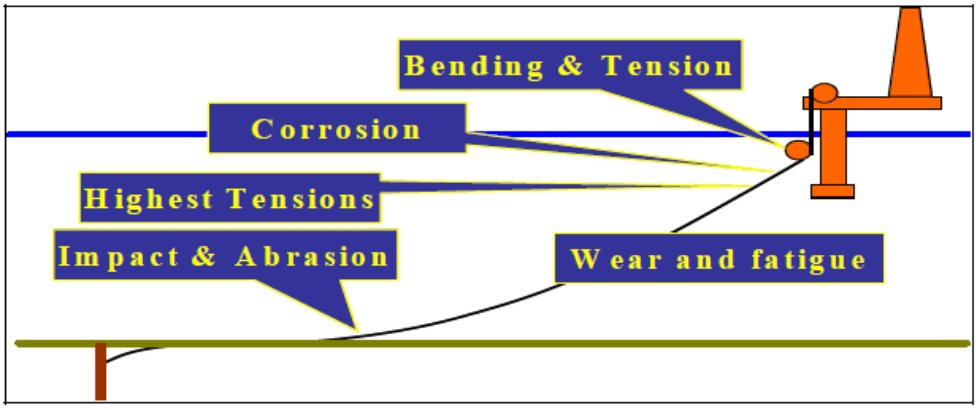

Figure 1-5 Main factors that affect mooring chain [2]

The acoustic emission technique (AET) has been promising in the monitoring crack growth. Over the past 20 years acoustic emission technique was developed as an effective non-destructive technique for the detection, localization and monitoring of cracks in a variety of metal structures, including airframes, steel bridges, pipelines and pressure vessels. Acoustic emissions are essentially elastic stress waves, generated by a rapid release of energy from a localised source within a stressed material which can be detected by AE sensors. Sources of acoustic emission are defect related processes such a crack propagation and evolution of plasticity in the material in the highly stressed zone adjacent to the crack tip [9].

Figure 1-6 shows the types of crack separation mode for a cylindrical bar, according to the type of loading a crack modes can be produced. For instance, Mode I is generated when an axial loading is applied at normal direction to the cross-section of the rod. Mode II is produced when a bending load is applied parallel to the cross-section, it can be considered like in-plane shear or out-of-plane to the cross-section. Mode III (out-of-plane shear) is produced from twist or torsion in a rod.

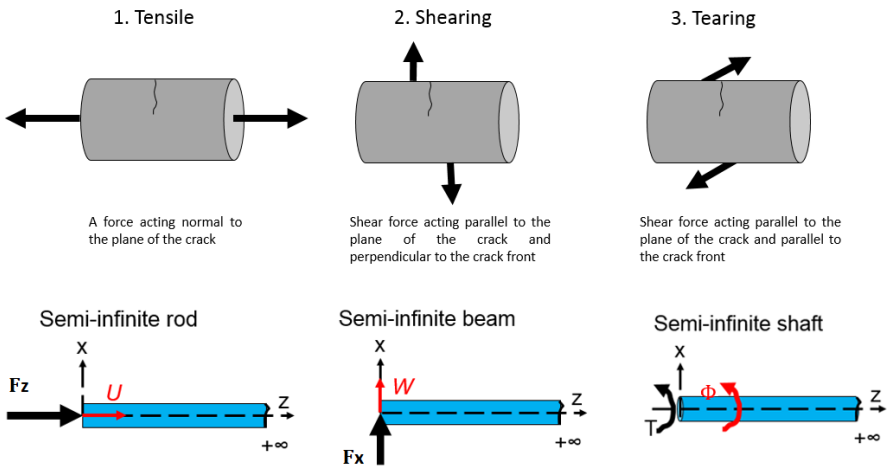

Figure 1-6 Crack type modes in a rod (top) [10]. Displacement models in a rod in order to analyse wave propagation (bottom) [11].

AE sources can be described as either transient waves or continuous waves. Typically, only transient waves are used in SHM as they are generated by the source mechanism (crack mode). Transient signals have a start and end point and hence it is possible to determine the arrival time.

1.2 Structural health monitoring using acoustic emission technique

The damage mechanism in a structure requires to be monitored, evaluated and detected. This can be done by Structural Health Monitoring (SHM). SHM aims to combine advanced sensing technology with intelligent algorithms to diagnose the health condition of structures [12].

There are four main objectives of a SHM system:

1. Detection: The ability to detect the presence of damage on structure as it occurs in real time.
2. Location: To locate the damage on the structure, this is particularly important for pipeline.
3. Characterisation: The ability for the system to determine the type of damage such as crack growth by tension, bending or torsion loading.
4. Evaluation: The ability for the system to understand the significance of the damage and make warning recommendations.

Non-Destructive Testing (NDT) is further used as an integral part of a more general SHM system. NDT methods are used to collect information about parameters that are related to structural performance. The main types of NDT for mooring systems are: Magnetic particle testing, penetrant testing, radiographic testing, ultrasonic testing and acoustic emission testing. Acoustic Emission (AE) technique is considered a unique NDT method, where the material has to be loaded and cracks must occurs in order to generate AE signals. Acoustic emissions are used to detect and monitor defects in complex structures. The technique can also be implemented to monitor flaws in mechanical tests in the laboratory. It is a method for assessing the behaviour of materials deforming under load. Acoustic emissions, or so-called '-hits' or events are the stress waves produced by the unexpected internal stress distribution of a material caused by modifications in the internal structure. Possible reasons of the internal structure changes are crack initiation and growth, crack opening and closure and dislocation movements. Materials release ultrasound when they are stressed and fail on a microscopic scale. The source of ultrasound can be crack initiation, crack growth, friction or undesired noise.

Acoustic emission sources, such as micro cracks, emit transient elastic waves. Elastic waves propagate through the test object (in this case the chain-link). The elastic waves produce a

displacement on the surface. The propagating displacement is monitored once it reaches an AE sensor. An AE-sensor converts the displacement into an electrical signal ($V_{\text{sensor in }\mu V}$), which is called burst emission (AE-signal), as Figure 1-7 shows. AE is typically monitored above the audible frequency range (often 20-1000 kHz) with piezo-electric sensors [13].

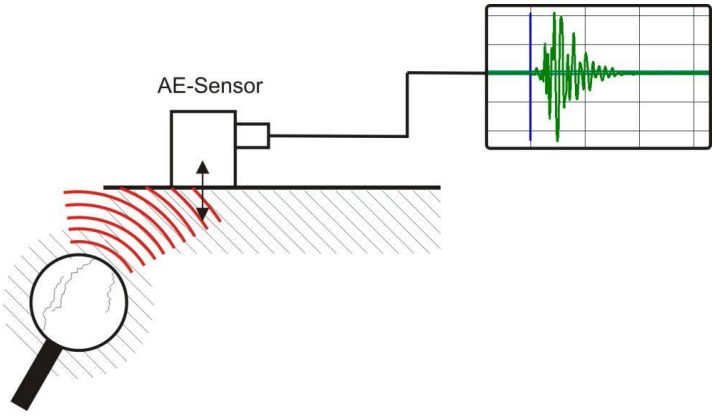

Figure 1-7 Schematic drawing of cracks emitting an acoustic wave [13].

A burst emission is distinguished by an intense increase of wave energy. The amplitude of a burst emission may have one or more peaks amplitude and then decrease, as Figure 1-9 is showed. Once a burst emission passes over the threshold, a hit or event will be recorded. The AE burst signal has important AE features that include: Arrival time, Peak Amplitude, Energy, Rise time, Counts and Duration, see Figure 1-8.

The Peak amplitude of a hit is given in dB_{AE} ($\text{dB}_{\text{AE}} = \text{Decibel} = 20\,\text{Log}(V_{\text{sensor}}/V_{\text{reference}})$. The Rise time is the time between the first threshold crossing and the first peak detected in a hit. The Duration is the time between the first and last threshold crossing of a hit. Counts are the number of positive threshold crossing of a hit. The Energy of each hit is the integral of the squared AE-signal over time.

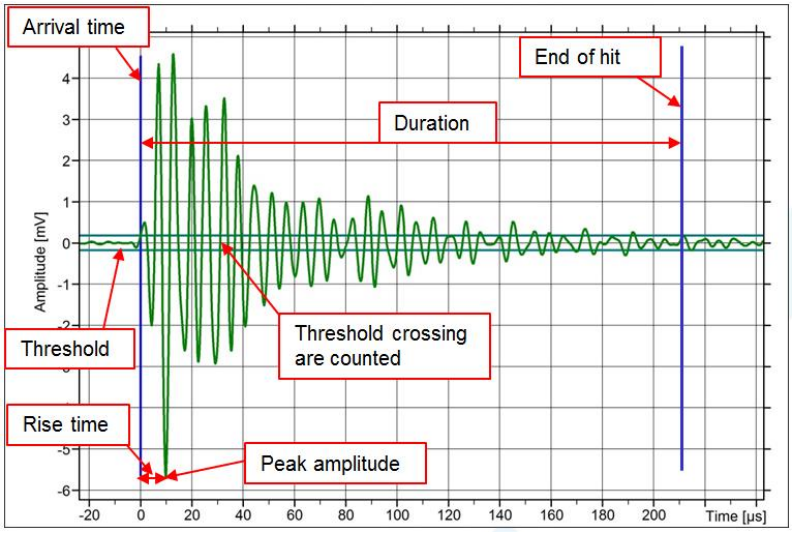

Figure 1-8 AE features extracted for every hit [6]

1.3 Application of AE to mooring chains

In 2013, Bastid et al. [14] presented a paper about numerical analysis of contact stresses between mooring links and potential consequences for fatigue damage. This paper shows the main damages areas as a result of cyclic loading. The design code standards have to be followed et al. [15] for offshore mooring systems from Lloyd's Register and DNV-OS-E301. This is primarily to check that the chain will resist the service load and will not excessively elongate. These codes are mainly based on mechanical testing. Bastid presented and discussed et al. [14] the results of finite element stress analysis of studless chains of different sizes and grades. The paper presented the damage areas in a link in tensile analysis. On the other hand, this static analysis was emulated in ANSYS for this thesis to validate the similar behaviour of damage areas, see Appendix A.

AET is used as a global, real time monitoring Non-destructive Testing (NDT) method for the assessment of structural integrity of large scale structures with an emphasis on metallic vessels, tanks and offshore structures. Acoustic emission is very effective in identifying crack growth and propagation during fatigue tests. It has been observed that different acoustic emission signal properties such as cumulative count or energy, increase as crack grows. According to Han et al. [16] and Chang et al. [17], at the moment of crack growing, the number of events or hits increase because every burst hit represents a micro-crack or material deformation, so the energy and counts are extracted from each hit generated from cracks. Lee and Wang showed et al. [18] that AET is a potential structural health monitoring tool, which can serve as an early warning system for the offshore industry. The acoustic emission signal reflects the dynamic internal stress redistribution within a material that occurs when an external stress is imposed on a component. In the acoustic emission test, piezoelectric transducers are attached to a structure. These sensors convert mechanical energy such as elastic waves into an electric impulse that is transmitted by wired cables or wireless communication to the AET computer.

In 2013, the USA American Bureau of Shipping and SFB NDT Consultant developed et al. [5] a project to investigate the feasibility of the acoustic emission technology for detecting cracks in a mooring chain during a laboratory fatigue test. A R4 grade studless mooring chain was tested with three links submerged in a bath containing simulated seawater. During the fatigue test, the chain was loaded in tension cycle with the stress range of 13% to 38% of yield strength. The position of the acoustic emission sensors is shown in Figure 1-9. Two sensors (#2 and #3) were mounted on the link submerged inside the simulation seawater tank to detect the acoustic emission activities. The other two sensors (#1 and #4) were mounted outside the tank to serve as guard sensors to filter out the external noise from the test machine. Lee and Stanley presented et al. [5] that the stress waves travel through the medium and are detected by acoustic emission sensors, and the

measurements of acoustic emission cumulative energy are relative quantities proportional to the fracture energy, as shown in Figure 1-10. However, Lee and Stanley only presented et al. [5] that the results for a short term test, and an overview about how to undertake a chain tensile test using AE technique. The paper does not cover wave propagation analysis in a chain. It is very important to implement wave propagation on a link because the waves are dispersive and the complex geometric such as bends can have an effect in the waves. For example, Sanderson proposed et al. [19] an analytical model that could predict the guided wave distortion caused by bends using results calculated from Finite Element Method (FEM).

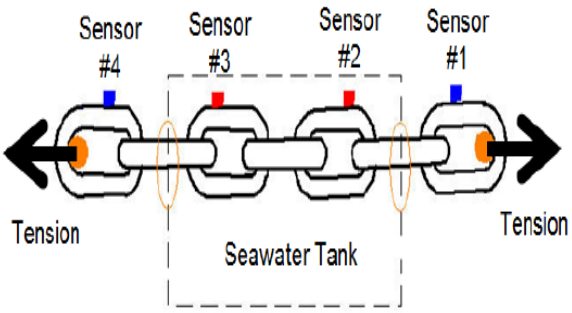

Figure 1-9 Position of AE sensors test [5]

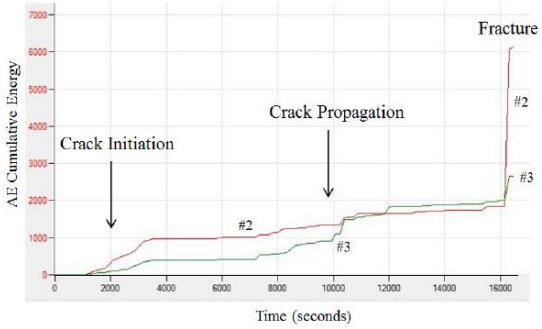

Figure 1-10 AE cumulative energy [5]

1.4 Research motivation

The acoustic emission technique is a method of SHM that senses micro-cracking and moves dislocations in metals. SHM is the process of implementing a damage detection and characterisation strategy for engineering structures. There is a necessity for implementing Structural Health Monitoring (SHM) in mooring chains, use of the best technology for damage detection and development of new post-processing diagnostic algorithms for characterisation. There is a need for technologies that can detect and predict the early stage of damage on a mooring chains. Therefore, it has been identified that the structural health monitoring of acoustic emission technique, would be ideally suited to addressing the issue of damage detection. However, the bent parts of the link, could have an impact during the wave propagation analysis. Therefore, a wave decomposition should be implemented to know what types of waves are excited during tension or bending loading (characterisation). Moreover, the complexity of the geometry in the chain could generates multiples reflections and the superposition of multiple waves, such that it could not be possible to identify the incident or reflecting signals without wave decomposition. Therefore a wave decomposition method should be implemented to know what type of incident wave has the highest amplitude during axial, transversal or rotational excitations.

1.5 Aim and specific objectives

The aim of this research project is to evaluate the possibility of using AET for monitoring of the crack growth on a mooring link. Moreover, implementation of waves decomposition in a bar, bent bar and link to know how the curvatures in a chain could have an effect in the wave propagation.

The key objectives of this work are:

- To undertake tensile tests of one industrial studless link with large diameter in a test rig, and implement a post-processing analysis of experimental data to identify the main AE features, which can detect crack growth.
- To compare analytical solution for fundamental waves in a straight and curved rod to know how the curvature might affect the fundamental waves.
- To develop a frequency numerical model of a rod and a link with capability of predicting the harmonic analysis response, and do wave decomposition in order to know the effect of the bends to identify the waves with high contribution.
- To carry out wave propagation analysis in time domain in a rod of small diameter (45 mm) and implement wave decomposition to know which waves are excited from different excitation conditions.
- To optimize the number of sensors to obtain wave decomposition and conduct measurements on a long rod to validate the wave decomposition from simulation results.
- To develop finite element modelling and wave decomposition in time domain in a bar, bend bar and chain of large diameter (160 mm) to do comparison between each model, and know how the bends have an impact in the wave propagation.
- To undertake experimental work in a bar and link of large diameter to validate the simulation work and wave decomposition.

1.6 Thesis layout

The following represents the structure of this thesis:

Chapter 2 covers the literature review. This chapter is divided into subsections, which describe an overview of mooring chains, advantages and limitations of acoustic emission technique. In addition, a literature review was done in rod and pipes about wave propagation. Finally, the types of methods for wave propagation analysis are presented.

Chapter 3 shows the results of an industrial chain tensile test to monitor crack growth in a test rig. A chain tensile test is carried out in artificial seawater, where different static loads are applied during almost a period of four months. The AE features are plotted versus time to monitor the crack growth. Selected peak amplitude filters are applied to plot the trends of the AE features.

Chapter 4 presents an analytical model of longitudinal and flexural wave propagation in a rod and a beam. The theory is implemented to understand the fundamentals of wave propagation. The analytical model is presented for a semi-infinite rod and a semi-infinite beam, where the mobility transfer function is obtained, and a Gaussian modulated sinusoidal pulse is applied to the bar to plot the longitudinal and flexural wave propagation. Necessary transformations are carried out from time domain to frequency domain and vice-versa. In addition, comparison of fundamental wave is carried out between straight and curved beam.

In Chapter 5 the methodology of wave decomposition in frequency domain is presented. In addition, a finite element analysis of harmonic response is carried out for a bar, half chain and full chain. Perfectly matched layer are used to avoid the reflections and represent semi-infinite bar. Then, a frequency domain wave decomposition is done, where comparison of semi-infinite bar (rod, beam, and shaft) and half chain are presented to show the impact of the curvature in a full link.

Chapter 6 describes the methodology of wave decomposition in time domain. The wave decomposition is implemented in a semi-infinite bar. The purpose of this chapter is to present a study of wave decomposition in a cylindrical steel bar of 45 mm diameter and the minimization of the number of sensors for wave decomposition. The work is carried out on simulation data and validated with experimental measurements.

Chapter 7 presents the wave decomposition for a bar and a link of larger diameter. This is more complex due to the higher number of excited waves for a rod of 160 mm diameter and the complex geometry of the link. Therefore, a Hilbert transform is applied to get that the components can be in phase during the wave decomposition. Wave decomposition in the time

domain is done in straight bar and an industrial link. Then, a comparison between a straight bar and link is made to determine the impact of the geometry. In addition, the work is carried out on simulation and experimental measurements.

Chapter 8 presents the general conclusions from the work carried out so far. The future work is presented as well.

1.7 Contributions

The main contribution in this research project is related to sensing AE waves and implementing a novel method to do wave decomposition in a bar, bend bar and link. In addition, this work focuses in using AET to monitor crack growth on a mooring link and tested in a test rig developed by TWI.

The contributions of this research are:

- A thorough experimental data of crack growth is presented from an industrial link subjected to a tensile loading during almost four months using AE technique. Trend curves of AE features during the chain tensile test are presented, which provide the moment of crack growth detection.
- A novel methodology to do wave decomposition in time and frequency domain are presented. Comparison of wave decomposition in a bar, bent bar and chain are presented, which shows how the bends on a link generate conversion modes.
- The wave decomposition methodology has evidenced the effect of the curvature in a link, where wave modes are converted from axisymmetric to antisymmetric, and reciprocally. Moreover, multiple reflections and distortion of the waves are observed due to the complex geometry on the link.
- Application of the wave decomposition methodology in time domain has identified the wave with higher contribution in a bar and in a link as possible characterisation, when an excitation is applied in-plane or out-of-plane.
- The framework of wave decomposition in time domain has shown that using the radial, circumferential and axial components, the contribution of each wave can be obtained in a bar and in a link.
- Use of the modelling framework to provide insight into the applicability of AE to links.

Chapter 2: Literature review

The purpose of this chapter is to present an overview of the mooring chains, Non-Destructive Testing and Structural Health Monitoring, focusing in advantages and limitation of acoustic emission technique. Moreover, stress corrosion crack using AE is introduced, where the AE features are used to know the crack growth. In addition, a literature review is considered about wave propagation for bar and pipes. Then, wave decomposition methods are reviewed. Finally, the modelling methods to simulate wave propagation in a bar are described.

2.1 Characteristics of mooring chains

There are five main different steel grades used in mooring chains. The international Association of Classification Society (IACS) denotes the steel grades with an R followed by a number. Steel grades R3S, R4 and R4S are considered as high strength steel. Offshore Standard DNV-OS-E302 et al. [1] provides minimum mechanical properties for different steel grades. The required minimum mechanical properties are listed in the Table 2-1.

Table 2-1 Minimum mechanical properties for chains [1]

Steel grade	Yield strength [MPa]	Ultimate tensile strength [MPa]	Elongation [%] at break
R3	410	690	17
R3S	490	770	15
R4	580	860	12
R4S	700	960	12
R5	760	1000	12

A fundamental characteristic of any mooring component is its minimum break load (MBL). Noble Denton Europe Limited et al. [2] presented that the behaviour past the beginning of the necking, see Figure 2-3, depends material characteristics as well as the rate at which the load is applied. The relationship between the stress and strain that a particular steel material display is known as that particular material's stress-strain curve (Figure 2-3). It is unique for each material and found by recording the amount of deformation (strain) at distinct intervals of a variety of loadings (stress). The stress and strain can be normal, shear, or mixture, also can be uniaxial, biaxial, or multiaxial, even change with time. The form of deformation can be compression, stretching, torsion, rotation.

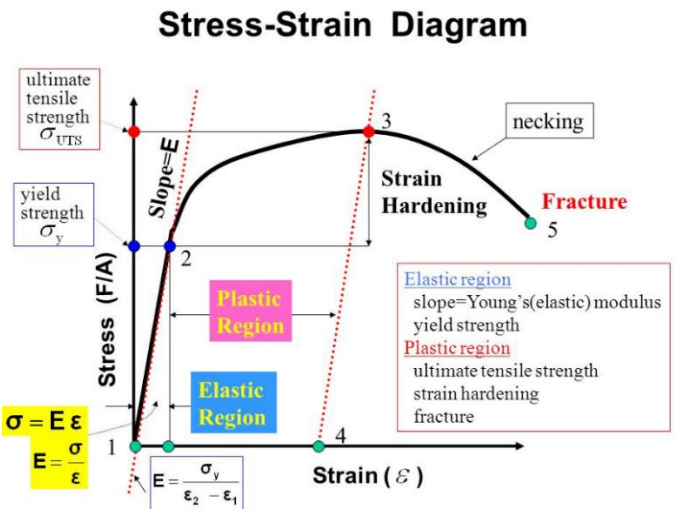

Figure 2-1 Elastic-plastic stress-strain behaviour [20].

The load recorded at which the material breaks is related to the strain rate at which the load is applied, so it is somewhat variable. International Association of Classification Societies (IACS) states: "each chain sample shall be capable of withstanding the specific break load without fracture and shall not crack in the weld. It shall be considered acceptable if the sample is loaded to the specified value and maintained at the load for 30 seconds". Noble Denton Europe Limited reported et al. [2] that there are primarily two types of chains links, stud link and studless links, common stud links have length 6.00 D, width 3.60 D and inner link radius equal to 0.65 D. Common studless links have length 6.00 D, width 3.4 D and an inner link radius equal to 0.60 D. The letter D stands for nominal diameter, common link design is sketched in Figure 2-4.

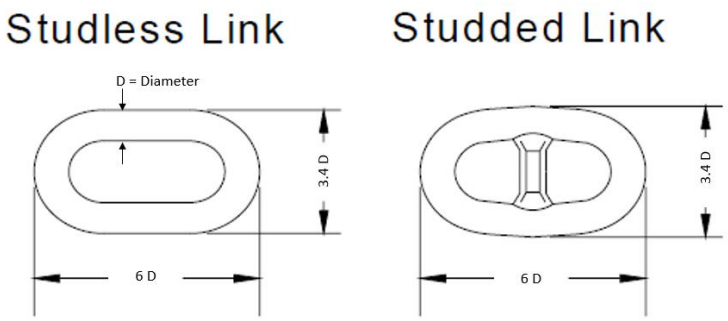

Figure 2-2 Common link design [2].

On the other hand, according to Health and Safety Executive JIP on FPS mooring integrity, suppliers of links have confirmed by physical testing that they have achieved the specified minimum break load (MBL) and proof load values [2]. Table 2-2 indicates the MBL and proof loads for various size and grades of chains. D is the expression referring to the chain diameter in mm.

Table 2-2 Stipulated MBL and proof load values of chains (courtesy of Vicinay) [2].

Chain	units	Stud link	Studless link
Proof load R3	kN	$0.0156\ \mathrm{D}^2\ (44 - 0.08\ \mathrm{D})$	
MBL R3	kN	$0.0223\ \mathrm{D}^2\ (44 - 0.08\ \mathrm{D})$	
Proof load R4	kN	$0.0216\ \mathrm{D}^2\ (44 - 0.08\ \mathrm{D})$	$0.0191\ \mathrm{D}^2\ (44 - 0.08\ \mathrm{D})$
MBL R4	kN	$0.0274\ \mathrm{D}^2\ (44 - 0.08\ \mathrm{D})$	
Proof load R5	kN	$0.0251\ \mathrm{D}^2\ (44 - 0.08\ \mathrm{D})$	$0.0222\ \mathrm{D}^2\ (44 - 0.08\ \mathrm{D})$
MBL R5	kN	$0.03186\ \mathrm{D}^2\ (44 - 0.08\ \mathrm{D})$	

The last stage of chain manufacturing is proof loading. The proof load depends on the link size and grade, and is approximately 70% of the minimum breaking load (MBL) for studless link. Yielding due to this high load causes a restructuring in the material that prevents elongation of the chain by falling under cyclic loading in service. Proof loading also gives assurance that the yield stress and plastic behaviour of the material meet the specification for the grade.

2.2 Non-destructive testing and structural health monitoring

There is a continuing need for methods of non-destructive testing (NDT), especially those capable of rapidly detecting even smaller sized defects, there is also a need to go further than just detection to the assessment of the effect of the defect on performance and life. This extension of NDT which includes the steps of diagnostic and prognosis is often known as structural health monitoring (SHM). In many cases the SHM of a component, structure or system can be conducted autonomously, or at least, without removing that item from service [21].

Thompson et al. [22] attempted to provide differentiation between NDT and SHM by stating that NDT refers to those situations in which the relative position of a measurement system and the component under inspection can be manipulated with respect to one another, whereas SHM refers to those situation in which fixed sensors are placed on a structure, either in-situ or ex-situ. One could also consider that NDT focuses on time-based, off-line, monitoring using passive systems that provide disparate and partial information about the condition of a material or structure, facilitating time-based maintenance that is time consuming and could necessitate downtime. SHM, on the other hand, focuses on condition based, on-line monitoring using combinations of active and passive systems that provide a comprehensive assessment of the health of the material or structure, facilitating proactive maintenance that results in intelligent asset management.

Traditional NDT technologies are based on the detection of damage or defect. There are a range of NDT techniques used and some of the most commonly used technique can be classified as

electromagnetic testing, ground penetrating radar, laser testing, magnetic flux leakage, microwave testing, ultrasonic inspections, guided wave testing, visual inspection and acoustic emission testing.

Electromagnetic testing uses a magnetic field, which is passed through a conductive part, there are three types of electromagnetic testing, including eddy current testing, alternating current field measurement. Forsyth presented et al. [23] that Eddy current testing, is commonly used to inspect objects throughout their life cycle, where the eddy current techniques employ alternating currents applied to a conducting coil held close to the test object. In response, the test object generated eddy current to oppose the alternating current in the coil. Changes in the induced eddy currents may be caused in geometry caused by cracks. Ground penetrating radar sends radars pulses through the surface of a material or subsurface. The waves are reflected when they encounter a buried object with different electromagnetic properties. Laser testing uses a laser to detect changes in the surface of the material, which has been subjected to stress such as heat, pressure or vibration. Lase shearography uses laser light to create an image before the surface is stressed and new image is created. Magnetic Flux Leakage (MFL) method uses a powerful magnet to create magnetic fields, which saturate steel structure such as pipelines and storages tanks. A sensor is then used to detect changes in magnetic flux density, which show any reduction in material due to pitting, erosion or corrosion. Wang presented et al. [24] the discussion of the physical mechanism and some important experimental results relevant to three NDT technologies about magnetic flux, Barkhausen noise and metal magnetic memory. Microwave testing method is restricted to use on dielectric material and uses microwave frequencies transmitted and received by a test probe. The test probe detects changes in dielectric properties such as cavities, pores, foreign material or cracks and display the results as B or C scans. Mazzinghi presented et al. [25] a paper, which exploits the possibility of extracting the geometry properties of a polymeric coating of periodic metal layers used in industrial products from non-contact microwave backscattering measurements. Guided wave testing is an ideal method for testing pipes over long distance, guided wave testing uses ultrasonic wave form to reflect changes in the pipes wall, which are sent to a computer for control and analysis. Visual testing also known as visual inspection is one of the most common techniques, which involves the operator looking at the test piece. Ultrasonic testing entails the transmission of high frequency sound into a material to interact with features within the material that reflect or attenuate. Seleznev presented et al. [26] that ultrasonic fatigue testing is an effective method for the rapid characterisation of the high cycle fatigue properties of structural materials. Acoustic emission testing is a passive NDT technique, which relies on detecting the short bursts of ultrasound emitted by active cracks under a load.

2.3 Advantage and limitation of Acoustic emission technique

Acoustic emission is a passive method that monitors the transient stress waves based on the rapid releases of energy within a material generating transient elastic wave propagation from localized sources, e.g. fracture, within a material. The sources of acoustic emissions are the mechanism of fracture or deformation phenomena within materials, such as crack initiation and growth. The AE technique offers some unique and advantageous capabilities, such as: Real-time and continues monitoring of the state of a material or structure under stresses, detection or growing defects or damage during its services life, unattended and remote monitoring, global monitoring of a large structure by a spare sensor network, detection of incident failures long before the final failure, which can prevent catastrophic failures. Xu et al. [27] presented that AE is very suitable to monitor structural integrity due to its advantages of continuous monitoring and location of dynamic defects. The difference between the AE technique and other non-destructive evaluation (NDE) methods is that the AE technique senses micro-cracking and moving dislocations in metal, while the other NDE methods are active methods. Miller et al. [28] described that an active method sends signals into the structure and analyses the response, whereas a passive method only receives the occurrence of the defect directly, being sensed from the damage site. Furthermore, Chai et al. [29] showed that AE only needs the input of one or more relatively small sensors on the surface of the structure or specimen being examined, so that the structure or specimen can be subjected to the in-service or laboratory operation, while the AE system continuously monitors the progressive damage. The AE technique has certain limitations: AE testing must be conducted under load, it is not suitable for determining the size of damage or flaw, data analysis and interpretation may be difficult in some cases, data interpretation mainly relies on AE experts. Smanio et al. [30] described that the disadvantage of AE is that AE systems can only estimate qualitatively the extent of damage or size of the defect, where a characterization is necessary to estimate the crack size. Hwang et al. [31] presented that other NDE methods are still needed to do more exhaustive examination and provide quantitative results. Moreover, service environments are generally very noisy, and the AE signals are usually very weak, so signal discrimination and noise reduction are very important for successful AE application. Another disadvantage explored by Rivera et al. [6] is that the structure has to be under load to detect damage. Lee et al. [5], [18] presented structural health monitoring on mooring chain and leakage in pressure vessels using AE including for the detection of defects. AE has also be used to monitor the welding process. Some limitations of AE testing are: repeatability (acoustic emission is stress unique and each loading is different), attenuation (the structure under test will attenuate the acoustic stress waves), history (tests are best performed if the loading

history of a structure is known) and noise (acoustic emission can be subject to extraneous noise) [28].

2.4 Monitoring of stress corrosion crack with AE

One of the most common failure mechanisms seen in the mooring line of floating units is the failure of an individual chain, due to Stress Corrosion Cracks (SCCs). Hwang et al. [31] presented that SCC is the cracking induced from the conjoint action of three components: a susceptible material, a specific chemical environment and tensile stress.

To ensure the integrity of structural materials, regular non-destructive inspections of chains are carried out. The state of the chain is monitored through a periodic inspection using non-destructive testing techniques such as the radiography, guided wave ultrasonic, visualization, etc. However, these techniques have certain limitations preventing them from adopting in continuous monitoring. Cracks can be detected only after they grow to certain relatively large size. Initiation of cracks can be missed if these techniques are adopted. For continuous monitoring, Mao et al.[32] presented and Bassim et al. [33] showed that AE is one of the promising methods for detecting both initiation and propagation of stress corrosion cracks. AE are elastic energy waves that are spontaneously released by a material undergoing deformation or crack initiation and crack growth processes.

Xu et al. [27] and Smanio et al. [30] have used AE to monitor crack initiation and growth for different specimens of different structures like pipe and tank, respectively. Chai et al. [29], Hwang et al. [31] found that AE features such as energy and counts can be correlated to estimate the crack growth rate. Han et al. [34] attempted to investigate the AE count behaviour and source mechanism during fatigue crack propagation in a micro-alloyed steel specimen. The results showed that the acoustic emission was more sensitive to the changes in the fracture mode. Yuyama et al. [35] reported that several processes are responsible for acoustic emissions during SCC. These include metal dissolution, hydrogen gas evolution, and fracture, plastic deformation by slip or twin and micro/macro-cracking. Smanio et al. [30] used AE for monitoring steel cracking during exposure to wet hydrogen environments. High increments of AE energy were detected. It was stated that this sudden increment in AE energy corresponded to initiation of SCC, which has caused high amplitude AE signal.

It is important to note that in most of the work done by researchers, the AE technique was used to monitor crack initiation and crack growth, but testing was carried out on small specimens and for only short periods of time. In this thesis, a long term chain tensile test was carried out, more details in chapter three can be found.

2.5 Wave propagation in bars and pipes

Effective inspections are necessary to monitor the health of cylindrical bar. A failure in a bar could arise from axial, bending and/or twisting loads. This type of failures excite longitudinal, flexural and/or torsional waves at ultrasonic frequencies in a cylindrical bar that propagate along its axis [36]. Elasticity is a solid's property for restoring its shape and volume after the termination of external forces applied to it. A medium that exhibits these properties is referred to as an elastic medium. Elastic or acoustic waves are mechanical disturbances that are produced in an elastic medium. Elastic vibrations and acoustic waves are widely used in Non-Destructive Testing (NDT) and material diagnostics. Elastic vibrations and waves can be used to investigate the processes of crack initiation and propagation in rods made of an elastic medium such as steel at the relatively low amplitudes of vibration involved [37].

An extended cylindrical structure like a rod provides the propagation of mechanical waves at ultrasonic frequencies along its axis. The government equations of mechanical wave propagation in cylindrical structures are described by the Pochhammer and Chree theory, but its complication stopped researchers from getting good results until the arrival of computers. The solutions linking the phase or group velocity with frequency remained unexplored until the middle of the last century, when the first branches of the dispersion curves were obtained numerically. Seco et al.[38] and Valsamos et al. [39] presented that the number of modes varies with the radius of the bar and with frequency. Gazis et al. [40] described the first exact solution of the Pochhammer-Chree frequency equation, including a full description of propagation modes and stress and displacement distribution for an isotropic elastic tube. Graff et al. [41] provided a modelling response of the wave propagation, which transforms the equations that physically model the excitation inputs and the behaviour of the waves into a group of algebraic equations. For over half a century, the theme of wave propagation in straight rod has been conducted by many researchers, who presented diverse theoretical approaches. A good summary is provided by Rose et al. [36]. Seco et al. [38] presented matlab routines to calculate the phase speed and the wave mode shape using the Porchhammer-Chree theory. Moreover, appendix B shows the government equations of mechanical wave propagation in cylindrical solid structures.

There are two important long range techniques for NDT of pipes and rods. One is called Ultrasonic Guided Wave (UGW) testing, which is an active technique that requires ultrasound transmitters and receivers to characterize the damage in the specimen [36]. The other is called Acoustic Emission (AE) testing, which is a passive technique that requires only ultrasound receivers to characterize the damage in the specimen. Yuyama et al. [35] presented that AE relies on the generation of transient elastic waves produced by the sudden redistribution of stress in a

material. This normally occurs when a crack initiates and grows and therefore requires the specimen to be under an external load.

Researchers have conducted numerous studies of wave propagation in pipes, due to the introduction of UGW as a NDT method. More recently, there has been an interest in developing UGW methods for NDT of pipes, but there have not been any studies of wave propagation in chains. Demma et al. [42]–[44] has done several studies about the effect of bent pipe on the propagation of guided waves. Mode conversion at the bend location has been validated by Demma. In addition, Demma studied bend radius, bend length and ultrasonic wavelength, which are the three parameters affecting wave propagation through the bend. Demma showed that for a large bend radius, there is little mode conversion from symmetrical to flexural modes in the curved pipe section. For an intermediate bend radius, there is some mode conversion at the start of the bend. Abbasi et al. [45] studied the detection of cracks in U-type bends using high frequency guided waves, where the behaviour of the crack signal as a function of time was studied, to estimate time of flight of the reflected wave and consequently the crack position. Sanderson et al. [19] proposed an analytical model that could predict the guided wave distortion caused by bends using results calculated from Finite Element Method (FEM). The orientation and amplitude of wave modes received after the bend in a pipe were quantified for a range of possible wave modes in the torsional family. This indicates that the standards guided wave inspection would be inaccurate and there would be greater potential for false calls. Verma et al. [46] investigated the effect of different bend angles on the propagation of guided waves, using the ratio of the mean bend radius to the wavelength of the mode. The study showed that as the bend angle is reduced, a progressively larger extent of mode conversion affects the transmission and velocity characteristics of the second longitudinal L(0,2) mode, he found that L(0,2) the velocities of the mode converted signal were close to that of F(1,1) mode for bend angles below 90 degrees and to the F(1,2) mode for bend angle above 90 degrees. Yamamoto et al. [47] evaluated the effect of multiples bends on the propagation of guided waves. The comparison between the simulation and experimental results shown in the paper implied that regions with high sensitivity correspond to high amplitude regions. This means that the location of a defect sensitive region is controlled by the centre frequency of the input signal.

Miller et al. [28] presented that the major difference between the AE method and all other NDT methods is that they are mostly active methods. The conventional AE method only captures certain AE features, including AE hit, count, peak level, rise time, duration, and energy. Then accumulated AE features are correlated with the defect formation and failure. These AE features are only related to the captured signal, which includes incident, multiple reflections and superposition of all the excited waves. They do not account for only the incident signal with

higher wave contribution.

To improve the effectiveness of AE features, research should be conducted on analysis of AE signals. It is possible to solve the inverse wave propagation problem to identify the source of the AE signal detected using one or more sensors, by analysing whole waveforms. However, it is difficult to solve the inverse problem without any information about the source. Alternatively, Marcus et al. [48] and Zarini et al. [49] have analysed the response from known AE sources, such as the elastic wave emitted from a Pencil Lead Break (PLB). PLB is a long established standard methods for the generation of artificial AE, namely the Hsu-Nielsen source methods. PLB consists of breaking the lead of a mechanical pencil on the structure. The process of breaking causes elastic wave to propagate in the structure. Thurston et al. [50] and Zemanek et al. [51] studied that wave propagation in structural components, such as a cylindrical solid bar, is more complex than in pipes, because the boundary conditions create AE signals which are the superposition of multiple guided wave modes. Lysak et al. [52] presented that the received signal is actually a combination of the longitudinal, torsional and flexural modes and their reflections. However, if a wave mode decomposition can be done before any reflections, it will help to make the signal easier to interpret. That way, the longitudinal or flexural waves with a high contribution from the incident wave can be used to describe the behaviour of AE directly from the source, for example a crack.

2.6 Wave modes decomposition

There are a number of papers available in the literature describing different methods for wave modes decomposition relevant to a cylindrical bar. One of the most basic methods is to use a discrete Fourier transform, where the contribution of the modes in a narrow frequency can be determined, but it cannot determine individual flexural modes because multiple wave can be excited in a narrow frequency, it is necessary to do a wave decomposition to determine the amplitude of individual flexural waves [53]. Alleyne et al. [54], [55] presented a technique for the analysis of propagating multimode signals, the method involves a two-dimensional Fourier transformation (2-D FFT) of the time history of the waves received at a series of equally spaced position along the propagation path. The method identifies and measures the amplitudes of Lamb modes in a plate. Pedram et al. [56] introduced an advanced signal processing technique called Split Spectrum Processing (SSP) to reduce the level of noise. The SSP methods involves filtering a signal using a bank of band filters in order to generate a set of sub-band signals. These sub-band signals are then subjected to a number of processing techniques in the time domain. Catton et al. [57] and Hayashi et al. [58], [59] presented a novel method of processing multi-mode signals from UGW in pipes, used in long range ultrasonic testing, in which it is possible to separate different

orders of flexural waves. The waves in this case are grouped by the same number of harmonic variations around the circumference of the pipe. However, it is not possible to differentiate between flexural waves with the same harmonic order but from different wave mode families. Zarini et al. [49] developed a wave decomposition in the time domain for a beam, to assess the most important contribution to the response to transient loads. Fateri et al. [60] and Lowe et al. [61] presented the reflection and mode conversion behaviour for the first longitudinal L(0,1) and flexural F(1,1) in an aluminium rod of 8 mm diameter. According to the dispersion curve only the first fundamental longitudinal mode L(0,1) and flexural F(1,1) are presented at frequency lower than 100kHz. However, Seco et al. [38] showed that multiple wave modes will exist within the same frequency range for a rod of large diameter, and signal interpretation will be more complex. Fateri et al. [52] and Rose et al. [53] concluded that the presence of higher order modes are a challenging scenario in UGW inspections.

2.7 Wave propagation modelling method

Seco et al. [38] mentioned that several approaches exist to consider modelling the response of the waveguide to external excitation. For instance, Integral transform method convert the differential equations that physically model the excitation forces and the behaviour of the waveguide into a set of algebraic equations, which are more easily solvable. However, in order to find the actual distribution of the elastic field excited in the waveguide, inverse contour integration in the complex plane has to be performed, which is usually complicated. Due to the complexity of the Pochhammer-Chree equations, this procedure is only practical with simplified versions of the wave equation, which in general are not accurate enough for ultrasonic frequencies.

Hosten et al. [62] described that many problems in engineering are either difficult or impossible to solve analytically due to the complexity involved in describing the geometry of a real life structure. As a consequence, analytical solutions can be obtained only for limited simple situations. For complex systems, engineers therefore resort to numerical methods, which provide an appropriate approximation to the solution. Sanderson et al. [63] described that most numerical methods, such as the Finite Element (FE) methods, use a technique of discretisation in which the solutions are formulated based on a constituent set of elements or nodes, which are then combined to obtain the solution for the whole structure. In the case of FE, as the size of the elements becomes smaller, the models form a continuum which represents the real structure with increasing accuracy. Thus numerical technique takes advantages of the recent rapid advance in the processing power of digital computer to include enormous complexity while being able to analyse the solution efficiently. FE procedures have been employed extensively in solid and fluid

structures for analyses of heat transfers, stress, etc. Recently, they have been used increasingly in simulating ultrasonic waveguide propagation. Sanderson carried out et al. [63]–[66] many FE model analysis method, these FE method provides a vital research tool for both academic and industrial use.

Hayashi et al. [58] described that the Semi-Analytical Finite Element (SAFE) method is a modification of Finite Element Method (FEM), in which the elastic field is expanded as a superposition of harmonic waves in the circumferential-axial plane, while discretised mechanical equations are used in the radial direction of the waveguide. This reduction of the number of dimensions permits a much higher efficiency in the computation of the elastic fields. Jia et al. [67] described that waveguides surrounded by infinite media can be handled by SAFE technique with proper discretized elements, as well as waveguides with arbitrary profile, for example Damljanovic et al. [68] implemented this SAFE technique in railroad rail, and Alleyne et al. [54] used the same SAFE technique for I-beam aircraft wing spar. Although finite element methods are powerful and flexible, they have the shortcoming of great requirements on computer memory and processing time when large structures or high frequencies of operation are considered.

Karpfinger et al. [69] applied spectral methods to model multi-layered cylindrical waveguides, spectral methods are another numerical technique to approximate the differential elastic equations of the waveguide, turning the problems of finding the wavenumber-frequency roots into a matrix eigenvalues determination. This numerical method, which is computationally simple and reportedly does not suffer from the problems associated with large diameter waveguides at high frequencies.

There are methods, which make use of finite elements in a different and more effective manner. Zarini et al. [49] implemented the Wave Finite Element (WFE) method, which uses conventional finite elements to models only a portion of the waveguide as a 3-D solid and approximates the wave propagation along one of the axes. The WFE method approximates the wave motion to be consistent with wave propagation along the axis of the waveguide. Pavlakovic et al. [70] mentioned that this WFE method can be convenient for studying the propagation of elastic waves in structures being either invariant or periodic along one axis.

Some commercial software suites specifically designed for modelling elastic wave propagation in cylindrical waveguides exist. Pavlakovic and Lowe et al. [70] developed a software called Disperse, which is a commercial package, based on matrix technique, capable of analysing cylindrical or plate waveguides made of perfectly elastic. Bocchini et al. [71] developed a similar software called GUIDUW, which is a Matlab-based software which utilizes a SAFE-based approach to model ultrasonic propagation in cylindrical, plate, and arbitrary cross section waveguides. Moreover,

there is a software package, named PCDISP, based on Pochhammer-Chree theory, written in the Matlab environment by Seco et al. [38] and freely available to be adapted to particular circumstances. However, none of these computer solutions permit to model the waveguide response to external excitations.

2.8 Conclusions

The link is one of the most important components of the mooring line because whether one chain fails the mooring line breaks and the floating unit could shut down. Design codes for offshore mooring system recommend proof loading link to around 70% of the specified breaking load of a chain, this is to verify that the chain will safely resist the service loads. Tests have shown that proof loading improves the fatigue performance of chain under axial loads. However, the proof loading also generates very high tensile residual stresses. Then, the combination of high tensile stress and seawater can generate stress corrosion cracks. Therefore, a structural health monitoring technique should be implemented to know the health in the link. There are some techniques for structural health monitoring. However, the majority are active techniques which requires a transmitter and receivers to assess the health in a structure. Acoustic Emission is a passive technique, which receives the waves generates from cracks and noise environment. The acoustic emission technique is a powerful technique, which could describe the health of the link and the AE features could be used to know the time when the crack grows. According to some authors, they defined that the cumulative energy and cumulative counts can be used to know how fast the crack is growing. However, they have done the conclusions in short term test or small specimens. Therefore, it is necessary to carry out a long term test in an industrial link to know the moment of crack growing. In the next chapter, a long term tensile test is carried out using AET.

On the other hand, the longitudinal, torsional and flexural waves can be excited in a solid bar from possible cracks. In literature was found that the bends can produce wave modes conversion. However, these conclusions are done for a bent pipe. It should be noted that the wave propagation for a rod or bent rod is more complex due to the high number of excited waves. The chain has two bends and two straight part, considering the straight part as a cylindrical bar, a study can be decomposed from complex to simple geometry. Cylindrical bars are components parts of many structures and could be exposed to both axial load in-plane and out-of-plane bending. The Pochhammer-Chree theory deals with wave propagation in structures with cylindrical symmetry like rods. Therefore, this theory can be used to extract the wave mode shape

and to get the dispersion curves for a straight bar. However, the link is a complex structure where the geometry could have an impact in the waveform. Therefore, finite element analysis should be carried out to do wave propagation analysis to research how the curvature and the diameter could have an effect in the excited waves within a frequency range.

The researchers mentioned in literature review only investigated the effect of bends in pipes, where the number of excited modes are fewer when compared with the bent rod. In a mooring chain, where there is in essence a double U-bend, the behaviour of wave propagation is even more complex. It is noticed that the chains used in offshore industry are normally of large diameter, this means that the number of excited waves is higher too compared to rod of small diameter. Therefore, a study is carried out in this thesis to do wave decomposition in the frequency and time domain for a link of large diameter. It should be mentioned that no research about wave decomposition has been done in link before.

Chapter 3: Experimental chain tensile test

3.1 Introduction

The purpose of this chapter is to present a feasibility study of AE testing in a test rig to monitor stress corrosion crack growth in a mooring link following application of a high tension load in a static manner. The tensile test was carried out in artificial seawater (3 % NaCl solution) using a single grade R5 link of diameter 160 mm for 3.7 months where a crack was initiated from a notch. AE features were plotted against time and these plots were extensively discussed with the view of contributing to the closure of a knowledge gap in the experimental literature.

The objective of the test is to establish the time when SCC initiation takes place and how SCC grows during a tensile test. This chapter is organized as follows. An overview of the AE monitoring set-up on a submerged link under uniaxial tension, the environmental conditions of the test rig, the types of sensors used and the way the threshold was selected to trigger the AE signals are described. Then, an overview of the AE features extracted during the chain tensile test is presented. Moreover, trial chain test, which was carried out for a week to verify that the sensors and equipment were working correctly and to check the machine noise and environment noise levels associated with this particular test rig, is described. In addition, the loads applied during the full test, the specific minimum break load and proof load applied by the chain manufacturer previously, are presented. Finally, the results and analysis of following post-processing respectively are shown, where three filters of peak amplitude were applied to the AE data, namely 45 dB, 55 dB and 65 dB. Each cumulative AE feature (energy, counts, duration, rise time, peak amplitude and hits) is plotted versus time, thus describing how fast the crack grows at the three recording threshold levels.

3.2 Experimental set up of acoustic emission test

A full-scale static tensile test of a studless link under cathodic protection was carried out in seawater at TWI laboratories. The link et al. [72] was grade R5 steel (C 0.24, Si 0.2, Mn 2.2, Mo 0.26), in this experiment the link was the same grade R5 with a diameter of 160 mm. The test lasted circa 4 months (2780 hrs) in order to monitor SCC initiation and growth. SCC was initiated from a notch (depth 1.5 cm) machined into the unwelded shank using an Electric Discharge Machine (EDM). According to the relevant codes and standards et al. [1], the link delivered for the test was proof loaded by supplier before the tensile test. Following Bastid at el. [14], this is to increase the service life of the link .

Figure 3-1(left) shows an overview of the monitoring set-up with the AE sensors on the tank and the AE sensor submerged on the chain. Figure 3-1 (right) shows the VALLEN AMSYS-6 AET system, which was used to record AE data. The sample rate in AMSY-5 system during the full chain tensile test was set as 5 MHz (0.2 µs). This is a multi-channel AE-measurement system with front-end software running on an external laptop. Each measurement channel consists of an AE-sensor, AE preamplifier and one channel of an ASIP-2 AE signal processor card [13]. The AE sensor for water environment was positioned on the same flank of the chain as the initial notch and on the opposite surface as shown in Figure 3-1 (left).

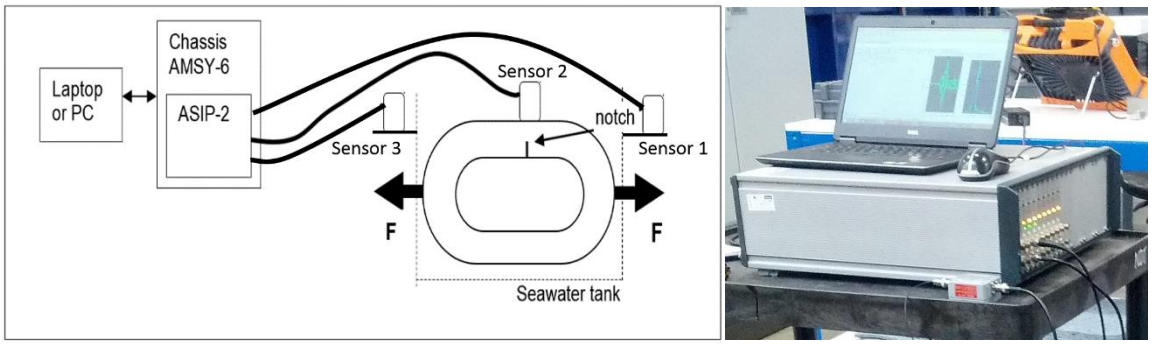

Figure 3-1 Diagram of AE monitoring set-up sensors of link under uniaxial tension (left), laptop with VALLEN AMSYS-6 AET monitoring system (right).

Figure 3-2(left) shows the dimension of the chain link used in the experiment, which has a length (960 mm) 6.0 time the diameter, width (544 mm) 3.4 time the diameter and an inner link radius (96 mm) equal to 0.60 time diameter [2]. Figure 3-2(right) shows the test rig customized for this experiment. The link was submerged in 3.5 % NaCl solution artificial seawater with cathodic protection at -1100 mV to replicate the operational environment of the mooring chain. The solution was circulated in the tank and was controlled at a temperature of 20±2 °C. During the full chain tensile test, the static tension load was applied in 5 steps. Application of a sufficiently high constant static load in seawater with cathodic protection is expected to lead to hydrogen embrittlement in the vicinity of the crack tip. This has the potential of making this area more brittle compared to the uncracked area and it is expected that the crack grows under these circumstances provided that the crack driving force exceeds the stress intensity threshold.

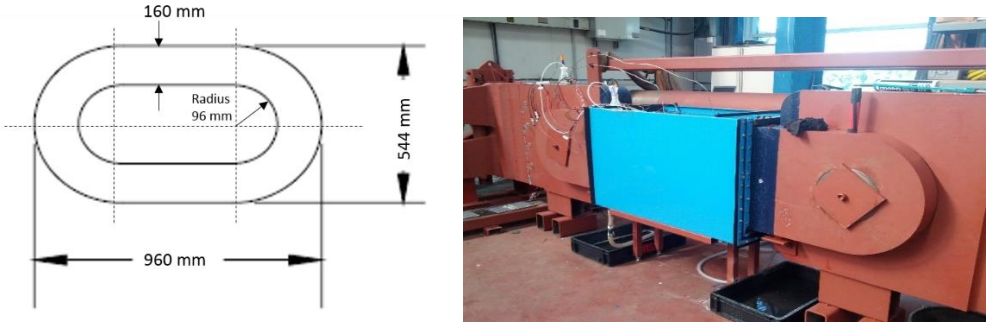

Figure 3-2 Dimensions of link (left), Mooring chain test rig (right)

Figure 3-3 (left) shows the AE sensor 2, which was mounted with a magnetic holder on the link, the sensor2 has a diameter of 32 mm and height of 48 mm. Grease couplant was used to improve the transmission between the contact surface and the sensor. The AE sensor 2 was type VS150-WIC-V01, which has a piezoelectric AE-sensor and an integrated preamplifier gain of 34 dB. Figure 3-3 (right) shows its resonance frequency of 150 kHz and the operating frequency range from 90 to 450 kHz. It is suitable for on-site monitoring of underwater installations.

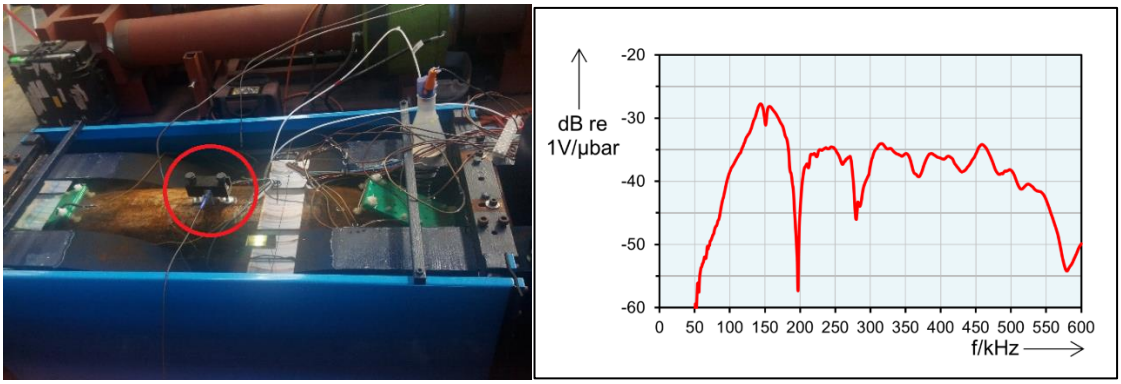

Figure 3-3 AE sensor 2 attached on the link for wet environment with 3.5 % NaCl solution artificial seawater (left). Frequency response of sensor 2 (right) [13]

The static chain test rig was also instrumented with two additional AE sensors to record the noise level from the machine during the test. These sensors (sensor 1 and sensor 3) were mounted with magnetic holders outside the tank to serve as 'guard' sensors (Figure 3-4). The guard sensors filter out the external noise from the test machine [5]. Sensors 1 and 3 are VS150-RIC, which has similar frequency response range as the VS150-WIC-V01 but a diameter of 28 mm and height of 32 mm. These sensors are suitable for testing on metal [13].

Figure 3-4 AE sensor type VS150-RIC (left: sensor 3, right: sensor 1)

The machine noise was recorded for a whole day with an unloaded link to define the threshold to trigger the AE-signal during the actual test. Figure 3-5 shows the machine noise in sensor 1 and

sensor 3. It can be seen that the average noise is below 45 dB. However, at time 18.5 hours, many hits are recorded specifically by sensor 3. These are thought to have been generated by people working around the tank near sensor 3.

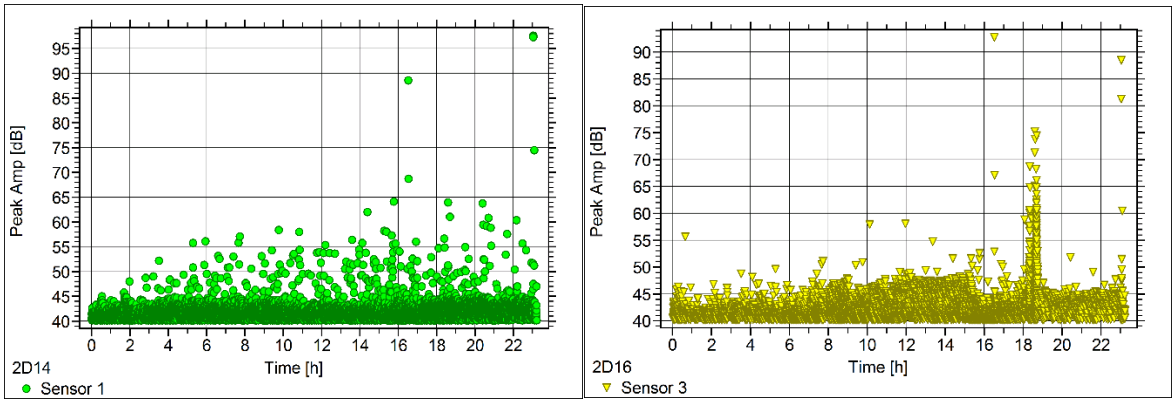

Figure 3-5 Envirotmental noise in sensor 1 (left) and sensor 3 (right) before starting a trial test, these sensors were attached outside the tank to know the machine noise on the test

Figure 3-6 shows the spectrum of some hits for sensor 1 and sensor 3, the spectrums were obtained from the hits at time 5 hrs, 10 hrs and 18.5 hrs (Figure 3-5) during the environmental noise measurement. It is observed that the frequency range of higher amplitude is between 90 and 300 kHz. The frequency response looks similar behaviour for each hit, this means that frequency analysis can provide few information about damage. Therefore, the AE features like peak amplitude in time domain are considered to measure how fast a damage is accumulated.

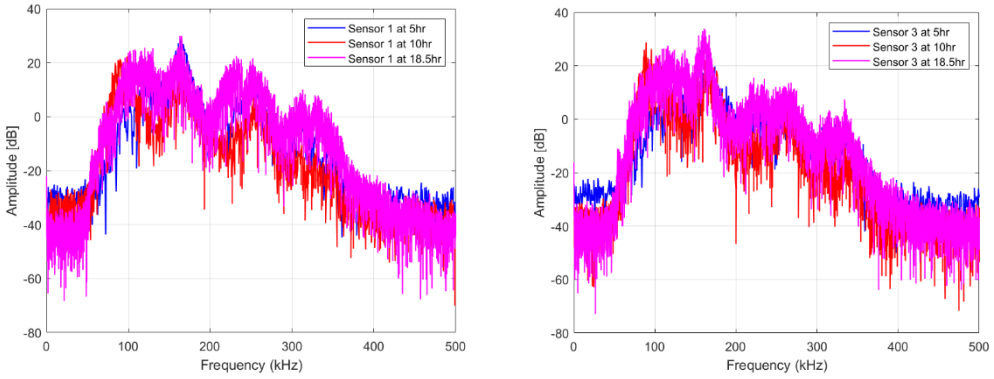

Figure 3-6 Spectrum signal of hit at time 5 hrs, 10hrs and 18.5 hrs: sensor 1 (left), sensor 3 (right)

AE acquisition parameters setup at the beginning of the test included the start and end criteria for the hits, the filter setting and the sample rate of each channel. After acquiring data with a lower threshold of 40dB for one day unloading the chain, the level of machine noise was tested. It was decided to add 5 dB to this noise threshold, giving a threshold setting of 45 dB. Moreover, a filter (90-300 kHz) to limit the frequency range of the signal was used. Figure 3-7 shows the spectrum

signal of one hit to show the data with filter and without filter. It can be observed that the signal without filter is within the frequency range of the sensor (90-450 kHz). However, when the filter is applied, the signal is cut after 300 kHz. I should be noted that the highest amplitude in the spectrum is in the same frequency for both signal.

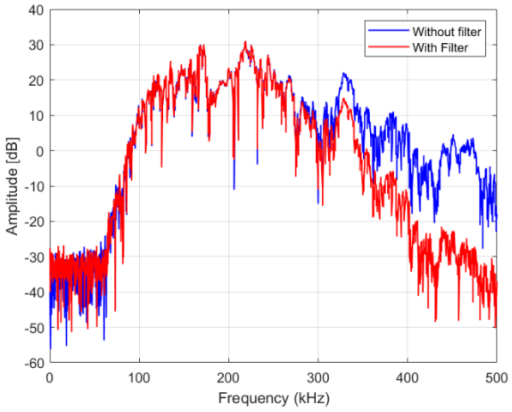

Figure 3-7 Spectrum signal of one hit to compare the data with filter and without filter in sensor 2

3.3 AE features extracted from waveforms

Measurements are made of the features of the signal such as Arrival time, Peak Amplitude, Energy, Rise Time, Counts and Duration. These features and their relationship to the detection threshold are shown in Figure 1-9. The signals were analysed in time domain because the number of hits or events generated during the experimental test was really higher. In fact, the peak amplitude of each hit were considered to plot the accumulative behaviour of crack growing. This cannot be obtained in frequency domain. A burst emission is characterized by a sharp increase of wave energy. The amplitude of a burst emission may reach one or more peak amplitudes and then decrease. Once a burst emission crosses a predetermined threshold, it is called an AE hit or event and is recorded. The Peak Amplitude of a hit is given in dB $(\mathrm{decibel} = 20\log(\mathrm{V_{sensor\ \mu V}}/1\mu\mathrm{V})$. This is an absolute value in dB used exclusively in AET where a base voltage of 1µV is used. The Rise Time is the time between the first threshold crossing and the first peak detected in a hit. The Duration is the time between the first and last threshold crossing of a hit. Counts are the number of positive threshold crossing of a hit. The Energy of each hit is the integral of the squared AE-signal over time, where the burst signal energy is the sum of all squared voltage samples of a hit multiplied by the sampling interval. The circuit resistance in the hardware of the VALLEN is $10\ \mathrm{k\Omega}$, which is used to convert $\mathrm{V^2s}$ units to Joules ($\mathrm{J = Ws = V^2s/R}$). Its unit is the energy unit eu $(\mathrm{eu} = 10^{-14}\ \mathrm{V^2s})$, where $1\mathrm{eu} = 1\ \mathrm{aJ\ (attojoule)} = 10^{-18}\mathrm{Joule}$ [17]. Note that all these features were considered in this test.

3.4 Trial chain test

A trial chain tensile test was carried out for almost a week before starting the long term chain tensile test. This was to confirm that the sensors and equipment were functioning correctly. In the trial test, a load of 1.2 MN was applied to the chain for almost three days. Then the load was removed and AE was recorded during the next three days to monitor the environmental noise in the tank and in the machine. Figure 3-8 shows the peak amplitude of each hit recorded by sensors 1 and 3 (outside of the tank) during this trial test. Figure 3-8 illustrates the fact that the machine noise now is higher compared to the noise level obtained before the trial test (Figure 3-5). This was considered due to the load of 1.2 MN which was applied during trial test, and therefore the noise level of the machine was increased. However, the noise level does not disappear altogether when the rig is unloaded. Therefore, it means that the reason for this is the noisy environment in the industrial laboratory. In next sections, peak amplitude filters (45 dB, 55 dB, 65 dB) are implemented to the whole test data to use them as baseline and compare the behaviour of the accumulated data, to see whether the noise environment data could have an impact in the crack growth.

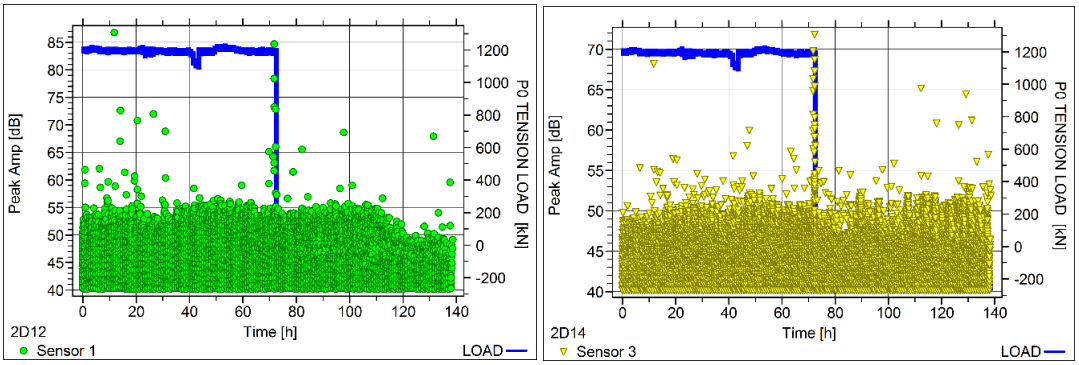

Figure 3-8 Peak amplitude behaviour of sensor 1 and 3 during trial test from load to unloaded

Figure 3-9 shows the peak amplitude values of the chain sensor during the trial test. A similar behaviour is observed with low loads (1.2 MN) and during unloading. It can be seen that although the majority of AE peak amplitude are below 55 dB, some hits exhibit peak amplitudes that are above 55 dB. This is due to the fact that the chain sensor is submerged in seawater and bubbles are generated due to the pH level in the tank. Similar behaviour et al. [30], [31] was reported, where AE signals with high peak amplitudes were generated due to the hydrogen gas bubbles. This means that the data below 55 dB are considered as noise environment in the tank, which can be identified as the frequency signals without interest.

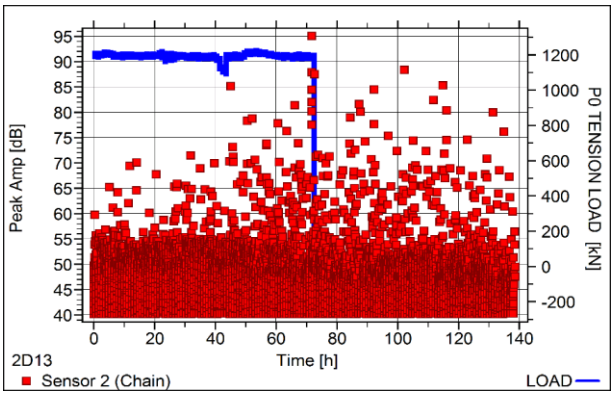

Figure 3-9 Peak amplitude behaviour of AE sensor in tank during trial test.

3.5 Loads applied during full chain tensile test

According to the HSE report et al. [2], a fundamental characteristic of any mooring chain is its percentage of Minimum Break Load (% MBL). Chain manufacturers have to confirm by physical testing that they have achieved the specific percentage of MBL and proof load values before the chains are in service. Proof loading gives assurance that the yield stress and plastic behaviour of the material meet the specification for the grade of steel used in the chain. Table 3-1 shows the percentage of Minimum Break Load (% MBL).and proof load calculated for the chain of diameter 160 mm, grade R5 studless link tested in this study [2]. In table 3-1, D is the chain diameter in mm. The % MBL and proof load applied by manufacturers to the chain depends on the chain diameter. Following the Det Norske Veritas (DNV) design code standard et al. [1] for offshore mooring systems, the % MBL and proof load are applied primarily to check that the chain will safely resist the service load and will not excessively elongate. This code is mainly based on mechanical testing and experience to prove that the deformation in chains is in the plastic region during service. The percentage of minimum break load (% MBL) is defined in function of the diameter and grade of the link as shown in table 3-1.

Table 3-1 Stipulated percentage of Minimum Breaking Load (% MBL) and proof load values of chain link of grade R5 applied before chains are in service [2].

Chain link	Stud link	Stud link R5, $D = diameter = 160\ mm$	% MBL
% MBL R5	$0.03186\ D^2\ (44 - 0.08\ D)$	25.447 MN	100 %
Proof load R5	$0.0251\ D^2\ (44 - 0.08\ D)$	20.047 MN	78.78 %

In general, the loading history for each link is as follows: before the chain is in service, a proof load of 70 % MBL is applied. During service, the chain can have a maximum wave load amplitude of 20 % MBL and a minimum load amplitude of 10 % MBL. Baptist et al. [14] defined that the

minimum load is mainly caused by the dead weight of the chain, and the maximum wave load is generated by sea currents. These loads are wave periodic, which can produce fatigue. However, in this tensile test, the load is kept static load for a long term to induce SCC in a corrosive environment with high tension. Table 3-2 shows the equivalent % MBL of the load applied during the full chain tensile test. The load was increased in a series of steps. The second load of 5.2 MN lead to exceeding the maximum load that a chain would experience in service (20 % MBL). Static load was gradually increased. During the application of load 5, a load level of 15.2 MN was achieved which is equal to 59.73 % MBL. However, the chain still did not break.

Table 3-2 Equivalent % MBL of load applied in the chain during the tensile test

Chain	Load applied to the stud-less link R5	% MBL
Load 1	0.50 MN	1.96 % MBL
Load 2	5.20 MN	20.43 % MBL
Load 3	7.10 MN	27.90 % MBL
Load 4	8.10 MN	31.83 % MBL
Load 5	15.20 MN	59.73 % MBL

3.6 Peak amplitude filters and tensile test results

During the 3.7-month lasting chain tensile test, a considerable amount of AE data were recorded in the form of AE features (78.2 GB). In the AE features analysis, three simple filters were applied to analyses the recorded data above specific peak amplitude:

1. First filter to plot all the AE data with Peak Amplitude higher than 45 dB
2. Second filter to plot the AE data with Peak Amplitude higher than 55 dB
3. Third filter to plot the AE data with Peak amplitude higher than 65 dB

These first two filters were chosen according to the noise levels obtained before and during the trial test (see Figure 3-5 and 3-8). The third filter was selected to filter out the AE data with peak amplitude lower than 65 dB, this peak amplitude was chosen because some AE signals with peak amplitudes higher than 55 dB, were also generated despite the fact that the average noise environment in the tank during load was about 55 dB. This is to reduce noise from the machine and the environment because the hits with high peak amplitude represents the events of crack growth.

Figure 3-10 shows the peak amplitudes with each filter and the nine parts of the test. Part 1 (a), concerns the first 700 hours of the test. During the first 200 hours, various events with high peak amplitudes were generated. This is attributed to the high pH level (9 %) in the sea artificial water during the first days of the test. When the pH level is very high, a higher cathodic reaction from the cathodic protection system is generated and hence corrosion can be accelerated. Therefore,

more hydrogen gas bubbles are generated and this produces high peak amplitudes [14, 15]. After 200 hrs, the pH level was controlled and reduced to 6%. Less events with high peak amplitude is observed. After 450 hours of the first part of the test the third load of 7.1 MN was applied. Between this specific time of 450 hours and 500 hours of the test more events with peak amplitude above 65 dB are obtained. SCC was likely to have initiated when the load increased and the pH was stable. The peak amplitudes above 65 dB are scattered, this indicates that SCC stopped. Actually, the peak amplitude data are concentrated below 60 dB between 500 and 700 hours of part 1(a). A simple parametric study was done in part 2 (b), where the couplant between the surface of the link and the face of the sensor was removed to know the behaviour of the hits. In part 2 (b) relates to the times between 230 and 340 hours where various events with a peak above 65 dB of amplitude are generated. This behaviour is observed due to the missing grease couplant between the chain surface contact and the sensor. It was observed that the grease couplant helps to improve the transmission and reduce the noise level of bubbles.

Figure 3-10 shows that the events are either concentrated or scattered during some specific periods of the test. For example, in parts 1 (a) and part 2 (b), the events look dispersed below 65 dB. However, in part 3 (c) almost all data are concentrated below 68 dB. This means that SCC grew during 1200 and 1500 hours of the test. This behaviour is due to the fourth load 8.1 MN applied at 1020 hours of the test. In fact, in the last 100 hours of part 3 (c), SCC grew faster such that it is observed in the concentrated data below 75 dB. In the first 60 hours of part 4 (d) the concentrated data returned to below 68 dB level, then data fluctuates between 68 and 75 dB. This means that during this fluctuation the SCC grew and then stopped and grew again. In fact, in the first 30 hours of part 5 (e) the fluctuation of the concentrated data still evident, then the peak are below 69 dB in the following hours. However during the first 350 hours of part 6 (f) the peaks are below 65 dB, so it means that the SCC stopped then SCC grew between 350 and 490 hours of part 6 (f).

Finally when the last load of 15.2 MN was applied (part 7 (g)), it was observed that a number of events with peak amplitudes of 85 dB was measured, but the peaks were generated only during the load increment. Then scattered data were observed with peak amplitudes higher than 60 dB. Following this, in the last 100 hours of part 7, the concentrated data were below 75 dB. In fact in almost all the time of the last parts 8 (h) and 9 (i), the events are concentrated below 75 dB. It can be postulated that the SCC propagated faster during these two last parts of the test due to the highest load applied and the corrosive environment.

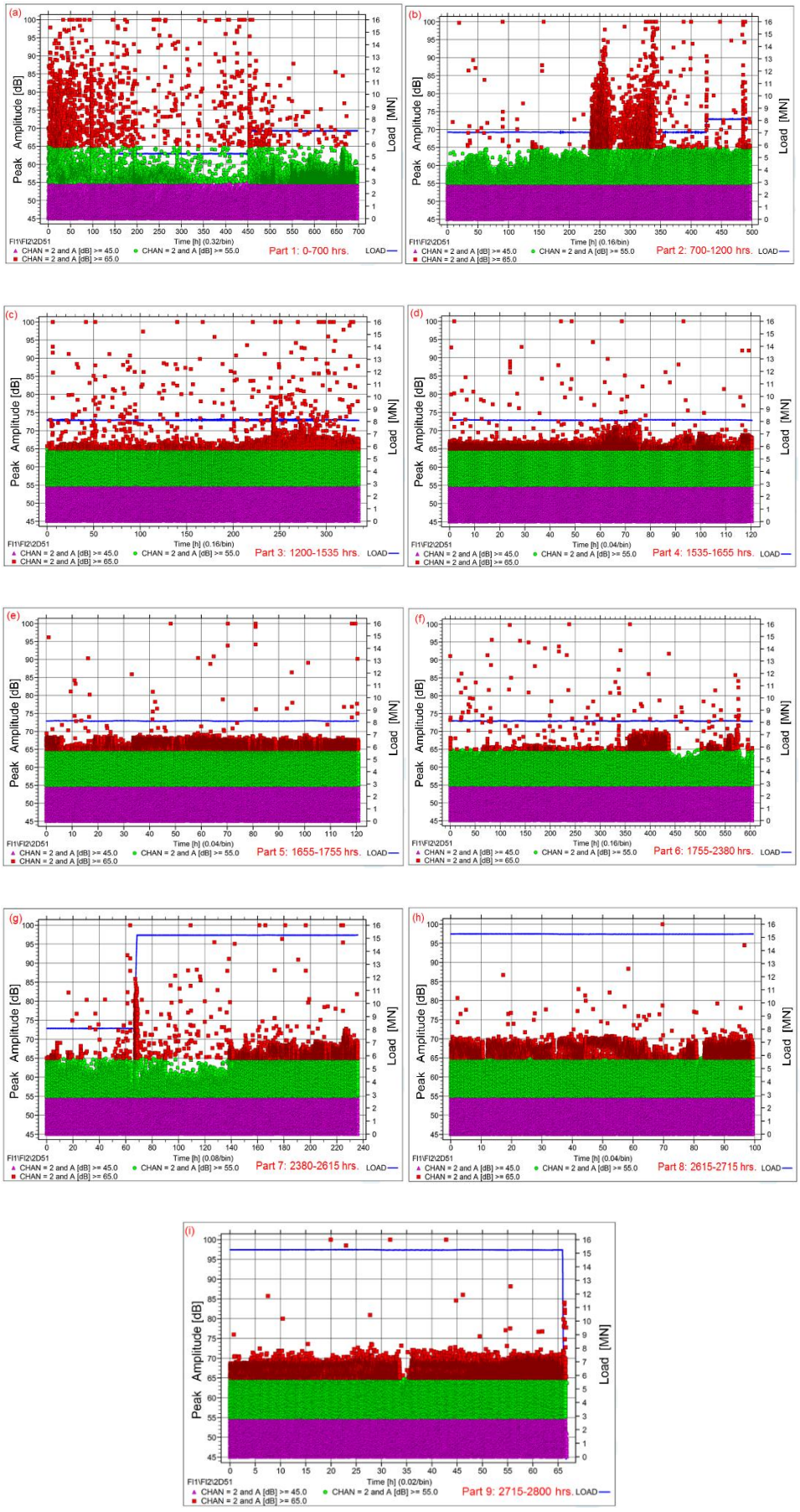

Figure 3-10 AE data events of the nine parts of the full test with three Peak Amplitude filter (45 dB, 55 dB and 65 dB), (A [dB] is equal to peak amplitude, CHAN2 is equal to sensor 2)

3.7 Analysis and results of the AE features

Lee and Wang et al. [31] reported that several processes are responsible for acoustic emissions during SCC. AE is a strong technique providing crucial information on fracture behaviour as elastic waves [73]–[75]. AE can occur due to atomistic processes like dislocation motion or due to macroscopic process like deformation, corrosion and crack growth, some process such as film cracking, gas evolution, hydrogen migration, plastic zone formation, discontinuous cracking during SCC and hydrogen cracking produce AE since all these processes strain the lattice [29]–[31], [34].

The AE generation during the initial stages of the test was related to the hydrogen bubble formation and motion. Mansfeld et al. [76] presented that the AE count rate was qualitatively linear with the amount of hydrogen collected. According to the papers et al. [5], [29]–[31], [33], the main AE features which can describe crack initiation and crack growth for short term test and small specimens are the AE Cumulative Energy and AE Cumulative Counts. However for large specimens and long term test, there is no literature which can describe the possible behaviour of the AE features. This study was carried out partially to close this knowledge gap and discusses the results obtained for all AE features for a large chain in a long term test. Additionally, the behaviour of the AE features was compared for the cases where different noise filters were used and the result were compared with the trend of the curvature during the test.

In Figure 3-11, cumulative hits (a), peak amplitude (b), duration (c), rise time (d), counts (e) and energy (f) are displayed for the three peak amplitude (PA) filters used in this work. The normalized cumulative AE features were obtained using the maximum cumulative value for each AE feature in each filter so that trends in the curves can be compared.

Figure 3-11(a) and 3-11(b) show the behaviour of normalized cumulative hits and normalized cumulative peak amplitude respectively. They exhibit almost a similar pattern as the cumulative rise time in Figure 3-11(d), it can be inferred that SCC initiates after the first 700 hrs of the test when the high load is applied. Then SCC starts to propagate slowly for the next 650 hrs and suddenly a fast SCC growth is observed between 1450 hrs and 1750 hrs, following this, SCC propagation slows down again. Finally, in the last 230 hrs SCC starts to grow faster.

Another AE feature of interest was the cumulative duration (Figure 3-11(c)). It shows a similar pattern to the pattern of normalized cumulative counts, see Figure 3-11(e). These slopes of duration and counts curve increase sharply between 1450 hrs and 1750 hrs like the normalized cumulative hits of Figure 3-11(a). Then they increase slowly between part 6 and 7, and finally they increase again sharply during the part 8 and 9 of the test. In all plots the trend of the curvature is flat and similar for the first 700 hrs, it is considered as noise environment due to the gas bubbles

and pH level, so there is no SCC for a long time. However, between 1450 hrs and 1750 hrs the SCC propagation is observed in all AE features representing similar behaviour due to high load and corrosive environment.

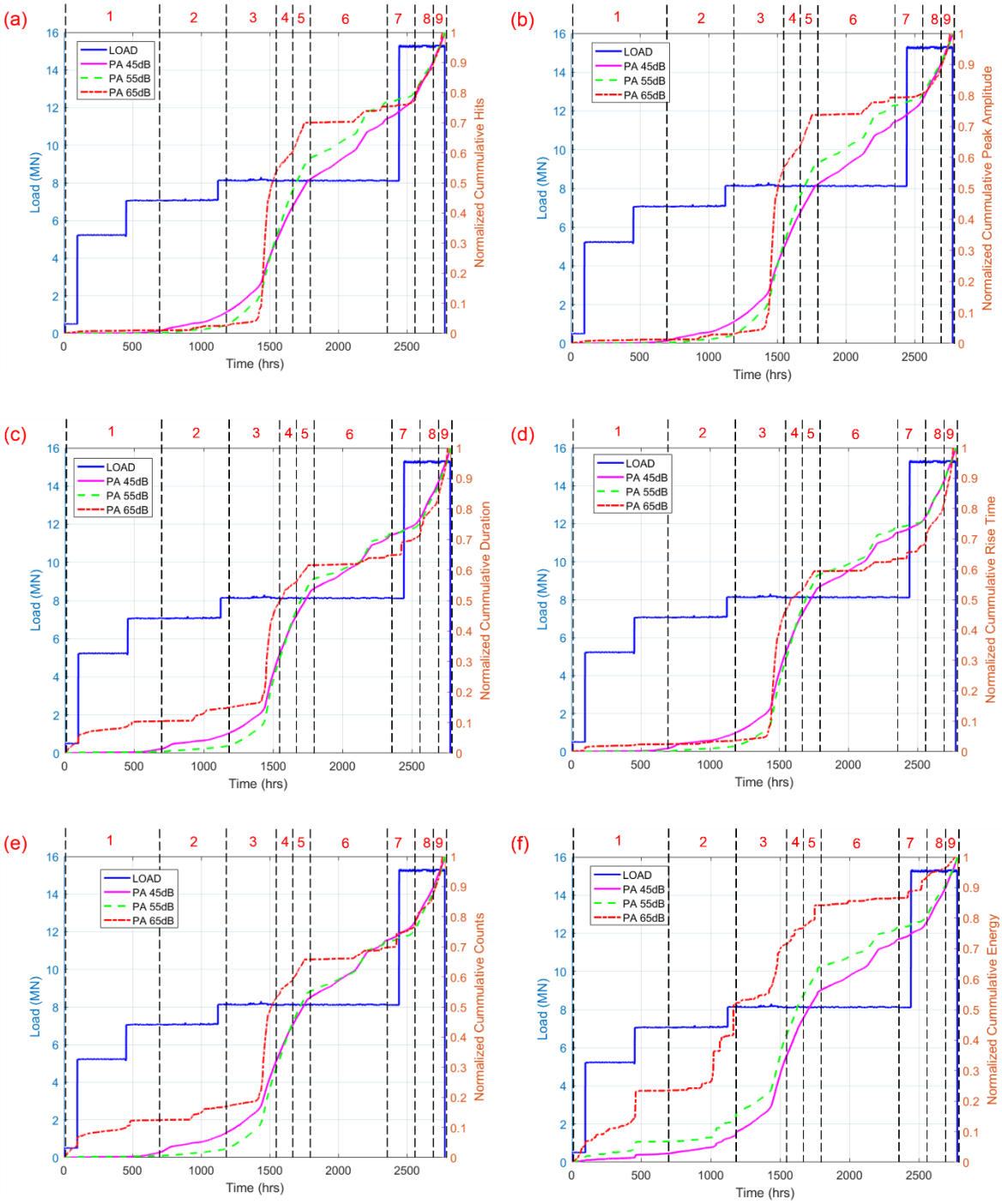

Figure 3-11 Cumulative AE features and loads versus time for AE data with filters of peak amplitude (PA) higher than 45 dB (ping solid line), 55 dB (greeen dashed line) and 65 dB (red dash-dotted line): (a) Hits, (b) Peak amplitude, (c) Duration, (d) Rise time, (e) Counts, (f) Energy.

In general the AE features exhibited almost a similar pattern during the entire test. However the cumulative AE features like hits, peak amplitude and rise time exhibit a similar trend. They match at the time when the slope of the curve changes, when it increases faster or slowly. The behaviours are very similar in the data obtained by filtering at 45 dB and 55 dB levels. Moreover, the behaviour observed during the analysis of data filtered at 65 dB is not very different from the other data sets filtered using lower peak amplitude filters. The trend of the curve can describe the profile of the SCC growth during the long term test. The red lines trend for hits, peak amplitude and rise time representing the signal filtered higher than 65 dB show that before 1450 hrs the SCC grew by only 5 %. However, between 1450 hrs and 1750 hrs it increases from 5 % to 70 % representing SCC propagation. Then it stabilizes for the next 350 hrs, so it means SCC stopped growing, and finally SCC started to propagate again for the last two parts (Parts-8 and 9) of the test.

The other three AE features with similar pattern are duration, counts and energy. It can be seen that the trend is similar for filters 45 dB and 55 dB. However for filter 65 dB in Figure 3-11(f), there are high jumps of released energy during the test. These represent SCC extension, for example, when the load is increased to 7.1 MN, there is a high jump of energy. Then, for the next 500 hrs there is not a high increment until 1020 hrs, 1070 hrs, and 1160 hrs. Then SCC increases gradually from 1400 hrs to 1740 hrs. From 1740 hrs to 2400 hrs it is almost constant. Finally, when the load increased to 15.2 MN, 20 hrs later, a gradual increment is observed until the end of the test. Here it is confirmed that for long term test, SCC is induced in the chain due to the combination of high tensile stress and corrosive environment [31].

Table 3-3 below shows in summary the behaviour obtained in each part of the test. In almost all AE features of the signal filtered with 45 dB and 55 dB filters, the first 700 hours gives the impression that noise data was generated by bubbles or the normal operation of the machine. Then part 2 SCC initiation and slow propagation. However fast SCC propagation is observed in parts 3, 4 and 5 where a high load with the magnitude of 8.1 MN was applied. In parts 6 and 7, slower SCC propagation is observed. Finally during parts 8 and 9, during the application of the last and highest load fast SCC propagation was observed again.

Table 3-3 SCC behaviour during the test

Parts of full tensile test	Hours	Day	SCC
Part 1	0-700	29 days	environment noise data
Part 2	700-1200	21 days	initiation/slow propagation
Part 3	1200-1535	14 days	fast propagation
Part 4	1535-1655	5 days	fast propagation
Part 5	1655-1775	5 days	fast propagation
Part 6	1775-2380	25 days	slow propagation
Part 7	2380-2615	10 days	slow propagation
Part 8	2615-2715	4 days	fast propagation
Part 9	2715-2780	3 days	fast propagation

Figure 3-12 shows the normalized released energy of individual AE events for filter 45 dB (a) and 65 dB (b), where possible crack extensions might have occurred: e.g. at 450 hrs, 1020 hrs, 1070 hrs, 1160 hrs, 1750 hrs and 2520 hrs approximately. Also, it can be seen that between 1000 hrs and 1800 hrs there is a greater number of high jumps of released energy which corresponds to the SCC propagation due to high load. It can be observed that the released energy of individual events filtered with 45 dB and 65 dB filters exhibit a similar pattern along the time. However, it is necessary to observe released energy of each event instead of cumulative energy to identify possible crack extension. Figure 3-12 describes that the noisy environment can be discriminated for long term static tensile test. Such as it was observed in the AE features with 45 dB and 55 dB filters during the first parts of the test.

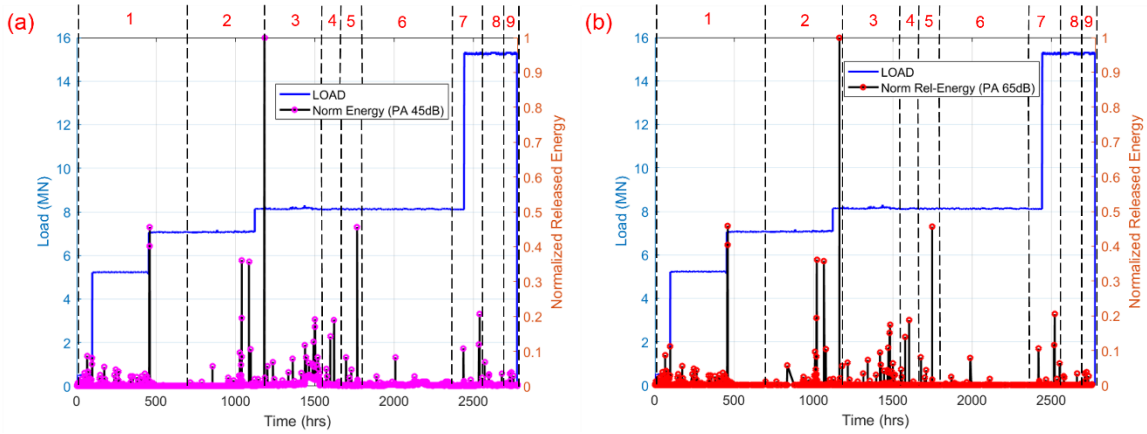

Figure 3-12 Load and normalized realised energy: (a) filter 45 dB, (b) filter 65 dB.

It is important to realize that AET cannot measure crack size. Therefore, for future long term test, a visual recording test should be considered to do a correlation between AE data and visible damage. However, it should be noted that recording data like images in long term test, it will produce a huge amount of data like the 78.9 GB AE data generated during this experimental test.

It will require a powerful computer to be able to process and analyse the huge AE data and images recorded during the test. In addition, for size measurements -at least during post-mortem analysis stage-, it is necessary to use other technique such as microscopy after the completion of tests. Figure 3-13 without detailed information about the crack length and depth were shared by TWI to visualize the crack growth during the test. Figure 3-13 shows the notch depth of 1.5 cm, which was machined using an Electric Discharge Machine. Moreover, Figure 3-13 shows after the notch the crack growth, according to TWI the maximum crack length and maximum crack depth were 78.26 mm and 891 µm, respectively.

Figure 3-13 Notch and crack growth (left), zoom of crack growth (right).

A zoom of part of the crack length and depth can be observed in Figure 3-14. At the end of the test, a microscopy examination was carried out by TWI to measure the crack length and depth developing at different stages of the damage propagation during the tensile test on the chain. It was confirmed that crack growth occurred. However, the information on the detailed crack length and depth cannot be disclosed in this thesis due to confidentiality agreements with the client.

Figure 3-14 Crack growth (inside red colour)

3.8 Conclusions

A long term chain tensile test was carried out to monitor stress corrosion crack initiation and growth using acoustic emission technique. The following observations were made in the course of this study:

- Two groups of AE features with similar trends were identified during the test. The first group of AE features was the cumulative hits, cumulative peak amplitude and cumulative rise time. The second group with similar pattern was the cumulative duration, cumulative counts and cumulative energy.
- The trend curves for each AE features are almost similar for 45 dB and 55 dB filters. Therefore, for a long term test a higher threshold of 55 dB can be used instead of 45 dB.
- The feasibility study of AE was assessed and proved to be a powerful tool for continuous monitoring of SCC initiation and SCC growth for a mooring chain, which can indicate the specific stages of SCC growth.
- For a long term test, all AE features have the potential of discriminating different stages of SCC not only energy and counts as many authors recommend.
- For a long term static chain tensile test, the noise level of the environment is discriminated easily from the high number of events generated during the SCC propagation.

This study demonstrated that it is, in principle, feasible to detect SCC initiation and growth with acoustic emission monitoring technique. However, the AE monitoring was carried out in the straight part of the link and near the notch. There is still missing the wave propagation analysis around the link and the behaviour of the waveforms due to the curvature of the link. Therefore, a research is carried out in the next chapters to analysis and understand the types of excited waveforms in a complex structure such as the link.

Chapter 4: Fundamental waves in a straight and curved bar

4.1 Introduction

Different types of elastic waves can propagate in solids depending on how the motion of points in the solid material is related to the direction of propagation of the waves. The primary elastic waves or fundamental waves are usually referred to as the longitudinal wave, flexural wave and torsional wave. Therefore, the theory is used in this chapter to understand the fundamentals of the wave propagation in a straight bar. An analytical model is presented for a semi-infinite rod and a semi-infinite beam to know what type of wave propagate. The mobility transfer function is obtained for each model, and a transient input instead of harmonic excitation is applied to the bar to plot the longitudinal and flexural wave propagation. Necessary transformations are carried out from time domain to frequency domain and vice-versa. In addition, it is carried out the comparison of the fundamental wave between straight and curved beam. It should be noted that the chain has two curvatures and this complex geometry could have an effect in the wave propagation. It very important to know how the curvature can have an impact in the fundamental waves.

4.2 Fundamental theory of wave propagation in a bar

The mobility representation is a very powerful tool in structural dynamics. It allows structures to be subdivided like rod (longitudinal wave), beam (flexural wave) and shaft (torsional wave).

The structure could be considered infinite, semi-infinite and finite rods, shafts and beams. A, E, ρ, G, I are the cross-sectional area, Young's modulus, density, shear modulus and second moment of area about the neutral axis of the elements, respectively. J is the polar second moment of area of the shaft, and $k_l = \sqrt{\frac{\rho}{E}}\omega$, $k_s = \sqrt{\frac{\rho}{G}}\omega$, $k_b = \sqrt[4]{\frac{\rho A}{EI}}\sqrt{\omega}$ are the quasi-longitudinal, shear and bending (flexural) wave numbers, respectively. It should be noted that the longitudinal and shear wavenumbers are proportional to frequency and the bending wavenumber is proportional to the square-root of frequency [11]. This means that the longitudinal and shear wave speeds $c = \frac{\omega}{k}$ are independent of frequency (non-dispersive), but the bending wave speed is proportional to the square root of frequency (dispersive).

4.2.1 Infinite and semi-infinite rod

Expressions for the mobilities of rods and beams are derived below as an examples, where the time dependency $e^{j\omega t}$ is assumed but omitted for simplicity.

The equation of motion of axial vibration of a rod due to an axial distributed force per unit length $f_z(z,t)$ is given by Bishop and Johnson (1960) as:

$$EA\frac{\partial^2 u(z,t)}{\partial z^2} - \rho A\frac{\partial^2 u(z,t)}{\partial t^2} = f_z(z,t), \tag{4.1}$$

which has a solution to harmonic excitation

$$U(z) = A_R e^{-jk_l z} + A_L e^{jk_l z}, \tag{4.2}$$

where A_R is the complex axial displacement of a right-going propagating wave, A_L is the complex axial displacement of a left-going propagating wave, and z is the distance along the rod. The amplitude of these waves are dependent upon the geometrical configuration and the amplitude and phase of the excitation force. They can be determined by applying the appropriate boundary conditions.

For an infinite rod excited at $z = 0$, one of the boundary condition is $F_z = -2EAU'(0)$, where the prime denotes differentiation with respect to z. The right-going wave amplitude is determined to be $A_R = \frac{F_z}{j2k_l EA}$. Applying the condition of continuity of displacement gives $A_L = -\frac{F_z}{j2k_l EA}$. To determine the mobility of the rod for $z \geq 0$, A_R is substituted into equation 4.2, A_L is set to zero, and equation 4.2 is differentiated with respect to time and rearranged to give the transfer mobility [11].

$$\frac{\dot{U}(z)}{F_z} = \frac{\omega}{2EAk_l} = \frac{1}{2A\sqrt{E\rho}} e^{-jk_l z} \tag{4.3}$$

To determine the driving point mobility, z is simply set to zero. Because this is entirely real, the rod has the characteristics of a damper. For a semi-infinite rod with the free end being at $z = 0$, the boundary condition is simply $F = -EAU'(0)$, which means that the point and transfer mobilities are twice that of an infinite rod, this has a behaviour such as a damper because has a constant speed along the frequency. A shaft has a very similar dynamic behaviour to that of a rod, but the motion is torsional [11].

$$\frac{\dot{\Phi}(z)}{T} = \frac{1}{2J\sqrt{G\rho}} e^{-jk_s z} \tag{4.4}$$

4.2.2 Infinite and semi-infinite Euler-Bernoulli beam

The equation of motion per unit length of flexural vibration of an Euler-Bernoulli beam due to a transverse distributed force per unit length $f_x(z,t)$ is given by Bishop and Johnson (1960) as

$$EI\frac{\partial^4 w(z,t)}{\partial z^2}+\rho A\frac{\partial^2 w(z,t)}{\partial t^2}=f_x(z,t), \tag{4.5}$$

which has a solution to harmonic excitation

$$W(z)=C_R\mathrm{e}^{-k_b z}+D_R\mathrm{e}^{-\mathrm{j}k_b z}+C_L\mathrm{e}^{k_b z}+D_L\mathrm{e}^{\mathrm{j}k_b z}, \tag{4.6}$$

where C_R and D_R are the wave amplitudes of the transverse displacement near-field in the region $z>0$ and propagating right-going waves, C_L and $D_L$are the wave amplitudes of the near-field or evanescent in the region $z<0$ and propagating left-going waves, respectively.

For an infinite beam with a lateral force applied at $z=0$, the boundary conditions are: shear force is equal to applied force $F_x=2EIW'''(0)$, bending moment to the left of the applied force is equal to bending moment to the right of the applied force $EIW_{-}''(0)=EIW_{+}''(0)$, and the lateral displacement to the left of the applied force is equal to lateral displacement to the right of the applied force $W_{-}(0)=W_{+}(0)$. The resulting wave amplitude are $C_R=C_L=-\frac{F_x}{4EIk_b^3}$ and $D_R=D_L=-\frac{\mathrm{j}F_x}{4EIk_b^3}$. To determine the mobility of the beam for $z\geq 0$, C_R and D_R are substituted into equation 4.6 with $C_R=C_L=0$, and the equation 4.6 is differentiated with respect to time and rearranged to give the transfer mobility [11].

$$\frac{\dot{W}(z)}{F_x}=\frac{-\omega}{4EIk_b^3}(\mathrm{j}\mathrm{e}^{-k_b z}-\mathrm{e}^{-\mathrm{j}k_b z}) \tag{4.7}$$

To obtain the driving point mobility, z is simply set to zero to give $\frac{\dot{W}(0)}{F_x}=\frac{\omega(1-\mathrm{j})}{4EIk_b^3}$. For a semi-infinite beam excited at the free end, the left-going waves are zero. Applying the boundary conditions of $EIW''(0)=0$ (zero bending moment) and $EIW'''(0)=F_x$ (shear force equal to applied force), gives the wave amplitudes as $C_R=C_L=-(1+\mathrm{j})\frac{F_x}{2EIk_b^3}$. Substituting this into equation 4.6, differentiating with respect to time and rearranging gives the transfer mobility as,

$$\frac{\dot{W}(z)}{F_x}=\frac{\omega(1-\mathrm{j})}{2EIk_b^3}(\mathrm{e}^{-k_b z}+\mathrm{e}^{-jk_b z}) \tag{4.8}$$

noting that $k_b\alpha\sqrt{\omega}$ in equations 4.7 and 4.8, it can be seen that the point and transfer mobilities of an infinite and semi-infinite beam are proportional to $\frac{1}{\sqrt{\omega}}$, this has a behaviour such as mass because the mobility decreases in high frequency [11].

4.3 General diagram of bar models

Figure 4-1 shows the general block diagram of the bar models, in this case a Gaussian modulated sinusoidal function $f_g(t)$ is used to excite the model instead of the harmonic force. Then a Fast Fourier Transformation is carried out from time domain to frequency domain to obtain $F(\omega)$. Having the mobility transfer function $M(\omega, x)$ with the input $F(\omega)$ and the output response is $V(\omega, z)$, then Inverse Fast Fourier Transformation to the output response $V(\omega, z)$ is obtained. From frequency domain to time domain the output velocity $v(z, t)$ is derived. The output could be the longitudinal, flexural or torsional waves depending the type of mobility considered during the analysis. It should be noted that in Figure 4-1, it is necessary to do the transformation from time domain to frequency domain and then from frequency to time domain again, because it is a time response wave analysis but as the transfer function of the mobility is in frequency, it is required to do transformation between time and frequency and vice versa. In addition, the time response of the wave analysis can provide information about the shape of the wave along the bar for different position.

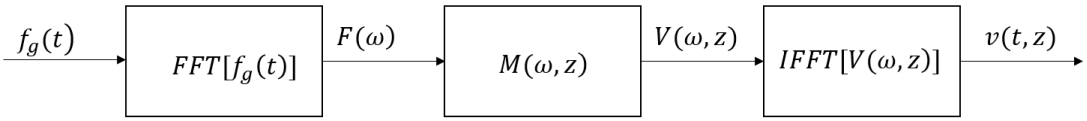

Figure 4-1 General block diagram of bar models

The mobility representation is a very powerful tool in structural dynamics. It allows structures to be subdivided like rod (longitudinal wave), beam (flexural wave) and shaft (torsional wave). The mobility methods can be used in a straightforward manner in the analysis of linear mechanical systems subject to three types of excitation: periodic, transient and stationary random. The mobility for one-dimensional distributed elements can be described in term of waves or modes. One advantage of the wave approach is that it is possible to relate the dynamic behaviour of finite structure to infinite structure and it allows exact mobility to be derived.

4.4 The pulse excitation waveform

For passive technique, Gaussian pulse can be used to represent a crack event or a pencil lead break force that generates the wave propagation in a structure [48], [49]. The width pulse duration in time determines its bandwidth in the frequency domain. The definition of Gaussian Pulse function is [77]

$$h_g(t) = A_f \, \mathrm{e}^{(-\frac{(t-t_s)^2}{2\,\sigma^2})}, \tag{4.9}$$

A_f is the constant amplitude of the height of the wave's peak, t_s is the time shift of the centre of the peak pulse, σ is the standard deviation sometimes called the Gaussian Root Mean Square width, the width of the pulse can be controlled by the number of standard deviation considered such as width equal to 8σ. A Gaussian pulse transient load is approximately normal distribution set (bell-shaped curved) considering the 68-95-99.7 rule [78],[79]. For example, six sigma is equal to 99.7% of the set ($6\sigma = \text{width}$), or eight sigma is equal to 99.99% of the set ($8\sigma = \text{width}$) Figure 4-2 shows the Gaussian pulse and its spectrum (blue solid line) considering 8σ equal to width (5 ms).

On the other hand, for active technique in structural health monitoring, the excitation signal used for inspections is a sinusoidal wave modulated. It is modulated using the Gaussian function, it is an useful transient load to do wave propagation analysis in structures like pipes [80], [81]. The definition of the modulated sinusoidal wave with Gaussian function window is:

$$f_g(t) = A_f \, \cos(\omega t) \, \mathrm{e}^{(-\frac{(t-t_s)^2}{2\,\sigma^2})} \tag{4.10}$$

Figure 4-2 shows the Gaussian modulated sinusoidal and its spectrum (red dashed line). The advantage of sinusoidal wave modulated is that highest magnitude of the spectrum is in the excitation frequency, which can be defined for each analysis. These are not lobes in Gaussian modulated sinusoidal thanks to the Gaussian envelope function. In fact, a comparison between the equation 4.10 and the Gaussian-Modulated sinusoidal pulse command (gauspuls) of Matlab are done as shown in Figure 4-2, it is confirmed that there are not lobes using Gaussian envelope because lobes are observed only for Hanning window envelope. The size of FFT was calculate for each function using the length of the time signal to a power of 2 to increase the performance of the FFT. Gaussian modulated function is considered in the rod and beam model for the wave propagation analysis in each model of this chapter. Some leakage can occur in the calculated transformation but a main transient can still be recognised clearly for the response to a transient load.

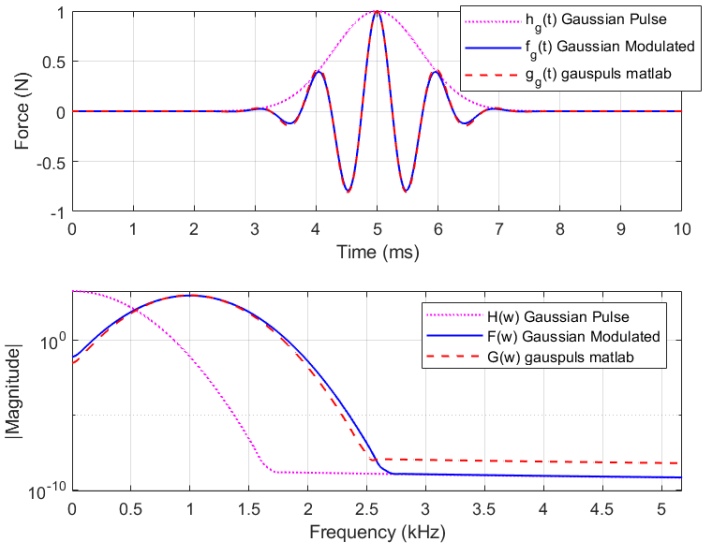

Figure 4-2 Functions and the spectrums: Gaussian pulse, Gaussian modulated, gauspuls matlab

4.5 Analytical model of a straight rod

A simple analytical model was considered to understand the basic knowledge of the longitudinal wave propagation in a rod, whose length is semi-infinite. Any lateral contraction or expansion of the semi-infinite rod was neglected. In addition, it is also assumed that the plane cross-section of the rod remains plane and parallel during the deformation associated with the wave motion. An analytical model was considered for a semi-infinite rod with the force applied at the end.

A transfer frequency response function of the semi-infinite rod was obtained. The output of the mobility is the longitudinal wave propagation at 1m position of the rod. An excitation force produces waves, which propagate through the structure and are reflected and transmitted at discontinuities, boundaries, and distributing vibrational energy through the structure. However for a semi-infinite rod no boundary conditions are considered at the end, neither discontinuities. A transient Gaussian modulated sinusoidal excitation force $f_z(t)$ in axial direction with an excitation frequency $1\ \mathrm{kHz}$ is applied to the end of the semi-infinite rod, the longitudinal wave extends in the positive z direction, see Figure 4-3.

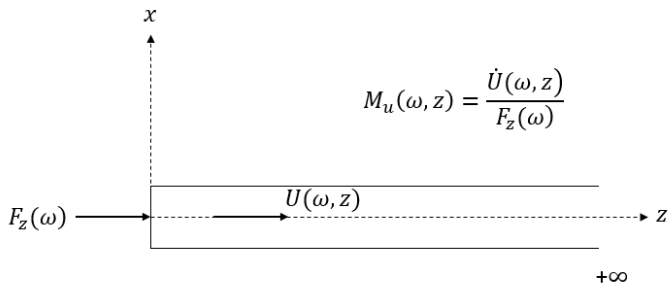

Figure 4-3 Semi-infinite rod diagram

The transient response of a bar at any point along its length can be straightforwardly computed in the frequency domain given expressions for transfer Frequency Response Functions (FRFs) reported in many seminal texts such as [41], [82]. Denoted $M_u(\omega, z)$ as the frequency response function (FRF) between any response quantity $v_u(t, z)$ at time t and position z arising from an axial point force $f_z(t)$ acting at the origin. The time response to a transient input is obtained applying the Inverse Fourier Transform,

$$v_u(t, z) = IFFT[V_u(\omega, z)] = IFFT[M_u(\omega, z)F_z(\omega)], \tag{4.11}$$

where $F_z(\omega)$ is the spectrum of $f_z(t)$. The longitudinal velocity $v_u(t, z)$ depends on both the spatial z and temporal t variables.

The transient axial velocity response of a semi-infinite rod is obtained by adopting the transfer mobility $M_u(\omega, z)$ from section 4.2 [11].

$$M_u(\omega, z) = \frac{V_u(\omega, z)}{F_z(\omega)} = \frac{\dot{U}(\omega, z)}{F_z(\omega)} = \frac{\omega}{EAk_l} \mathrm{e}^{-\mathrm{j}k_l z} = \frac{1}{A\sqrt{E\rho}} \mathrm{e}^{-\mathrm{j}k_l z}, \tag{4.12}$$

where $k_l = \sqrt{\frac{\rho}{E}}\omega$

The force generates an excited wave ${a_u}^+ \mathrm{e}^{-\mathrm{j}k_l z}$, where ${a_u}^+$ is the amplitude of the excited wave and the exponential terms represent propagating longitudinal wave. In Eq. 4.12, A, E, ρ are the cross-section area (πr^2), Young's modulus and density of a steel rod of diameter 160 mm. This diameter is considered because it is the diameter used for the link in chapters three and seven, k_l is the longitudinal wavenumber and z is the position along the rod. It should be noted that the longitudinal wavenumber is proportional to the frequency. This means that the longitudinal wave speed $c_p = \frac{\omega}{k_l} = \sqrt{\frac{E}{\rho}}$ is independent of frequency (non-dispersive).

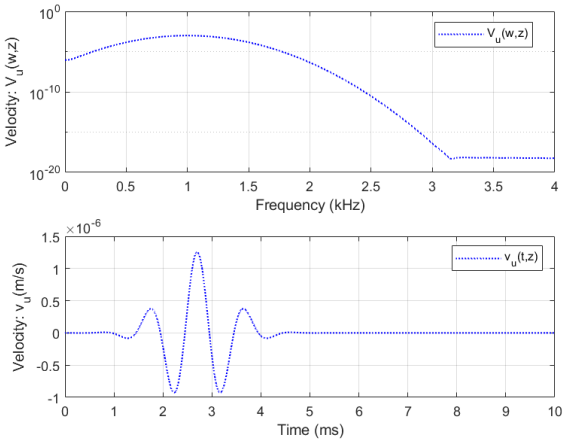

Figure 4-4 Response of semi-infinite rod: Frequency response (top) and time response (bottom) at z = 1 m

Figure 4-4 shows the output response in frequency and time domain, it is noticed that in time domain the width pulse is the same as the input, so it means that the longitudinal wave is not dispersive and will be the same along the rod.

4.6 Analytical model of a straight beam

The classical theory of beams is known as Euler-Bernoulli beam theory, which includes only transverse inertia and bending deformation. Later, it was modified by Rayleigh in 1877 with the introduction of the correction for rotary inertia. This eliminated the contradictions of infinite phase and group velocities for infinitely small wavelengths that results from the classical theory.

In this section Euler-Bernoulli was considered. In Euler-Bernoulli, two deformation coordinates are obtained at any cross-section $(W, \emptyset)$. Therefore, two transfer frequency response functions of the semi-infinite beam are considered, M_w and $M_\emptyset$ [11]. The outputs of each mobility is the transverse and rotation wave propagation at 1m position of the beam, respectively. A transient Gaussian modulated sinusoidal excitation force $f_x(t)$ in transverse direction with an excitation frequency $1\ kHz$ is applied to the origin of the semi-infinite beam, the transverse $W(\omega, z)$ and angular $\emptyset(\omega, z)$ waves travel in the positive z direction, see Figure 4-5.

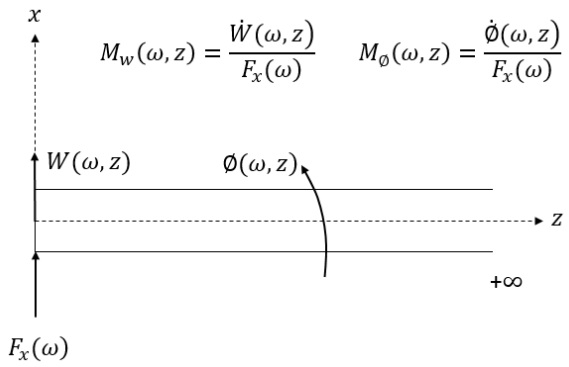

Figure 4-5 Semi-infinite beam diagram

The transient responses of a beam at any point along its length can be computed in frequency domain. $M_w(\omega,z)$ and $M_\emptyset(\omega,z)$ are the frequency response functions (FRF) between any response quantity $v_w(t,z)$ and $\dot{\varphi}(t,z)$ at time t and position z arising from a transverse point force $f_x(t)$ acting at the origin. The $v_w(t,z)$ and $\dot{\varphi}(t,z)$ time responses to a transient input are obtained applying the Inverse Fourier Transform to $V_w(\omega,z)$ and $V_\emptyset(\omega,z)$, respectively.

$$v_w(t,z)=IFFT[V_w(\omega,z)]=IFFT[M_w(\omega,z)F_x(\omega)], \tag{4.13}$$

$$\dot{\varphi}(t,z)=IFFT[V_\emptyset(\omega,z)]=IFFT[M_\emptyset(\omega,z)F_x(\omega)], \tag{4.14}$$

where $F_x(\omega)$ is the spectrum of shearing force $f_x(t)$. The transverse velocity $v_w(t,z)$ and angular velocity $\dot{\varphi}(t,z)$ depends on both the spatial z and temporal t variables. The angular velocity is transformed to axial velocity $v_\emptyset(t,z)=r_b\,\dot{\varphi}$

The transient transverse velocity response of a semi-infinite beam is obtained by adopting the transfer mobility $M_w(\omega,z)$ from section 4.2 [11].

$$M_w(\omega,z)=\frac{V_w(\omega,z)}{F_x(\omega)}=\frac{\dot{W}(\omega,z)}{F_x(\omega)}=\frac{\omega(1-\mathrm{j})}{2EIk_b^3}\left(\mathrm{e}^{-k_bz}+\mathrm{e}^{-\mathrm{j}k_bz}\right), \tag{4.15}$$

where $k_b=\sqrt[4]{\frac{\rho A}{EI}}\sqrt{\omega}$

In beam model, the force generates nearfield or evanescent wave and wave propagation, where the exponential term e^{-k_bz} represents nearfield and $\mathrm{e}^{-\mathrm{j}k_bz}$ represents wave propagation. Nearfield waves are waves that decay exponentially with distance. It should be noted that nearfield and evanescent wave are the same, which are much localised and do not carry energy.

The transient angular velocity response of a semi-infinite beam is obtained by adopting the transfer mobility $M_\emptyset(\omega,z)$ from section 4.2 [11].

$$M_{\emptyset}(\omega, z) = \frac{V_{\emptyset}(\omega, z)}{F_x(\omega)} = \frac{\dot{\emptyset}(\omega, z)}{F_x(\omega)} = \frac{-\omega(1-\mathrm{j})}{2EIk_b^2}\left(\mathrm{e}^{-k_b z} + \mathrm{j}\mathrm{e}^{-\mathrm{j}k_b z}\right), \tag{4.16}$$

In beam model, I is the second moment of area defined as $\frac{\pi {r_b}^4}{4}$ for cylindrical beam, k_b is the flexural wavenumber and z is the position along the rod. It should be noted that the bending wavenumber is proportional to the square-root of frequency. This means that the bending wave speed is proportional to the square root of frequency (dispersive), so the phase speed is dependent of frequency and the transient response will be dispersed.

$$c_p = \frac{\omega}{k_b} = \sqrt[4]{\frac{EI}{\rho A}}\sqrt{\omega}, \tag{4.17}$$

Figure 4-6 shows the magnitude and phase of the mobility for a semi-infinite beam. In the mobility plot can be observed that the transverse M_w has a behaviour such as mass because the mobility decreases in high frequency, and the mass does not dissipate power and is thus referred as being reactive. However, the angular $M_{\emptyset}$ is like a damper when nearfield wave is neglected because the mobility is constant along the frequency, thereby damper is seen to dissipate power. In addition, there is a phase shift of 90 degrees between M_w and $M_{\emptyset}$ because it is expected that the angular velocity should be perpendicular to the transverse velocity. It should be noted that the plot of Figure 4-6 is comparing the mobility with and without nearfield waves. Figure 4-6 shows that nearfield or evanescent wave do not have an impact in the result for frequency higher than 0.4 kHz because nearfield or evanescent waves do not carry out energy and decay along the rod, and we are interested in wave propagation in a structure.

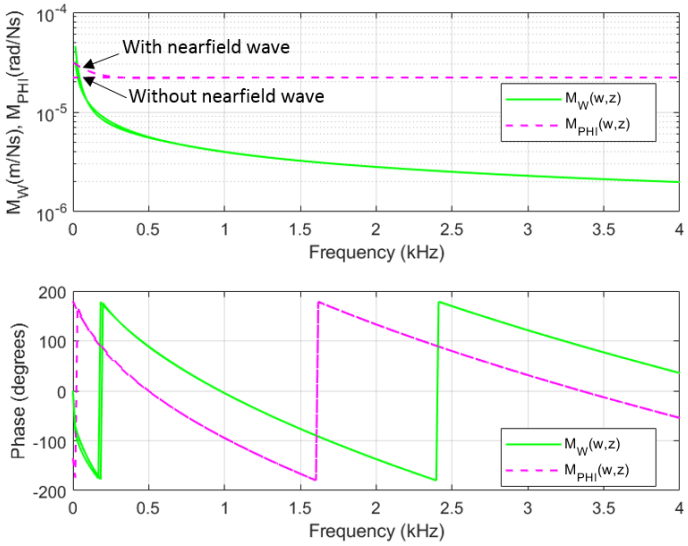

Figure 4-6 Magnitude (top) and phase (bottom) of the mobility at z = 1 m for a semi-infinite beam (with nearfield and without nearfield wave): M_w is the transverse mobility, $M_\emptyset$ is the angular mobility

Figure 4-7 shows the output response in frequency and time domain, it is observed the two degree of freedom in Euler-Bernoulli, transverse velocity and angular velocity. In addition, the nearfield or evanescent wave has decayed at 1 m from the source and it does not have any effect in the wave propagation.

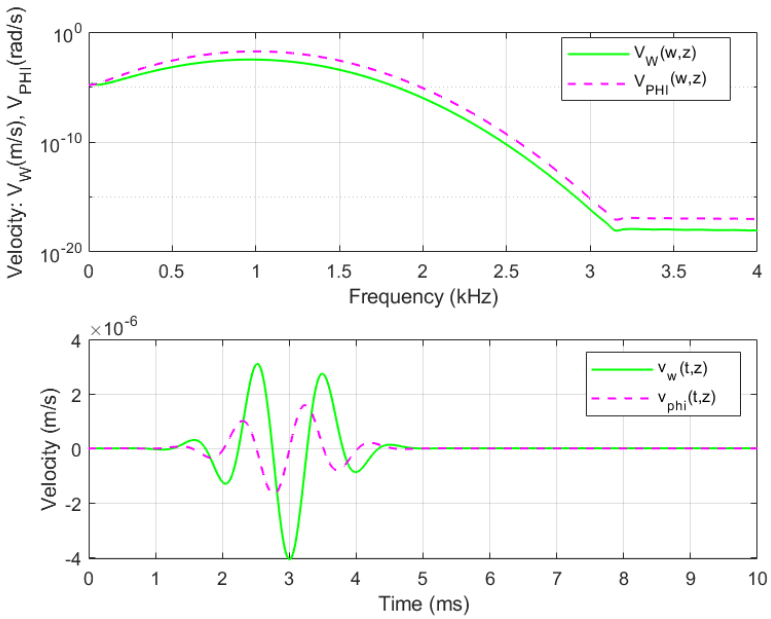

Figure 4-7 Response of semi-infinite beam: frequency domain (top) and time domain (bottom) at z = 1 m

4.7 Phase speed and group speed of flexural wave

It has been demonstrated et al. [11] that the phase velocity of flexural waves is related to the angular frequency, presented in equation 4.17. This therefore means that the velocity of flexural wave is dependent on the frequency of the wave, which can therefore be described as dispersion curves of the phase velocity or wavenumber. From equation 4-17, it is possible to derive the relationship for the phase velocity, which is defined as a function of the angular frequency and the wavenumber $c_p = \frac{\omega}{k_b}$.

On the other hand, another important parameter is the group velocity c_g, which is defined as the derivative of the angular frequency with respect to the wavenumber [82] as shown in Equation 4.18. It is associated with the propagation velocity of a group of waves of similar frequency. It is noted that the group velocity of the flexural wave is twice the phase velocity.

$$c_g = \frac{\mathrm{d}\omega}{\mathrm{d}k_b} = \frac{2}{\sqrt[4]{\frac{\rho A}{EI}}}\sqrt{\omega}\,, \tag{4.18}$$

Figure 4-8 shows the dispersion curves as function of phase velocity or wavenumber. It can be observed that flexural wave has a dispersion behaviour and longitudinal wave does not have a dispersion behaviour. However, it should be noted that the longitudinal wave is not dispersive because the fundamental theory was used for bulk waves, but in high frequency the longitudinal waves can have a dispersion behaviour using Pochhammer-Chree theory.

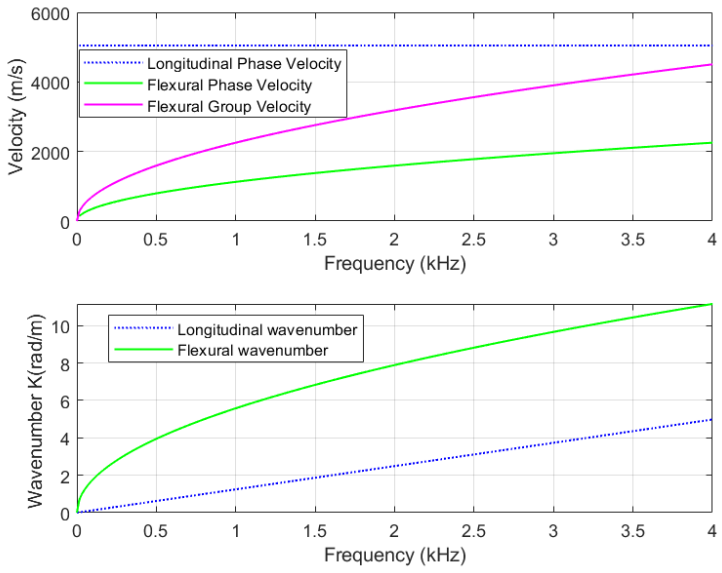

Figure 4-8 Phase velocity (top), Wavenumber (bottom)

4.8 Timoshenko beam theory

The Rayleigh beam theory, which includes the correction for rotary inertia, was then modified by Timoshenko in 1921, who introduced the shear deformation effects. The Timoshenko beam theory has been used in the study of vibrations and wave propagation problems by many years.

Beam whose description include both shear correction and rotary inertia are referred to as Timoshenko Beams. Wang reviewed et al. [83], [84] the Timoshenko beam theory from the point of view of wave mechanics. Following Timoshenko beam theory, the beam vibration can be described et al. [88] by a vector,

$$\mathbf{s}_{(z,t)} = \begin{Bmatrix} w(z,t) \\ \phi(z,t) \end{Bmatrix}, \tag{4.19}$$

where $w(z,t)$ is transverse displacement in the x-direction and $\phi(z,t)$ is the bending rotation of the cross section about the y-axis, which is related through,

$$\phi(z,t) = \frac{\partial w(z,t)}{\partial z} - \vartheta(z,t), \tag{4.20}$$

where $\vartheta(z,t)$ is the shear deformation as is shown in Figure 4-9.

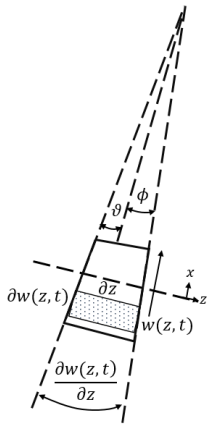

Figure 4-9 Diagram of Timoshenko beam

Considering the waves in a semi-infinite isotropic and homogeneous beam extending along the z-axis, the governing equation of Timoshenko beam theory can be written et al. [88] as,

$$\left\{\frac{\partial^4}{\partial z^4} - \left(\frac{1}{c_l^2} + \frac{1}{c_s^2\kappa}\right)\frac{\partial^4}{\partial z^2 \partial t^2} + \left(\frac{1}{c_l r_g}\right)^2 \frac{\partial^2}{\partial t^2} + \left(\frac{1}{c_l c_s \sqrt{\kappa}}\right)^2 \frac{\partial^4}{\partial t^4}\right\}\{\mathbf{s}_{(z,t)}\} = \{\mathbf{0}\}, \tag{4.21}$$

where $r_g = \sqrt{\frac{I}{A}}$ is the radius of gyration, $c_l = \sqrt{\frac{E}{\rho}}$ is the longitudinal wave speed, $c_s = \sqrt{\frac{G}{\rho}}$ is the shear wave speed and κ is the shear coefficient. The shear deformation was introduced by Timoshenko to account for non-uniform distribution of shear stress across the cross-section of the beam. Assuming a harmonic traveling wave in the beam given by

$$\mathbf{s}_{(z,t)}) = \begin{Bmatrix} w(z,t) \\ \phi(z,t) \end{Bmatrix} = \boldsymbol{a}\, \mathrm{e}^{\mathrm{j}(\omega t - kz)}, \tag{4.22}$$

where $\boldsymbol{a}$ is the complex amplitude vector of wave motion, $\omega = 2\pi f$ is the circular frequency of the harmonic wave with f frequency in Hz, $k = \frac{2\pi}{\lambda}$ is the wavenumber and λ is the wavelength.

Using the harmonic traveling wave equation 4.22 and calculating the differential partial equation with respect to time and space in equation 4.21

$$\frac{\partial^4 \mathbf{s}_{(z,t)}}{\partial z^2 \partial t^2} = \boldsymbol{a}\, \omega^2\, k^2 \mathrm{e}^{\mathrm{j}(\omega t - kz)}, \qquad \frac{\partial^4 \mathbf{s}_{(z,t)}}{\partial z^4} = \boldsymbol{a}\, k^4 \mathrm{e}^{\mathrm{j}(\omega t - kz)}, \tag{4.23}$$

$$\frac{\partial^4 \mathbf{s}_{(z,t)}}{\partial t^4} = \boldsymbol{a}\, \omega^4 \mathrm{e}^{\mathrm{j}(\omega t - kz)}, \qquad \frac{\partial^2 \mathbf{s}_{(z,t)}}{\partial t^2} = -\boldsymbol{a}\, \omega^2 \mathrm{e}^{\mathrm{j}(\omega t - kz)}, \tag{4.24}$$

Then, substituting the differential partial equations 4.23, 4.24 with respect to time and space in equation 4.21, it yields the dispersion relation

$$k^4 - \left(\frac{1}{c_l^2} + \frac{1}{\kappa\, c_s^2}\right)\omega^2 k^2 + \frac{1}{c_l^2 c_s^2 \kappa}\omega^4 - \frac{1}{c_l^2 r_g^2}\omega^2 \; = 0, \tag{4.25}$$

where $\frac{\omega^2}{c_l^2 r_g^2}$, $\frac{\omega^2}{c_l^2}$, $\frac{\omega^2}{c_s^2 \kappa}$ are related to the bending, rotary and shear effect, respectively. The solutions of equation 4.25 gives two roots for k, which can be written as,

$$k_1^2 = \left(\frac{\omega^2}{2c_l^2} + \frac{\omega^2}{2\, c_s^2 \kappa}\right) + \frac{1}{2}\sqrt{\left(\frac{\omega^2}{c_l^2} - \frac{\omega^2}{c_s^2 \kappa}\right)^2 + \frac{4\omega^2}{c_l^2 r_g^2}}, \tag{4.26}$$

$$k_2^2 = \left(\frac{\omega^2}{2c_l^2} + \frac{\omega^2}{2\, c_s^2 \kappa}\right) - \frac{1}{2}\sqrt{\left(\frac{\omega^2}{c_l^2} - \frac{\omega^2}{c_s^2 \kappa}\right)^2 + \frac{4\omega^2}{c_l^2 r_g^2}}, \tag{4.27}$$

In Figure 4-10, Timoshenko beam theory predicts two waves at each frequency. From eq. 4.26, it can be observed that k_1^2 is positive, this means that k_1 is real. This $k_1$represent the flexure wave propagating (the transversal displacement) in the whole frequency range. On the other hand, there is a critical frequency ω_c at $k_2 = 0$, below this critical frequency, shear wave (the bending rotation) is evanescent, where k_2 is imaginary. In addition, the wave characterized by k_2, where k_2 is real, only above this critical frequency, the shear wave (bending rotation) is propagating.

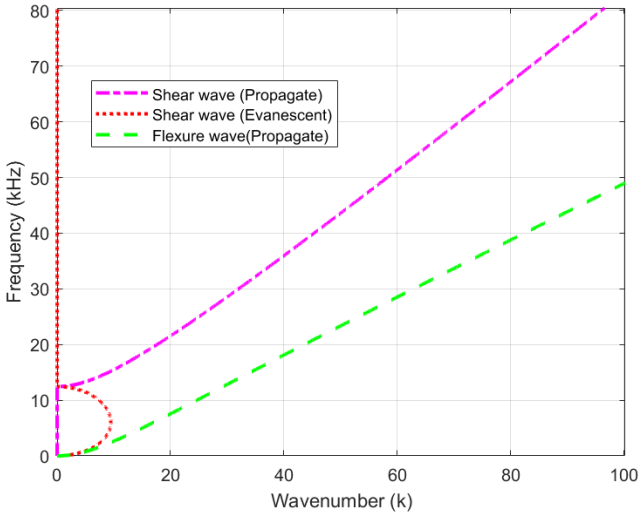

Figure 4-10 Dispersion relation of a Timoshenko beam (shear evanescent wave-red dotted line, shear wave propagating-ping dash-dotted line, flexure wave propagating-green dashed line)

Using the definition of $\widetilde{\omega}$ and $\tilde{k}$, where $\widetilde{\omega} = \frac{\omega\, r_g}{c_l}$ (non-dimensional circular frequency), and $\tilde{k} = r_g k$ (non-dimensional wavenumber). Thus, ω and k of a traveling harmonic wave are not independent. These two roots can be obtained as,

$$\widetilde{\omega}_1^2 = \frac{1}{2}\left[\gamma^2 + (1+\gamma^2)\,\tilde{k}^2 + \sqrt{\left[(1-\gamma)^2\,\tilde{k}^2 + \gamma^2\right]\left[(1+\gamma)^2\,\tilde{k}^2 + \gamma^2\right]}\right], \tag{4.28}$$

$$\widetilde{\omega}_2^2 = \frac{1}{2}\left[\gamma^2 + (1+\gamma^2)\,\tilde{k}^2 - \sqrt{\left[(1-\gamma)^2\,\tilde{k}^2 + \gamma^2\right]\left[(1+\gamma)^2\,\tilde{k}^2 + \gamma^2\right]}\right], \tag{4.29}$$

These two roots typically would give a phase velocity dependence, where $\gamma^2 = \frac{\kappa\, c_s^2}{c_l^2}$ is a non-dimensional parameter, $\gamma^2 = \frac{\kappa\, G}{E} = \frac{\kappa}{m_r}$, $m_r = \frac{E}{G}$ is the ratio of material. Thus, there are two branches of the dispersion relation (wave mode) of a Timoshenko beam as shown in Figure 4-11. This suggests that Timoshenko beam theory provides two waves at each frequency. It can be seen that $\tilde{k}$ is real for frequency $\widetilde{\omega}_2$, this flexure wave is a propagating wave in the whole frequency spectrum. On contrary, there exists a critical frequency ($\widetilde{\omega}_c = \gamma$), corresponding to $\tilde{k} = 0$, only above which the wave is propagating, below this critical frequency, the wave is evanescent. This means, below a certain cut-off frequency given by $\widetilde{\omega}_c = \gamma$, there is only one real value of $\tilde{k}$, implying that there is only one propagating mode (flexure wave).

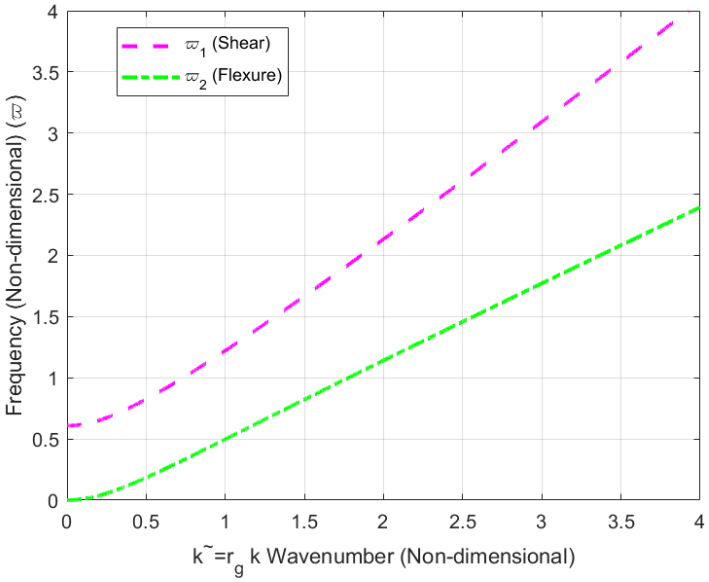

Figure 4-11 Non-dimensional dispersion relation of a Timoshenko beam (shear-ping, flexure-green)

From equation 4.26 and 4.27 the phase speed of $c_{p1}^2 = \frac{\omega^2}{k_1^2}$ and $c_{p2}^2 = \frac{\omega^2}{k_2^2}$ waves are obtained as

$$c_{p1}^2 = \frac{2}{\left(\frac{1}{c_l^2} + \frac{1}{c_s^2 \kappa}\right) + \frac{1}{2}\sqrt{\left(\frac{1}{c_l^2} - \frac{1}{c_s^2 \kappa}\right)^2 + \frac{4}{c_l^2 r_g^2 \omega^2}}} \tag{4.28}$$

$$c_{p2}^2 = \frac{2}{\left(\frac{1}{c_l^2} + \frac{1}{c_s^2 \kappa}\right) - \frac{1}{2}\sqrt{\left(\frac{1}{c_l^2} - \frac{1}{c_s^2 \kappa}\right)^2 + \frac{4}{c_l^2 r_g^2 \omega^2}}} \tag{4.29}$$

It can be deduced that to normalized the phase speed with respect to c_l, $\frac{c_{p1}^2}{c_l^2} < 1$ and $\frac{c_{p2}^2}{c_l^2} > 1$.

Figure 4-12 shows the normalized phase speed of the two waves propagating and the evanescent wave. It can be observed that at cut-off frequency 12.44 kHz the shear wave (bending rotation) starts to propagate, and below 12.44 kHz the evanescent shear waves is presented. Moreover, it can be seen that the flexure wave (transversal velocity) has a propagating behaviour in the whole range of frequency.

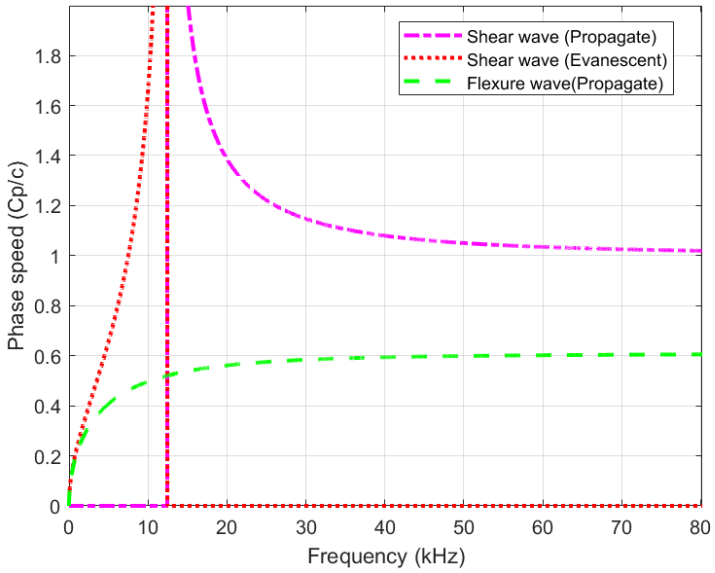

Figure 4-12 Phase speeds of Timoshenko beam (shear evanescent wave -red dotted line, shear wave propagating-ping dash-dotted line, flexure wave propagating-green dashed line)

4.9 Fundamental elastic waves in a curved beam using Morley's model

In the elementary Euler-Bernoulli theory [85], the effects of rotatory inertia and radial shear are not considered. Moreover, it is supposed that the central line keeps without extension when flexural motion happens, while the flexural characteristics are neglected when the extensional behaviour is considered. In Rayleigh theory the effects of rotatory inertia are included but the shear deformation effects are neglected but they are included in Timoshenko theory [86], [87].

A Timoshenko theory [88] was implemented to study the propagation of free elastic waves in a bent rod by Morley et al. [89]. Timoshenko's theory is an unified theory, which considers the impact of rotatory inertia, radial shear and evaluates also the effect of extension of neutral axis for straight rods [87]. However, Herrmann and Mirsky presented et al. [90], when the curvature is slight, it is allowed to make simplification to the equations because the extension of neutral axis has no impact at the flexural motion. Thus Morley et al. [89] presented a Timoshenko equation to govern the flexural motion [86], [87]. Morley found that exit a relationship between the phase velocity of flexural waves in the straight rod and cross section. These relationships are often satisfactory for low frequency modes of vibration in rods, which are only slightly curved, but they are not necessarily valid for the high frequency wave motions. For pronounced curvature, the accuracy requires investigation by making comparison with experiment and exact theory.

The free body diagram of Morley's curved rod is shown in Figure 4-13, where the non-dimensional radial coordinate is $r = \frac{r'}{R}$, the radial coordinate is r' and the radius of neutral axis is R. The non-dimensional displacements are denoted respectively by $\bar{v}$ and $\bar{w}$, as $\bar{v} = \frac{\bar{v}'}{R}$ and $\bar{w} = \frac{\bar{w}'}{R}$, where $\bar{v}'$ and $\bar{w}'$ are the components of displacement respectively in the s and x directions. The stress-strain relation are $\sigma_r = 0, \sigma_s = E\epsilon_s$, $\tau_{rs} = G\gamma_{rs}$, where ϵ_s and γ_{rs} are the circumferential and shearing strain respectively. The strains are related to the non-dimensional displacement $\bar{v}$ and $\bar{w}$ in the usual way by.

$$\epsilon_s = \frac{1}{r}\frac{\partial \bar{v}}{\partial s} - \frac{\bar{w}}{r}, \qquad \gamma_{rs} = \frac{\partial \bar{v}}{\partial r} - \frac{\bar{v}}{r} - \frac{1}{r}\frac{\partial \bar{w}}{\partial s} \tag{4.30}$$

Following Timoshenko theory for straight rods, it is assumed that the displacement are represented by,

$$\bar{v}\,(s,x,t) = v_c(s,t) - x\beta(s,t), \qquad \bar{w}\,(s,x,t) = w_c(s,t), \tag{4.31}$$

where v_c and w_c are the non-dimensional components of displacement at the neutral axis and β is the change in slope of the normal to this line.

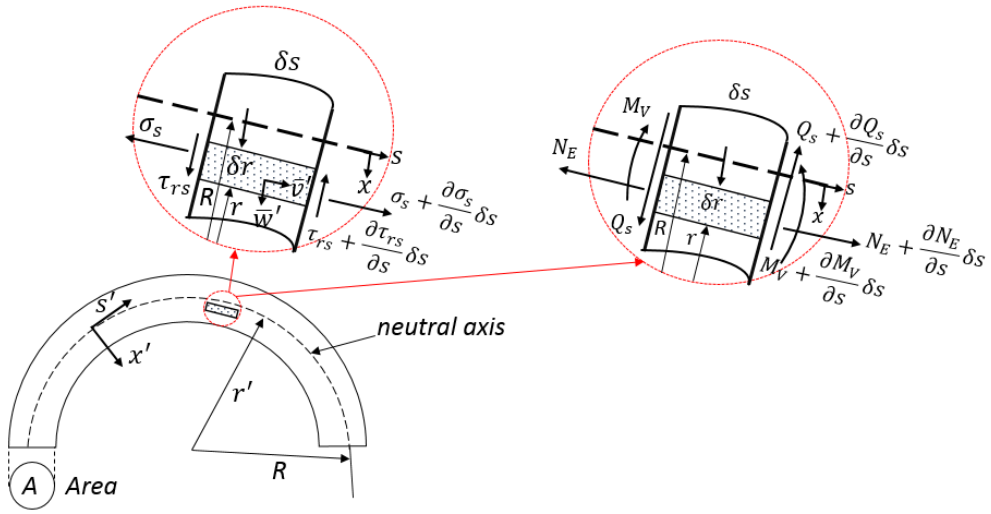

Figure 4-13 The diagram of Morley's curved beam model with constant radius (force acting on an element slice, resultant forces)

On the other hand, the resultants are related to the stress-strain relation, performing the necessary integrations in Morley paper [89], the resultants are expresses in terms of the displacements such as the next equations.

$$N_E = EA\left(\frac{\partial v_c}{\partial s} - w_c\right), \qquad Q_S = \kappa^2 GA\left(-v_c - \frac{\partial w_c}{\partial s} + \beta\right), \qquad \left(\frac{M_V}{R}\right) = -EAq^2\frac{\partial \beta}{\partial s}, \tag{4.32}$$

where N_E is considered the resultant circumferential force over the cross-section, Q_S is the radial shearing force and M_V is the resultant moment referred to the neutral axis. Moreover, κ is the shear coefficient over the cross-section, A is cross-sectional area of rod, E is the Young's modulus of elasticity, G is shear modulus, q is the geometrical constant which defines the curvatures in the rod. According to Morley et al. [89], the curvature is slight when $3q \ll 1$, and the propagation of free harmonic waves is evaluated by the form $w_c = W_c e^{j(\omega t - Ks)}$, where W_c is a constant amplitude and ω is the natural frequency, s is the non-dimensional coordinate around the neutral axis, the non-dimensional wavenumber is defined as $K = Rk$, the dimensional wavenumber is k. The dimensional wavelength λ along the neutral axis is given by $\lambda = \frac{2\pi R}{K}$. The phase velocity c_p of wave propagation along neutral axis is related to the natural frequency by $c_p = \frac{\omega R}{K} = \frac{\omega}{k}$.

Following to Morley et al. [89], the characteristic equation of the wave motions is obtained , when the rotatory inertia, radial shear deformation and the extension of neutral axis are considered, such as,

$$q^2(K^2-1)^2 - \left(\frac{c_p}{c}\right)^2\left\{1 + K^2 + K^4q^2\left(2 + \frac{E}{\kappa^2 G}\right)\right\} + \left(\frac{c_p}{c}\right)^4\left\{K^2 + K^4q^2\left(1 + \frac{2\,E}{\kappa^2 G}\right)\right\} - \left(\frac{c_p}{c}\right)^6 K^4q^2\frac{E}{\kappa^2 G} = 0, \quad (4.33)$$

where the normalized phase speed is define as $\left(\frac{C_p}{c}\right)^2$ with the extensional phase speed $c = \sqrt{\frac{E}{\rho}}$. Calculating the roots of the cubic equation 4.33, the normalized phase velocities are obtained, three different types of wave motion are found. These are radial shear, extension of the neutral axis and flexure.

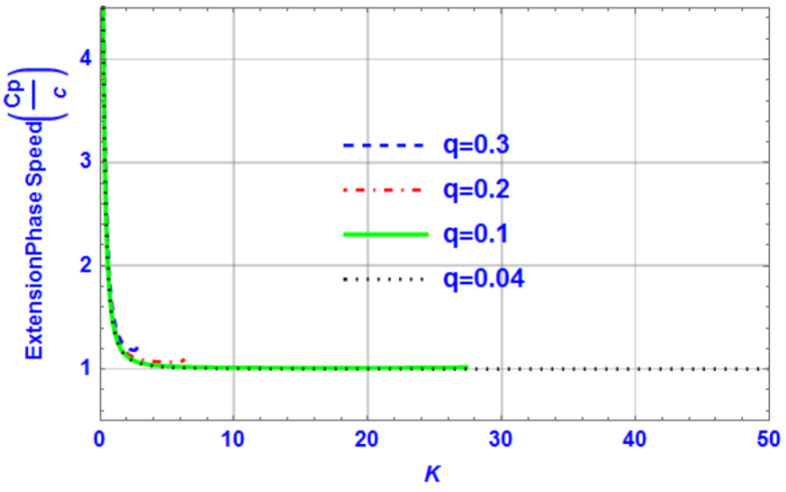

Figure 4-14 Extension phase speed versus non-dimensional wavenumber $(K = Rk)$ for different curvatures $(q = 0.3, q = 0.2, q = 0.1, q = 0.04)$

Herrmann and Mirsky presented et al. [90] that the extension of neutral axis has no effect in the pronounced curvature of rod for different values of q, as it can be shown in Figure 4-14.

Therefore, the characteristic equations 4.33 can be done considerable simplification, such as neglecting the extensional behaviour to obtain only the shear and flexure wave.

So, when the neutral axis is assumed to be inextensible $N_E = 0$ equations of 4.32 can be

$$N_E = 0, \qquad Q_S = \kappa^2 GA\left(-v_c - \frac{\partial w_c}{\partial s} + \beta\right), \qquad \left(\frac{M_V}{R}\right) = -EAq^2\frac{\partial \beta}{\partial s}, \tag{4.34}$$

Now, the characteristic equation instead of equation 4.33 is

$$q^2(K^2-1)^2 - \left(\frac{c_p}{c}\right)^2\left\{1 + K^2 + K^4 q^2\left(1 + \frac{E}{\kappa^2 G}\right)\right\} + \left(\frac{c_p}{c}\right)^4 K^2(1+K^2)\, q^2\frac{E}{\kappa^2 G} = 0, \tag{4.35}$$

where κ is the shear coefficient. Equation 4.35 is quadratic $\left(\frac{c_p}{c}\right)^2$, so two roots are expected. The smaller root gives the phase velocity of the flexural wave and the higher root gives the phase velocity of the shear wave.

Figure 4-15 shows the flexure phase speed for different curved rods. The curvature is pronounced when q increases, and the flexure phase speed increases as well. This means that for pronounced curvature, the flexure wave travels faster. It should be noted that the flexure phase speed decreases for low non-dimensional wavenumber. However, for wavenumber lower than 1, it is observed that the phase speed starts to increase again instead of reducing in each case. This means that the waves with larger wavelength start to travel fast again in curved rods.

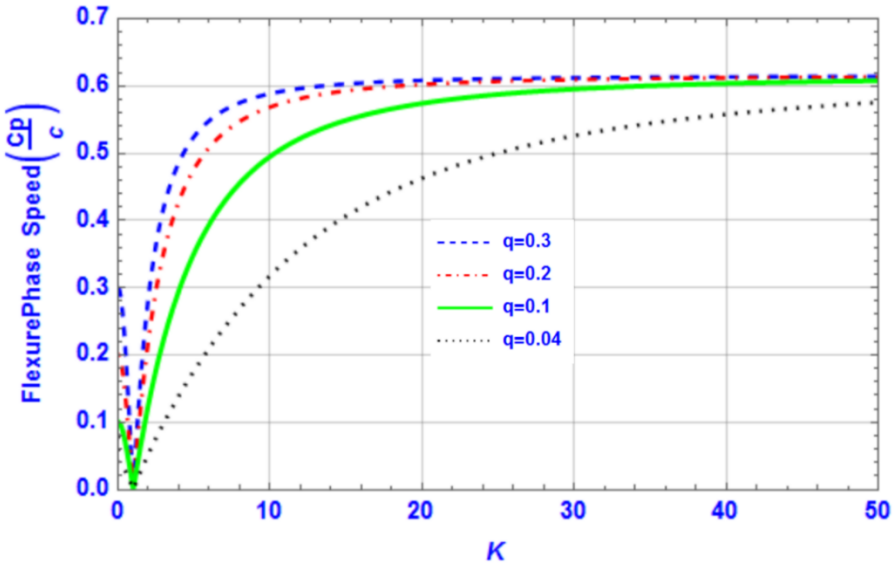

Figure 4-15 Flexure phase speed versus non-dimensional wavenumber $(K = Rk)$ for different curvatures $(q = 0.3, q = 0.2, q = 0.1, q = 0.04)$

According to Morley et al. [89], the non-dimensional wavenumber K is equal to $R\frac{2\pi}{\lambda}$, i.e. when $K = 2\pi$ rad there is one wavelength λ per radius of curvature R. So it should be noted that $K\sim1$ is a very long wavelength. This means that at $K\sim1$ the wavelength is the same as the radius of the beam, it can be observed that flexure phase speed increases again when the wavelength is larger than the radius of the beam. In addition, the dispersion caused by the curvature is greatest for the long wavelengths.

Figure 4-16 shows the behaviour of shear wave. It is observed how the shear phase speed decreases when q increases. This means that for pronounced curvature the shear wave travels slowly. For instance, at wavenumber ($K = 10$), the shear phase speed is almost the double faster for slight curvature ($q = 0.04$) than for pronounced curvature ($q = 0.3$). It is noted that in lower wavenumber is not observed the same behaviour such as flexure wave. In this case the shear phase speed is always decreasing for pronounced curvature.

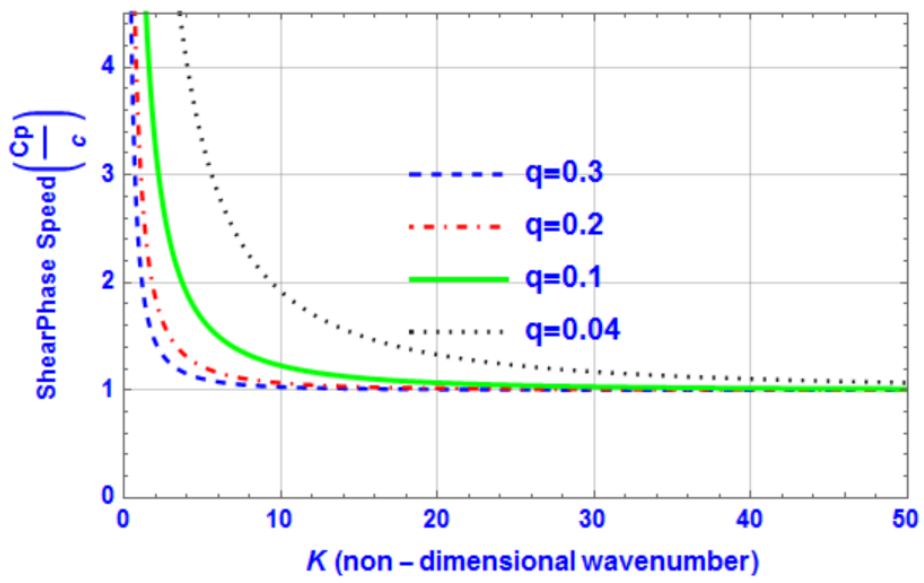

Figure 4-16 Shear phase speed versus non-dimensional wavenumber ($K = Rk$) for different curvatures ($q = 0.3, q = 0.2, q = 0.1, q = 0.04$)

In general, the impact of the phase speed behaviour can be seen more easily when wavenumber K is lower, because when the wavenumber is higher the curvature does not have an effect in the flexure and shear phase speed due to the asymptote of all curves trends to a constant phase speed value for different values of q.

Moreover, it is noted that c_p is always greater than the velocity c of long wavelength propagation. However, although individual waves travel with the phase velocity, the disturbance associated with a particular wavelength λ travels with the group velocity c_g where

$$c_g = c_p - \lambda \frac{\mathrm{d}c_p}{\mathrm{d}\lambda} = \frac{\mathrm{d}(Kc_p)}{\mathrm{d}K}, \tag{4.36}$$

Figure 4-17 shows the group speed of flexure wave, it can be observed that for pronounced curvature the group speed of flexure wave is faster when the wavenumber is lower. However, the group speed is similar when the wavenumber is higher in the case of pronounced curvature. It should be noted that for smaller wavenumber, the group speed of flexure wave starts to increase again. It is important to note that for pronounced curvature, the group speed is almost constant for large wavenumber. This means that the group speed could be the same for waves with shorter wavelength or waves travelling in high frequency. However, in low frequency or low wavenumber, the pronounced curvatures have a high effect in the group speed, where the flexure waves are travelling faster as the curvature increases.

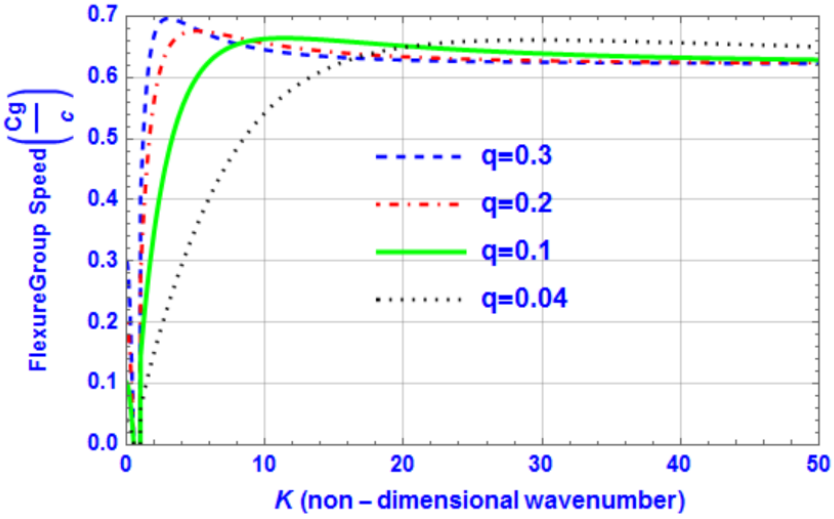

Figure 4-17 Flexure group speed versus non-dimensional wavenumber ($K = Rk$) for different curvatures ($q = 0.3, q = 0.2, q = 0.1, q = 0.04$)

On the other hand, Figure 4-18 shows that the group speed of shear wave is always higher when the curvatures is pronounced, so as the curvature increases the shear group speed increases as well. However, similar effect is observed for pronounced curvature, where the group speed is almost constant for shear waves travelling with large wavenumber. This means that for pronounced curvature, the shear waves of short wavelength are travelling in a constant group speed. In addition, Figure 4-18 shows large discrepancy of shear group speed between pronounced curvature ($q = 0.3$) and slight curvature ($q = 0.04$) in low and high frequency. In fact, it is considered that for slight curvature the behaviour could be similar to Timoshenko straight beam. Therefore, in the next section a comparison between Timoshenko beam and curved beam is done.

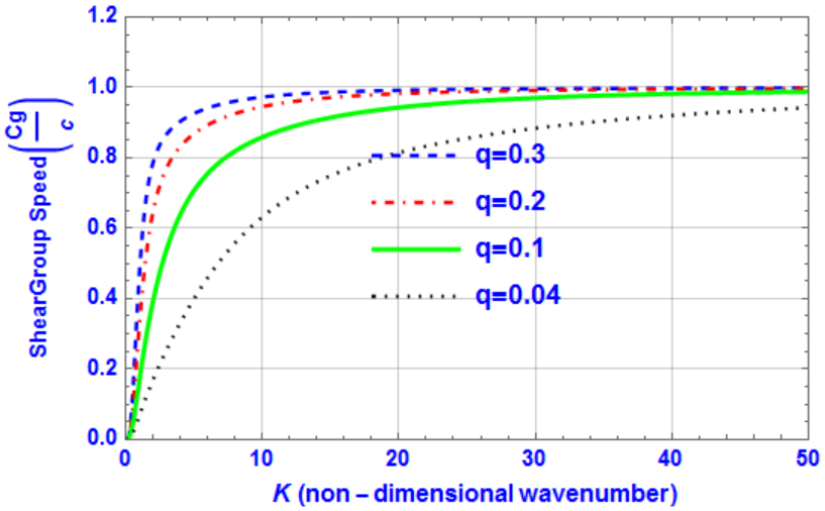

Figure 4-18 Shear group speed versus non-dimensional wavenumber ($K = Rk$) for different curvatures ($q = 0.3, q = 0.2, q = 0.1, q = 0.04$)

4.10 Comparison of Timoshenko (straight beam) and curved beam

From equation 4.28 and equation 4.29 the non-dimensional phase speed of Timoshenko beam is calculated. The phase speed is given by $\frac{c_p}{c_l} = \frac{\tilde{\omega}}{\tilde{k}}$. The limiting values of the phase velocities for infinitive non-dimensional wavenumber $\tilde{k} \to \infty$ for the two branches are $c_{p1} = c_l$ and $c_{p2} = \gamma\, c_l$. Figure 4-19 shows the flexure and shear phase speed of Timoshenko beam, in small wavenumber the wave is dispersive and in large wavenumber the wave is not dispersive. In addition, a comparison of phase speed was done between pronounced curvature ($q = 0.2$) and slight curvature rod ($q = 0.04$) straight beam. Figure 4-19 shows that slight curvature could have a similar behaviour as Timoshenko beam [91]. It can be observed that pronounced curvature could have an impact on lower wavenumber. For instance, the shear phase speed is lower for pronounced curvature than for slight curvature. On the contrary, the flexure wave phase speed is higher for pronounced curvature than for slight curvature of the rod.

Morley defined et al. [89] that the quantity $r_g = Rq$ is the radius of gyration about the neutral axis, and, since $q \ll 1$, this is the same as the radius of gyration about the central line of a cylindrical rod, which is defined as $r_g = \sqrt{\frac{I}{A}}$. Replacing the second moment of area $I = \frac{\pi\, {r_b}^4}{4}$ and the area $A = \pi\, {r_b}^2$ for cylindrical beam. The radius of gyration for a cylindrical rod is $r_g = \frac{r_b}{2}$. Now, using the definition of radius of gyration $r_g = Rq$ from Morley, the radius of neutral axis can be obtained as $R = \frac{r_b}{2\,q}$. For instance, a bend rod of radius ($r_b = 80$ mm), the radius of the curvature is $R = 133.33$ mm for pronounced curvature ($q = 0.3$) and $R = 1000$ mm for slight curvature ($q = 0.04$). This mean that the bend rod with the radius curvature R equal to 1m could

have similar behaviour like straight beam of Timoshenko as it is shown in Figure 4-19 and 4-20. On the other hand, Offshore Standards shows et al. [1] that the link has a curvature radius R equal to $2.25\, r_b$, so for similar radius ($r_b = 80$ mm) the curvature R is equal to 180 mm, which is equivalent a pronounced curvature $q = 0.222$.

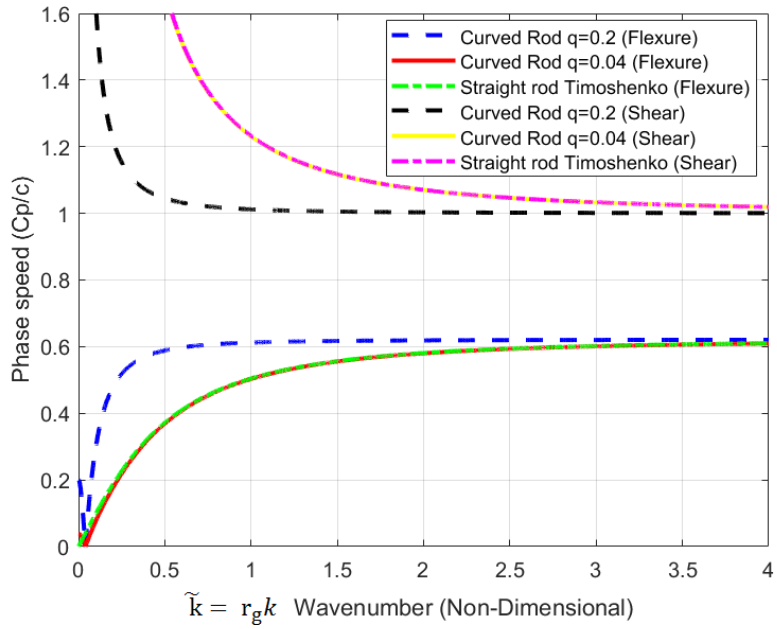

Figure 4-19 Comparison of phase speed of curved rod and straight rod in non-dimensional wavenumber (flexure wave is equal to transverse velocity and shear wave is equal to bending rotation velocity of the cross section)

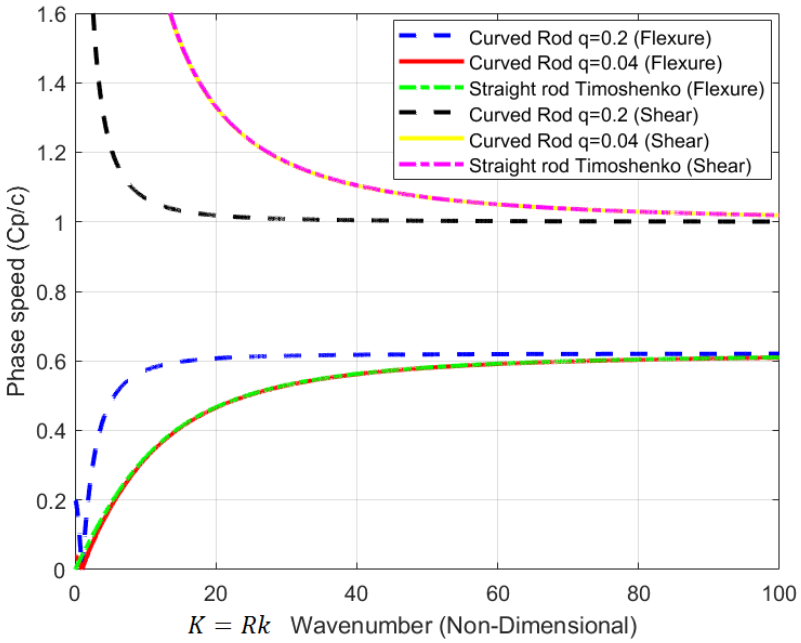

Figure 4-20 Comparison of phase speed of curved rod and straight rod in non-dimensional wavenumber (flexure wave is equal to transverse velocity and shear wave is equal to bending rotation velocity of the cross section)

4.11 Conclusions

The implementation of the fundamental theory to obtain the mobilities for a semi-infinite rod and semi-infinite beam provides an understanding of dispersion curves in a bar. It was observed how the dispersion has an impact on the original signal. For example, the longitudinal wave was not dispersive and the original input signal was the same along the semi-infinite rod. However, the fundamental flexural wave spreads out along the distance of the bar, so it means that the original signal can be transmitted with distortion because the phase speed depends on the frequency. In addition, the flexural and shear waves have some nearfield wave when the recording signals are done near of source but they do not carry out energy and they will vanish along the bar.

On the other hand, Morley derived a Timoshenko-like theory for the propagation of flexural elastic waves in an infinite curved rod. Morley's model included both the rotary inertia and radial shear deformation about the neutral axis as in the Timoshenko theory. However, the model is only valid for rods with a slight curvature, allowing the extension of the neutral axis to be neglected, and the governing equations can then be simplified significantly.

Moreover, the comparison of the fundamental wave between straight bar and curved bar, shows how for pronounced curvature the shear phase speed decreases and flexural phase speed increases. This effect was observed only for flexural and shear waves, because the extension wave was similar for pronounced and slight curvature. However, the group speed of the shear and flexural waves increase for pronounced curvature. It means that group speed could be a better parameter of the package wave propagation in a bent bar. In addition, good agreement was observed in the flexural and shear waves between Timoshenko and slight curvature model of Morley. This means that Morley's curved bar model can provide a good estimation, to know how the pronounced curvature has a high impact in fundamental waves.

Deriving the equation of motion for axial and bending of fundamental waves involve assumptions and approximations. These become less accurate at high frequencies, so more refined models should be used. For example, Euler–Bernoulli theory is used for low frequencies, which includes only transverse inertia and bending deformation, and for high frequencies Timoshenko beam theory include rotary inertia and shear deformation effects. However, Pochhammer-Chree theory is used for high frequency and multiple wave modes to obtain the mechanical wave propagation in cylindrical structures like pipes and rods. Multiple waves can be generated in high frequency, and the fundamental theory cannot provide the behaviour of the waves of high order. Therefore, exact theory or Pochhammer-Cheer Theory should be used to identify the multiple waves propagating in high frequency for a solid bar. In addition, a wave decomposition should be implemented to know the contribution of each wave at different frequencies.

Chapter 5: Wave mode decomposition in frequency domain for a straight and curved bar

5.1 Introduction

The purpose of this chapter is to present the study of wave decomposition in a curved cylindrical bar, in order to establish the effects of the curvature in a complex structure like the chain. A straight bar and curved bar are compared to show the impact of the geometry and the contributions to the response of the various waves. The wave decomposition is very important to identify what wave could have the highest magnitude in a frequency range. In addition, the wave decomposition can provide what type of wave is excited because multiples waves travel in a rod at different frequencies. The wave decomposition is done in frequency domain analysis for a straight and curved bar. The wave mode shape is obtained from Pochhammer-Chree theory, which is described in appendix B. Finite element analysis is carried out to obtain the nodal magnitude velocity in frequency domain. A frequency domain study was carried out in COMSOL over a frequency of 1-30 kHz. A frequency resolution of 200 Hz was considered to compute the nodal magnitude velocity response at 0.9 m from the point of harmonic excitation in a bar and a half chain of length 1 m

Three Finite element Analysis (FEA) models are presented and validated against analytical models [11]. The first model is a semi-infinite rod to excite longitudinal waves, the second model is a semi-infinite beam to excite flexural waves and the third model is a semi-infinite shaft to excite torsional waves. The fundamental waves are validated against the analytical models of semi-infinite rod, semi-infinite beam and semi-infinite shaft. Perfectly matching layer was used to avoid the reflections in each finite element analysis of the straight rod and half chain. Comparison of wave mode decomposition for a straight rod and a half chain are presented as well.

There are some papers available in the literature describing the effect of pipe bend, bent bar and bent plate on guided waves. Demma presented et al. [43] a paper focusing in the understanding of guided wave propagation through pipes with bends, wave mode conversion were obtained after the bend. Sanderson et al. [83] has reported that the effect bends on wave propagation in pipes, is to distort the signal, this could represent false identification of flaws that are not actually there or missing flaws that are not present. Morley derived et al. [89] a theoretical model for propagation of flexural waves in an infinite curved rod, but the model is only valid for rods with slight curvature. Liu and Qu investigated et al. [92], [93] wave propagation using the exact theory

of the dispersion relation in curved plates. However, the theoretical proposal used by the authors for plates is not suitable to the structures like pipes and rods [44]. Aristegui presented et al. [94] a simple finite element model to investigate the effect of a $90°$ bend on the axisymmetric wave modes in a pipe. The mode conversions generated by the bend were reported. These days the published trends show the complex behaviour of waves over pipe bend. However, wave propagation in a chain has not been addressed yet. The effect of bends in a chain and the wave decomposition have been not reported before. In order to obtain a more in-depth understanding of the wave propagation around the curvature of a chain, the current study has been carried out using full 3D finite element analysis in COMSOL and Pochhammer-Chree theory.

This chapter is organized as follows. Pochhammer-Chree theory is presented to calculate the wave mode shapes and the dispersion curves in a cylindrical bar. The dispersion curve is plotted for a frequency range (1-30 kHz), and the wave mode shapes for a specific frequency. Then, the methodology of wave decomposition is introduced in frequency domain. In addition, finite element analysis is carried out for the model semi-infinite rod, semi-infinite beam and semi-infinite shaft. Comparison of the wave decomposition between the straight rod and curved rod is made. Also, this chapter shows the wave mode decomposition for a full chain. Finally, general conclusions are presented from the wave decomposition.

5.2 Pochhammer-Chree theory

Pochhammer-Chree theory deals with wave propagation in structures with cylindrical symmetry like rods and tubes, which behave as wave guides. Waveguide behaviour occurs in axially long prismatic structure and is characterized by the existence of discrete propagation modes and dispersion. The solution of the wave equations in a cylindrical material are readily found by the use of potentials and the technique of separation of variables. The equation are solved by the Singular Value Decomposition (SVD) method to find the mode's amplitude [38]. The solution of the wave equations follows largely the treatment given by Gazis et al. [40] for wave propagation in an infinite hollow cylinder, and also work of Zemanek et al. [51] and Thurston et al. [50] for solid cylinders. The starting point is the following general equation 5.1 for the displacement distribution vector $\hat{u}$.

$$\hat{\mathbf{u}}(r,\theta,z) = \tilde{\mathbf{u}}(r,\theta)\, \mathrm{e}^{-\mathrm{j}kz} = \mathbf{u}(r)\, \mathrm{e}^{\mathrm{j}n\theta} \mathrm{e}^{-\mathrm{j}kz} \tag{5.1}$$

where the cylindrical system is used with coordinates (r,θ,z), harmonic time variation $\mathrm{e}^{\mathrm{j}\omega t}$ is assumed, and ω is the angular frequency, k is the wavenumber and integer n is a separation constant called the circumferential order, which determines the symmetry of the solution in the

circumferential direction. Well known references can be consulted for further information, for example, Graff [41] and Rose [36].

The radially dependent part of the wave mode shape vector $u(r)$ for a rod is expressed in matrix form of equation 5.2 by Seco et al. [38], Zemanek et al. [51] and Thurston et al. [50]:

$$\mathbf{u}(r) = \begin{bmatrix} u_r(r) \\ u_\theta(r) \\ u_z(r) \end{bmatrix} = \mathbf{D}^u(r) \cdot A_{coeff} = \begin{bmatrix} D_{11}^u & D_{12}^u & D_{13}^u \\ D_{21}^u & D_{22}^u & D_{23}^u \\ D_{31}^u & D_{32}^u & D_{33}^u \end{bmatrix} \begin{bmatrix} A \\ B \\ C \end{bmatrix} \tag{5.2}$$

The coefficients of matrix $\mathbf{D}^u(r)$ are given explicitly in Appendix B, table B-1, which depends on Bessel functions, the longitudinal speed c_L and the transverse speed c_T of the solid in infinite media. Where ${c_L}^2 = \frac{(1-\upsilon)}{(1+\upsilon)(1-2\upsilon)}$, and ${c_T}^2 = \frac{1}{2(1+\upsilon)}$, υ is the Poisson's ratio. The Bessel functions describe the radial part of the modes of vibration of a circular cross section [36]. The amplitude coefficients vector $A_{coeff} = [A_c \quad B_c \quad C_c]^T$ consists of longitudinal (A_c), shear vertical (B_c) and shear horizontal (C_c) deformation components. The unknown coefficients A_c, B_c and C_c are determined by application of the boundary conditions. They specify that the traction part of the stress tensor σ_t is null at the cylindrical outer surface of the rod [36], [38], [40], [51], so.

$$\sigma_t = [\sigma_{rr}, \sigma_{r\theta}, \sigma_{rz}]^T = 0 \tag{5.3}$$

where $\sigma_{rr}, \sigma_{r\theta}, \sigma_{rz}$ are the components of outer surface stress, which leads to the following matrix determinant equation.

$$det[\mathbf{D}^{\sigma t}] = \det \begin{bmatrix} \sigma_{rr} \\ \sigma_{r\theta} \\ \sigma_{rz} \end{bmatrix} = \det \begin{bmatrix} D_{11}^\sigma & D_{12}^\sigma & D_{13}^\sigma \\ D_{21}^\sigma & D_{22}^\sigma & D_{23}^\sigma \\ D_{31}^\sigma & D_{32}^\sigma & D_{33}^\sigma \end{bmatrix} = \begin{bmatrix} 0 \\ 0 \\ 0 \end{bmatrix} \tag{5.4}$$

The coefficients of the stress tensor matrix $\mathbf{D}^{\sigma t}$ are given in Appendix B, table B-2. Equation 5.4 is called the frequency or characteristic equation of the waveguide, and its roots (ω, k) determine the proper modes supported by it. Once these roots are known, the vector of amplitude coefficients, A_{coeff} are determined by solving the following homogenous system of equations.

$$\mathbf{D}^{\sigma t}(\omega, k) \cdot A_{coeff} = 0 \tag{5.5}$$

Since matrix $\mathbf{D}^{\sigma t}(\omega, k)$ is singular at the mode's frequency wavenumber roots, a robust method like the singular value decomposition (SVD) for computing the amplitude can be implemented

[38]. Knowing the amplitude coefficients A_{coeff}, the displacement distribution of the wave mode shape vector in equation 5.2 is obtained $\mathbf{u}(r) = [u_r(r) \quad u_\theta(r) \quad u_z(r)]^T$.

5.3 Dispersion curve and wave mode shapes for a cylindrical bar

Three categories of wave mode can propagate in a solid cylindrical bar. The solutions of the wave equations are assembled into so-called 'families' of wave modes, which are depending on their displacement profile behaviour. Longitudinal waves are axisymmetric with radial and axial displacement components. Torsional waves are also axisymmetric, with only circumferential displacement. Flexural waves are the antisymmetric modes and require the three displacement components (radial, circumferential and axial). The Silk and Bainton named et al. [95] a wave rule to identify each wave mode, this rule is used in this thesis, where $\mathrm{L}(0,m)$, $\mathrm{F}(n,m)$ and $\mathrm{T}(0,m)$ are defined for longitudinal, flexural and torsional, respectively. The letter n in the bracket is the order of harmonic variation around the circumference of the rod, and the second number m in the brackets is an index of propagating wave, which increases with increasing frequency of a wave mode's cut off. Number m can be understood as the variation in shape in radial direction. Sanderson presented et al. [19], [64] and Catton showed et al. [57], [65] that the wave mode with n is equal to zero, do not have variation around the circumference, and the waves are called axisymmetric (longitudinal, torsional). However, the waves mode, which have dependence on the three components are called flexural and n is equal or greater than one. In this thesis, Pochhammer-Chree theory is considered to obtain the wave mode shapes and the dispersion curves in a straight rod.

The dispersion curves and wave mode shape are obtained from PCDISP, which was programmed in Matlab by Seco et al. [38], the solution of the roots of the waveguide's frequency equation, which satisfy the boundary condition described in section 5.2. In order to do the wave mode decomposition and identify the number of wave modes for a specific range of frequency, the dispersion curve was obtained from PCDISP for a steel rod of 80 mm radius with the material properties of Young's modulus 200 GPa, shear modulus 76.9 GPa, density 7850 $\frac{\mathrm{kg}}{\mathrm{m}^3}$ and Poisson's ratio 0.3. Publicly available PCDISP software et al. [38], was used to calculate the group speed of propagation modes in a frequency range from 0 to 30 kHz [38]. The dispersion curve of a cylindrical bar can be obtained from Pochhammer-Chree theory, which is described section 5.2. PCDISP was used to plot the dispersion curve, the dispersion curve is plotted in Figure 5-1, where the blue lines of longitudinal mode are denoted by L, the red line of torsional mode is denoted by T (circumferential order $n = 0$ for axisymmetric) and the green lines of flexural modes are

denoted by F (circumferential order $n \geq 1$ for antisymmetric). In Figure 5-1, only nine wave modes exist at the maximum frequency of 30 kHz. In fact, for frequency lower than 14.5 kHz, there are only three fundamental modes L(0,1), T(0,1) and F(1,1). Above a cut-off frequency of 22.5 kHz the nine wave modes exist.

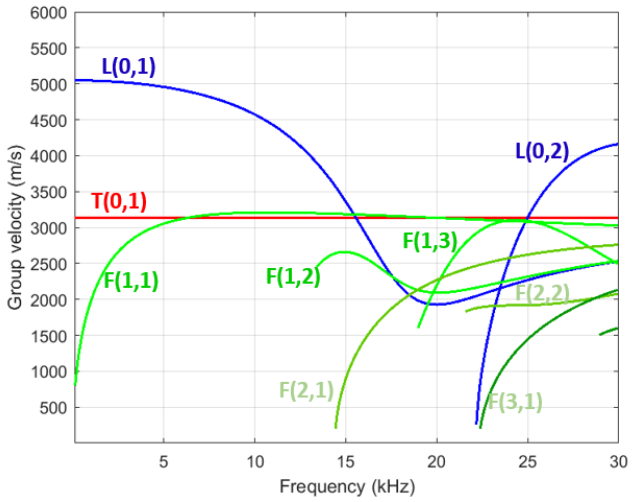

Figure 5-1 Group speed dispersion curve for steel rod of 80 mm radius

Figure 5-2 shows the wavelength $\lambda = \frac{c_p}{\omega}$ of each wave mode over the range of frequencies (1-30 kHz). It is observed that the smallest wavelength for a straight section of rod with radius of 80 mm is 0.1m. The wavelength is an important parameter to define the size of the mesh during the finite element analysis. It is defined that the minimum wavelength should cover at least 8 elements size of the mesh to get accurate results during wave propagation analysis [54], [66]. Catton presented et al. [57] that eight elements per the smallest wavelength is enough to define the element size of the mesh.

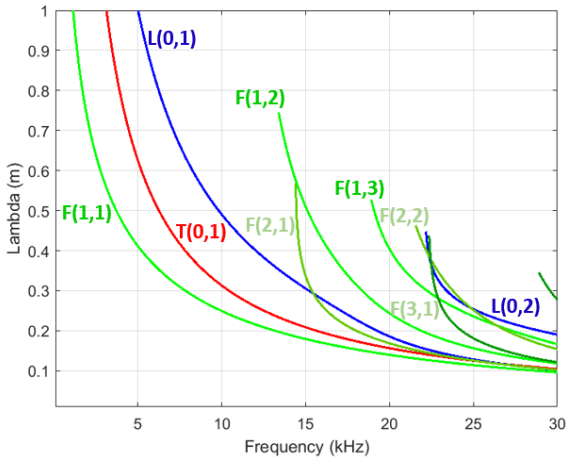

Figure 5-2 Wavelength for steel rod of 80 mm radius

The work described in appendix B has resulted in some routines written in Matlab environment by Seco et al. [38], which were used to plot the dispersion curves and the wave mode shape. Figure

5-3 shows a comparison of wave mode shape (radial u_r, circumferential u_θ and axial u_z) components between Disperse and PCDISP at 30 kHz for a bar of 80 mm radius. It can be observed a good agreement in the normalized displacement profile distribution for each component. This means that the matlab routine of PCDISP has accurate results as the commercial software called Disperse. It should be noted that to use commercial software, it is necessary to pay a license. However, the matlab routines of PCDISP are free but the Pochhammer-Chree theory should be studied to be able to update the code in the routines. For example, the flexural wave F(1,1) is an antisymmetric wave, which depends of the radial u_r, circumferential u_θ and axial u_z components. It should be note that the radial component has the maximum contribution on outer surface of the rod. However, the circumferential component is almost constant across the radius of the rod. On the contrary, the axial displacement component, which is initially zero at the centre of the rod, becomes dominant on the outside surface as the radius increases. Figure 5-3 shows helpful plots to understand the profile distribution displacements of the wave mode shape for a specific frequency. Rose presented et al. [36] similar plots to visualize the symmetric or antisymmetric behaviours of the normalized displacement profile distribution of the wave mode shape along the radius of the pipe to know what components is dominant on the outside surface of the pipe.

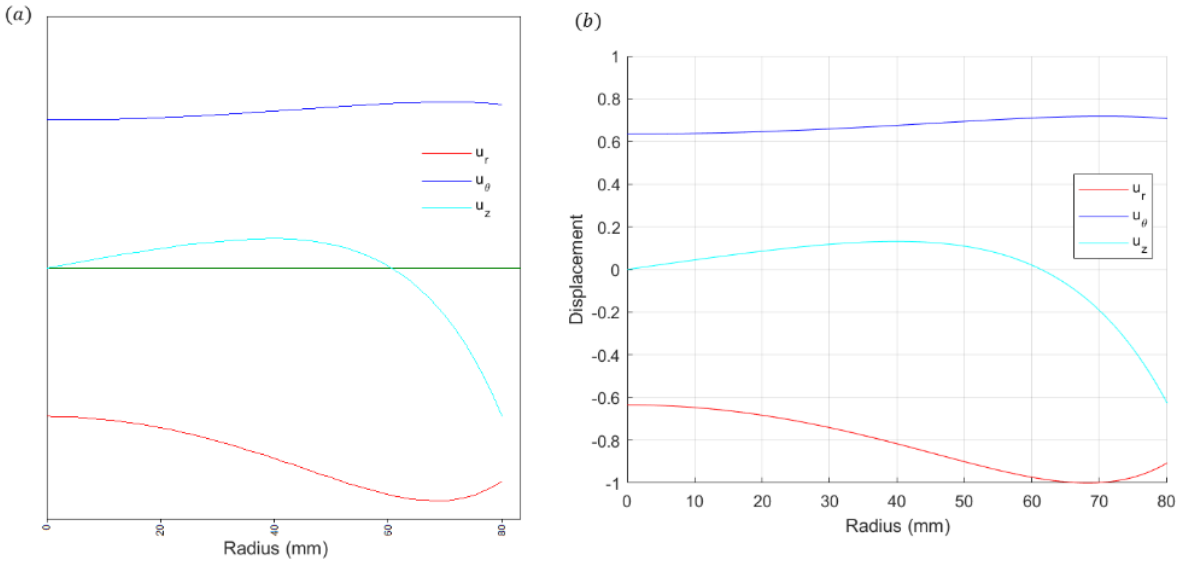

Figure 5-3 Comparison of displacement profile distribution of wave mode shape F(1,1) at 30kHz: Disperse (left), PCDISP (right).

In Figure 5-4, 2D plots (cross-section) of the wave mode shapes are shown for a frequency of 25 kHz. The 2D plots were obtained in Matlab, using the normalized displacements distribution $u_r(r), u_\theta(r), u_z(r)$ from PCDISP et al. [38] of equation 5.2. So, the wave mode shape in cylindrical coordinate system are defined as,

$$\begin{Bmatrix}\tilde{u}_r\\ \tilde{u}_\theta\\ \tilde{u}_z\end{Bmatrix} = \tilde{\mathbf{u}}(r,\theta,z) = \tilde{\mathbf{u}}(r,\theta) = \begin{Bmatrix}u_r(r)\\ u_\theta(r)\\ u_z(r)\end{Bmatrix} \mathrm{e}^{\mathrm{j}n\theta} \tag{5.6}$$

Transformation of wave mode shape is done from cylindrical to cartesian.

$$\begin{Bmatrix}\tilde{u}_x\\ \tilde{u}_y\\ \tilde{u}_z\end{Bmatrix} = \begin{bmatrix}\cos\theta & -\sin\theta & 0\\ \sin\theta & \cos\theta & 0\\ 0 & 0 & 1\end{bmatrix}\begin{Bmatrix}\tilde{u}_r\\ \tilde{u}_\theta\\ \tilde{u}_z\end{Bmatrix} \tag{5.7}$$

Figure 5-4 shows the cross section of the wave mode shapes for a frequency of 25 kHz. For example, F(1,1), F(1,2) F(1,3) show one cycle variation around the circumference of the rod but for the third flexural wave mode F(1,3) has higher radial variation shape than F(1,1). The wave mode shape with two harmonic variation can be observed for F(2,1), F(2,2). The first flexural wave mode F(3,1) is the only one with three cycles of particle displacement variation around the circumference. It should be noted that the universally used term is flexural waves for antisymmetric waves, the standard terminology is used as described in many papers such as [57], [63]–[65], [96]. For longitudinal wave modes, there are zero cycle variation around the circumference in each wave mode, but the shape in radial direction is higher in L(0,2) than L(0,1).

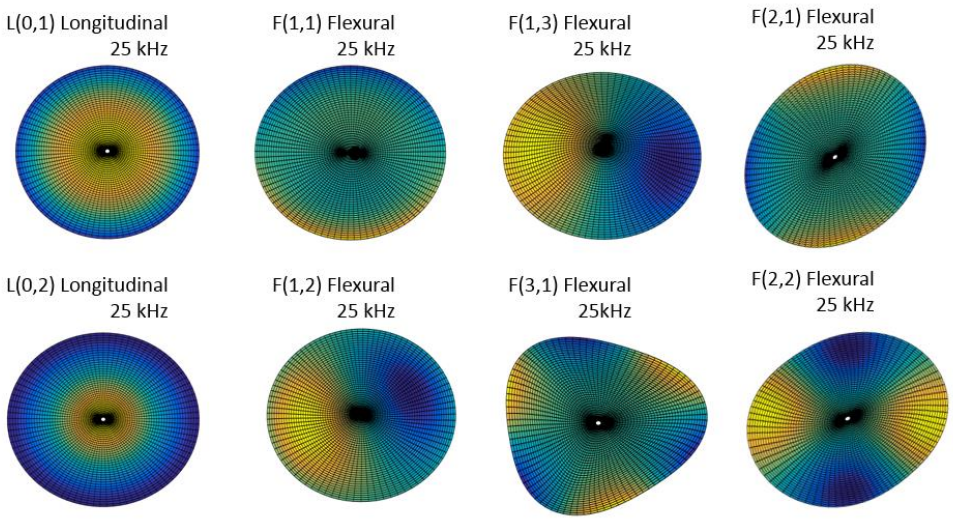

Figure 5-4 Cross section wave mode shape surface at 25 kHz (blue=max, yellow=min)

In addition, the axisymmetric behaviour for longitudinal wave and the antisymmetric behaviour for flexural waves can be observed. All axisymmetric waves have the same displacement profile in each angle of the cross-section. However, the antisymmetric waves, the displacement profile is different in each angle of the cross section, this produces harmonic variation around the circumference.

5.4 Wave mode decomposition method

Multiple waves travel in a rod of specific radius within a frequency range, where the superposition of the multiple wave is still today a challenging topic. It should be noted that the separation of the wave mode is very important to know what wave could be excited with higher wave contribution. Catton et al. [57] presented a cosine filter to obtain the contribution of waves of the same harmonic in a pipe, but the cosine filter is not able to obtain the contribution of individual waves. In fact, the number of generated wave is higher in a rod than in a pipe. Therefore, a new wave mode decomposition methodology is presented in this thesis, where a harmonic excitation is considered in this chapter. For a harmonic wave propagation in the z direction, the nodal amplitude at any point along the cross section of the rod is defined as

$$[\mathbf{N}(\omega)]_{dof\ x\ ndf} = [\mathbf{Q}(\omega)]_{dof\ x\ nw}\,[\mathbf{A}(\omega)]_{\ nw\ x\ ndf} \tag{5.8}$$

where:

$[\mathbf{N}(\omega)]_{dof\ x\ ndf}$ is the nodal velocity matrix along the cross section of the rod, the size of $\mathbf{N}(\omega)$ degree of freedom (dof) by the number of delta frequencies ndf, $\mathbf{N}(\omega)$ is obtained from finite element analysis.

$[\mathbf{Q}(\omega)]_{dof\ x\ nw}$ is the wave modes shape matrix of the cross section rod (see Figure 5-5), where nw is the number of the wave modes excited within the frequency range. $\mathbf{Q}(\omega)$ is built from the displacement distribution of each component of equation 5.6.

$$[\mathbf{Q}(\omega)]_{dof\ x\ nw} = \begin{bmatrix} wave_{mode1} & wave_{mode2} & & & wave_{mode\ nw-1} & wave_{mode\ nw} \\ \tilde{u}_{r\,c_1,\theta_1} & \tilde{u}_{r\,c_1,\theta_1} & & & \tilde{u}_{r\,c_1,\theta_1} & \tilde{u}_{r\,c_1,\theta_1} \\ \vdots & \vdots & & & \vdots & \vdots \\ \tilde{u}_{r\,c_i,\theta_1} & \tilde{u}_{r\,c_i,\theta_1} & \cdots & & \tilde{u}_{r\,c_i,\theta_1} & \tilde{u}_{r\,c_i,\theta_1} \\ \tilde{u}_{r\,c_1,\theta_2} & \tilde{u}_{r\,c_1,\theta_2} & \cdots & & \tilde{u}_{r\,c_1,\theta_2} & \tilde{u}_{r\,c_1,\theta_2} \\ \vdots & \vdots & & & \vdots & \vdots \\ \tilde{u}_{r\,c_i,\theta_j} & \tilde{u}_{r\,c_i,\theta_j} & \cdots & & \tilde{u}_{r\,c_i,\theta_j} & \tilde{u}_{r\,c_i,\theta_j} \\ \tilde{u}_{\theta\,c_1,\theta_1} & \tilde{u}_{\theta\,c_1,\theta_1} & & & \tilde{u}_{\theta\,c_1,\theta_1} & \tilde{u}_{\theta\,c_1,\theta_1} \\ \vdots & \vdots & & & \vdots & \vdots \\ \tilde{u}_{\theta\,c_i,\theta_1} & \tilde{u}_{\theta\,c_i,\theta_1} & \cdots & & \tilde{u}_{\theta\,c_i,\theta_1} & \tilde{u}_{\theta\,c_i,\theta_1} \\ \tilde{u}_{\theta\,c_1,\theta_2} & \tilde{u}_{\theta\,c_1,\theta_2} & \vdots & & \tilde{u}_{\theta\,c_1,\theta_2} & \tilde{u}_{\theta\,c_1,\theta_2} \\ \vdots & \vdots & \cdots & & \vdots & \vdots \\ \tilde{u}_{\theta\,c_i,\theta_j} & \tilde{u}_{\theta\,c_i,\theta_j} & \vdots & & \tilde{u}_{\theta\,c_i,\theta_j} & \tilde{u}_{\theta\,c_i,\theta_j} \\ \tilde{u}_{z\,c_1,\theta_1} & \tilde{u}_{z\,c_1,\theta_1} & \cdots & & \tilde{u}_{z\,c_1,\theta_1} & \tilde{u}_{z\,c_1,\theta_1} \\ \vdots & \vdots & & & \vdots & \vdots \\ \tilde{u}_{z\,c_i,\theta_1} & \tilde{u}_{z\,c_i,\theta_1} & \vdots & & \tilde{u}_{z\,c_i,\theta_1} & \tilde{u}_{z\,c_i,\theta_1} \\ \tilde{u}_{z\,c_1,\theta_2} & \tilde{u}_{z\,c_1,\theta_2} & \cdots & & \tilde{u}_{z\,c_1,\theta_2} & \tilde{u}_{z\,c_1,\theta_2} \\ \vdots & \vdots & & & \vdots & \vdots \\ \tilde{u}_{z\,c_i,\theta_j} & \tilde{u}_{z\,c_i,\theta_j} & & & \tilde{u}_{z\,c_i,\theta_j} & \tilde{u}_{z\,c_i,\theta_j} \end{bmatrix}_{dof\ x\ nw} \tag{5.9}$$

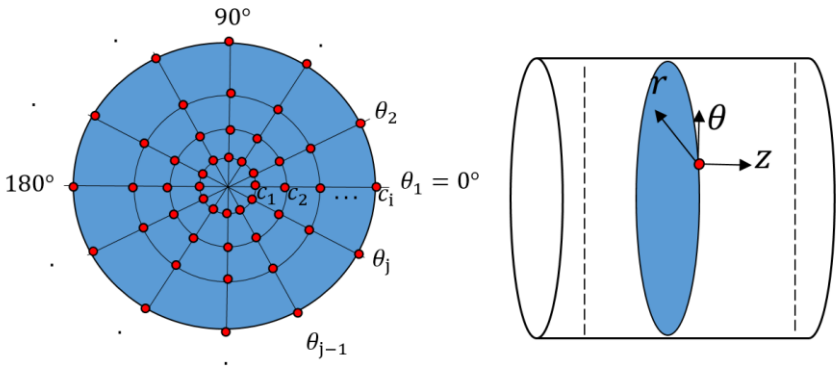

Figure 5-5 Distribution of nodes to obtain the wave mode shape of each *dof* along the cross section ($c_i$is the maximum number of division along the radius, θ_j is the maximum number of division along the surface)

$[\mathbf{A}(\omega)]_{nw\ x\ ndf}$ is the unknown wave amplitude matrix for each delta frequency.

Doing matrix algebra operation the unknown $[\mathbf{A}(\omega)]$ amplitude of each wave can be obtained, calculating the pseudo-inverse of the wave mode shape matrix $[\mathbf{Q}(\omega)]$.

$$[\mathbf{A}(\omega)]_{nw\ x\ ndf} = [\mathbf{Q}(\omega)]^{+}_{nw\ x\ dof}[\mathbf{N}(\omega)]_{dof\ x\ ndf} \tag{5.10}$$

It should be noted that the dimensions of matrix $\mathbf{Q}(\omega)$ change according to the number of the nw excited waves over the frequency range. For example for a frequency lower than 14.5 kHz, there are only three wave modes. However, for a frequency higher than the cut-off frequency of 22.5 kHz, there are nine wave mode, see Figure 5-1. The pseudo-inverse of $\mathbf{Q}(\omega)$ was calculated for the frequency range (1-30 kHz) every 200Hz. A computationally simple and accurate way to compute the pseudoinverse $\mathbf{Q}(\omega)$ is by using the singular value decomposition (SVD), which is a factorization of a real or complex matrix that generalizes the eigen-decomposition (eigenvalues and eigenvectors) of a square normal matrix. As the matrix $\mathbf{Q}(\omega)$ is not square, the condition number was calculated to measure how sensitive the matrix is, to know how much the output can change for a small change in the input argument, with low condition number is said to be the well-conditioned, the rank of the matrix was obtained to know the number of linearly independent waves. Figure 5-6 shows an example of the condition number and rank for the frequency range. It is observed full rank, it means that all the propagate waves amplitudes as represented by the chosen dofs, are linearly independent. For example, the rank is three for a frequency lower than cut-off frequency 14.5 kHz (there are only three propagate waves below cut-off frequency 14.5 kHz), so it means that the three fundamental waves are independent because the rank is three. In addition, the rank is nine for a frequency higher than the cut-off

frequency 22.5 kHz and lower than 30 kHz, so this means that the nine existing waves in this range of frequency (22.5-30 kHz), are linearly independent. It should be noted that in this analysis, there is not evanescent wave, it is considered only propagate waves, which carry out energy. On the other hand, the condition number is near a values of one, this means that the linear system has a unique solution. So the matrix is non-singular and well-conditioned, because when the condition number is infinite, the linear system does not have a unique solution and has many solutions, it is considered as ill-conditioned, this means that the correct pseudo inverse solution becomes hard to find.

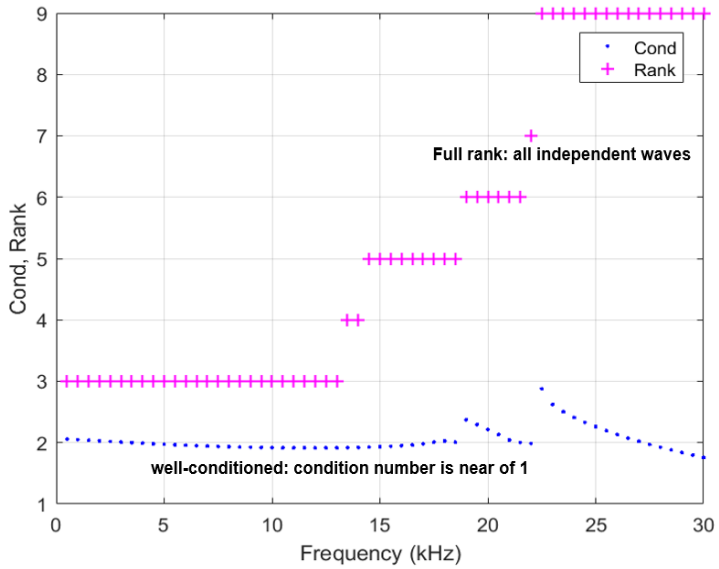

Figure 5-6 Condition number (blue dots) and rank (pink+) of pseudo-inverse matrix $\mathbf{Q}(\omega)$

5.5 Finite Element Analysis of the steady state response

The nodal velocity matrix $\mathbf{N}(\omega)$ was obtained from the finite element analysis of the steady state response, where a frequency domain study was done in COMSOL over a frequency of 1-30 kHz. A frequency resolution of 200Hz was considered to compute the nodal amplitude velocity response of the travelling waves at 0.9m from the point of harmonic excitation in a rod and a half chain of length 1m. Catton presented et al. [57] that a point load excites all the wave modes. Therefore, an excitation source is considered to excite all the modes in this thesis because it is important to know what type of wave could have the higher contribution during the wave decomposition. Catton showed et al. [57] that some waves cannot be excited if multiples forces are equally distributed around the surface of a pipe. However, when only a point force is applied, multiple

wave modes over the frequency bandwidth of the excitation signal would be generated. Figure 5-7 shows the rod and half chain model, where the red dots represent the point load of 1N amplitude at the centre of the circular face for a rod (axial force) and a beam (transverse force). Some nodes (probes) were used to monitor the nodal amplitude (velocity) along the cross section of the rod. The monitoring nodes (blue cross-section) were considered at 0.9 m from the excitation point load to know the nodal amplitude in each components (r, θ, z). In the half chain, the nodal amplitudes were obtained at the same distance from the excitation point as the rod to know the effect of the curved rod in the wave decomposition. At the end face of each model, a so-called Perfectly Matched Layer (PML) was used to represent an infinite domain to avoid the reflections and to obtain only the effect of the curved rod [97].

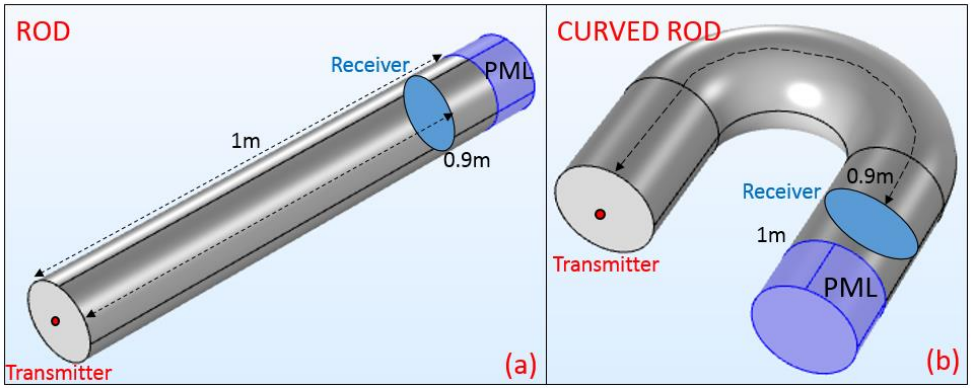

Figure 5-7 COMSOL Model with receiver at 0.9 m (a) Rod, (b) Half chain

Sanderson implemented et al. [63], [66] the same rule to define the element size of the mesh, Sanderson considered eight elements per the smallest wavelength. For this FEM analysis, the element size was 10mm, which was sufficient to capture the smallest possible wavelength λ_{min} of 0.1 m for a straight section of the rod (see Figure 5-2). In fact, for the simulations 10 elements per wavelength were considered, so $size = \frac{\lambda_{min}}{10} = 0.01$ m. The element type used, was quadratic 3D solid elements (COMSOL element type 3-D hexahedron, which has 8 vertices, 12 edged, bounded by 6 quadrilateral faces, it is also called brick. The accuracy of solution in hexahedral meshes is the highest). Sanderson validated et al. [66], this mesh size definition and element type in previous work. The material properties for steel rod were the same as defined in section 5.2. The dimensions of bend part in the half chain were defined according to the offshore mooring chain standard dimension [1], see Figure 5-8. The link has a curvature radius equal to $2.25\, r_b$, so for a rod of radius $(r_b = 80$ mm$)$, the curvature radius is equal to 180 mm.

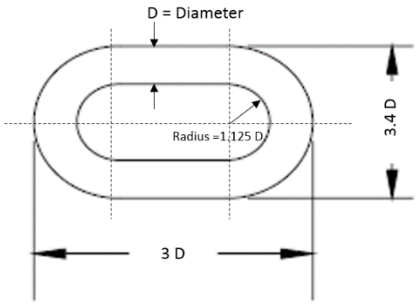

Figure 5-8 Studless link [2].

Figure 5-9 shows the distribution of the nodal points along the cross section. The nodal velocity was recorded every 20mm along the radius and every 30 degrees along the cross section for each component (r, θ, z). The number of degree of freedom (dof) is 144 (4x12x3), where $4 = \frac{80\ \text{mm}}{20\ \text{mm}}$, $12 = \frac{360°}{30°}$ and 3 is for each components (r, θ, z) of the cylindrical coordinate system.

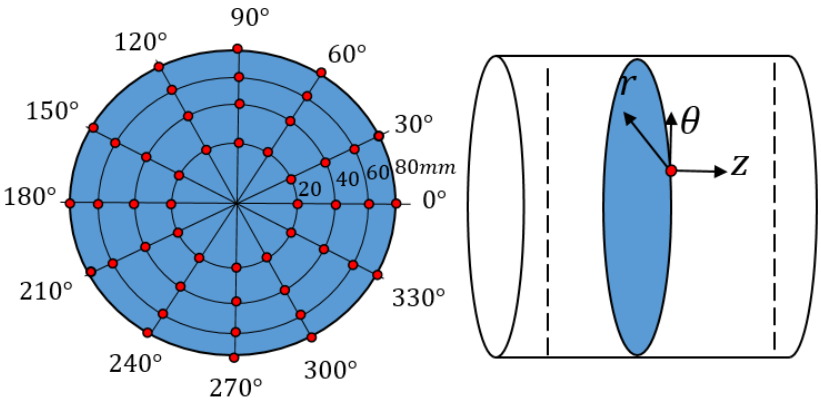

Figure 5-9 Distribution of probes to obtain the nodal velocities of each *dof* along the cross section

In COMSOL, a Perfectly Matched Layer (PML) uses some layers to model an infinite domain for the elastic waves. The key property of the PML formulation is the complex scaling function, which controls anisotropic damping. These non-physical layers absorb all outgoing waves only in frequency domain analysis avoiding reflections at the boundary. Zampolli showed et al. [98] that the PML normally only attenuates propagating waves because evanescent waves decay exponentially and do not carry energy. Morvaridi presented et al. [99] that PML can be seen as a coordinate transformation, where the propagation waves are replaced by exponentially decaying waves. Morvaridi showed et al. [99] that the transformation must damp the incoming waves, by applying a complex transformation $\tilde{z}(z) = z + \mathrm{j}f_s(z)$, the generic wave $\mathrm{e}^{\mathrm{j}kz}$ is transformed into the wave $\mathrm{e}^{\mathrm{j}k\tilde{z}(z)} = \mathrm{e}^{\mathrm{j}k[z+\mathrm{j}f_s(z)]}$. However, the attenuation can be accelerated in evanescent wave by including a real coordinate stretching. This means to have a complex stretching function $f_s(z)$,

where the imaginary part becomes a real coordinate stretching causing evanescent wave decaying more quickly. Figure 5-10 shows the behaviour of the original wave e^{jkz} and transformed wave $e^{jk[z+jf_s(z)]}$ at PLM using a polynomial stretching scaling function 5.11 with a scaling factor $s_f = 0.05, s_f = 0.2$. Figure 5-10(a) shows the behaviour of the original wave and the transformed wave for $s_f = 0.05$, it can be observed that the transformed wave with PLM layer is exponentially decaying for $z > 0.5$, where the PLM layers are considered, corresponding to an absorbing region. Figure 5-10 (b) shows a similar behaviour of the waves decaying for $z > 0.5$ but as the scaling factor increases ($s_f = 0.2$), the absorbing region has a better Perfect Matched Layer performance.

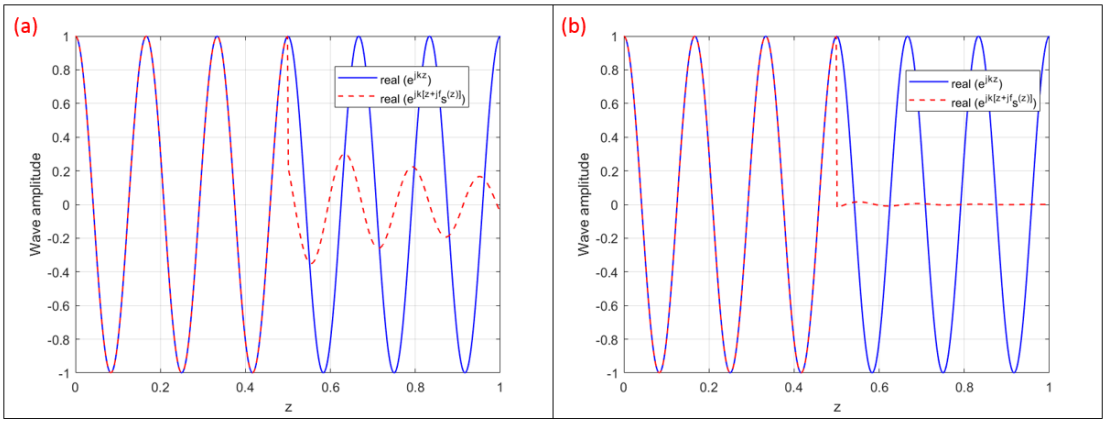

Figure 5-10 Original wave e^{jkz} and transformed wave $e^{jk[z+jf_s(z)]}$ using a scaling factor (a) $s_f = 0.05$, (b) $s_f = 0.2$ along $z < 0.5$ (non PLM) and $z > 0.5$ (PLM)

Figure 5-7 shows the PML at the end face of each model to absorb all possible reflections. In 3D COMSOL models, PMLs implement a complex coordinate stretching in the three directions (r, θ, z). In each direction, the same form of stretching $f_s(\xi)$ is used, defined as a function of a dimensionless coordinate ξ. The complex displacement for stretching in a single direction is defined in COMSOL as,

$$\Delta u_i = \lambda f_s(\xi) - \Delta_w \xi \tag{5.10}$$

where λ is the typical wavelength parameter, $f_s(\xi)$ is the stretching complex scaling function and Δ_w is the original width of the perfectly matched Layer. In the Perfectly Matched Layer nodes simulation, a polynomial stretching scaling function was used, which is defined as,

$$f_s(\xi) = s_f \xi (1 - j) \tag{5.11}$$

where s_f is a scaling factor. The typical wavelength parameter corresponds to the longest wavelength of propagation wave in an infinite medium, in this study case it was considered equal

to 0.16 m, which is equivalent to the diameter of the rod. Zienkiewicz presented et al. [100] that the polynomial stretching is the most suitable when there is a combination of different wave families in the model, like longitudinal, torsional and flexural. Moreover, in the polynomial function, the equal real and imaginary part indicate that propagation and evanescent waves with the similar scaling parameter are treated equally. To obtain an appropriate scaling parameter s, several simulations were carried out in COMSOL until the parameter s was tuned. With the tuned parameter, the reflections were avoided and the models were represented as semi-infinite models. In fact, the results were compared against semi-infinite analytical models. These results are presented in the next sub-sections with good agreements with analytical models, where one dimensional analytical model such as rod, beam and shaft can be described as the fundamental longitudinal, flexural and torsional waves, respectively [11]. The analytical models are introduced in chapter 4 section 4.2.

5.5.1 Comparison between a semi-infinite rod and a half chain models

In this section, a semi-infinite rod and a half chain model are presented to carry out a frequency domain study to compute the steady state response of the models subjected to harmonic excitation for several frequencies. The types of travelling waves that can be excited in a model depend upon the direction of applied point load. For a semi-infinite rod, a 1 N harmonic excitation force in axial direction was applied at the centre of the cross section of one face. Figure 5-11(a) shows the analytical model for a semi-infinite rod [11], where S, E, ρ, k_l are the area of the cross-section, Young's modulus, density and longitudinal wave number respectively. It should be noted that the longitudinal wavenumber is proportional to the frequency, this means that the longitudinal wave speed $(c = \frac{\omega}{k})$ is independent of frequency (non-dispersive). It can be observed that the velocity of the analytical model (dash black line) is in good agreement with the fundamental longitudinal wave (solid blue line) L(0,1) for a frequency lower than 10kHz (Figure 5-10(c)). In fact, it is observed that the PML is working as infinite elements because the semi-infinite rod model is matching with the fundamental longitudinal wave. After 10 kHz, the longitudinal velocity (blue solid line) from finite element results has a dispersion behaviour. This is not observed in the analytical model, where the wave amplitude is constant and the wave is not dispersive. It is observed how the fundamental theory has some limitations after 10 kHz. However, the finite element results provide better results in high frequency because the finite element model uses more complex solution and has an approach to exact theory, where the dispersion behaviour can be observed.

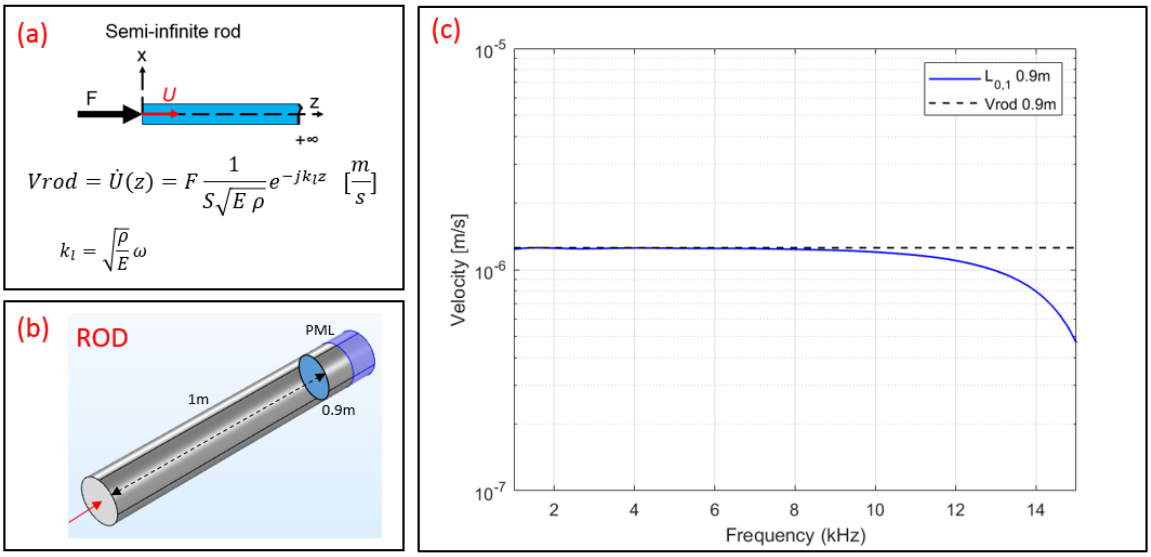

Figure 5-11 (a) Analytical model of rod, (b) 3D FEM with receivers at 0.9 m, (c) Comparison of analytical model and fundamental longitudinal wave during axial excitation

In Figure 5-12 (a), (b), the comparison of the semi-infinite rod and the half chain is presented, respectively. It is observed how the curved rod has an impact in the wave decomposition. In fact, wave conversions are presented. For example in the semi-infinite rod (Figure 5-12(a)), only the longitudinal L(0,1) and L(0,2) are excited, L(0,2) starts to be excited at the cut-off frequency of 23 kHz. However, in the curved rod (half chain) some flexural waves such as F(1,1), F(1,2) and F(2,1) are excited with high wave amplitude (Figure 5-11(b)). This means that the bend converts axisymmetric to antisymmetric waves but the highest wave contribution can still be observed for L(0,1). Moreover, in the straight rod, the wave amplitude is constant for a frequency lower than 10 kHz. Then, some resonances are observed between 16 kHz and 18 kHz, it is because the cut-off frequency of new wave modes are added, a similar behaviour is observed between 22 kHz and 24 kHz. However, in the curved rod, the wave amplitude has some variations in a frequency lower than 10 kHz, this means that the curvature produces some reflections and the Perfectly Matched Layer is not able to absorb them.

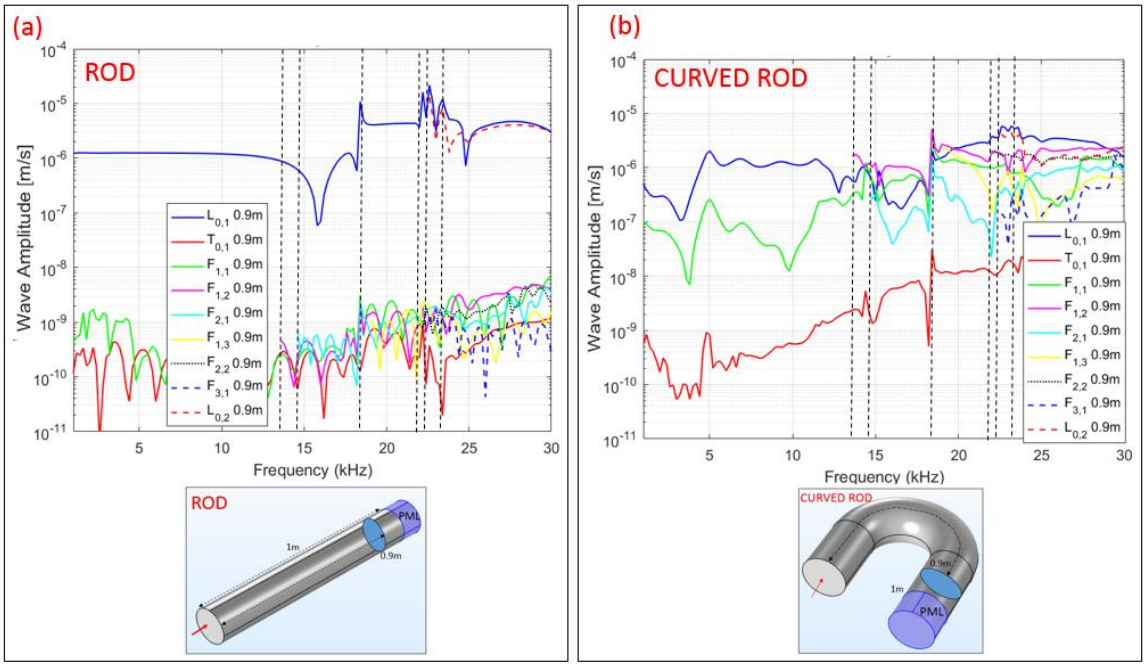

Figure 5-12 Comparison of wave decomposition at 0.9 m during axial excitation for a semi-infinite rod (a) and a half chain (b) (dashed lines mean the cut-off frequencies)

5.5.2 Comparison between a semi-infinite bar beam and a half chain model

In this part a semi-infinite beam model and half chain model are presented to show the comparison of the wave decomposition in frequency domain. For a semi-infinite beam, a harmonic excitation force in transversal direction is applied at the centre of the cross section of one face. Figure 5-13(a) shows the analytical model for a semi-infinite beam [11], where I, k_b are the second moment of area about the neutral axis and flexural wavenumber, respectively. It should be noted that the bending wavenumber is proportional to the square root of frequency. This means that bending wave speed has differing dependencies on frequency (dispersive). In Figure 5-13(c), it can be observed that the velocity of the analytical model (dash pink line) is in good agreement with the fundamental flexural wave (solid green line) F(1,1) for a frequency lower than 5kHz. Again, the Perfectly Matched Layer is working as infinite elements, because the semi-infinite beam model is matching with the fundamental flexural wave.

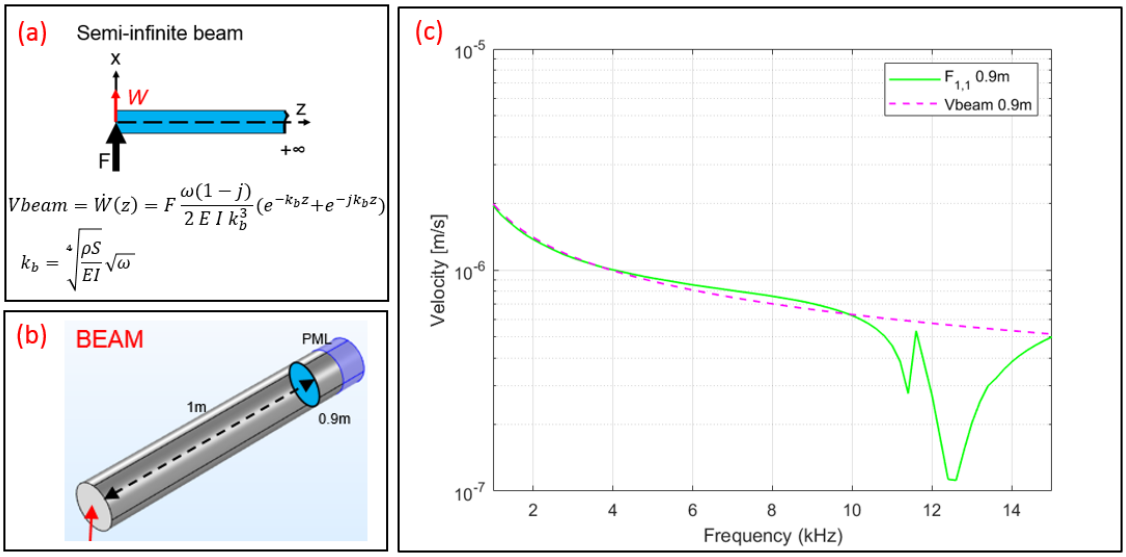

Figure 5-13 (a) Analytical model of beam, (b) 3D FEM with receiver at 0.9 m, (c) Comparison of analytical model and fundamental flexural wave of FEM during transversal excitation

Figure 5-14(a) shows that Perfectly Matched Layer (PML) is working and attenuating the waves because there is not resonance peak amplitude, which could be generated due to the free end of the rod. This means that thanks to the PLM, which represents an infinite domain, the reflections of the free end are avoided. Moreover, Figure 5-14(a) and (b) show the comparison of the semi-infinite beam and the half chain models, respectively. Again, it is observed how the curved beam has an impact in the wave decomposition. For example in the semi-infinite beam only (Figure 5-14(a)), the flexural F(1,1), F(1,2) and F(1,3) are excited. However, in the curved beam (half chain), new flexural waves like F(2,1), F(2,2), and F(3,1) are excited with low amplitude in the bent beam, and the converted torsional mode T(0,1) is excited with the highest wave amplitude (Figure 5-14(b)). This means that wave conversions are presented from antisymmetric to axisymmetric waves.

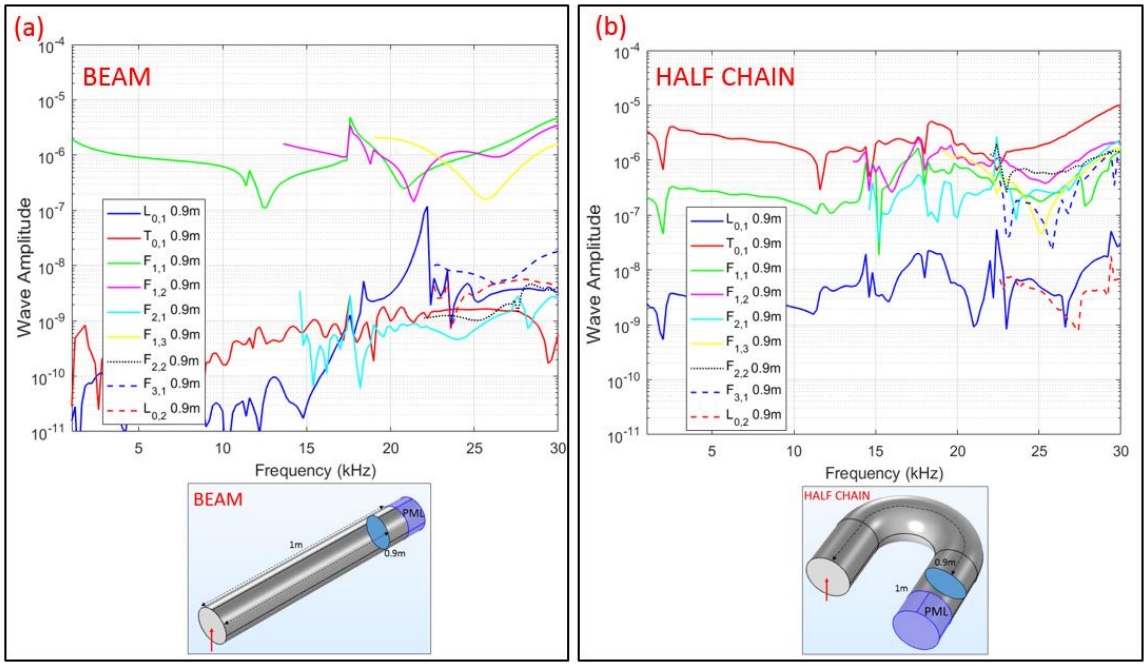

Figure 5-14 Comparison of wave decomposition at 0.9 m during transversal excitation for a semi-infinite beam (a) and a half chain (b)

5.5.3 Comparison between a semi-infinite shaft and a half chain model

Finally, a semi-infinite shaft and half chain models are presented to compare the wave decomposition in frequency domain. For a semi-infinite shaft, to excite the torque a harmonic excitation transverse force and a second force in opposite direction are applied at external radius of one face. Figures 5-15(a) shows the analytical model for a semi-infinite shaft [11], where G, I, r_b, T, k_s are shear modulus, the second moment of area, radius of rod, torque equal to $2r_bF$ and shear wavenumber, respectively. The shear wavenumber is proportional to the frequency like the longitudinal wavenumber. This means that the shear wave speed $(c = \frac{\omega}{k})$ is independent of frequency i.e. is non-dispersive. It is observed in Figure 5-15 that the wave amplitude of the analytical model (dash cyan line) is converted from angular speed Ø to tangential speed $Vshaft$ to get the same scale. In Figure 5-15(c), good agreement is observed with the fundamental torsional wave (solid red line) T(0,1) for the frequency range. In fact, it is observed that the Perfectly Matched Layer works as infinite elements, because the velocity of the semi-infinite shaft model is almost the same to the fundamental torsional wave.

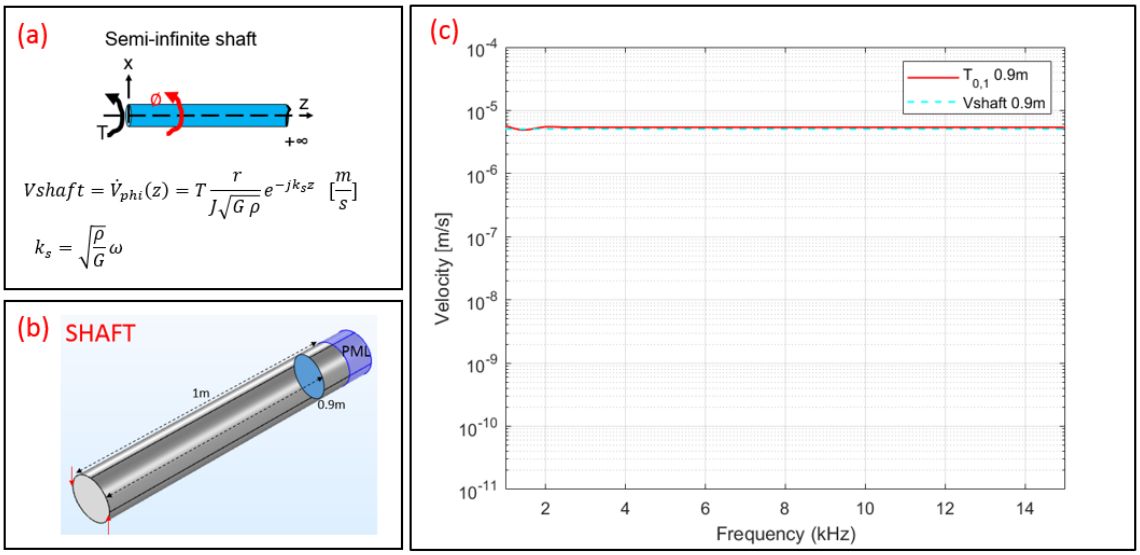

Figure 5-15 (a) Analytical model of shaft, (b) 3D FEM with receiver at 0.9 m, (c) Comparison of analytical model and fundamental torsional wave

In Figure 5-16(a) and (b), the comparison of the semi-infinite shaft and the half chain is presented, respectively. For example in the semi-infinite shaft (Figure 5-16(a)), the magnitude of the torsional T(0,1) is the same in the range of frequency. However, in Figure 5-16(b), it is observed how the bent shaft has an impact in the wave decomposition. Again, wave mode conversions are presented after the curvature. Figure 5-16(b) (bent shaft) the magnitude of the torsional wave is oscillating, new flexural modes F(1,1), F(1,2) F(3,1) are excited with high contribution to the propagated wave. For a frequency higher of 23 kHz, axisymmetric torsional wave is converted to antisymmetric waves F(1,1) and F(1,2) due to the curvature.

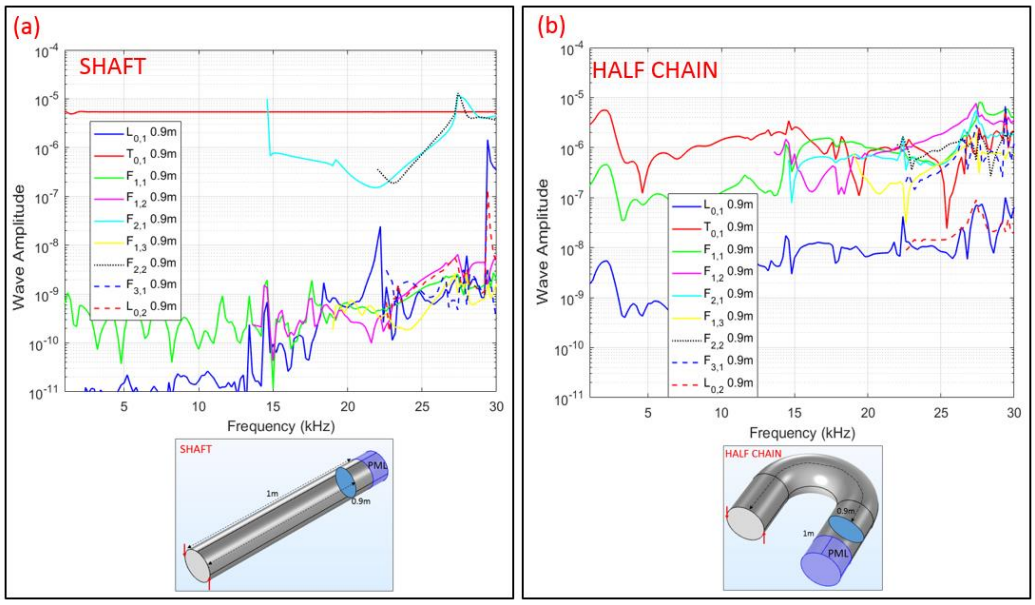

Figure 5-16 Comparison of wave decomposition at 0.9 m for a semi-infinite shaft (a) and a half chain (b)

5.5.4 Wave decomposition in a full link

PML is an area bordering the computational domain where waves are damped so that propagating waves become evanescent, more frequently used to avoid reflections and to simulate infinite elements, as the previous results have shown. However in real world, the boundary conditions of each structure should be considered. Now, considering the wave decomposition for a full chain, multiple reflections will be obtained due to the bends at either end parts of the chain. Comparing Figure 5-12(b) (half chain) and Figure 5-17 (full chain). Figure 5-17 shows the wave decomposition, when an axial point load is applied in the straight part. Multiple resonance peaks are observed, which are produced from multiple reflections due to the bents, and the interference between incident and reflected waves at different frequencies, this behaviour is not observed in Figure 5-12(b). In Figure 5-17, it is also observed that many flexural waves are converted with high contribution. It means that the wave decomposition in a full chain may provide only limited information as to wave contributions. In frequencies lower than 23 kHz, the longitudinal wave L(0,1) has the highest contribution. The L(0,2) has the higher contribution for frequencies higher than 23 kHz. However, at high frequencies, it is difficult to describe the differences in contribution between each wave, because almost all the waves are excited and converted with similar amplitude.

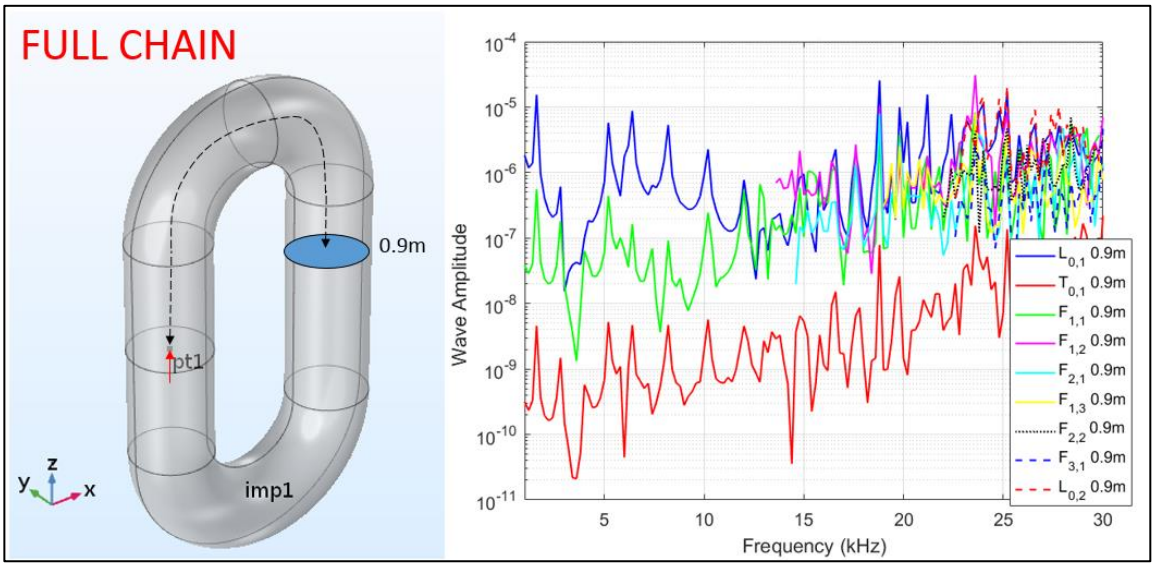

Figure 5-17 Travelling waves decomposition at 0.9 m from excitation for a full chain with axial point load at the centre of the straight part

Figure 5-18 shows the wave decomposition when a transverse point load is applied in the straight part of a full chain. Again, multiple resonance peaks are observed, which are produced from multiple interferences between incident and reflected waves at different frequencies. However, in this occasion the wave with the highest contribution is for torsional. A similar behaviour of the

wave conversion from flexural to torsional was observed in the half chain of Figure 5-13(b) with Perfectly Matched Layer. However, Figure 5-18 shows multiple resonances frequencies due to the reflections generated from the bends.

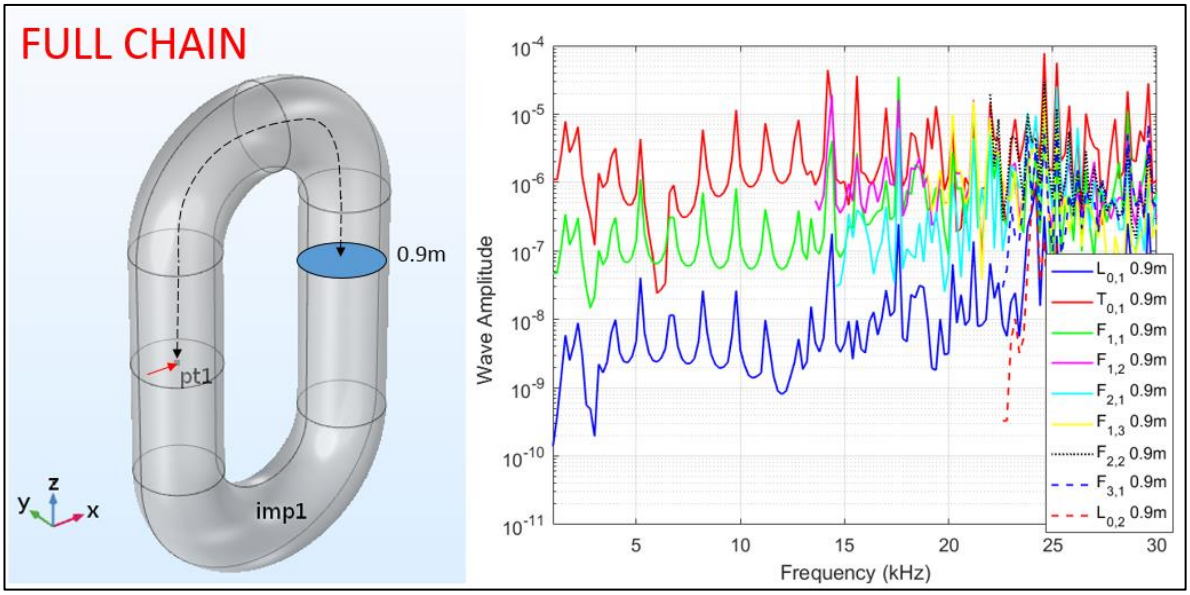

Figure 5-18 Travelling wave decomposition at 0.9 m from excitation for a full chain with transverse point load at the centre of the straight part

Finally in Figure 5-19, wave decomposition is presented for the full chain and excitation in the bend. In this simulation, the point load was applied in the bend part of the chain. Bastid and Perez presented et al. [14], [101], respectively, that the curved part is the area where failure is most likely, due to the highest tensile loads. These tensile loads can cause fatigue in the interlink contact area. Figure 5-19 shows that, when the point load is applied in the bent part, the longitudinal wave L(0,1) has again the highest contribution in a frequency lower than 18 kHz. It has a similar behaviour, as in the case when the point load is applied in the straight part (Figure 5-16). In addition, for a frequency higher than 23kHz, the longitudinal wave L(0,1) and L(0,2) have high contribution. There are many resonance peaks, which are generated by the multiple reflections of the bends in the chain. It is hard to see the contribution of each wave in high frequency because the number of excited wave increases and the contributions are very similar. This multiple reflections cannot be eliminated in frequency domain analysis with harmonic excitation. Therefore, wave decomposition in time domain are considered in the next chapters, where only the incident and the first reflections wave are analysed.

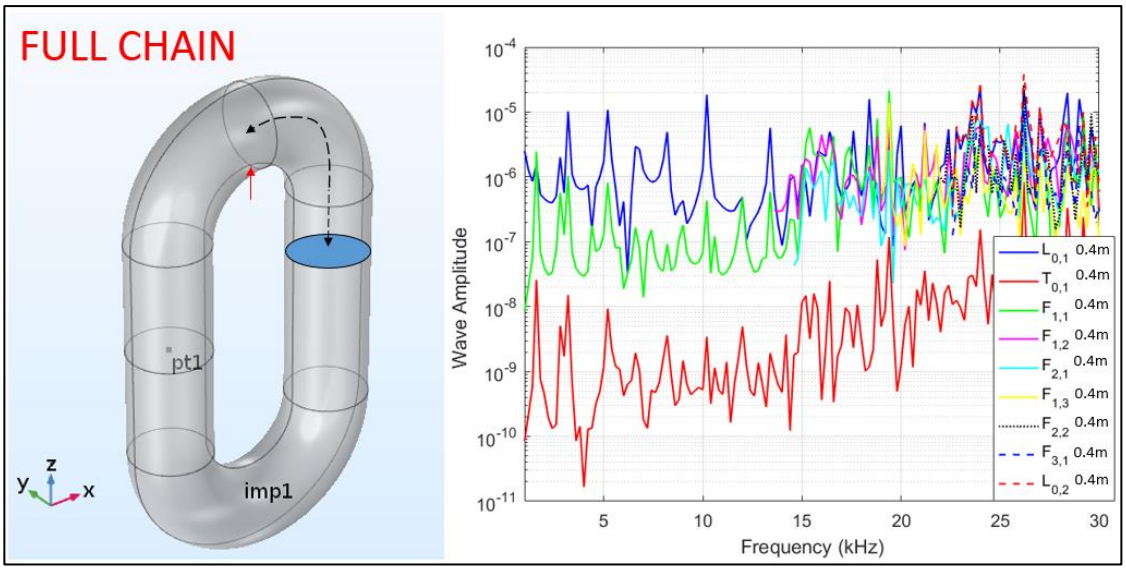

Figure 5-19 Travelling wave decomposition at 0.4 m from excitation for a full chain with point load at the bend of the chain

5.6 Conclusions

An approach to do wave decomposition in frequency domain was presented for a straight rod, half chain and full chain. The following conclusions were obtained from the results:

- For tensile point load in the straight part of the chain, longitudinal waves were converted to flexural waves due to the curved part of the chain. However, the longitudinal waves still have the highest contribution in the half and full chain. Therefore, the longitudinal wave could describe a possible tensile displacement when a tensile force acts at the straight part of the chain.
- For transverse point load in the straight part of the chain, the flexural waves were converted to torsional waves with the highest contribution in the half and full chain. Therefore, the torsional wave could describe the shearing displacement when a transverse force acts at the straight part of the chain.
- In the half chain model during torsional excitation, the torsional wave has the highest contribution at low frequencies up to 16 kHz. However, the torsional wave is converted in flexural at high frequencies. Therefore, the new flexural waves could describe a possible bending displacement when a torque acts at the straight part of the half chain.
- In the full chain, the longitudinal wave has the highest contribution when the transverse point load is applied in the bend part of the chain. It is concluded that the longitudinal wave could describe a possible tensile displacement when transverse load acts in the bend.
- In the models with bend, the chain bends have a high impact in the wave propagation. In fact, for a full chain many resonance peaks in the wave are generated due to the multiple interferences between the incident and reflected waves from the bends. However, the wave decomposition methodology can still provide the waves with the highest contribution at various values over the frequency range.

The study demonstrated that it is, in principle, feasible to do wave decomposition in a chain. It should be emphasized that this wave decomposition method can quantify individual wave contributions, not just wave families because internal dof along the cross section were used. However, at the moment, the wave decomposition is done only in simulation for frequency domain where multiples reflection are observed. It is important to realize that for next chapters, wave decomposition in time domain is done to eliminate multiple reflections. In addition, experimental validation is considered. However, the sensors can be installed only around the surface of the straight part of the chain (external radius).

Chapter 6: Wave decomposition in time domain for a cylindrical steel bar

6.1 Introduction

The purpose of this chapter is to present a study of wave decomposition in a cylindrical steel bar, it is a similar method to that proposed in chapter five but in time domain instead of frequency domain. It is important to realize that wave decomposition in time domain is done to eliminate multiple reflections and analyse the behaviour of the incident wave before reflections. The work has been carried out on simulation data and validated with experimental measurements. Finite element analysis models in ABAQUS have been carried out in time domain to simulate propagating wave from a transient input. The wave mode shape matrix of a cylindrical bar are obtained from Pochhammer-Chree theory of chapter 5.2. Then, the wave decomposition is done applying the pseudo-inverse to the wave mode shape matrix to find the contribution of each wave in different excitation conditions in a long bar. An excitation point load of a 60 kHz Hann-windowed pulse was applied to excite all the wave modes in the spectrum (20-80 kHz).

The wave decompositions for four different excitation conditions are compared to show the contribution of each wave. The effect of reducing the number of measurements locations has also been studied. The simulation has been validated against the experimental results using only the radial component, where the wave decomposition has been obtained for waves of the same harmonic order. In addition, pencil lead breaks experiments, which represent a crack-like event, were done to find the contribution of each wave from in-plane and out-of-plane excitations.

Moreover, two more finite element analysis models were also validated against experiments using all the components. The first model is a long rod with an axial force excitation, the second model is a long rod with a transverse force excitation. A 3 m long cylindrical bar was used to avoid reflections from the free end face. An experimental comparison of the wave mode decomposition for the rod two cases is also presented. The method appears to work effectively, however, in the real world, the nodal acceleration can be measured only at the outer surface of the bar and it may only be possible to measure it at a few locations.

6.2 Dispersion curve and wave mode shapes for a cylindrical bar

In chapter 5.2, equation 5.44 is called characteristic equation of the waveguide, and its roots (ω, k) determine the proper modes supported by it. In order to do the wave mode decomposition and identify the number of wave modes for a specific frequency range, dispersion curves were obtained for a steel rod of 45 mm diameter and common steel material properties of Young's modulus 200 GPa, shear modulus 76.9 GPa, density of 7850 $\mathrm{kg/m^3}$ and Poisson's ratio 0.3. Seco developed et al. [38] some routines in Matlab to calculate the roots of the waveguide's frequency equation and the group velocities, these routines were used to obtain the dispersion curve for a frequency range of 0 to 100 kHz. The resulting dispersion curves are plotted in Figure 6-1, the longitudinal modes are labelled by L (blue lines), the torsional mode is labelled by T (red line) and the flexural modes are labelled by F (green lines). In Figure 6-1, only eight wave modes with two harmonic exist at the maximum frequency of 100 kHz. In fact, for frequencies lower than about 50 kHz, there are only the three fundamental modes L(0,1), T(0,1) and F(1,1). It is notable that the only non-dispersive wave is the lowest torsional mode T(0,1), where the phase velocity is equal to the shear velocity c_T. In addition, lower dispersion can be observed in F(1,1) after 60 kHz. The other wave modes exhibit dispersion in the frequency range studied (0-100 kHz).

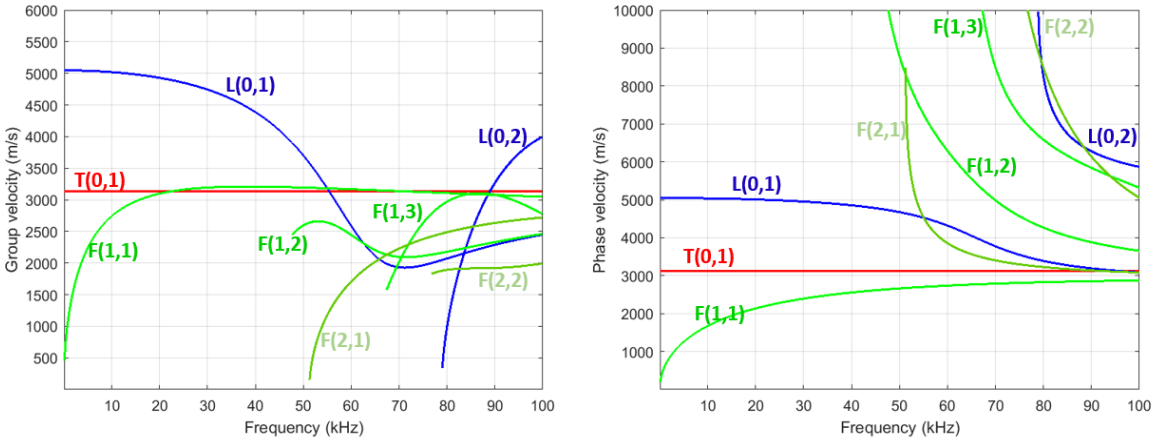

Figure 6-1 Group velocity (left), Phase velocity (right) dispersion curve for steel bar of 45 mm diameter

Figure 6-2 shows the profile displacement distribution of wave mode shape across the radius of the bar. Seco presented et al. [38] some routines to obtain the wave mode shape using Matlab, where the Pochhammer-Chree theory is described in chapter 5.2. Many interesting observations can be made on the wave mode shape distributions. Notice for example, the dominant radial u_r component on the outer surface for L(0,1) and F(2,1). However, for both F(1,1) and F(1,3) the circumferential u_θ component is the dominant on the outer surface of the rod at 60kHz and 80 kHz, respectively. This is unusual in the case of F(1,3) where it would expect the axial component to be dominant throughout. In the case of the torsional wave mode, it only has circumferential

component dependency, as expected. This displacement represents the lowest torsional mode. Rose presented et al. [36] that in the lowest non-dispersive mode, the amplitude of u_θ is proportional to the radius, the higher torsional modes are dispersive. The only flexural wave mode with dominant axial u_z component is F(1,2). It is important to notice that the wave mode shape is dependent on both the frequency and the radius of the cylindrical bar, and that there is variation in each component along the radius. Seco presented et al. [38] that the wave mode shape components can be normalized by dividing each component with the maximum value components.

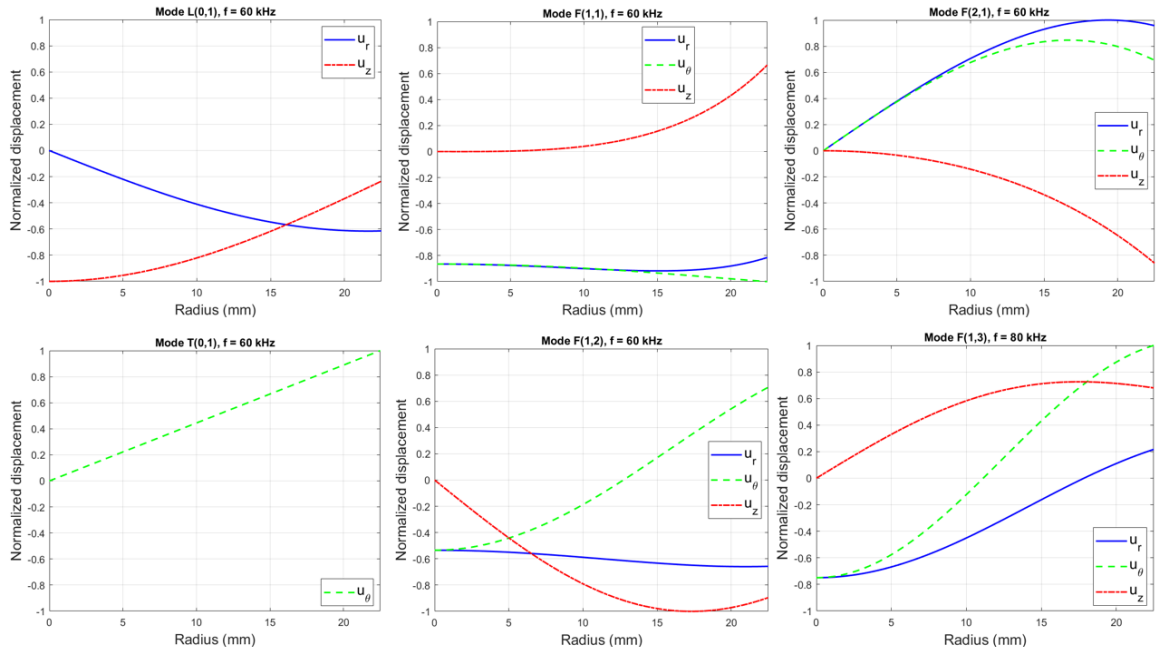

Figure 6-2 Displacement profile distribution of wave mode shapes for rod of 45 mm diameter

6.3 Methodology of wave decomposition in time domain

A method of analysis, based on combined finite element analysis and analytical wave mode shape, is presented here for wave decomposition. Abduljabbar presented et al. [102] a hybrid method that combines analytical and finite element to investigate the dispersion of Lamb waves in a plate. Nassar also presented et al. [102] a combined finite element and analytical technique for analysing the scattering of Lamb waves. Boucheron showed et al. [103] an experimental modal decomposition of an acoustic field in a cavitation tunnel with a square duct section but this one was done in frequency domain. Hayashi et al. [52] and Catton et al.[57], [59] presented a novel cosine filter method to do wave decomposition in time domain for pipeline. However, the cosine filter can do the decomposition for the family of waves and not for the individual waves. There is not methodology currently presented, which can provide individual wave mode decomposition in a chain. Therefore, this methodology is presented in this thesis to analyse the wave propagation

in a rod and the effect of the bends in a link. Alleyne et al. [96], Al-Nassar et al. [104] and Subhendu et al. [106] showed that the wave propagation at any point could be expressed as a superposition of several wave modes. This superposition is a combination of multiple wave mode shapes and the wave amplitudes. It should be noted that to do a wave decomposition is a challenge. In this new thesis work, the wave decomposition technique has been adapted and applied to rods where the wave modes are more abundant and more complex. This has meant that the wave modes can be extracted without the need for temporal gates or multiple signal processing techniques.

For wave propagation in the z direction, the nodal amplitude at any point on the cross section of the rod is defined as the combination of the wave mode shape matrix and the wave amplitudes vector as follows:

$$[\mathbf{N}(t)]_{dof\ x\ ndf} = [\mathbf{Q}]_{dof\ x\ nw}\,[\mathbf{A}(t)]_{nw\ x\ ndf} \tag{6.1}$$

where:

$[\mathbf{N}(t)]_{dof\ x\ ndf}$ is the transient nodal acceleration vector every delta time ndt in each degree of freedom (*dof*) on the cross section of the rod, which can be obtained from finite element analysis, or experimental measurements.

$[\mathbf{Q}]_{dof\ x\ nw}$ is the wave mode shape matrix for a specific frequency, which is built from the normalized displacement distribution of Equation 6.3, the matrix size is the number degree of freedom dof by the number of the excited waves nw .

$[\mathbf{A}(t)]_{nw\ x\ ndt}$ is the unknown amplitudes of the nw excited waves in every delta time. ndf is the number of delta time.

The number of degrees of freedom is defined as $\#dof = \#nodes \cdot \#components \cdot \#rings$, where $\#nodes$ is the number of nodes in the cross section, $\#components$ is the component considered in each direction (radial, circumferential, axial), $\#rings$ is the number of rings considered along the radius as is shown in Figure 6-3.

Now, through matrix algebra, the unknown $\mathbf{A}(t)$ can be obtained by calculating the pseudo-inverse of the wave mode shape matrix $\mathbf{Q}$.

$$[\mathbf{A}(t)]_{nw\ x\ ndf} = [\mathbf{Q}]^{+}_{nw\ x\ dof}[\mathbf{N}(t)]_{dof\ x\ ndf} \tag{6.2}$$

In chapter 5.2, Equation 5.41 defines a spatially dependent complex displacement. The general solution for the displacement distribution in cylindrical coordinates has the form of Equation 5.41. The propagate waves modes were only considered because the evanescent wave do not carry out energy, the wave mode shape displacement distribution of Equation 6.3 is denoted simply by $\tilde{\mathbf{u}}(r,\theta) = \mathbf{u}(r)\, \mathrm{e}^{\mathrm{j}n\theta}$, the wave mode shape matrix $\mathbf{Q}$ was built, using the real part:

$$\tilde{\mathbf{u}}(r,\theta) = \mathrm{real}(\mathbf{u}(r)\, \mathrm{e}^{\mathrm{j}n\theta}) = \mathrm{real}\left(\begin{bmatrix} u_r(r) \\ u_\theta(r) \\ u_z(r) \end{bmatrix} \mathrm{e}^{\mathrm{j}n\theta}\right) = \begin{pmatrix} u_r(r)\cos(n\theta) \\ -u_\theta(r)\sin(n\theta) \\ -u_z(r)\sin(n\theta) \end{pmatrix} \qquad (6.3)$$

It should be noted that the dimensions of matrix $\mathbf{Q}$ changes according to the number of the nw excited waves at the frequency of interest. For example, for a frequency at 30 kHz, there are only three wave modes $nw = 3$. However, for a frequency at 80 kHz, there are six wave modes $nw = 6$, see Figure 6-1, where the dispersive curve shows the number of the excited waves in the frequency range of interest. According to the dispersion curves shown in Figure 6-1, it is expected that around eight wave modes could be excited within the frequency bandwidth (20-100 kHz). The disadvantage of the wave decomposition method in time domain is able to do the decomposition only in a specific frequency and no in broadband spectrum. Therefore, since knowing the centre frequency of the excitation, the mode shape matrix is computed at that frequency to estimate the wave decomposition. However, in chapter five the method of wave decomposition in frequency domain is able to do the decomposition in broadband spectrum.

Figure 6-3 shows the distribution of the nodal points in the cross section. The nodal acceleration was recorded at each of these locations. In this work, the maximum number of degrees of freedom (*dof*) is $324 = (12 \cdot 3 \cdot 9)$, where $12 = \frac{360^\circ}{30^\circ}$, 3 is for each direction component (r, θ, z) and the number nine of rings along the radius $9 = \frac{22.5\ \mathrm{mm}}{2.5\ \mathrm{mm}}$.

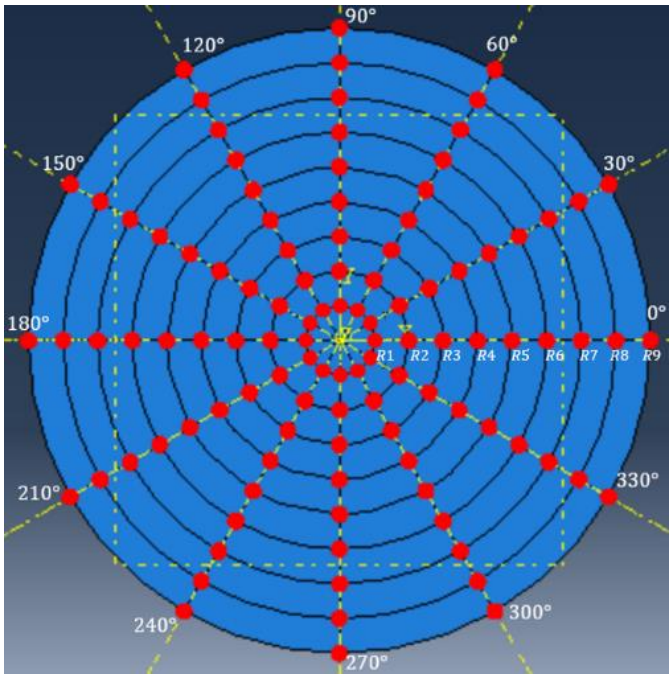

Figure 6-3 Distribution of point used to obtain the nodal acceleration on the cross section

The pseudo-inverse was calculated for the wave mode shape matrix $\mathbf{Q}$. In fact, the condition number and rank number was calculated for each wave mode shape matrix $\mathbf{Q}$, to confirm that the linear system has a solution that is well-conditioned and each wave is independent. It was confirmed that the condition number was near 1 (from 1.1 to 1.8) and the rank number was the same as nw wave of interest.

6.4 Finite element analysis of the transient response

6.4.1 Finite element approach

In order to verify the wave decomposition method, Finite element analysis (FEA) was carried out to obtain the transient nodal accelerations for a rod with four different simple excitation arrangements. The wave propagation in the time domain was considered for only the incident and first reflected wave, where time is gated out owing to the length of the rod. The test specimen modelled was a steel cylindrical bar of 3 meter long with a diameter of 45 mm. ABAQUS Explicit was used to simulate the wave propagation in each case of study. In this chapter of the thesis, an excitation was applied at the end face of the bar in each model as shown in Figure 6-5. The excitation was a 5-cycle Hanning-windowed (see equation 6.4) with a centre frequency $f = 60\ \mathrm{kHz}, nc = 5$. It should be noted that five cycles were used to have a short width pulse because the width pulse of 10-cycle Hanning-window is larger and could affect the analysis from possible reflection before the full incident pulse is applied. Catton presented et al. [57] that all possible wave modes over the frequency bandwidth of the excitation signal would be generated due to it

being a point source excitation. Figure 6-4 shows the Hann-windowed pulse of duration T and its spectrum. Hann-windowed function is considered in the rod and beam model for the wave propagation analysis in each model of this chapter. The width of the pulse is $\text{width} = \frac{nc}{f} = \frac{5}{60\ \text{kHz}} = 83.33\ \mu\text{s}$.

$$g(t) = \frac{1}{2}\sin(2\pi f t)\left[1 - \cos\left(\frac{2\pi f t}{nc}\right)\right] \qquad t \leq 0 \leq T \qquad (6.4)$$

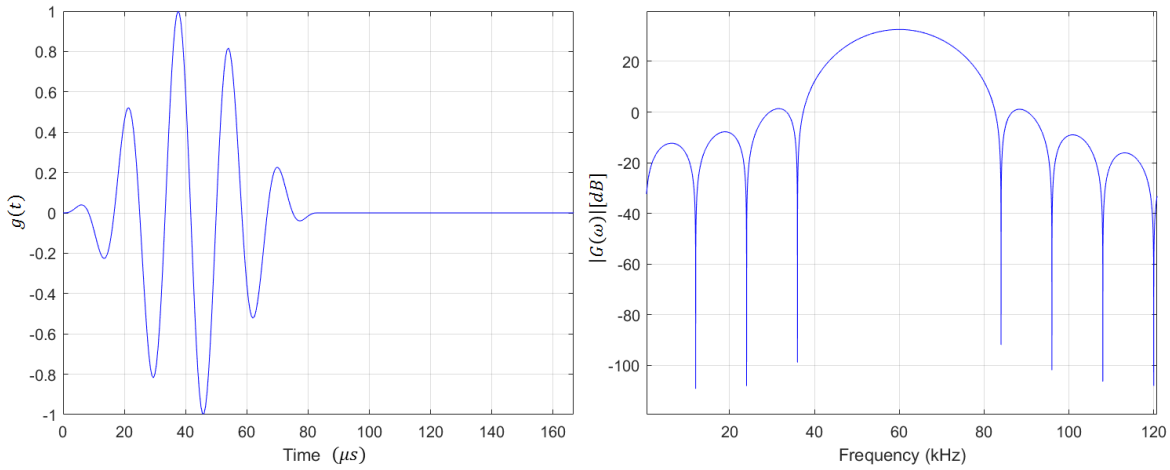

Figure 6-4 Hann-windowed 5 cycle excitation pulse with centre frequency 60 kHz (left), Excitation spectrum (right)

Figure 6-5 shows the models and the positions where the point of excitation was applied. For case A (Figure 6-5(a)), the excitation was applied at the centre of the end of the face in the axial direction. This was expected to excite purely longitudinal waves. Figure 6-5(b) shows case B, where the excitation was designed to excite mainly T(0,1). Finally, the excitation was applied at the end face in the transverse direction in the centre as shown in Figure 6-5(c) (case C). Moreover, Figure 6-5(d) (case D) shows the excitation applied at outer surface of the end face in transverse direction. Flexural waves are expected to be excited for these two last cases C and D. A set of nodes (receivers) were used to monitor the acceleration in the cross section of the rod, 0.5m from the excitation point load in order to obtain the nodal acceleration in each of the cylindrical components (r, θ, z).

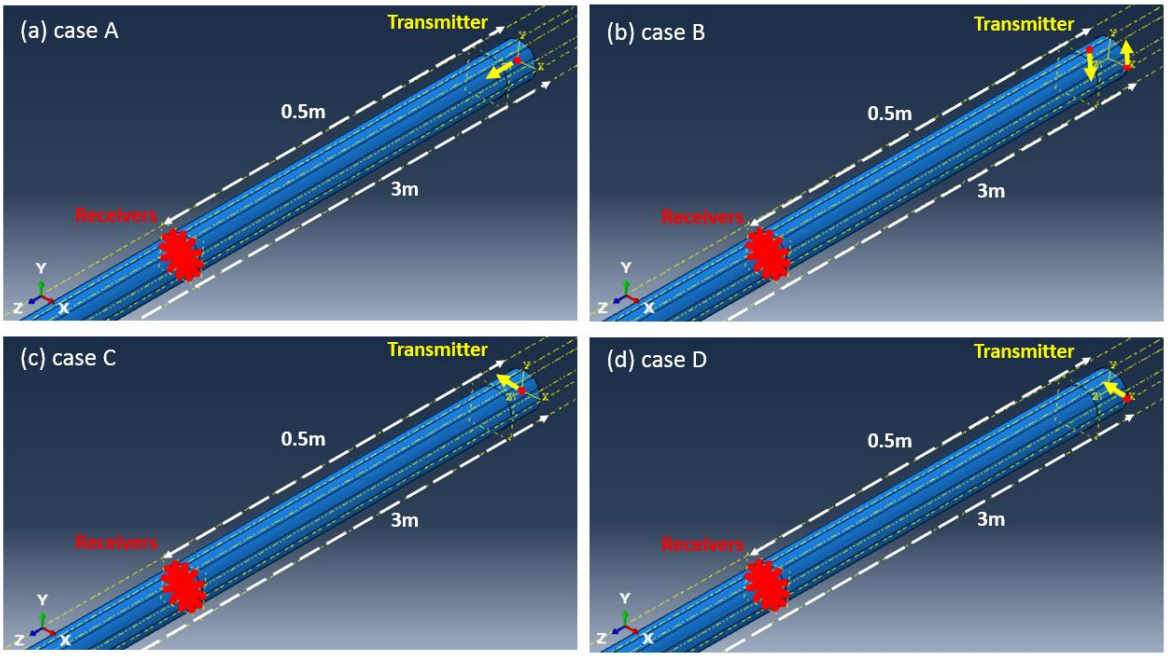

Figure 6-5 Models for cylindrical rods with different loading conditions: (a) excitation in axial direction at the centre, (b) torsional excitation at outer surface, (c) traverse excitation at the centre, (d) transverse excitation at the outer surface

The element size was around 3 mm, which was sufficient to capture the smallest possible wavelength λ_{min} of 0.03 m for a cylindrical bar [66]. There were therefore around ten elements per minimum wavelength. The element type used, was quadratic 3D solid elements with reduced integration (ABAQUS element type C3D8R, which has 8 vertices in linear brick with reduced integration). Sanderson validated et al. [64], [66], this mesh refinement and element type in previous finite element work. The material properties for steel were the same as given in Section 6-2 (Young's modulus 200 GPa, shear modulus 76.9 GPa, density 7850 $\frac{\text{kg}}{\text{m}^3}$ and Poisson's ratio 0.3).

6.4.2 Finite element results and wave decomposition in time domain

The nodal acceleration in the time domain was obtained in ABAQUS, in each degree of freedom, for the grid shown in Figure 6-3. The wave mode decomposition technique was applied to the four cases (A, B, C and D) as illustrated in Figure 6-5. Figure 6-6 shows the normalized wave decomposition results, where the waves with higher contributions can be observed for each case. It should be noted that the normalization was done by dividing each wave with the maximum wave amplitude in each case of study. Figure 6-6(a) confirms that only the longitudinal L(0,1) is obtained, when an axial load is applied at the centre of the end face. It can be seen that the longitudinal wave is dispersive at 60 kHz, as expected from the dispersion curve shown in Figure 6-2. Also, as expected, Figure 6-6(b) (case B), the torsional T(0,1) is dominant and non-dispersive throughout the frequency range. In addition, a lower contribution of F(2,1) is observed. This is,

because only two excitation points were considered, which avoids all the flexural waves with one harmonic around the circumference but nothing higher.

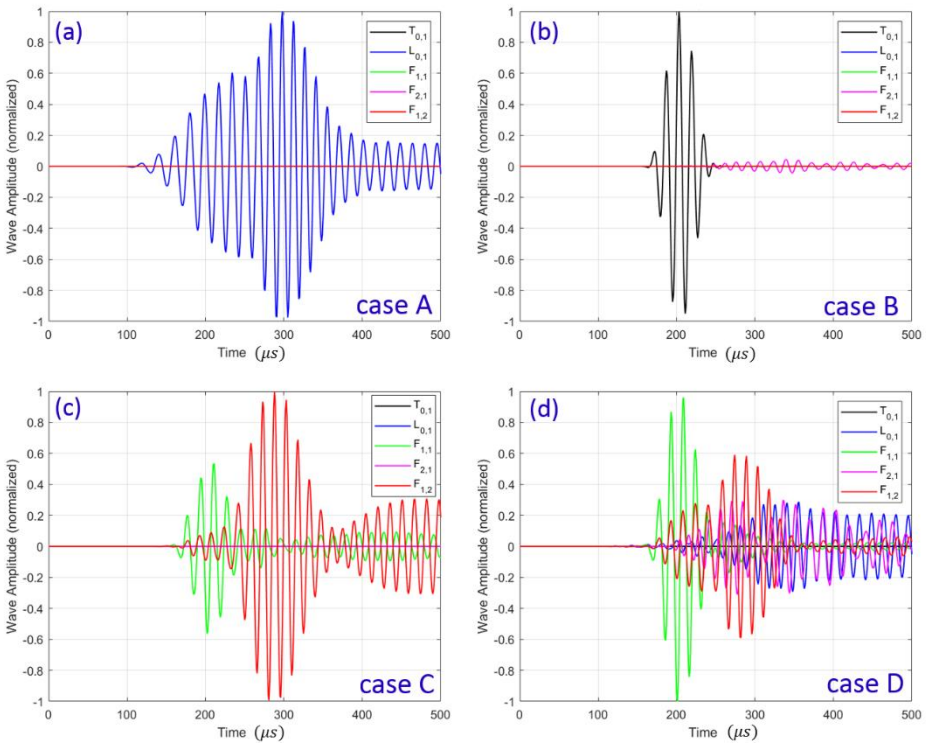

Figure 6-6 Wave decomposition at 60 kHz centre frequency for four different excitation conditions: (a) axial excitation at the centre of the bar, (b) torsional excitation at the outer surface of the bar, (c) traverse excitation at the centre, (d) transverse excitation at the outer surface

Figures 6-6(c) and (d) show the comparison of the wave decomposition when a transverse force is applied at the end of the face. The case C shows the wave decomposition when the transverse force is applied at the centre of the end face and the case D when the force is applied at the outer surface of the end face. In Figure 6-6(c) it can be observed that only the flexural waves of order one F(1,1), F(1,2) are excited, because the force is applied at the centre. In Figure 6-6(d), the flexural wave of order two F(2,1) is excited because the profile displacement at the outer surface is higher than in radius zero, the longitudinal L(0,1) with lower contribution is excited as well. In this comparison for cases C and D, it should be noted that there is potential for the waves with higher contribution to indicate location of the excitation source. For example, for case C, the flexural wave F(1,2) has the higher contribution, but for case D the higher wave contribution is in F(1,1). In addition, this wave decomposition can potentially describe whether the excitation source is internal or external. It is possible that the wave with the highest contribution could describe whether the excitation is due to tensile, shear or bending forces, potentially providing information about the excitation location.

The method appears to work effectively, however, in the real world, the nodal acceleration can only be measured at the outer surface of the bar and it may only be possible to measure it at a few locations. Also, in the first experiments, it was not practical to measure all three displacement/acceleration components at the same location. Therefore, the method was tested for four different reduced measurement conditions. Figure 6-7 shows the comparison of the wave decomposition when only the nodal accelerations are considered on the external surface of the bar and for different combinations of the displacement/acceleration components. A comparison between Figure 6-6(d) against Figure 6-7(a) was done. Figure 6-6(d) has the maximum number of 324 dof, Figure 6-7(a) has only 36 dof considering only the outer surface. It is observed that there is not a big difference in the wave decomposition between Figure 6-6(d) and Figure 6-7(a). Moreover, Figure 6-7(b) shows the result when the nodal acceleration in radial, circumferential, axial are considered every 90 degrees instead of every 30 degrees and there is a similar behaviour with the flexural wave F(1,1) remaining the highest contributor. However, Figure 6-7(c) with only 8 dof (four points around the circumference and only radial and axial components) shows a big difference in the wave mode amplitude of F(1,1), F(1,2) and F(2,1). Then, Figure 6-7(d) with only radial and circumferential components shows a large discrepancy between the F(1,1) and F(1,2) wave modes where the higher contribution is from F(1,2) instead of F(1,1). In addition, when the dof are reduced, the accuracy in the results of higher order modes such as F(2,1) is reduced as well as it might expect due to its additional variation around the circumference. However, the difference between Figures 6-7(a) and (b) is minimal, so as Catton confirmed et al. [57] that the minimum number of sensors to capture the wave or order n should be 2^n. On the other hand, it should be noted that in Figure 6-7(c), there is no torsional wave, because only the radial and axial components were considered.

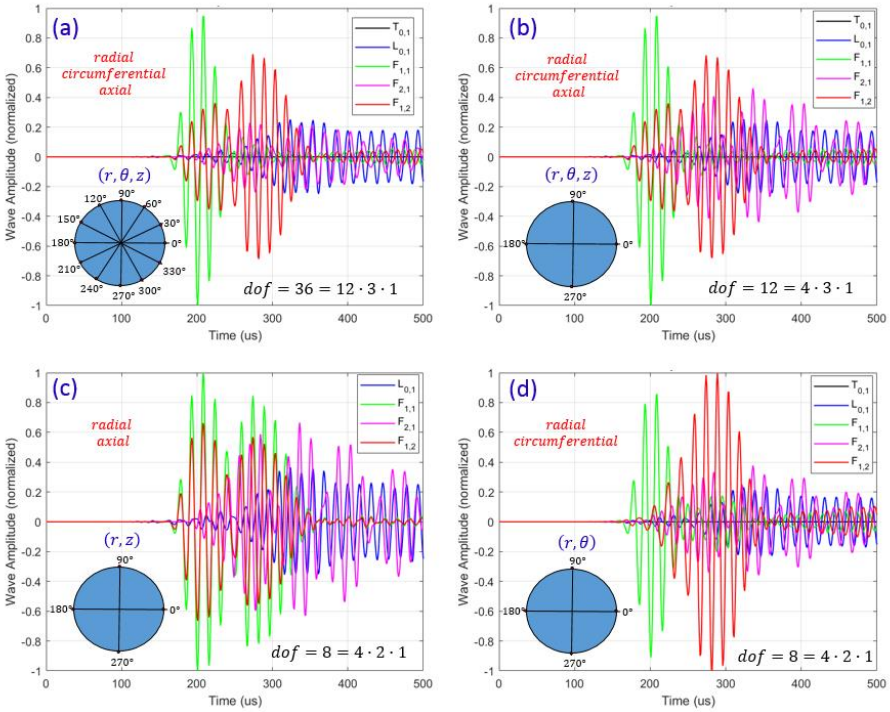

Figure 6-7 Wave decomposition at 60 kHz centre frequency for case D with different reduced degrees of freedom: (a) 36dof (r, θ, z), (b) 12dof (r, θ, z), (c) 8dof (r, z), (d) 8dof (r, θ)

6.4.3 Optimization of the number of sensors to obtain the wave decomposition

The optimum number of sensors to obtain the contribution of each individual wave is obtained. In addition, cross correlation coefficient was used to measure the similarity of each wave with minimum dof versus the wave with the maximum dof (324).

For this analysis, a new finite element model (case E) was created. Figure 6-8 shows the transverse point load applied 4 cm from the end face on the outer surface to observe the effect of the boundary condition and possible reflection from the near end face.

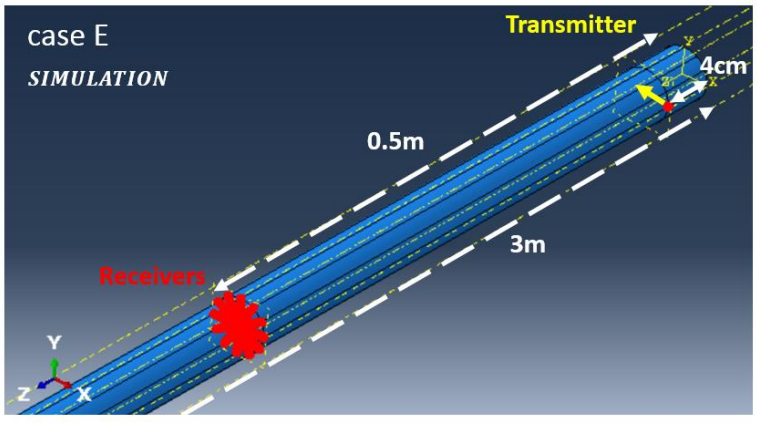

Figure 6-8 Model of cylindrical rod for Case E (transverse excitation at 4 cm from end face)

Figure 6-9 shows the comparison of the wave decomposition, when the nodal acceleration in radial, circumferential and axial direction are considered for the case E. Comparing Figure 6-9(a), which has the maximum number of 324 dof (internal nodal acceleration along the radius of cross section), versus Figure 6-9(b) which has only 36 dof (12 points around the circumferential only on the outer surface), there is not a big difference in the wave decomposition. Figure 6-9(c) shows the result of the nodal acceleration every 90 degrees instead of every 30 degrees and there is a similar behaviour with the flexural wave F(2,1) remaining the highest contributor. In addition, Figure 6-9(d) with only 8 dof (four points around the circumference and only radial and circumferential components) does not show a big difference in the wave decomposition. It should be noted that in simulation is very simple to obtain the nodal accelerations along the radius of the cross section. However, in experiment, it is not practical and simple to record the signals in the three components on the same node or point. One option could be to use a 3D laser vibration vibrometer but it will require to rotate the bar to be able to obtain the acceleration in different angle along the surface of the bar. On the contrary, in section 6.6 the experiments were carried out using a normal and shear transducers to record the signal in radial, circumferential and axial direction but the experiment needed to be repeated to be able to record the acceleration in each components on the same point, more details are shown in section 6.6.

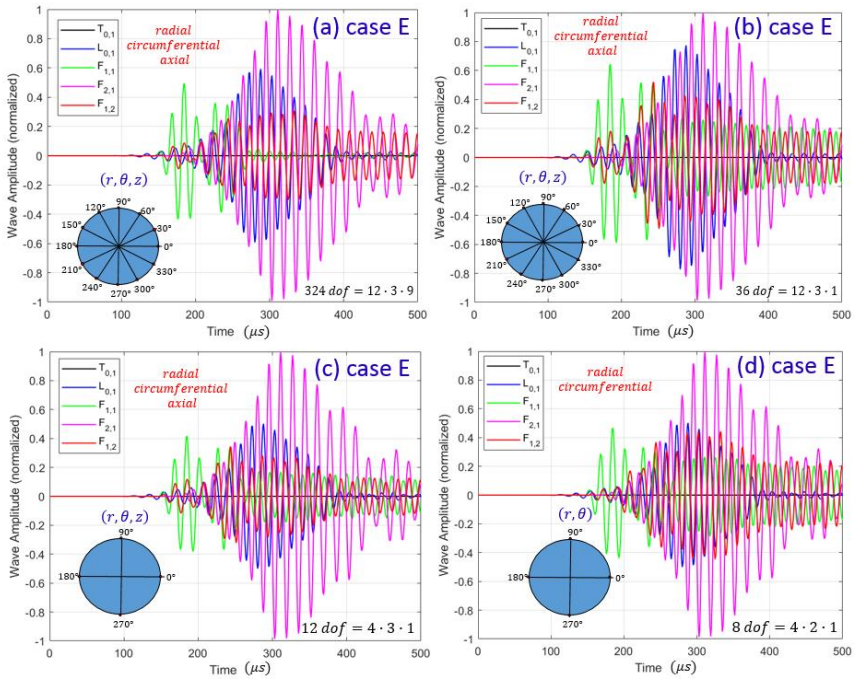

Figure 6-9 Comparison of wave decomposition at 60 kHz centre frequency with different degree of freedom for case E: (a) 324dof (r,θ,z), (b) 36dof (r,θ,z), (c) 12dof (r,θ,z), (d) 8dof (r,θ)

However, Figure 6-10(b) with only radial and axial components shows a large discrepancy between the F(1,1) and F(1,2) wave modes but the highest contribution is still in F(2,1). Then,

Figure 6-10(c) with only circumferential and axial components shows a large disagreement in all the waves, but Figure 6-10(d) with only radial component presents better agreements than Figure 6-10(c). It should be noted how the radial component is very important to be able to observe the wave decomposition with the same harmonic order around the surface because when the radial component is missing, there is discrepancy in all the waves. However, it is necessary to have a least radial and circumferential components to be able to see the contribution of F(1,1) and F(1,2). Therefore, having the three components (radial, circumferential, axial) provides more accurate results to determine the difference between individual waves with the same number of harmonics around the circumference.

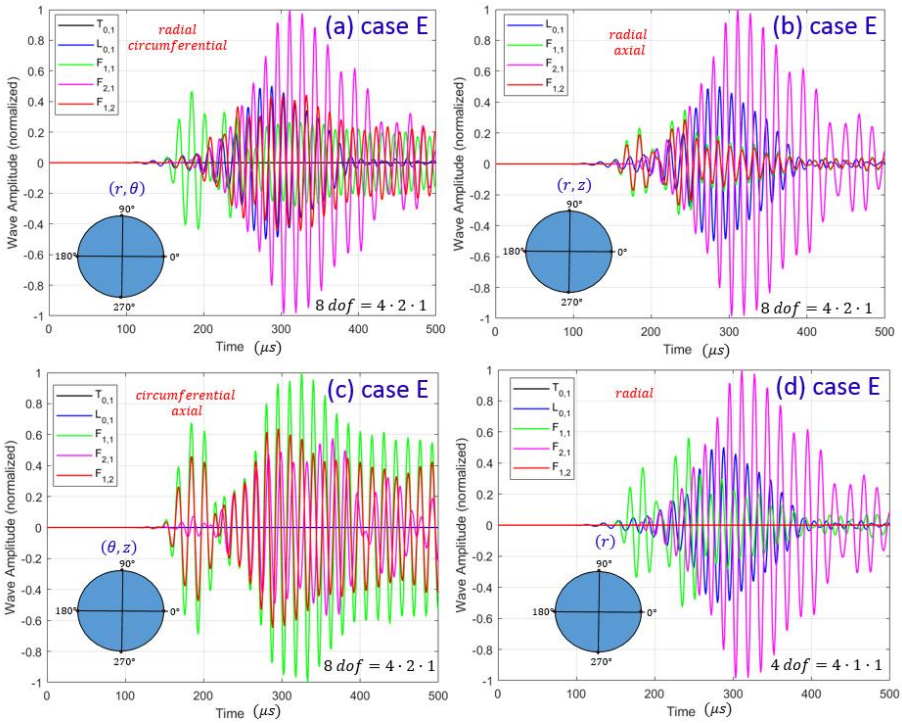

Figure 6-10 Comparison of wave decomposition at 60 kHz centre frequency with different degree of freedom: (a) 8dof (r,θ), (b) 8dof (r,z), (c) 8dof (θ,z), (d) 4dof (r)

A cross correlation coefficient was obtained to know the similarity between each wave of reduced dof and the accurate wave of the highest number of 324 dof. The normalized cross correlation coefficient is defined as

$$\hat{R}_{xy,coeff}(j) = \frac{\hat{R}_{xy}(j)}{\sqrt{\hat{R}_{xx}(0)\hat{R}_{yy}(0)}} \tag{6.6}$$

The normalization of the cross- correlation is done, considering that the autocorrelation at zero delay is equal to one. The result of cross correlation can be understood as an estimation of the

correlation between two random sequences [104], [105]. The cross-correlation sequence of two random processes (x_i and y_i) without normalization is given by

$$\hat{R}_{xy}(j) = \mathrm{E}\{x_{i+j}y_i^*\} = \begin{cases} \sum_{i=0}^{L-j-1} x_{i+j}y_i^*, & j \geq 0 \end{cases} \tag{6.7}$$

, where L is the greater of the lengths of x and y time series data, and i and j is the index time of each data, respectively. E is the expected value, which can be also known as average, mean value or mathematical expectation. Matlab command $xcorr$ was used to obtain the cross correlation coefficient values of Figure 6-11.

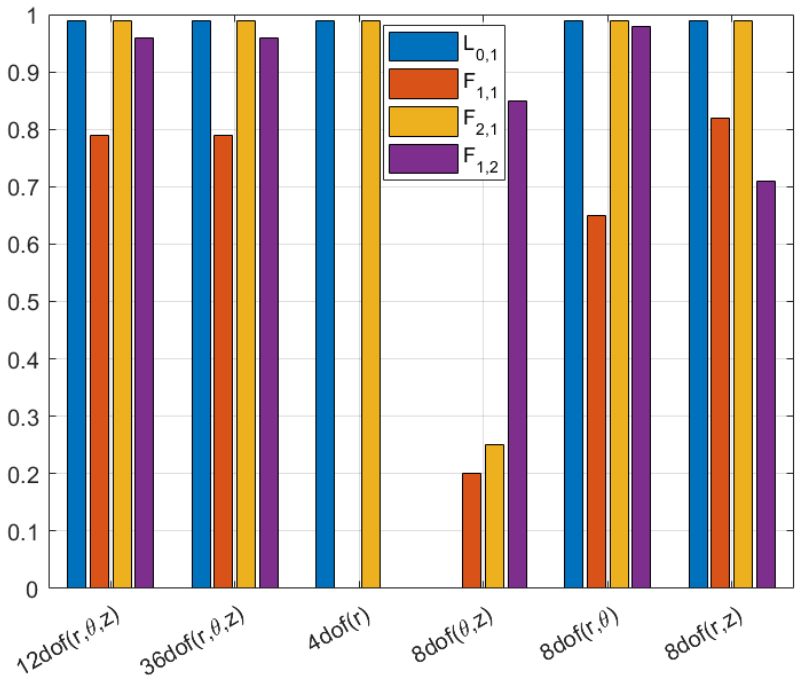

Figure 6-11 Cross correlation coefficient of different dof with the reference of maximum 324dof (simulation results)

Figure 6-11 shows the cross correlation coefficient comparison to know the similarity of the waves with reduced dof versus the reference maximum dof (324). Wave L(0,1) does not show a big difference when dof is reduced in each case, so it means that the radial component is enough to know the contribution of axial symmetry wave. In addition, the wave F(2,1) does not show a big change when the radial component is considered. However, the non-axial symmetry waves show a large discrepancy when only circumferential and axial components are used. In addition, the cross correlation coefficient drops at 0.82 for F(1,1) when only radial and axial component are considered. It should be noted that the minimum number of dof to obtain the contribution of each wave decomposition is the case of 12 dof when radial, circumferential and axial components are used. Table 6-1 shows the cross correlation coefficients of Figure 6-11. Again, it can be seen

that to be able to record the waves with two harmonic around the surface and to difference each wave of one harmonic, the 12dof is the minimum number.

Table 6-1 Values of cross correlation coefficient with the reference of 324dof (simulation)

Wave	*36dof(r,θ,z)*	*12dof(r,θ,z)*	*8dof(r,z)*	*8dof(r,θ)*	*8dof(θ,z)*	*4dof(r)*
L(0,1)	0.999	0.999	0.999	0.999	-	0.999
F(1,1)	0.793	0.792	0.829	0.651	0.209	-
F(2,1)	0.999	0.998	0.998	0.998	0.253	0.998
F(1,2)	0.962	0.960	0.712	0.985	0.852	-

6.5 Experimental validation using only radial component

6.5.1 Experimental set-up using only radial component

Experiments were carried out to validate the wave decomposition behaviour obtained by applying the technique to FEA-simulations. The new finite element model (case E) was created to exactly match with the experiment so that the transverse point load was applied 4 cm from the end face on the outer surface, to allow the magnetic holder used to attach the transducer to the steel rod. Figure 6-12 shows the experimental set-up for the two cases (case A and case E), where the centre frequency of 60 kHz 5-cycle Hann-windowed pulse (Figure 6-13) was transmitted using a single compressional transducer (Figure 6-14).

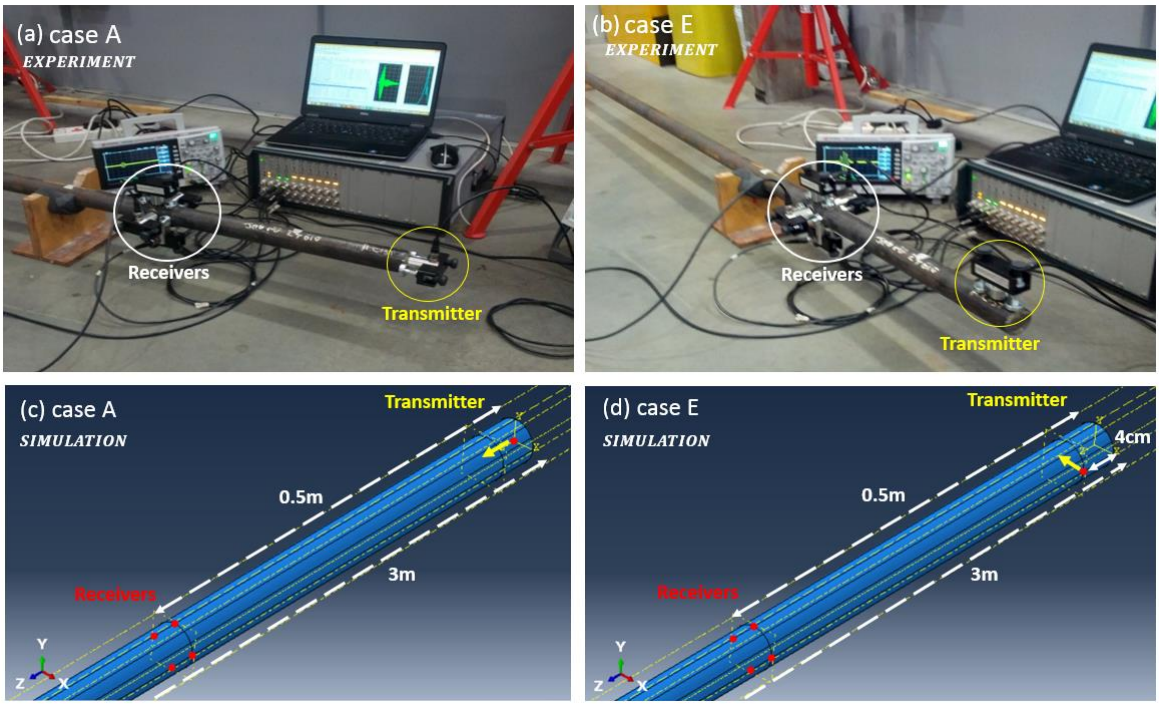

Figure 6-12 Experimental set-up for only radial component: (a) Experiment (axial excitation), (b) Experiment (transverse excitation), (c) Simulation (axial excitation), (d) Simulation (transverse excitation)

The steel cylindrical bar has the same dimensions as the FEA model. The bar was resting on a wooden block and supported with foam in order to avoid disturbance from the surroundings area. A magnetic clamp was used to attach the compression transducer, Figure 6-12 (a) shows the orientation of the transducer designed to apply the pulse in the axial direction to match case A (Figure 6-12 (c)). Then, Figure 6-12 (b) presents the case E set-up where a transverse load is applied to the outer surface, 4cm from the end face (Figure 6-12(d)).

A function generator was used to apply the centre frequency of 60 kHz 5-cycle Hann-windowed pulse (Figure 6-13). It should be noted that a centre frequency 60 KHz was considered because at this centre frequency exits waves with first and second harmonic around the surface. So, it is of interest to know the contribution of waves with first and second harmonic. In addition, the sensors used in the experiments are more sensitive near this resonance frequency of 60 kHz (see Figure 6-14). During the experiment, four AE-sensors were used to measure the acceleration at 0.5m from the excitation source and every 90 degrees around the surface of the bar. A VALLEN AMSYS-6 AET system was used to record the accelerations. This is a multi-channel AE-measurement system with front-end software running on an external laptop. Each measurement channel consists of a single AE-sensor, AE preamplifier and one channel of an ASIP-2 AE signal processor card, which allows sample rate up to 40 MHz [13].

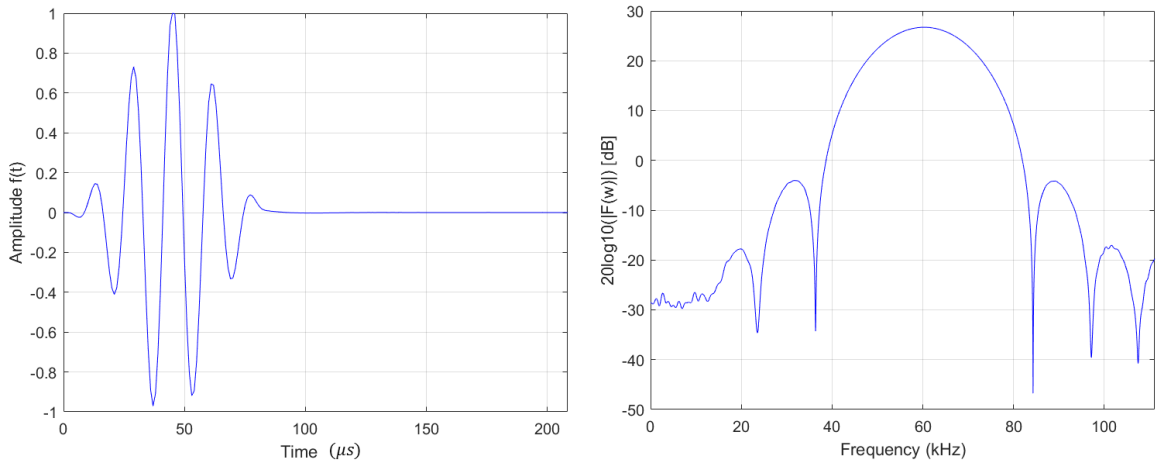

Figure 6-13 Hann-windowed 5 cycle excitation pulse with a central frequency 60 kHz (left), Excitation spectrum (right)

A VS30-SIC-46dB compression piezo-electric AE sensor with integrated preamplifier was used as both transmitter and receiver. The integrated preamplifier had 46dB gain and support pulse trough. The sensor has a frequency range from 20 kHz to 80 kHz, see Figure 6-14. This type of AE-sensor can record and transmit the signals in the normal direction on the surface (compression). It means that only the radial direction component was considered in the experiments. The diameter (15 mm) of the compressional transducer is smaller than the minimum wavelength (30 mm) at the

maximum excited frequency of the spectrum, so the excitation can be considered as a point load as it is in the finite element models [57].

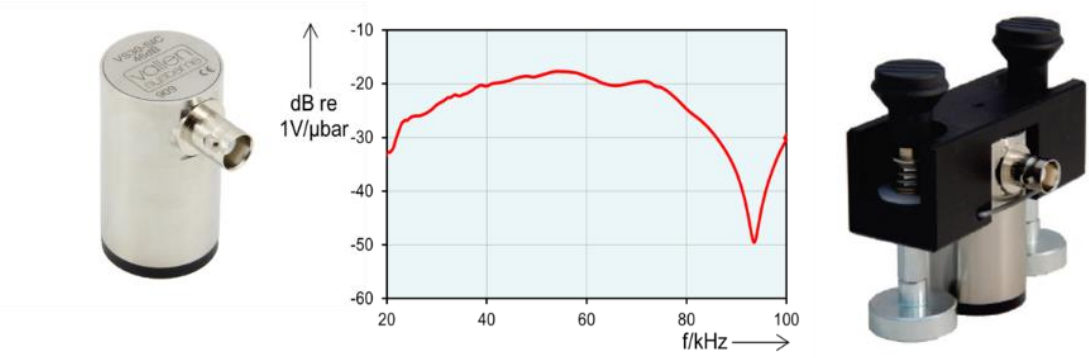

Figure 6-14 VS30-SIC-46dB piezoelectric sensor (left), frequency range (centre), magnetic holder (right) [13]

6.5.2 Experimental results using only radial component

Figure 6-15 shows the wave decomposition for case A and case E. In general, there is a good agreement in the wave decomposition between the experimental and simulation results. There is excellent agreement between the relative wave mode amplitudes. For instance, for a point load at the centre of the end face with an excitation in the axial direction both the experiment and model find the longitudinal L(0,1) to have the highest contribution (Figures 6-15(a) and 15(c)). In the experiment results for this case A, there is some contribution of flexural wave modes F(1,m) and F(2,m) whereas this is negligible in the simulation case. This is thought to be because the transmitter excites a small pulse in parallel direction on the surface as it is not capable of pure compression. For case E, the highest wave contribution is from F(2,m) in both the experiment and the simulation (Figures 6-15(b) and 15(d), respectively). It is noted, however, that the highest contribution is from F(1,m), when the transverse load is applied exactly at the end of the face, instead of 4 cm from it (Figure 10(d) and 6-15(d)). It should be noted that during this experimental work, the wave decomposition was done for the family of waves instead of individual waves because the receiver sensors can record the signals only in normal direction on the surface. It should be noted that the family waves means the waves with similar harmonic around the surface. For example, F(1,1) and F(1,2) are the family waves with first harmonic around the surface, but F(2,1) and F(2,2) are the family wave with the second harmonic around the surface.

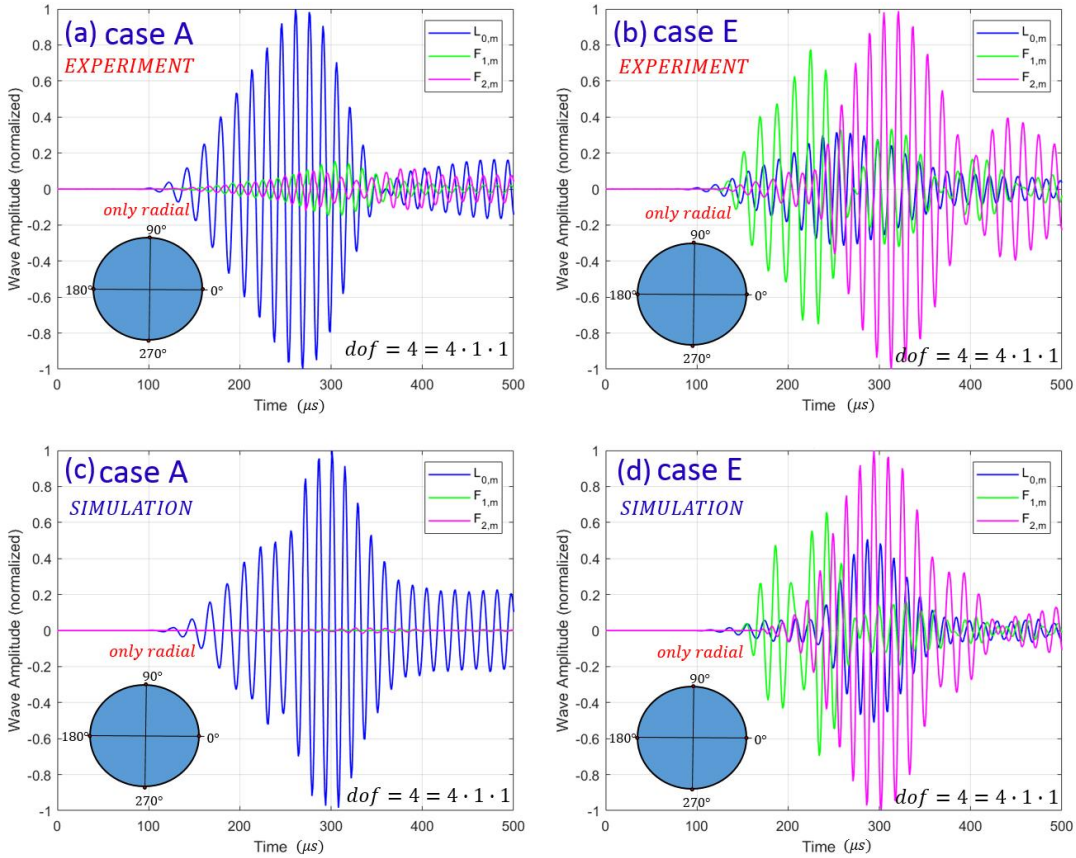

Figure 6-15 Comparison of wave decomposition using only radial component every 90 degrees along the surface during simulation and experiment for case A ((a) Experiment, (b) Simulation) and case E ((c) Experiment, (d) Simulation)

As discussed in Section 6.4.3, when only the radial component is considered, the wave decomposition method is only able to identify waves of the same harmonic order around the circumference. It should be noted that this wave decomposition can still be helpful in determining what type of wave is generated when tensile or bending loads are applied to a structure. For example, when a material is loaded, it changes shape, stretches, compresses or shears. Elastic waves propagate outward from the source, to the AE sensors. It is important to understand what type of wave is generated during such an excitation so that a future monitoring device can be designed accordingly, taking into account that the sensors may be sensitive to in-plane or out-of-plane movement at the surface.

On the other hand, acoustic emission occurs at locations where the local stress is high enough to cause cracking in a structure. Acoustic emissions result from strain during crack initiation or crack growth, the most widely used simulated AE source in the laboratory is the breaking of a pencil lead against the specimen. The Hsu-Nielsen presented at al. [106] the pencil leak break as a standard simulated AE source, it is convenient and cheap that has been used in practical AE

testing. Miller showed et al. [28] that the breaking of the lead creates a very short-duration and localized impulse, which is quite similar to a nature acoustic emission source such as a crack.

In the next part of the experimental work, a pencil lead break (PLB) was used as crack AE-source instead of the Hanning pulse. By its nature, the PLB source has a wide frequency spectrum that cannot be controlled because the width of the pulse is too short that produces a broadband frequency spectrum. In fact, the wave decomposition was done at 60 kHz because it is the frequency where wave mode has first and second harmonics along the surface, it is of interest to know what type of wave with first or second harmonic has the highest contribution to use it as possible location of the type of excitation source. PLB was used to generate in-plane or out-of-plane motions and generate AE waves from possible cracks during tensile or bending forces. Figure 6-16(a) shows the wave decomposition when a PLB was applied at the end of the face of the bar in axial direction (as shown in Figure 6-16(c)). It is observed that the L(0,1) is the wave with the highest contribution. Figure 6-16(b) presents the wave decomposition when a PLB was applied in normal direction to the outer surface of the bar (as shown in Figure 6-16(d)). It is observed in Figure 6-16(b) that the flexural wave with second harmonic F(2,m) has the highest contribution. Similar behaviour is observed in Figure 6-15(b) for 5-cycle Hann-windowed instead of PLB. For both cases the highest contribution is from F(2,m) when the excitation is applied 4 cm from the end face. This means that the wave with second harmonic are excited with higher amplitude when the excitation is applied 4 cm from the end face. It should be noted that this experiment was carried out using the four compressional sensors, which can record only the radial components because the signals are recoded every 90 degrees along the surface in normal direction to the surface of the rod. This means that using only the radial components, it is not possible to do the wave decomposition to know the contribution of individual waves F(2,1), F(2,2), it is only possible to do the wave decomposition for family waves F(2,m), this means for wave with same harmonic around the surface of the rod.

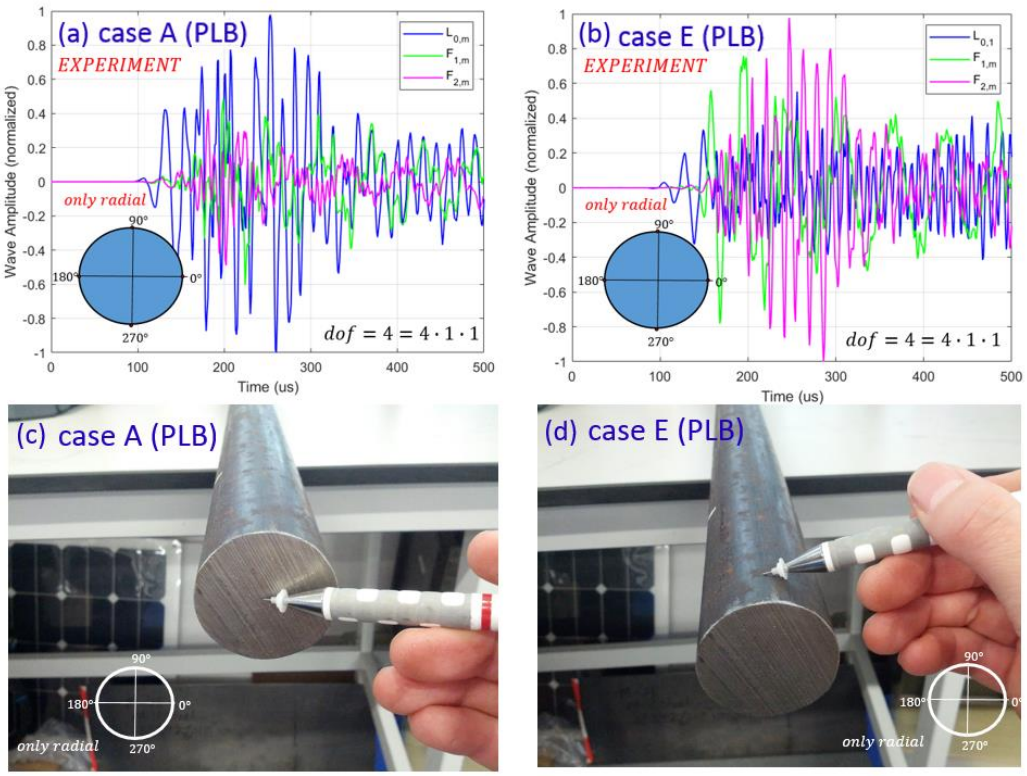

Figure 6-16 Wave decomposition for PLB experiments in plane (case A) and out of plane (case E), measuring with VS30-SIC-46dB piezoelectric sensor at 0.5 m from PLB only in radial direction every 90 degrees

Thus, it has been demonstrated that there is potential for the wave with highest contribution to be used to describe the type of crack growth (Figure 6-17); tensile or bending. Acumulative plots of AE features (peak amplitude, rise time, duration, counts and energy) against time for the waves of higher contribution can also be extracted to show how fast a crack is growing under tensile or bending load [6].

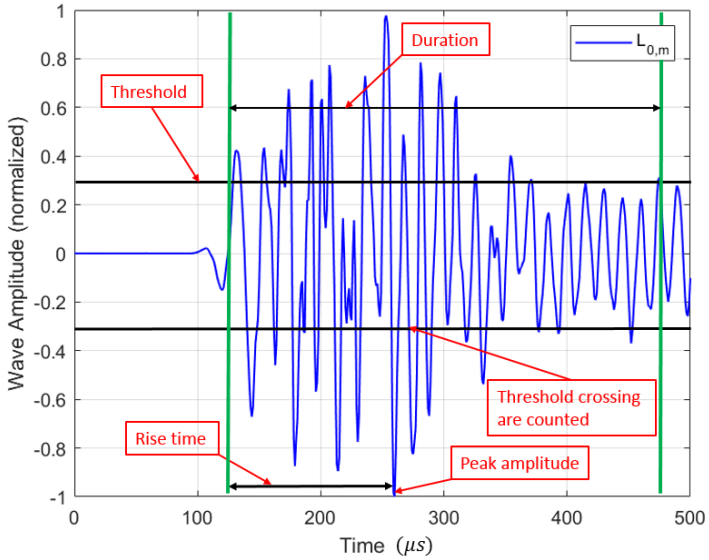

Figure 6-17 AE features to the highest contribution wave amplitude during PLB in plane (case A)

6.6 Experimental validation using all components

It should be emphasized that to get the contribution of individual waves instead of the family of waves. It is mandatory to use the radial, circumferential and axial components to obtain accurate results of the contribution of each wave and to know the wave of the highest amplitude. Therefore, experimental work was done to validate this novel wave decomposition methodology using all the components. However, each case of the test was repeated 12 times to record the 12 degree of freedom, this means every 90 degrees along the surface to record the signal in each coordinate component (radial, circumferential, axial) because only two sensors are available, one compressional to record the radial component and one shear sensor to record the circumferential and axial components.

6.6.1 Experimental set-up using all components

Figure 6-18 (a) shows the case A set-up, the orientation of the compressional transducer is in the axial direction. Figure 6-18 (b) presents the case E set-up where a transverse load is applied to the outer surface, 4cm from the end face. A VALLEN AMSYS-6 AET system was used to record the accelerations. The multi-channel AE-measurement system with front-end software running on an external laptop was used. Each measurement channel consists of a single sensor, AE preamplifier and one channel of an ASIP-2 AE signal processor card [13]. A function generator was used to apply the 5-cycle Hann-windowed pulse of 60 kHz central frequency (Figure 6-13). A VS30-SIC-46dB compression piezo-electric AE sensor with integrated preamplifier was used as transmitter. The integrated preamplifier had 46 dB gain and support pulse trough. The transmitter has a frequency range from 20 kHz to 80 kHz, see Figure 6-14.

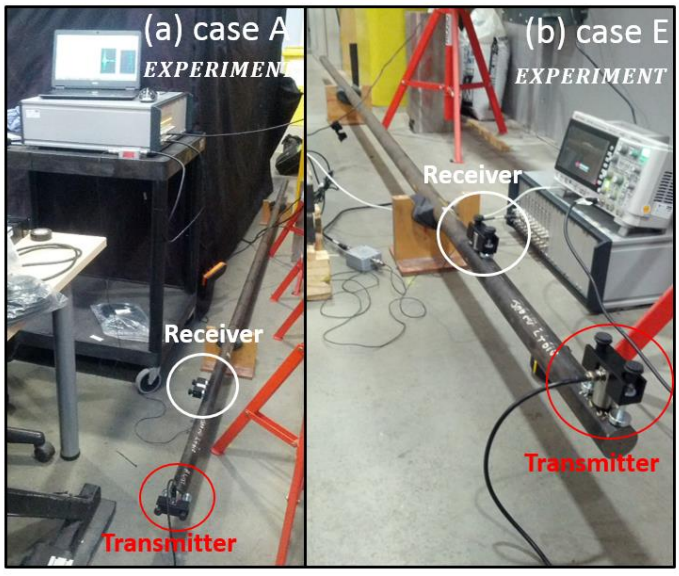

Figure 6-18 Experimental set-up for all components: (a) axial excitation, (b) transverse excitation

Two receiver sensors were used to measure all the accelerations at 0.5 m from the excitation source and every 90 degrees around the surface of the bar in radial, circumferential and axial direction. One sensor is compressional and the second one is shear sensor (Figure 6-19). The compressional sensor was used to record the radial direction on the surface, and the shear sensor was used to record the circumferential and axial direction on the surface, this is an uniaxial shear sensor, this means that to record the signal at the same point in circumferential and axial, the test was repeated for each component, the sensor has a frequency range from 20 kHz to 90 kHz. At the end, the test was repeated 12 times to record the 12 degree of freedom because only two sensors are available and to be sure that the signal can be recorded every 90 degrees in radial, circumferential and axial direction. The receiver channels were synchronised to ensure that the receiver signals are triggered at the same time. In this case, channel one was used as master and channel two as slave. The master channel (transmitter pulse) was used as reference to trigger slave channel (receiver signal). A preamplifier type AEP4 was used to record the signals (see Figure 6-19). It is a general preamplifier supporting single ended sensor. This preamplifier is a wide-band preamplifier with a frequency response from 5 kHz to 1 MHz, the preamplifier has 34 dB gain [13].

Figure 6-19 Sensors (left), Magnetic holder (centre), Amplifier (right)

6.6.2 Experimental results using all components

Figure 6-20 presents the wave decomposition for case A (axial excitation) and case E (transverse excitation). In general, there is excellent agreement between the relative waves of the highest amplitudes for the experimental and simulation results. For instance, for a point load in the centre of the end face with an excitation in the axial direction both the experiment and model find the longitudinal L(0,1) to have the highest contribution (Figures 6-20(a) and 20(c)). In the experiment results for this case A, there is some contribution of flexural wave whereas this is negligible in the simulation case. Again like in the previous experiment, this is thought to be because the transmitter excites a small pulse in parallel direction on the surface as it is not capable of pure

compression. For case E, the highest wave contribution is from F(2,1) in both the experiment and the simulation (Figures 6-20(b) and 20(d), respectively). It is noted, that now using the radial, circumferential and axial components, the wave decomposition is able to identify the contribution of individual wave with similar harmonic order around the surface. For example, Figures 6-20(b) and 20(d) shows the contribution of individual waves F(1,1) and F(1,2), it was not possible to obtain them using only the radial component as it is shown in Figure 6-15(d), where only the family waves F(1,m), F(2,m) are obtained instead of the individual waves. In addition, it is observed that the longitudinal L(0,1) is excited because the exciter pulse is 4 cm from the end face. Then, a conversion mode is observed due to the boundary of the face end. However, in the experiment, the exciter is not pure compression so a contribution due to shear in axial direction can excite L(0,1) as well.

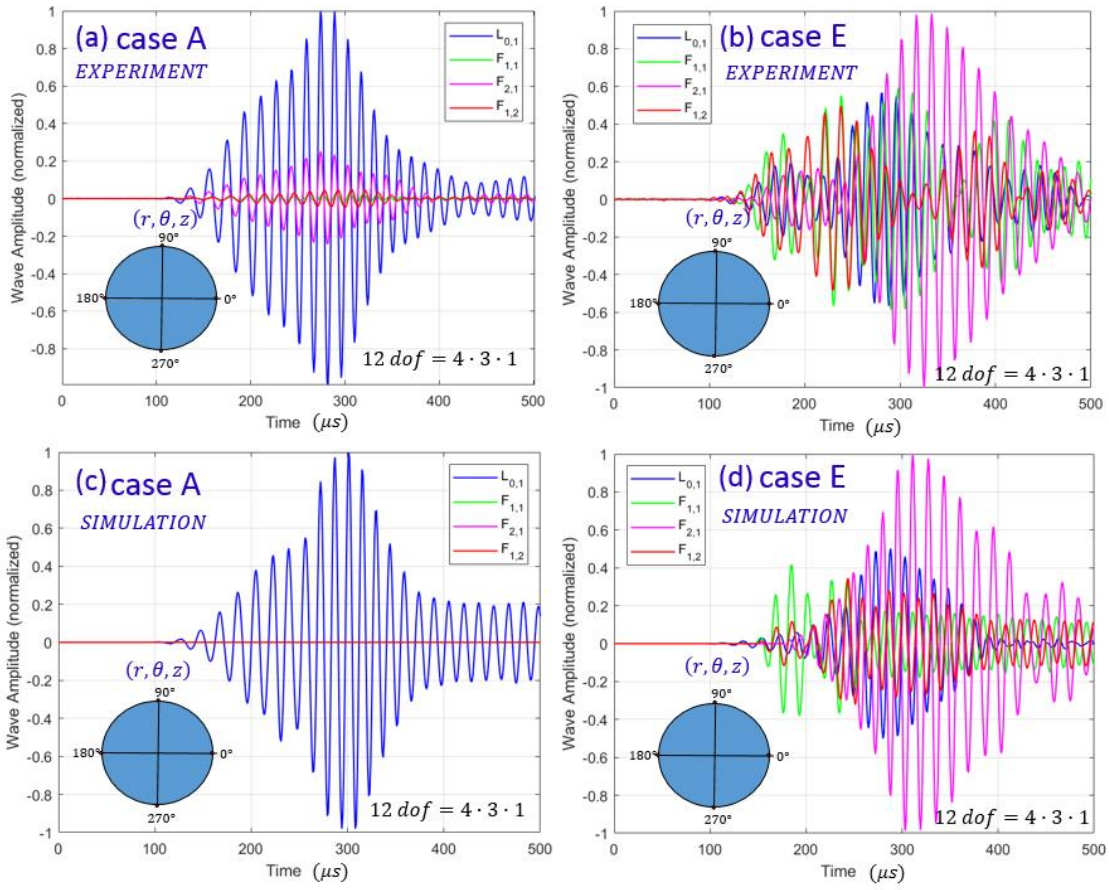

Figure 6-20 Comparison of wave decomposition at 60 kHz centre frequency of excitation for simulation and experiment in case A and case E (using all components)

Figure 6-21 shows the cross correlation comparison to know the similarity of the waves with reduced dof (experiment) versus the maximum 324 dof (simulation). The wave F(2,1) does not show a large discrepancy between the experiment and simulation. This wave F(2,1) shows similarity using radial-circumferential or radial-axial components. In addition, wave L(0,1) shows a small difference when dof is reduced in each case of reducing dof. However, the cross correlation

coefficient drops at 0.62 for F(1,1) and 0.48 for F(1,2) when the three components are considered. It should be noted that the minimum number of dof to obtain the contribution of each wave decomposition is the case of 12 dof, when radial, circumferential and axial components are used. It is noted that using only the radial-axial or radial-circumferential components the cross correlation coefficient drops more and the results are less accurate.

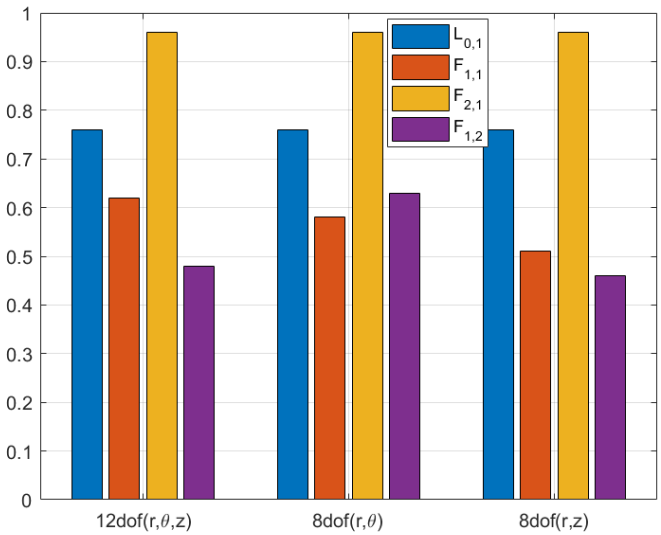

Figure 6-21 Comparison of cross correlation coefficient for different dof (Experiment) with reference 324 dof (Simulation): 12 dof (radial, circumferential, axial), 8dof (radial, circumferential), 8dof (radial, axial)

Finally, the wave decomposition method was also applied at one more frequency for case E. Figure 6-22 shows the wave decomposition for a centre frequencies of 40 kHz simulation (left Figure) and experiment (right Figure), considering the three components. It is noted that the bandwidth spectrum of 5 cycle Hann-windowed pulse with central frequency 40 kHz, excites only L(0,1) and F(1,1) within the frequency range 30-50 kHz, as it is shown in Figure 6-1 of the dispersion curve. This means that this methodology of wave decomposition presented in this thesis is able to obtain the highest wave amplitude of the excited centre frequency. Again, it is only possible to estimate wave decomposition at a specific frequency to identify the contribution of each wave, when the three components are considered. For example, in Figure 6-22(a) and 6-22(b) the highest contribution is in F(1,1) for simulation and experiment, respectively. However, again L(0,1) is excited because a conversion mode is observed due to the free end face for case E. This methodology of wave decomposition with the three components can estimate which wave has the highest contribution at a centre frequency.

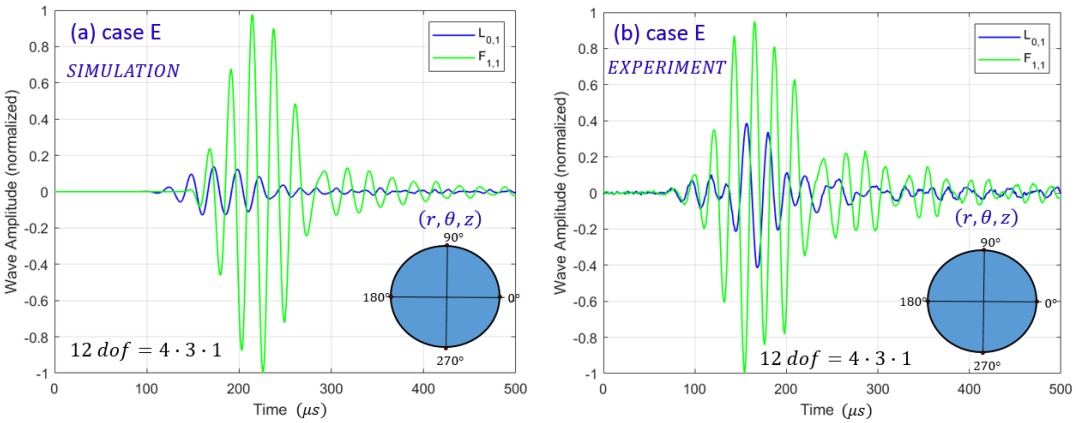

Figure 6-22 Wave decomposition for case E at 40 kHz centre frequency of excitation

6.7 Conclusions

An approach to estimate the wave decomposition in the time domain was presented for a cylindrical steel rod of small diameter for different excitation conditions. The following conclusions were drawn:

- Considering reduction in the dof around the external surface instead of the cross-section, the behaviour of the wave decomposition with up to twelve dof is very similar. It can be concluded that using the radial, circumferential and axial component with only 12dof around the circumference instead of 364dof, it is possible to capture the contributions of waves with second order variation around the circumference.
- It is confirmed that to capture the wave of n order, it is enough to have 2^n as the minimum number of sensors. In addition, it can be concluded that with only sensors every 90 degree around the circumference instead of every 30 degree, it is possible to obtain the contribution of each wave and in certain cases when only the radial and axial components are considered.
- Using only the radial component, the wave decomposition was validated with good agreement between the simulation and the experimental work. It was demonstrated that the wave decomposition method can obtain the highest contribution from family waves of the same harmonic order for each specific frequency. In addition, the PLB experiments shows that this technique has the potential to be implemented to determine the type of waves generated during tensile or bending internal forces. This means it could be used in structural health monitoring of cylindrical bars.
- Considering the three components (r, θ, z) in simulations, the wave decomposition method is able to obtain the wave with highest contribution arising from axial, shear or

bending forces. The correct wave modes has the highest contributions from the four different excitation conditions designed to excite them.

- This wave decomposition method can potentially describe whether the excitation source is internal or external. It is possible that the wave with the highest contribution could describe whether the excitation is due to tensile, shear or bending forces, potentially providing information about the excitation location.
- Numerical analysis were carried to simulate wave propagation using the maximum number of degree of freedom and implement wave decomposition to correlate the experimental work with the minimum degree of freedom. These comparisons helped to obtain the minimum number of sensors necessary to get the wave amplitude of each wave. The wave decomposition in time domain has the potential to obtain the highest incident wave amplitude and avoid reflection from free end. It should be noted that damage was not considered in this chapter but the wave decomposition from PLB were done. It can be concluded that the wave decomposition method can provide what type of wave is excited during PLB excitation in plane or out of plane.

The study demonstrated the feasibility of doing wave decomposition in a cylindrical bar and identifying the contribution of each wave mode at a centre frequency. However, wave decomposition in the experimental work has been done only for a rod of small diameter. It is important to realize that to have an impact in the industry, wave decomposition in a rod and link of large diameter should be considered because the number of waves increases when the diameter increases as well. In addition, experimental validation should consider using the three components, in order to do complete wave decomposition and identity the contribution of individual waves. In next chapter, wave decomposition is done in a rod of 160 mm diameter. This is more complex due to the higher number of excited waves at the same frequency range (1-100 kHz). In addition, wave decomposition in the time domain should be done in straight cylindrical rod and curved rod. Then, comparison between a straight and curved rod should be implemented to determine the impact of the geometry. The ultimate aim is to apply the wave decomposition method to the mooring link of 160 mm diameter. This would be attractive to the offshore industry, where there is interest in structural health monitoring technique for mooring chains.

Chapter 7: Wave decomposition in the time domain for an industrial mooring link

7.1 Introduction

This chapter presents the wave decomposition for a bar and a link, both of relatively large diameter. This is more complex due to the higher number of excited waves for a rod of 160 mm diameter and the complex geometry of the link. It is important to realize that wave decomposition in time domain is done to analyse the behaviour of the incident wave before and after the bent. In fact, a problem was found at the moment of doing the wave decomposition like in chapter six. It was discovered that the pseudo-inverse of the wave mode shape matrix was ill-conditioned. Moreover, the new wave modes shapes were not independent at the specific frequency of wave decomposition. Therefore, a novel method using the Hilbert transform is proposed. Wave decomposition in the time domain is done in straight bar and the link.

This chapter is organized as follows. A comparison of the dispersion curves for bars of different diameters is presented. Then, the validation of wave mode shape using the Euler-Bernoulli methods is done. In addition, wave decomposition methodology using the Hilbert transform in the axial component was carried out to harmonic and transient analysis. Moreover, the comparison of wave decomposition in straight bar, bent bar and chain are done for different types of excitation. Finally, the experimental validation for straight bar and link is presented.

7.2 Comparison of dispersion curves for bars of small and large diameter

The dispersion curve is an important graph that describes the changes in the velocity of each wave mode in a plate, pipe or bar with frequency, for a specific material. In order to do the wave mode decomposition and identify the number of wave modes for a specific range of frequency and specific geometry, dispersion curves were obtained for steel rods of 45 mm and 160 mm diameter, with the material properties of Young's modulus 200GPa, shear modulus 76.9GPa, density 7850 kg/m3 and Poisson's ratio 0.3. The publicly available matlab routines of 'PCDISP' et al. [38] was used again to calculate the group speeds of propagation modes in a frequency range. The dispersion curve is plotted in Figure 7-1, where the blue lines of longitudinal mode are denoted by L, the red lines of the torsional modes are denoted by T and the green lines of the flexural modes are denoted by F, similar like in chapter six. In Figure 7-1 (left) for rod of 45 mm

diameter, only three fundamental wave modes are excited at the maximum frequency of 47 kHz. However, above a cut-off frequency of 52 kHz, five wave modes are excited. In Figure 7-1 (right) for rod of larger diameter (160 mm), the number of excited wave in a frequency lower than 47 kHz is higher (14 modes). Thus it can be seen how the bar of larger diameter is more complex, because the number of excited wave modes is higher. For instance, at a frequency lower than 60 kHz, four longitudinal waves are shown in a bar of large diameter, but only one longitudinal wave in a bar of small diameter. It should be noted that the dispersion curve was considered only for the wave with second harmonic ($n = 2$), considering that the number of sensors to do the wave decomposition should be 2^n. It is possible to do the wave decomposition for higher harmonics around the surface and this could be more complex. However, at the moment, the most important matter is to investigate and validate the effect of wave propagation after the bend in the link.

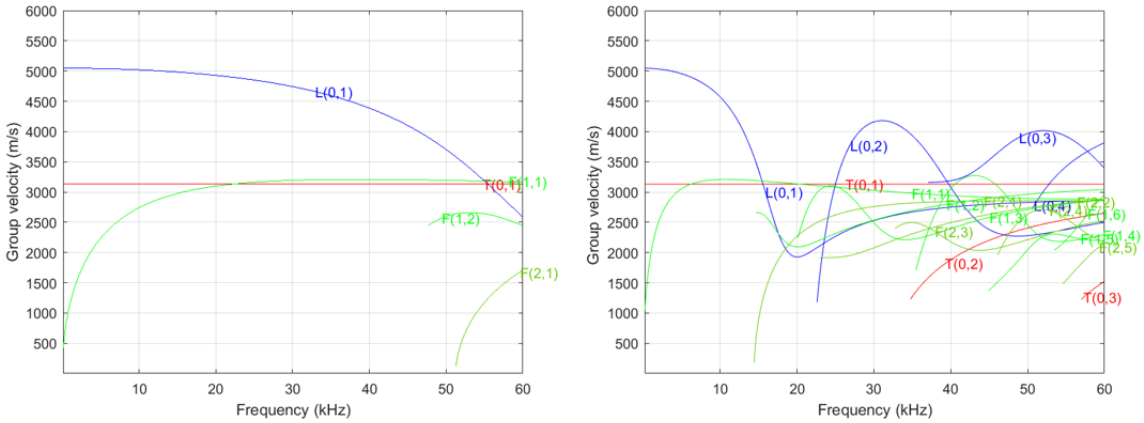

Figure 7-1 Dispersion curve of group velocity for steel bar: 45 mm diameter (left), 160 mm diameter (right)

The methodology to do the wave decomposition in time domain for a bar of large diameter was the same as that given in chapter six (Equation 7.1). This equation is mentioned again because it is the core of the research work to implement new methodology of the wave decomposition and obtain the contribution of each wave.

$$[\mathbf{A}(\mathrm{t})] = [\mathbf{Q}]^{+}[\mathbf{N}(\mathrm{t})] \tag{7.1}$$

However, in building the wave mode shape matrix $\mathbf{Q}$ and looking the solution of the system $\mathbf{A}(\mathrm{t})$ (wave amplitudes), it was discovered that the pseudo-inverse of the matrix $\mathbf{Q}$ was ill-conditioned, and has infinite solutions. The main problem was that the number of excited waves increased in a

bar of large diameter. Moreover, they were not independent and the rank number was lower than the number of expected excited waves at the specific centre frequency of wave decomposition. For instance, the axisymmetric ($n = 0$) longitudinal wave modes have radial and axial components. However, the way as the wave mode shapes were obtained in chapter six, L(0,1) and L(0,2) were dependent, because both waves had only radial component, when $n = 0$ (the axial component $\tilde{u}_z$ was zero, $\sin(n\theta) = 0$).

$$\tilde{\mathbf{u}}(r,\theta) = \text{Real}(\mathbf{u}(r)\, e^{jn\theta}) = \text{Real}\left(\begin{bmatrix} u_r(r) \\ u_\theta(r) \\ u_z(r) \end{bmatrix} e^{jn\theta}\right) = \begin{pmatrix} u_r(r)\cos(n\theta) \\ -u_\theta(r)\sin(n\theta) \\ -u_z(r)\sin(n\theta) \end{pmatrix} \tag{7.2}$$

According to Thurston [50], the wave mode shape for the displacement distribution in cylindrical coordinates has the form of Equation 7.3:

$$\tilde{\mathbf{u}}(r,\theta) = \begin{bmatrix} \tilde{u}_r(r,\theta) \\ \tilde{u}_\theta(r,\theta) \\ \tilde{u}_z(r,\theta) \end{bmatrix} = \mathbf{u}(r)\, e^{jn\theta} \rightarrow \begin{pmatrix} u_r(r)\cos(n\theta) \\ -u_\theta(r)\sin(n\theta) \\ u_z(r)\cos(n\theta) \end{pmatrix} \text{ or } \begin{pmatrix} u_r(r)\sin(n\theta) \\ u_\theta(r)\cos(n\theta) \\ u_z(r)\sin(n\theta) \end{pmatrix} \tag{7.3}$$

,where $\tilde{u}_r$ is the radial component of the wave mode shape displacement profile, $\tilde{u}_\theta$ is the circumferential component of the wave mode shape displacement and $\tilde{u}_z$ is axial component of the wave mode shape displacement profile. The displacement profiles distribution $u_r(r), u_\theta(r), u_z(r)$ are given by Seco et al. [38], more details can be found in chapter 5.2.

It is well known than modes with $n = 0$ are axisymmetric because the same distribution displacement is observed in each angle of the cross-section. For example, $\sin(n\theta) = 0$, $\cos(n\theta) = 1$. The axisymmetric modes described by the second set of trigonometric functions in Equation 7.3 are for the torsional modes because radial and axial are vanished ($\sin(n\theta) = 0$), circumferential is the only non-vanishing displacement component ($\cos(n\theta) = 1$). However, the first set of trigonometric functions in Equation 7.3 are for longitudinal modes because circumferential is vanished ($\sin(n\theta) = 0$) but the radial and axial displacement components are not vanished ($\cos(n\theta) = 1$).

The antisymmetric modes with $n \geq 1$ are called flexural because the bending or flexing behaviour is obtained in the cross-section, where the different distribution displacement is observed in each angle of the cross-section. The first set of trigonometric functions in Equation 7.3, when $n \geq 1$ no component has vanished, that way the flexural waves mode have radial, circumferential and axial component. Theory based on the Pochhammer-Chree equations can show that in the low

frequency limit the mode $n = 1$ could be described by the elementary theory of flexure (Euler-Bernoulli theory). Therefore, in the next section, validation of the wave mode shape from Pochhammer-Chree was done against the Euler-Bernoulli theory.

7.3 Validation of wave mode shape Euler-Bernoulli vs Pochhammer-Chree at low frequency to validate PCDisp

The comparison of the wave mode shape Euler-Bernoulli versus Pochhammer-Chree (PCDisp) is done in low frequency to validate the wave mode shape of PCDisp, where the wave mode are extracted to do the wave decomposition. It should be noted that at low frequency is possible to know if the wave mode shape components (radial, circumferential, axial) are in phase or out of phase. In this case the fundamental flexural F(1,1) is considered to carry out the validation of the wave mode shape. The family of modes with $n = 1$ are called flexural, because it belongs to the lowest branch of this family. The lowest mode with $n = 1$ is characterised at low frequencies by the familiar bending motion, in which one side of the rod is stretched along the axis and the opposite side compressed. Two deformations transversal $u_x(z,t)$ and rotational $\varphi_u(z,t)$ are at any cross-section of a bar. The elementary theory of flexure provides the equation (7.4) of motion [50], [107].

$$EI\frac{\partial {u_x}^4}{\partial z^4} + \rho A\frac{\partial^2 u_x}{\partial t^2} = 0 \tag{7.4}$$

Time harmonic motion $u_x(z,t) = U_x(z)\,\mathrm{e}^{\mathrm{j}\omega t}$

$$\frac{\mathrm{d}^2 U_x(z)}{\mathrm{d}z^4} + k^4 U_x = 0; \qquad k^4 = \frac{\rho A\omega^2}{EI} \tag{7.5}$$

, which has a particular solution, including time $\mathrm{e}^{\mathrm{j}\omega t}$ dependence

$$u_x(z,t) = D\,\mathrm{e}^{\mathrm{j}(\omega t - kz)} \tag{7.6}$$

, where D is the complex axial amplitudes of the transverse wave. It can be determined by applying the appropriate boundary conditions, as described in chapter 4.2. The resulting wave amplitude is $D = -\frac{\mathrm{j}F_x}{4EIk^3}$, where $k = \sqrt[4]{\frac{\rho A}{EI}}\sqrt{\omega}$. The amplitude of these waves is dependent upon the geometrical configuration and the amplitude and phase of the excitation force [11].

The lateral deformation $u_x(z,t)$ and the rotation of a cross-section through the small angle $\varphi_u(z,t)$ are related by the expression $\varphi_u(z,t) = \frac{\partial u_x(z,t)}{\partial z}$

$$\frac{\partial u_x(z,t)}{\partial z} = D\,(-\mathrm{j}k)\mathrm{e}^{\mathrm{j}(\omega t - kz)} \tag{7.7}$$

Nearfield, or evanescent waves are waves that decay exponentially with distance. For this analysis, they are not considered, because they are localised and do not carry energy. However, the propagating waves travel with phase speed c and they are dispersive, since c depends on frequency as presented in chapter 4.2

$$c = \frac{\omega}{k} = \left(\sqrt[4]{\frac{EI}{\rho A}} \right) \sqrt{\omega} \tag{7.8}$$

Figure 7-2 shows the 3D diagram of the Euler-Bernoulli cross-section deformation when it beams, where one side of the rod is stretched along the axial axis and the opposite side is compressed. The deformation in the axial direction u_z increases linearly with the distance $x = r_b \cos\theta$ from a neutral axis. At very low frequencies, where the elementary theory of flexure applies, the cross section oscillates essentially rigidly, while the axial component of displacement varies linearly with the distance from the neutral plane.

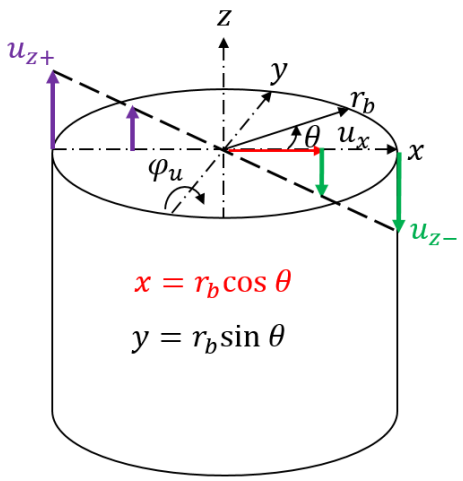

Figure 7-2 3D diagram of Euler-Bernoulli cross section deformation

Putting the two deformations (Equation 7.6 and 7.7) of Euler-Bernoulli in a Cartesian system (Equation 7.9), it can be seen that the axial component is out of phase from the other components:

$$\begin{Bmatrix} \hat{u}_x \\ \hat{u}_y \\ \hat{u}_z \end{Bmatrix} = \begin{Bmatrix} u_x(z,t) \\ 0 \\ -x\,\varphi_u(z,t) \end{Bmatrix} = D \begin{Bmatrix} 1 \\ 0 \\ -x(\mathrm{j}k) \end{Bmatrix} (\mathrm{e}^{\mathrm{j}(\omega t - kz)}) \tag{7.9}$$

, and the wave mode shape of Euler-Bernoulli in Cartesian is defined as

$$\begin{Bmatrix} \tilde{u}_x \\ \tilde{u}_y \\ \tilde{u}_z \end{Bmatrix} = \begin{Bmatrix} 1 \\ 0 \\ -\mathrm{j}kx \end{Bmatrix} \tag{7.10}$$

Then, doing a transformation from a Cartesian to Cylindrical coordinate system, the wave mode shape of Euler-Bernoulli is defined in Equation 7.11. It is observed that the axial components is imaginary and out of phase of the radial and circumferential components. It should be mentioned that this fundamental theory of Euler-Bernoulli was included in this chapter to validate the components of the wave mode shape of PCDisp (Pochhammer-Chree theory) at low frequency. This is very important to know if the components are in phase or out of phase because during the wave decomposition methodology only the real part of the wave mode shape should be considered to be able to obtain the pseudo inverse of the wave mode shape matrix $\mathbf{Q}$.

$$\begin{Bmatrix}\tilde{u}_r\\ \tilde{u}_\theta\\ \tilde{u}_z\end{Bmatrix}=\begin{bmatrix}\cos\theta & \sin\theta & 0\\ -\sin\theta & \cos\theta & 0\\ 0 & 0 & 1\end{bmatrix}\begin{Bmatrix}\tilde{u}_x\\ \tilde{u}_y\\ \tilde{u}_z\end{Bmatrix}=\begin{Bmatrix}\cos\theta\\ -\sin\theta\\ -\mathrm{j}kx\end{Bmatrix}=\begin{Bmatrix}\cos\theta\\ -\sin\theta\\ -\mathrm{j}k\,r\cos\theta\end{Bmatrix} \tag{7.11}$$

From equation 7.3 and following Thurston [50], the wave mode shape of Pochhammer-Chree in cylindrical coordinates is defined as:

$$\tilde{\mathbf{u}}(r,\theta)=\begin{Bmatrix}\tilde{u}_r\\ \tilde{u}_\theta\\ \tilde{u}_z\end{Bmatrix}=\mathbf{u}(r)\,\mathrm{e}^{\mathrm{j}n\theta}\rightarrow\begin{pmatrix}u_r(r)\cos(n\theta)\\ -u_\theta(r)\sin(n\theta)\\ u_z(r)\cos(n\theta)\end{pmatrix} \tag{7.12}$$

Now, comparing wave mode shape components of Equation 7.11 and Equation 7.12. Figures 7-3 to 7-5 present the comparison of the displacement profile of the wave mode shape F(1,1) along the radius, for Euler-Bernoulli (EB) and Pochhammer-Chree (PC). It can be observed that the wave mode shapes are matching for radial, circumferential and axial components for different angles of the cross-section in the rod.

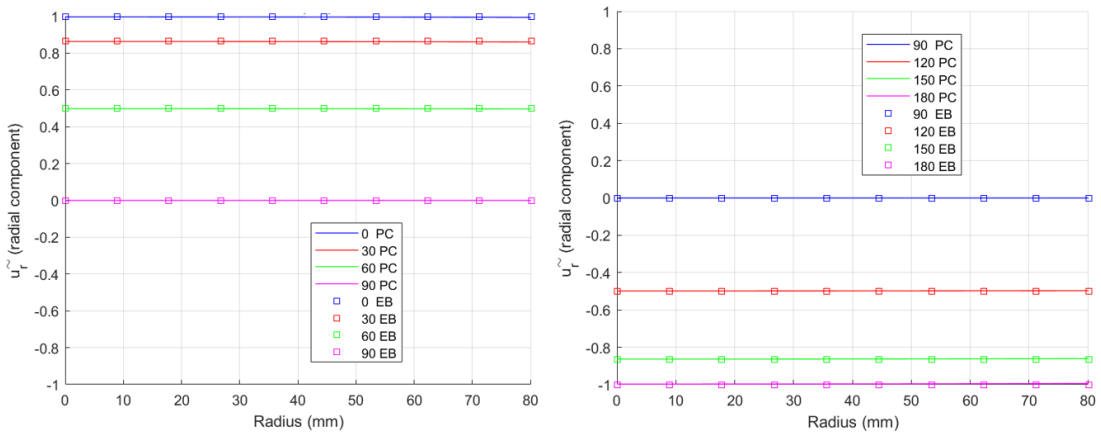

Figure 7-3 Radial component: Euler-Bernoulli (EB) vs Pochhammer-Chree (PC) at 0.1 kHz

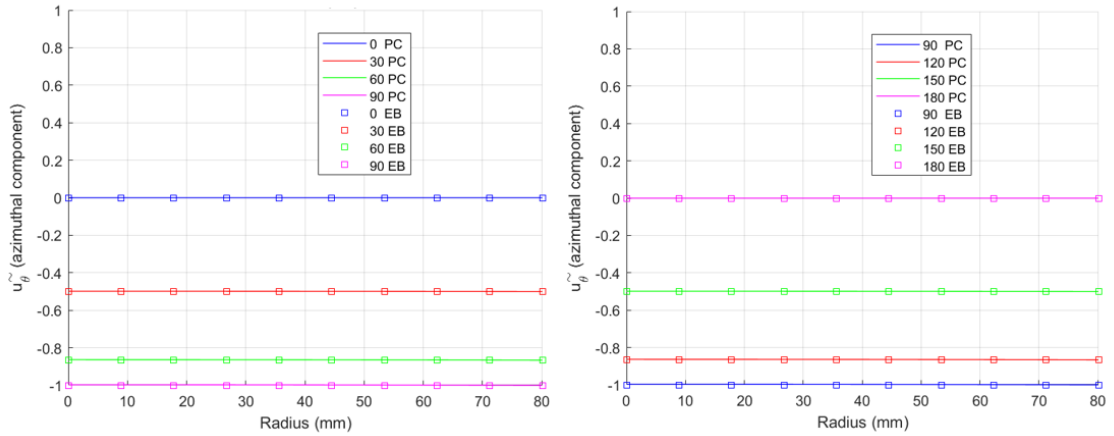

Figure 7-4 Circumferential component: Euler-Bernoulli (EB) vs Pochhammer-Chree (PC) at 0.1 kHz

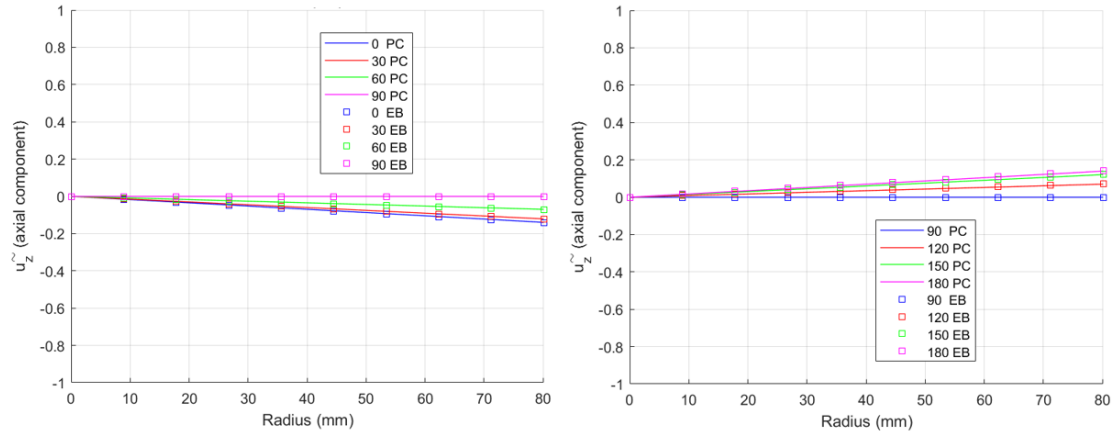

Figure 7-5 Axial component: Euler-Bernoulli (EB) vs Pochhammer-Chree (PC) at 0.1 kHz

7.4 Application of Hilbert transform to axial component

In equation 7.11, it is noted that the radial and circumferential components are real components but the axial component is complex (out of phase j). As the axial component is out of phase, a Hilbert transform in the axial component is considered in the next section to get that the three components can be in phase before applying the wave decomposition method. It is considered to apply Hilbert transform to the axial component so that this can be in phase with the other two components radial and circumferential, because the wave decomposition in the time domain can be only done when the three components of the wave propagation are in phase. In the next section a harmonic analysis is done to visualize how the radial and circumferential components are in phase but the axial component is out of phase. It shows that it is necessary to apply Hilbert transform to the axial component to be able to obtain the three components in phase.

7.4.1 Hilbert transform to harmonic analysis

Now, considering the three components of wave propagation in cylindrical system for a harmonic motion, the real part describes the physical wave propagation of a displacement field for a positive wave as

$$\hat{\mathbf{u}}(t) = \begin{bmatrix} \hat{u}_r \\ \hat{u}_\theta \\ \hat{u}_z \end{bmatrix} = \text{real}\left\{[\mathbf{Q}]\text{e}^{\text{j}(\omega t - kz)}\right\} \tag{7.13}$$

, where $[\mathbf{Q}]$ is the complex wave mode shape, which has real part $[\mathbf{Q_R}]$ and imaginary part $[\mathbf{Q_I}]$ as

$$[\mathbf{Q}] = \begin{bmatrix} \tilde{u}_r \\ \tilde{u}_\theta \\ \tilde{u}_z \end{bmatrix} = [\mathbf{Q_R}] + \text{j}[\mathbf{Q_I}] \tag{7.14}$$

, where $\mathbf{Q_R}$ and $\mathbf{Q_I}$ are real numbers vectors defined from equation 7.11 as

$$\mathbf{Q_R} = \begin{bmatrix} \cos\theta \\ -\sin\theta \\ 0 \end{bmatrix}, \ \mathbf{Q_I} = \begin{bmatrix} 0 \\ 0 \\ -k\, r\cos\theta \end{bmatrix} \tag{7.15}$$

Expanding the equation 7.13, 7.14 and taking only the real part, the equation 7.16 is the solution of harmonic wave propagation, which describes the physical displacement field, it can be observed that the axial component is out of phase but the radial and circumferential are in phase.

$$\hat{\mathbf{u}}(t) = \begin{bmatrix} \hat{u}_r \\ \hat{u}_\theta \\ \hat{u}_z \end{bmatrix} = [\mathbf{Q_R}]\cos(\omega t - kz) - [\mathbf{Q_I}]\sin(\omega t - kz) \tag{7.16}$$

Now, applying the Hilbert transform to equation 7.16, the transformation is

$$\mathbf{H}_{(u)}(\text{t}) = \begin{bmatrix} \bar{u}_r \\ \bar{u}_\theta \\ \bar{u}_z \end{bmatrix} = [\mathbf{Q_R}]\sin(\omega t - kz) + [\mathbf{Q_I}]\cos(\omega t - kz) \tag{7.17}$$

From equation 7.16 taking only $\hat{u}_r, \hat{u}_\theta$ and from 7.17 taking only $\bar{u}_z$, the three components of wave propagation are now in phase

$$\hat{\mathbf{u}}(t) = \begin{bmatrix} \hat{u}_r \\ \hat{u}_\theta \\ \bar{u}_z \end{bmatrix} = ([\mathbf{Q_R}] + [\mathbf{Q_I}])\cos(\omega t - kz) = [\mathbf{Q_{RI}}]\cos(\omega t - kz) \tag{7.18}$$

, where $\mathbf{Q_{RI}} = \begin{bmatrix} \cos\theta \\ -\sin\theta \\ -k\, r\cos\theta \end{bmatrix}$ are the real numbers of the complex wave mode shape

Analytically, it is shown in equation 7.18 that it is possible to get the three components in phase for a steady state harmonic wave. It should be noted that Hilbert transformation is a specific linear operator that takes a function, $\hat{u}(t)$ of a real variable and produces another function of real variable $H_{(u)}(\mathrm{t})$. The Hilbert transform can be understood in terms of a pair of functions $g_1(x)$ and $h_1(x)$ such that the function $G(x) = g_1(x) + \mathrm{j}\, h_1(x)$. Under these circumstances, if $g_1(x)$ and $h_1(x)$ are sufficiently integrable, then one is the Hilbert transform of the other [108].

7.4.2 Hilbert transform to axial component during a transient analysis

For a transient response analysis, numerical simulation is considered, because it was not possible to obtain the results analytically as the harmonic analysis of previous section. Figure 7-6 shows the general block diagram of the numerical analysis. In this case a Gaussian modulated sinusoidal excitation input $f_g(t)$ is used to obtain the transient wave response instead of the harmonic wave motion. Then, a Fast Fourier Transformation is applied to the excitation input to go from time domain to frequency domain to obtain $F(\omega)$. Using the mobility transfer function $M(\omega, x)$ of chapter 4.2 with the input $F(\omega)$ and the output response $V(\omega, z)$, the Inverse Fast Fourier Transformation to the output response $V(\omega, z)$ is calculated to know the response in time domain, where the output velocity $v(t, z)$ is derived from frequency domain to time domain.

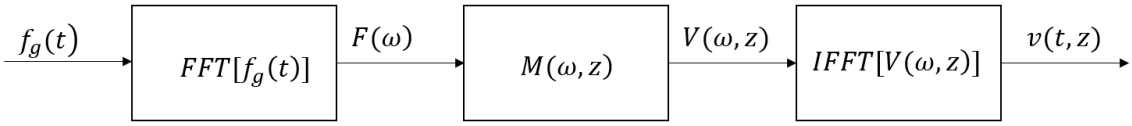

Figure 7-6 General block diagram of numerical analysis:$f_g(t)$ is the excitation input in time domain, $F(\omega)$ is the excitation input in frequency domain, $M(\omega, x)$ is the mobility transfer function of the rod, $V(\omega, z)$ is the output response in frequency domain, $v(t, z)$ is the output response in time domain.

Figure 7-7 shows the Gaussian modulated sinusoidal and its spectrum for a low excitation frequency $f = 1\ kHz$, as in chapter four.

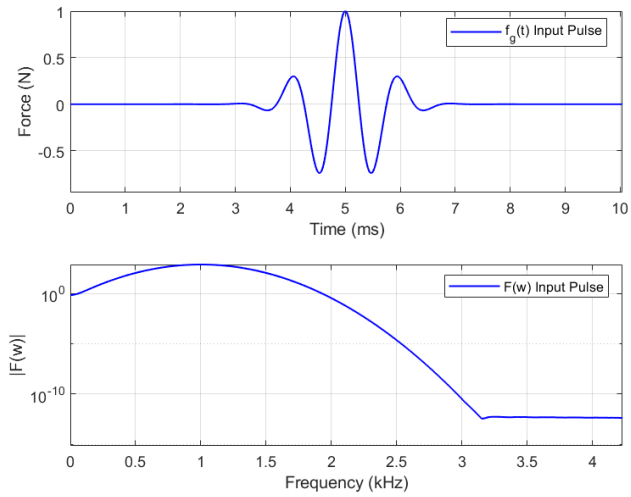

Figure 7-7 Gaussian modulated sinusoidal function and its spectrum

In chapter 4.2, the mobility of a semi-infinite beam model is presented, where the transversal and rotational velocity responses were obtained. Fahy presented et al. [11] that the transient transverse velocity response of a semi-infinite beam is obtained by adopting the transfer mobility $M_w(\omega, z)$ as

$$M_w(\omega, z) = \frac{V_w(\omega, z)}{F_x(\omega)} = \frac{\dot{W}(\omega, z)}{F_x(\omega)} = \frac{\omega(1-\mathrm{j})}{2EIk_b^3}(\mathrm{e}^{-\mathrm{j}k_b z}) \tag{7.19}$$

$$k_b = \sqrt[4]{\frac{\rho A}{EI}}\sqrt{\omega}$$

In a beam model, the transversal force generates evanescent waves and propagating waves. evanescent wave was neglected because we are interested in the wave propagation. The term $\mathrm{e}^{-\mathrm{j}k_b z}$ represents wave propagation.

Fahy presented et al. [11] that the transient angular velocity response of a semi-infinite beam is obtained by adopting the transfer mobility $M_\emptyset(\omega, z)$, as

$$M_\emptyset(\omega, z) = \frac{V_\emptyset(\omega, z)}{F_x(\omega)} = \frac{\dot{\emptyset}(\omega, z)}{F_x(\omega)} = \frac{-\omega(1-\mathrm{j})}{2EIk_b^2}\left(\mathrm{j}\mathrm{e}^{-\mathrm{j}k_b z}\right), \tag{7.20}$$

The $v_w(z,t)$ and $\dot{\varphi}(z,t)$ time responses to a transient input are obtained applying the Inverse Fourier Transform to $V_w(\omega, z)$ and $V_\emptyset(\omega, z)$, respectively.

$$v_w(t,z) = IFFT[V_w(\omega, z)] = IFFT[M_w(\omega, z)F_x(\omega)], \tag{7.21}$$

$$\dot{\varphi}(t,z) = IFFT[V_\emptyset(\omega, z)] = IFFT[M_\emptyset(\omega, z)F_x(\omega)], \tag{7.22}$$

where $v_w(t,z) = v_x(t,z)$ is the transverse velocity. The rotational velocity $\dot{\varphi}(z,t)$ was transformed to the axial velocity $v_\varphi = v_z = x\,\dot{\varphi}(z,t)$ at the distance $x = r_b \cos\theta$ from a neutral axis in a rod of radius r_b.

Figure 7-8 shows the mobility and transient response at $z = 1$ m (Euler-Bernoulli theory). For instance, Figure 7-8(a) presents the mobility and phase for each degree of freedom (transverse M_w and rotational $M_\emptyset$). Figure 7-8(b) shows the frequency response and phase for transverse V_w and rotational velocity $V_\emptyset$. It is observed that the transverse V_w and rotational velocity $V_\emptyset$ are 90 degrees out of phase. Then, Figure 7-8(c) shows the frequency (V_w, $V_\emptyset$) and time response (v_w, v_φ) of Euler-Bernoulli semi-infinite beam. It should be noted that the rotational velocity was converted to axial velocity v_z.

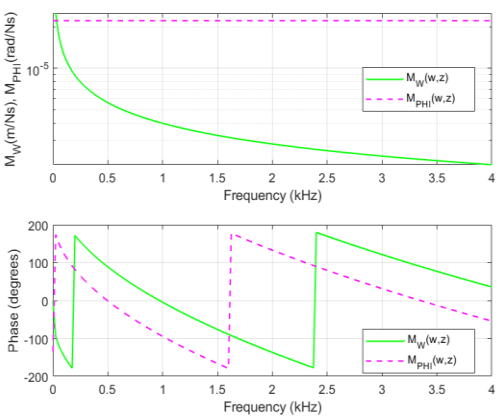

(a)

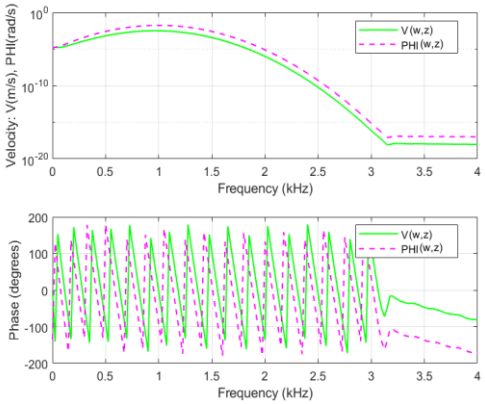

(b)

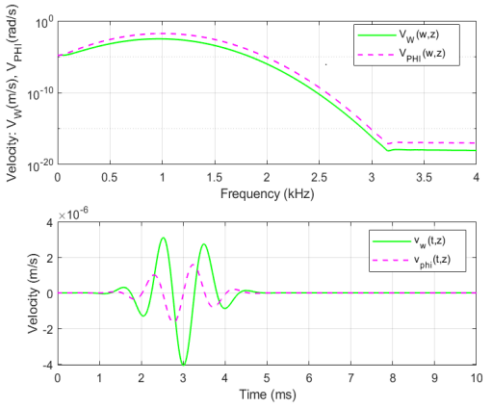

(c)

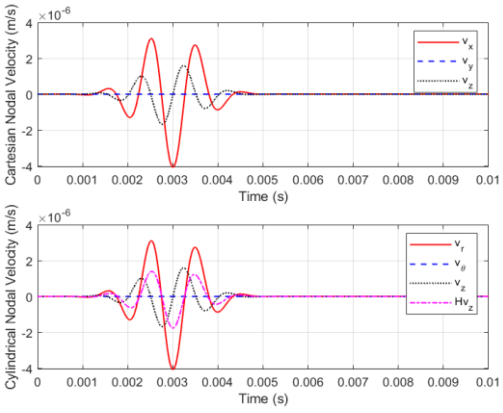

(d)

Figure 7-8 Mobility and transient response of a semi-infinite beam at 1m: (a) Mobility and phase (transverse M_w, rotational $M_\emptyset$), (b) Frequency response and phase (transverse V_w, rotational $V_\emptyset$), (c) Frequency response and transient response (transverse v_w, axial v_φ), (d) Cartesian (v_x, v_y, v_z), cylindrical (v_r, v_θ, v_z) of transient responses and axial Hilbert transform Hv_z applied to v_z.

Finally, Figure 7-8(d) shows the velocity time response in Cartesian and Cylindrical coordinate system, it is noted that the Hilbert transform was applied to the axial velocity v_z to obtain the three components (v_r, v_θ, Hv_z) in phase and do the wave decomposition. It is observed how the new axial component Hv_z is shifted and now it is in phase with radial v_r and circumferential v_θ components.

The wave decomposition was calculated, where the nodal velocity vector was obtained from the numerical simulation (Figure 7-8(d)). Using the definition of equation 7.1 the wave decomposition was done, where the three components (radial, circumferential and axial) of the nodal velocity without Hilbert transformation $\mathbf{N}(t)$ and with Hilbert transformation $\mathbf{N_H}(t)$ in axial component were considered.

$$\mathbf{N}(t) = \begin{Bmatrix} v_r \\ v_\theta \\ v_z \end{Bmatrix}, \qquad \mathbf{N_H}(t) = \begin{Bmatrix} v_r \\ v_\theta \\ Hv_z \end{Bmatrix}$$

Now, comparisons of the wave decompositions are done, where the wave amplitude was obtained for four cases:

1. The wave decomposition was done using only radial and circumferential of the wave mode shape $\mathbf{Q_R}$ and without Hilbert transform in the nodal axial velocity $\mathbf{N}(t)$.

$$\mathbf{a_R}(t) = \left[\mathbf{Q_R}\right]^{+}\mathbf{N}(t), \tag{7.23}$$

2. Using only the axial component of the wave mode shape $\mathbf{Q_I}$ and without Hilbert transform $\mathbf{N}(t)$.

$$\mathbf{a_I}(t) = [\mathbf{Q_I}]^{+}\mathbf{N}(t), \tag{7.24}$$

3. Using only the axial component of the wave mode shape $\mathbf{Q_I}$ and Hilbert transform $\mathbf{N_H}(t)$.

$$\mathbf{Ha_I}(t) = [\mathbf{Q_I}]^{+}\mathbf{N_H}(t), \tag{7.25}$$

4. Using the three components of the wave mode shape $\mathbf{Q_{RI}}$ and Hilbert transform $\mathbf{N_H}(t)$.

$$\mathbf{Ha_{RI}}(t) = [\mathbf{Q_{RI}}]^{+}\mathbf{N_H}(t), \tag{7.26}$$

where: $[\mathbf{Q_R}] = \begin{Bmatrix} \cos\theta \\ -\sin\theta \\ 0 \end{Bmatrix}$, $[\mathbf{Q_I}] = \begin{Bmatrix} 0 \\ 0 \\ -k\,r\cos\theta \end{Bmatrix}$, $[\mathbf{Q_{RI}}] = \begin{Bmatrix} \cos\theta \\ -\sin\theta \\ -k\,r\cos\theta \end{Bmatrix}$ and

$\mathbf{N}(t)$ is the nodal velocity without Hilbert transform in axial component.

$\mathbf{N_H}(t)$ is the nodal velocity with Hilbert transform in axial component.

$\mathbf{a_R}(t)$ is the wave amplitude using only radial and circumferential of the wave mode shape $\mathbf{Q_R}$,

$\mathbf{a_I}(t)$ the wave amplitude using only the axial component of the wave mode shape $\mathbf{Q_I}$,

$\mathbf{Ha_I}(t)$ the wave amplitude using only the axial component of the wave mode shape $\mathbf{Q_I}$ and the nodal vector with Hilbert transform,

$\mathbf{Ha_{RI}}(t)$ the wave amplitude using three components of the wave mode shape $\mathbf{Q_{RI}}$ and the nodal vector with Hilbert transform.

Figure 7-9 shows the wave decomposition of the fundamental flexural wave. It should be noted that after the Hilbert transform, the wave amplitude $\mathbf{Ha_I}(t)$ is matching with the wave decomposition $\mathbf{a_R}(t)$, which is done using only radial and circumferential components. However, when the wave decomposition is done without Hilbert transform, it can be observed that the wave amplitude $\mathbf{a_I}(t)$ is out of phase with $\mathbf{a_R}(t)$. It should be noted that to get the wave decomposition $\mathbf{Ha_{RI}}(t)$ of multiple flexural waves, it is necessary to use the three components of the wave mode shape $\mathbf{Q_{RI}}$ to be able to get a well-condition solution, at the moment of calculating the pseudo-inverse of the wave mode shape matrix.

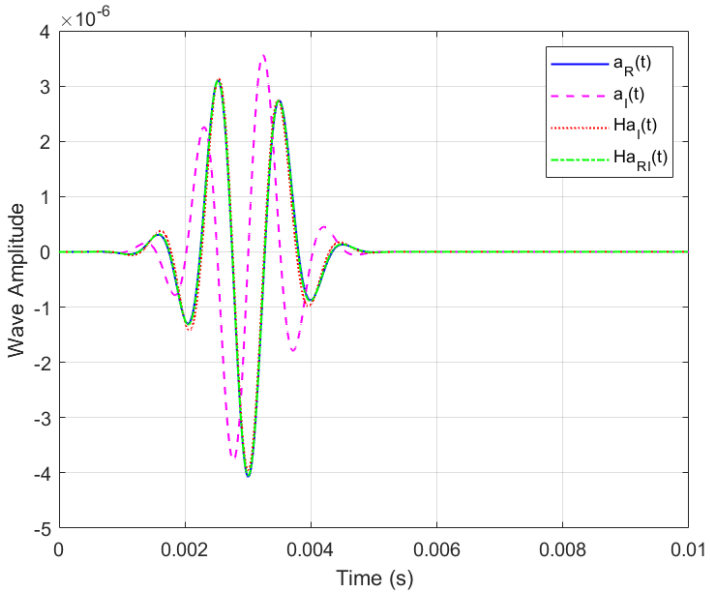

Figure 7-9 Comparison of wave decomposition with and without Hilbert transform: $\mathbf{a_R}(t)$ is the wave amplitude using only radial and circumferential of the wave mode shape $\mathbf{Q_R}$, $\mathbf{a_I}(t)$ the wave amplitude using only the axial component of the wave mode shape $\mathbf{Q_I}$, $\mathbf{Ha_I}(t)$ the wave amplitude using only the axial component of the wave mode shape $\mathbf{Q_I}$ and the nodal vector with Hilbert transform, $\mathbf{Ha_{RI}}(t)$ the wave amplitude using three components of the wave mode shape $\mathbf{Q_{RI}}$ and the nodal vector with Hilbert transform

Now, applying Hilbert transformation to the nodal acceleration of the axial component, using the radial and circumferential nodal accelerations without Hilbert transform, and using the three components of the wave mode shape $\mathbf{Q_{RI}}$, the wave decomposition $\mathbf{A_H}(t)$ in high frequency is

obtained, where multiple waves are excited. The nodal accelerations $\mathbf{N_H}(t)$ are obtained from simulations or experimental work.

$$[\mathbf{A_H}(t)] = [\mathbf{Q_{RI}}]^{+}[\mathbf{N_H}(t)] \tag{7.27}$$

For example, according to the dispersion curve of the rod with diameter 160 mm (Figure 7.1(right)), eight waves are excited at 30 kHz. In the next section, wave decomposition is done for a long bar, bent bar and chain. Simulations in ABAQUS were done to obtain the nodal acceleration vectors in a cylindrical coordinate system.

7.5 Comparison of wave decomposition in a straight bar, bent bar and chain link of large diameters

Wave decompositions were done in a long bar, bent bar and chain model with a diameter of 160 mm. Three cases of study (position of excitation) were considered in each model (bar, bent bar, chain link) to do comparison of wave decomposition, and to analyse how the geometry can have an impact on the waves.

7.5.1 Finite element approach

Finite element analysis (FEA) in ABAQUS was carried out to obtain the transient nodal accelerations for a rod, bent rod and chain with three different simple excitation arrangements. The excitations were applied at the end face of each model as shown in Figure 7-10. Case A is an excitation in axial direction at the centre, Case B is a transverse excitation at the centre and Case C is a transverse excitation at the outer surface.

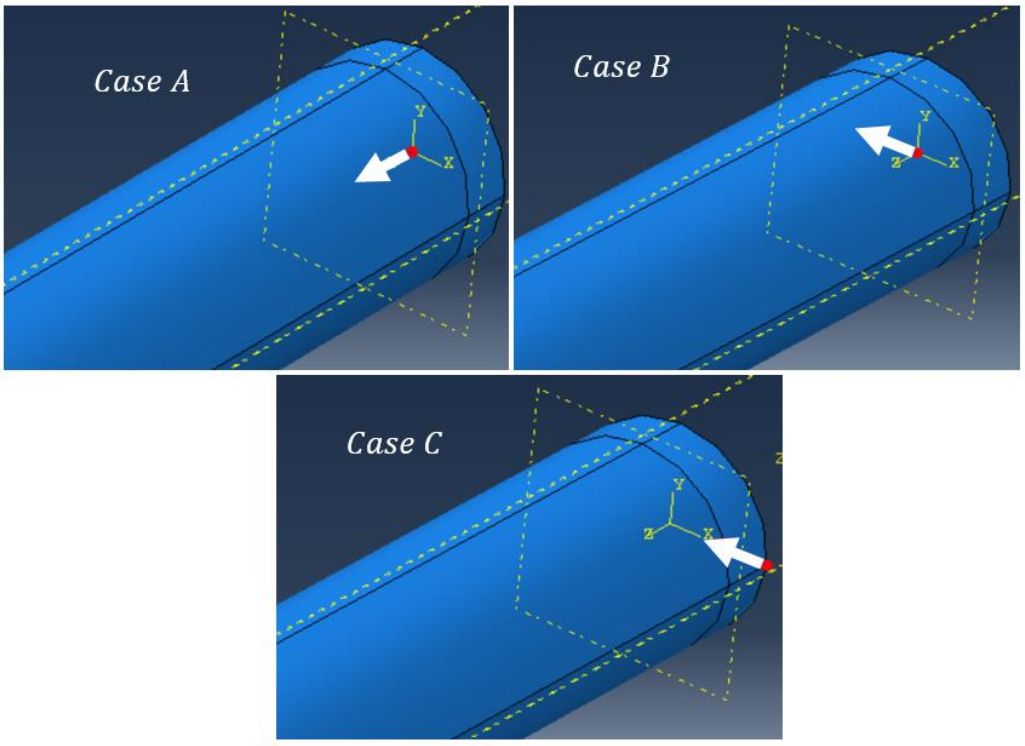

Figure 7-10 Excitations applied at the end face of each model

The excitation function was a Gaussian modulated sinusoidal (see equation 4.2) with a centre frequency of 30 kHz. The width of the pulse was controlled by the number of standard deviations considered, such a 99.7 % of the set $6\sigma = width = \frac{5}{30\ kHz} = 166.66\ \mu s$. Figure 7-11 shows the Gaussian modulated sinusoidal excitation input $f_g(t)$ and its spectrum. It is compared with the 'gauspuls' command of Matlab $g_g(t)$ (Modulated-Gaussian Sinusoidal), which has a centre frequency of 30 kHz and a default fractional bandwidth of 0.5. Catton presented et al. [57] that all possible wave modes in the dispersion curves for the frequency bandwidth (20-40 kHz) of the excitation signal would be generated due to point source excitation.

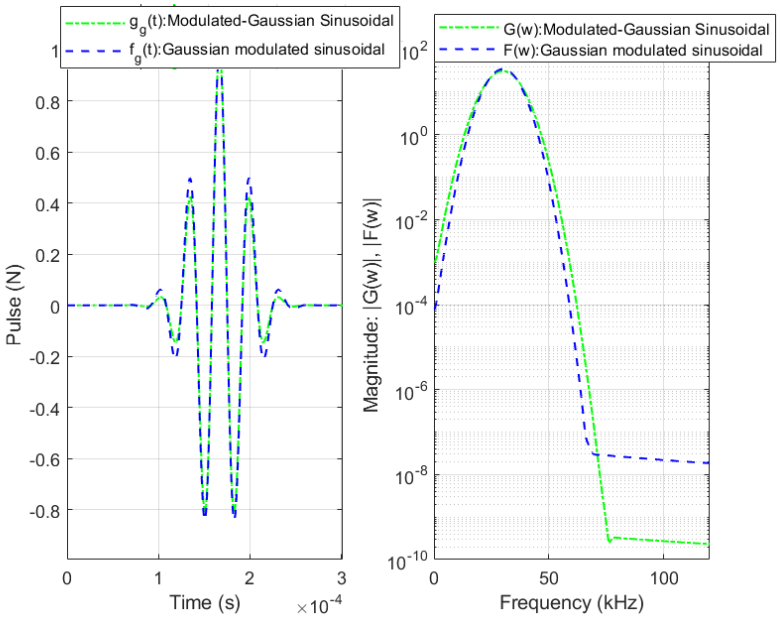

Figure 7-11 Gaussian modulated sinusoidal functions (left), Spectrums (right)

The first test specimen modelled was a steel cylindrical bar of 3 metre length, the second test specimen was a bent bar to represent half a link, and the third specimen modelled was a full link. Figure 7-12 shows the models and the positions where the signals were received. A set of nodes every 90 degrees (receivers) was used to monitor the accelerations at the outer surface of the rod, 0.9 m from the excitation point, in order to obtain the nodal amplitude in each of the cylindrical components (r, θ, z). The same distance of 0.9 m was considered for receiving signals at the bent bar and the chain for the comparison of the wave decomposition.

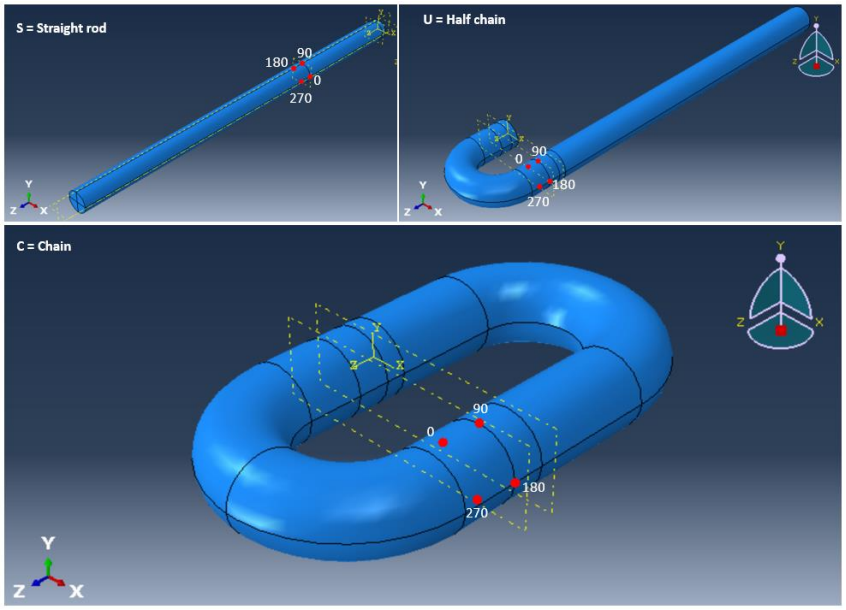

Figure 7-12 Receiver signals for Bar model (S), Bent bar model (U), Link model (C)

The element size was around 5 mm, which was sufficient to capture the smallest possible wavelength λ_{min} of 0.05 m at the maximum frequency of 60 kHz (see Figure 7-13) for a cylindrical bar of 160 mm diameter [66]. There were therefore around ten elements per minimum wavelength. The element type used, was a quadratic 3D solid, with reduced integration (ABAQUS element type C3D8R). The material properties for steel were the same as given chapter six (Young's modulus 200 GPa, shear modulus 76.9 GPa, density 7850 $\frac{\mathrm{kg}}{\mathrm{m}^3}$ and Poisson's ratio 0.3).

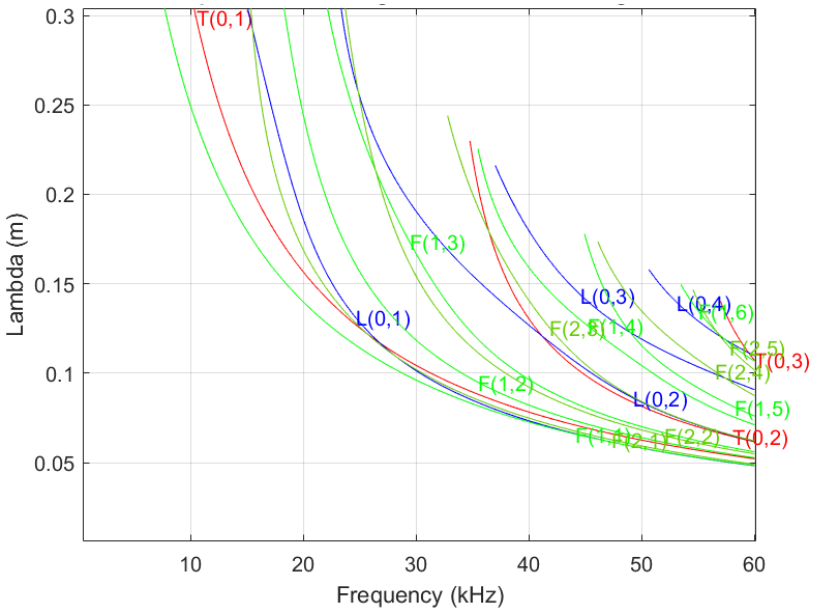

Figure 7-13 Wavelength for a rod with diameter of 160 mm

7.5.2 Comparison of wave decomposition for case A (axial excitation)

Figure 7-14 shows the comparison of the wave decomposition, where the nodal acceleration in radial, circumferential and Hilbert transform in axial direction are considered for the case A. For better visualization and better understanding of comparison between the models, the wave envelope was plotted only for each wave. Comparing Figure 7-14, which has the first waves (T(0,1), L(0,1), L(0,2), F(1,1)), against Figure 7-15, which has the next four flexural waves (F(1,2), F(1,3), F(2,1), F(2,2)), there are no flexural and torsional wave in the straight bar (solid line pink colour) as expected. In the case A, it can be observed that only L(0,1) and L(0,2) are excited and the highest contribution is obtained in L(0,1). However, in the bent bar (dash-dot line blue colour), the longitudinal waves are converted to flexural waves. Moreover, L(0,1) wave shape is scattered due to the bent bar and chain (dotted line black colour). It should be noted that L(0,1) is less dispersed in the bent bar. However, L(0,1) is more scattered in the chain. In the case of the chain, the two bends produce the major scattering in the waves L(0,1) and L(0,2). In fact, similar scattering behaviour is observed in the flexural wave F(1,1), but the two pulses of the wave form are kept in the chain model. According to the dispersion curve, the torsional T(0,1) is the only non-dispersive wave. However, for this analysis of axial excitation, only a negligible wave amplitude of T(0,1) can be observed after the bends.

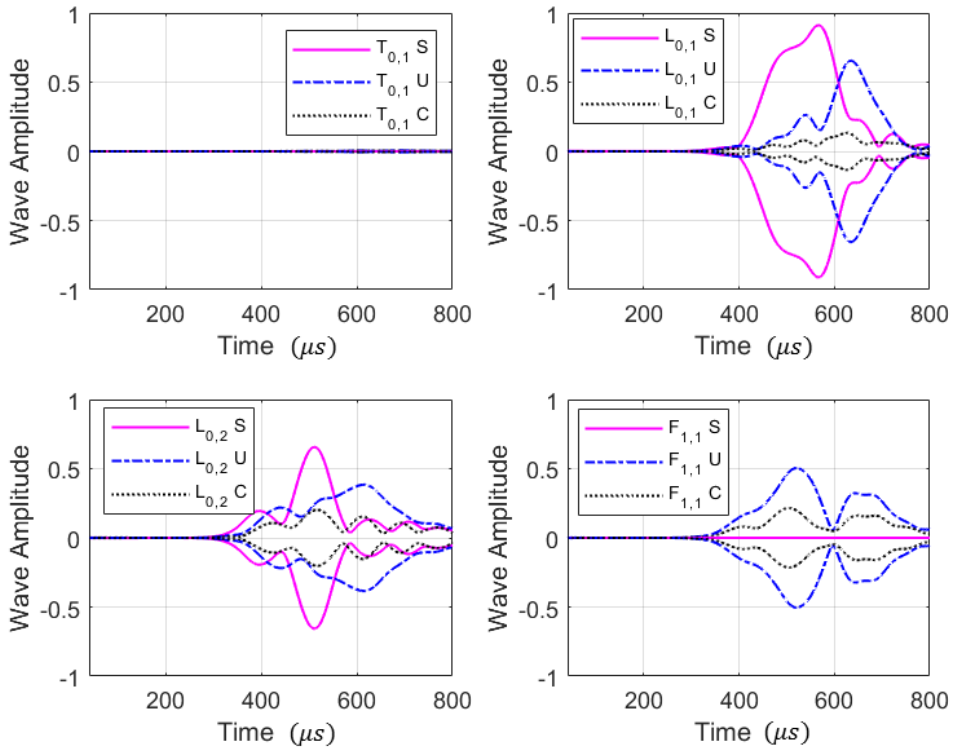

Figure 7-14 Waves comparison (T(0,1), L(0,1), L(0,2), F(1,1)) of wave decomposition at centre frequency of 30 kHz for the three models (axial excitation): Bar model (S), Bent bar model (U), Chain link model (C)

Figure 7-15 shows the comparison of the next four flexural waves. These converted flexural waves are observed only in the half and full chain. The wave amplitudes are likely to be altered by the bend. In this case, the highest wave amplitude is obtained in F(1,2) for half chain and F(1,3) for full chain. In fact, it can be visualised that the F(1,2) in the bent bar has a similar wave form to L(0,2) of the straight bar, so it is possible that L(0,2) converted to F(1,2). There are many different wave modes that can exist at a given frequency, each with a different mode of deformation. Most of these are dispersive, where their velocity changes significantly with frequency. Dispersion is generally undesirable in non-destructive testing, because the pulse spreads out and distorts, making results difficult to interpret. Dispersion and wave mode conversions are behaviours observed after the bends in a half and full chain. It should be noted that the wave decomposition is done for a central frequency of 30 kHz because at this frequency 8 wave modes are excited. The wave decomposition was done at this frequency to know how the geometry has a high impact in the wave conversion. For example wave mode conversion are observed after the bents in the link and in the U shape model.

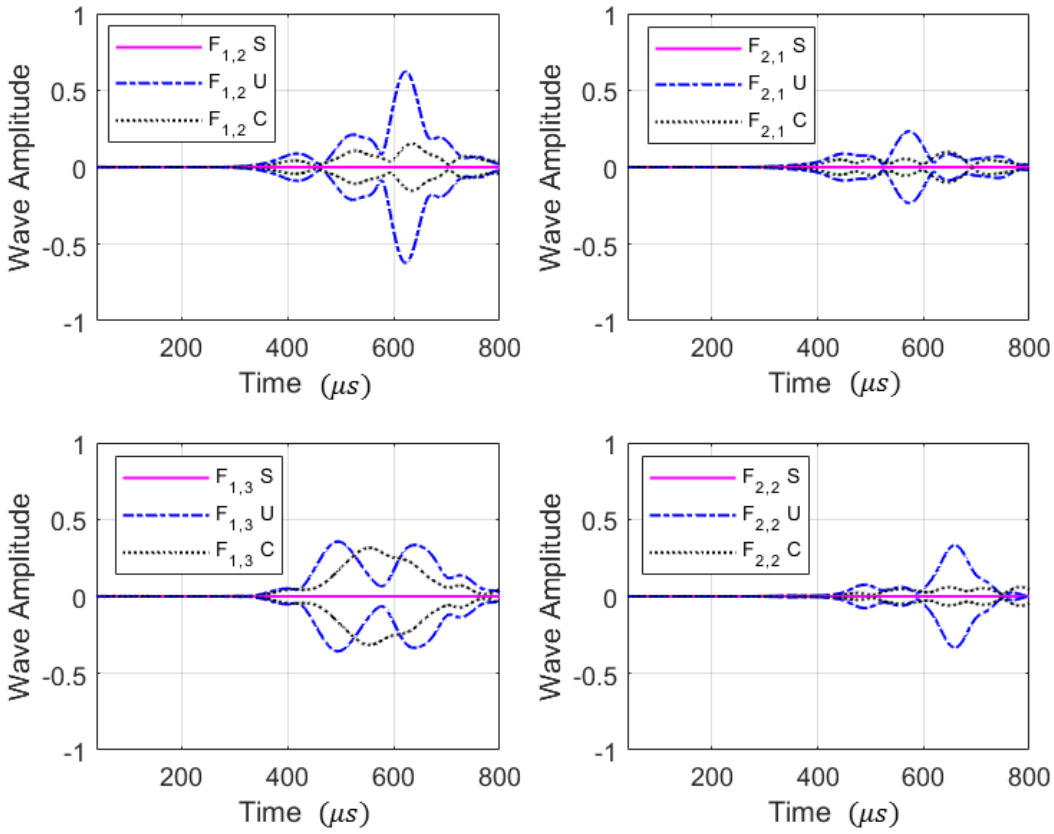

Figure 7-15 Waves comparison (F(1,2), F(2,1), F(1,3), F(2,2)) of wave decomposition at centre frequency of 30 kHz for the three models (axial excitation): Bar model (S), Bent bar model (U), Chain link model (C)

7.5.3 Comparison of wave decomposition for case B (transversal excitation)

Figure 7-16 presents the comparison of the first four waves (T(0,1), L(0,1), L(0,2), F(1,1)) in each model for case B, where a transverse excitation is applied at the centre of the free end face. As expected, unlike the predominance of longitudinal waves are excited in straight bar model, it can be observed that there are only flexural waves, as was expected in case B. However, in the bent bar and chain, the bends converts some flexural waves to longitudinal ones. It is important to note that L(0,1) has a similar wave form in bent bar and chain, but the scattering is higher in the chain model. Also, L(0,2) the wave form is spread out in the chain model. In addition, the amplitude of the flexural wave F(1,1) is spread out after the bend. In fact, a time shift in the pulse of higher amplitude is observed in F(1,1) for both the bent bar and chain models, this is because the pulse is spreading out after the bend. Again, T(0,1) has a very small wave amplitude after the bend. The F(1,1) is the wave with the highest amplitude in a link.

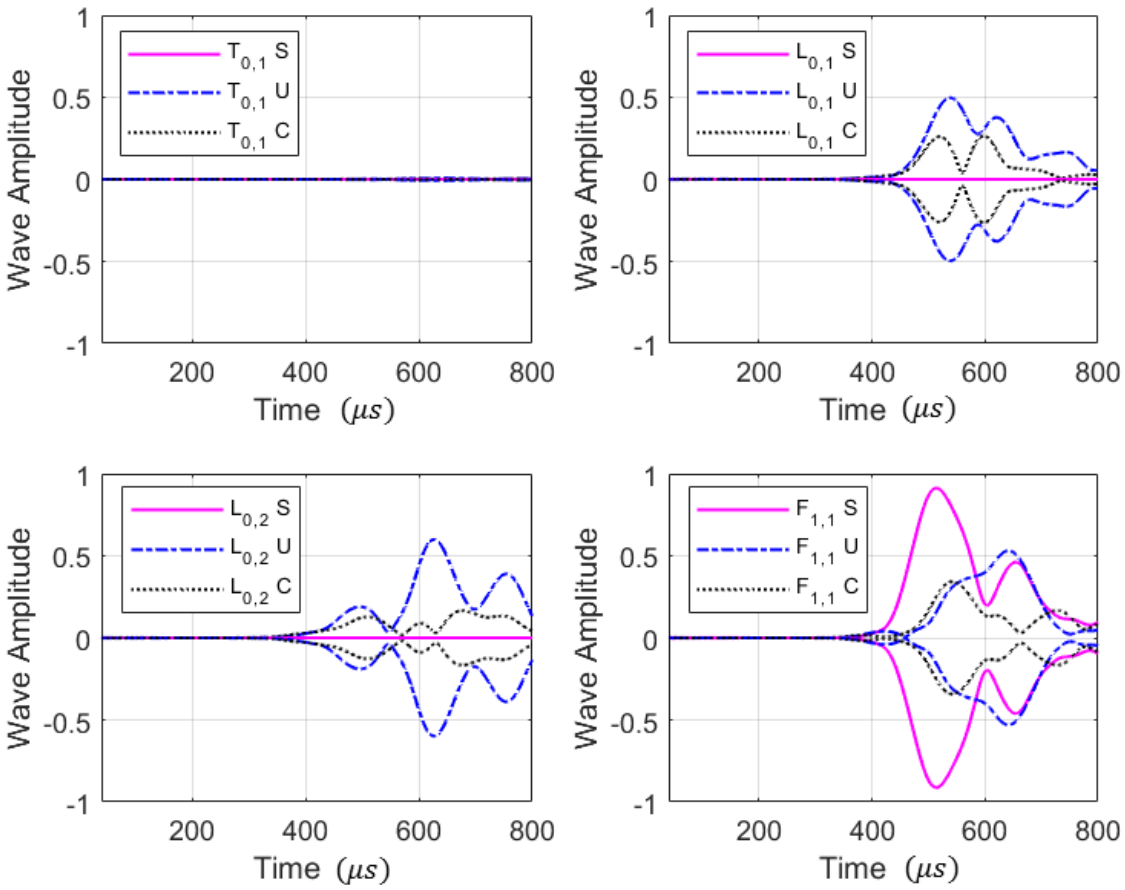

Figure 7-16 Waves comparison (T(0,1), L(0,1), L(0,2), F(1,1)) of wave decomposition at centre frequency of 30 kHz for the three models (transversal excitation): Bar model (S), Bent bar model (U), Chain link model (C)

Figure 7-17 shows the comparison of the flexural wave F(1,2), F(1,3), F(2,1), F(2,2). In this comparison, when the excitation is done at the centre in transverse direction in the straight bar, there is no excitation of any wave with second harmonics around the surface, because the wave mode shape contribution is zero at the centre. However, the flexural wave mode F(1,2) and F(1,3) have a higher contribution at radius zero. It is important to observe that after the bend, the waves F(2,1) and F(2,2) with second harmonic are excited. This means that they were converted due to the bends in the U and link models. This is a good example of how the complex geometry of the half and full link has a high impact in wave conversions. These two waves F(2,1) and F(2,2) are not excited in the straight bar. It can be seen how the link has higher effect in the scattering of the waves, because the wave amplitudes are spread out more than in half chain model. For instance, the F(1,2) has almost the same amplitude in straight and half chain, but the wave amplitude is reduced by more than three quarters in the link. It is considered that the high scattering in the chain is due to the pulse propagating in positive and negative axial direction. However, in a bar and bend bar the free end produces that the total pulse propagates only in positive axial direction. F(1,3) is the only wave with lower scattering in the three models, but the amplitude is shorter that F(1,2). Finally, the converted flexural F(2,1) and F(2,2) waves amplitudes are reduced by half wave amplitude between bent bar and chain.

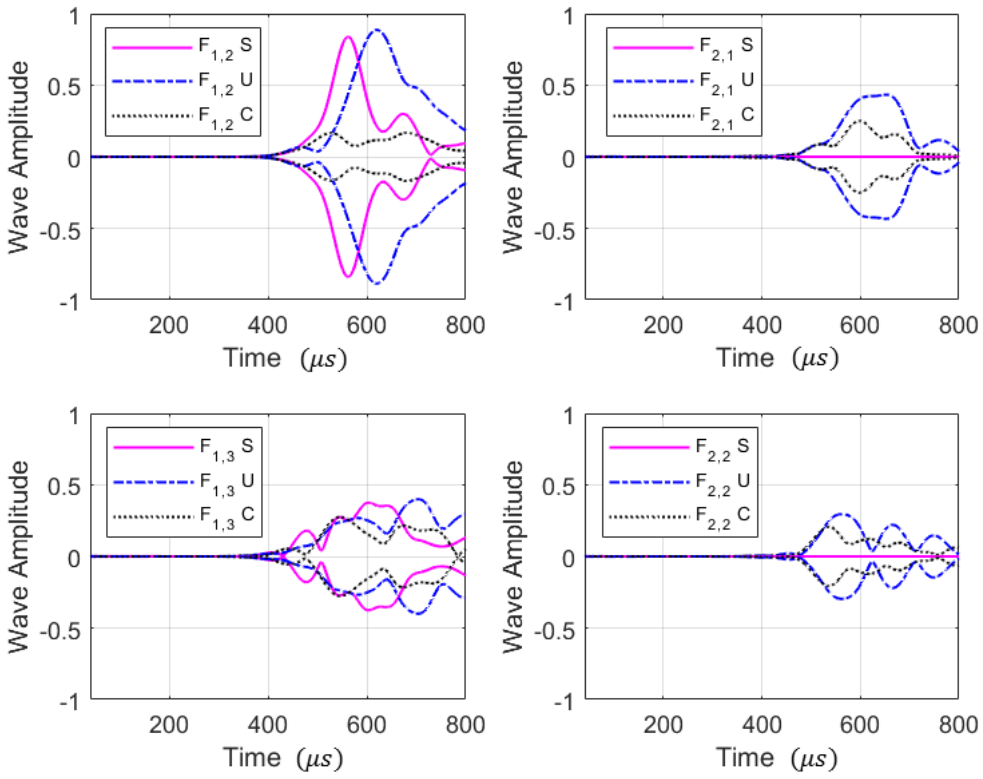

Figure 7-17 Waves comparison (F(1,2), F(2,1), F(1,3), F(2,2)) of wave decomposition at centre frequency of 30 kHz for the three models (transversal excitation): Bar model (S), Bent bar model (U), Chain link model (C)

7.5.4 Comparison of wave decomposition for case C (transverse excitation outer surface)

In case C, there is a transverse excitation applied at the outer surface of the free end face. Figure 7-18 presents the comparison of the first four waves (T(0,1), L(0,1), L(0,2), F(1,1)) in each model. In this case, it is observed that L(0,1) and L(0,2) are excited in the straight bar model. This behaviour was not observed when the transverse excitation was applied at the centre. This means that the free end face generates an axisymmetric conversion mode, when the traverse excitation is done at the outer surface. In general, it is important to note the loss of wave amplitude and signal distortion caused by bends is observed as in previous cases. However, for case C, in the half chain, the wave L(0,2) and F(1,1) is spread out, but the wave amplitude increases instead of being reduced. This behaviour is not observed in the chain. To the contrary, the wave is scattered. In addition, it can be seen that the wave received beyond the bend arrives at a slightly different time. Similar time shifts were observed for all excitation cases. A very small amplitude mode converted T(0,1) wave can be observed after the bends for bent bar and chain.

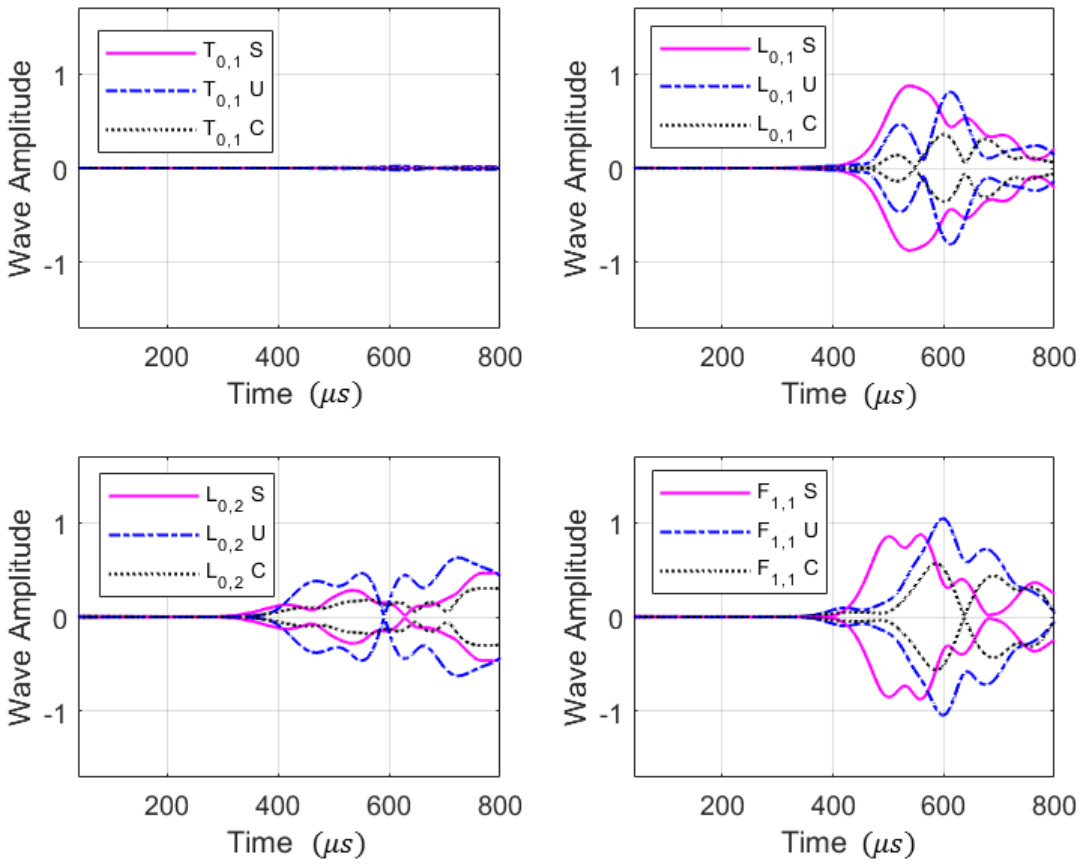

Figure 7-18 Waves comparison (T(0,1), L(0,1), L(0,2), F(1,1)) of wave decomposition at centre frequency of 30 kHz for the three models (transversal excitation at outer surface): Bar model (S), Bent bar model (U), Chain link model (C)

Figure 7-19 illustrates the comparison of the wave decomposition for F(1,2), F(1,3), F(2,1), F(2,2). In case C, the amplitudes of the flexural waves F(1,2) and F(1,3) increase instead of decreasing for the bent bar model. It is observed that the wave form is not spread out. On the other hand, it is observed that for case C, the flexural waves with two harmonics F(2,1), F(2,2) are excited for the straight bar mode. The main reason is that the excitation is done at the outer surface. This was not observed in case B, when the excitation was applied at the centre of the bar, because the contribution of the flexural wave of second order is zero at radius zero. On the other hand, the complex bend geometrics show that the interpretation of the results is not simple, because as was expected, the wave amplitude of F(1,2) and F(1,3) are scattered. However, F(1,2) and F(1,3) show the highest wave amplitude with similar wave form for the bent bar model. Finally, the wave amplitude of F(2,1) appears to be slightly similar in bent bar and chain, while the wave amplitude of F(2,2) is not. Wave modes that exhibit velocity changes with frequency are dispersive and hence their pulse shape will change as they propagate, so further scattering may be an issue if inspection was to be carried out at a more remote location.

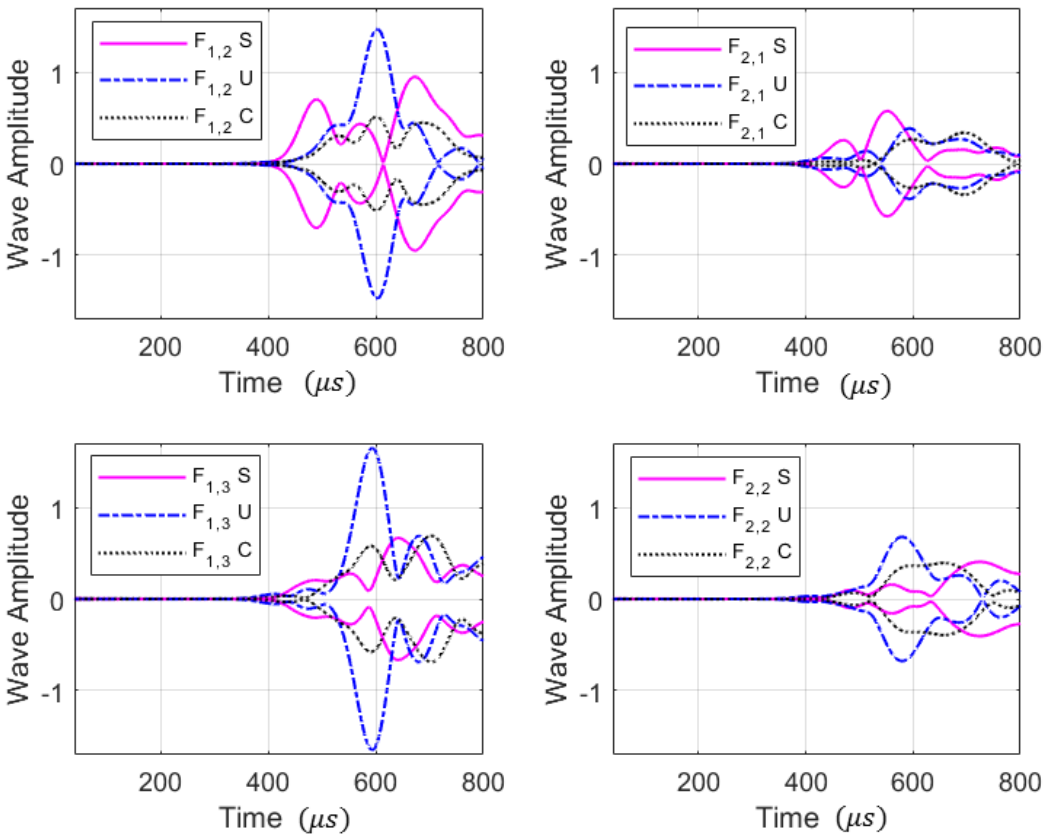

Figure 7-19 Waves comparison (F(1,2), F(2,1), F(1,3), F(2,2)) of wave decomposition at centre frequency of 30 kHz for the three models (transversal excitation at outer surface): Bar model (S), Bent bar model (U), Chain link model (C)

The finite element modelling was used to investigate the behaviour of the wave propagation and the impact of the geometry in a bent bar and chain. However, experiments are required to validate the simulations as described in the next section.

7.6 Experimental validation for straight bar and link

The simulations were validated with experimental work on a straight bar and link. Two cases were considered for straight bar. In the first case axial excitation was used (case A) and the second case transverse excitation at the outer surface was used (case D). In case D, excitation at 4 cm distance from the free end face was necessary to be able to attach the transmitter. For the link, two cases were also considered. For Case E, transverse excitation was applied at one straight part of the chain and Case F, the transverse excitation was applied at one bend. More details are provided in the next sub-sections.

7.6.1 Experimental set-up for bar and link of large diameter

Experiments were carried out to validate the wave decomposition simulation. Additional finite element models were generated in ABAQUS, to exactly match the excitation functions used in the experiment. Figure 7-20 presents the function excitation of 30 kHz centre frequency 5-cycle Hann-windowed pulse and its spectrum. It is observed that this pulse will predominantly excite waves between 20 kHz and 40 kHz.

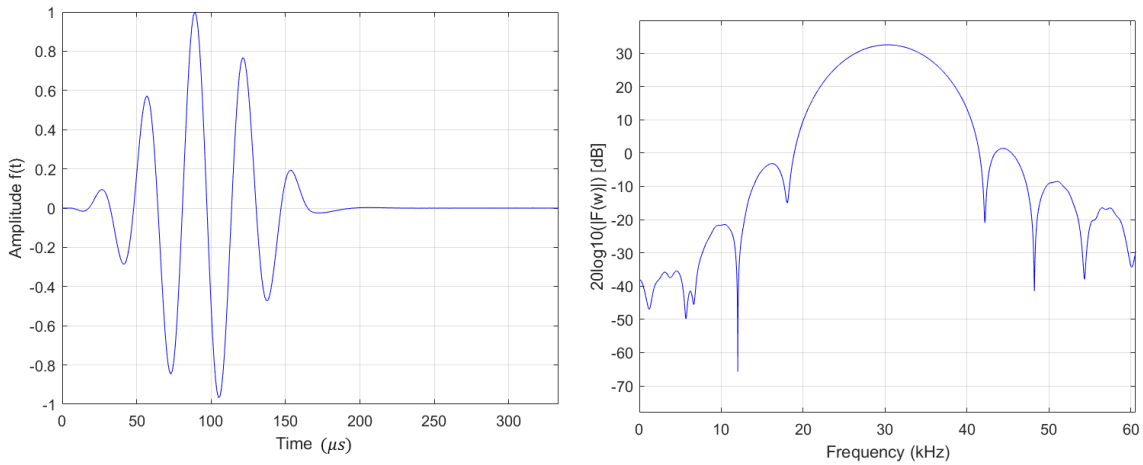

Figure 7-20 Hann-windowed 5 cycle excitation pulse with centre frequency of 30 kHz (left), Excitation spectrum (right)

Figure 7-21 shows the experimental and simulation set-up for case A and case D on the straight bar. For case D, an additional finite element model was carried out to exactly match the experiment. The steel cylindrical bar had the same dimensions as the FEA model (3 m length and 160 mm diameter). The bar was resting on two industrial supports and isolated with rubber material to avoid disturbance from the surroundings. A magnetic clamp was used to attach the compression transducer. Figure 7-21 (a) shows the orientation of the transducer for applying the pulse in the axial direction (case A), and simulation in Figure 7-21 (c). Then, Figure 7-21 (b) presents the case D set-up, where a transverse load is applied to the outer surface, 4 cm from the end face, and simulation in Figure 7-21(d).

The same VALLEN AMSYS-6 Acoustic Emission Testing system was used to record the accelerations at 0.9 m from the excitation. A function generator was used to apply the 5-cycle Hann-windowed pulse of 30 kHz central frequency (Figure 7-20). The VS30-SIC-46dB compression piezo-electric AE sensor with integrated preamplifier was used as a transmitter.

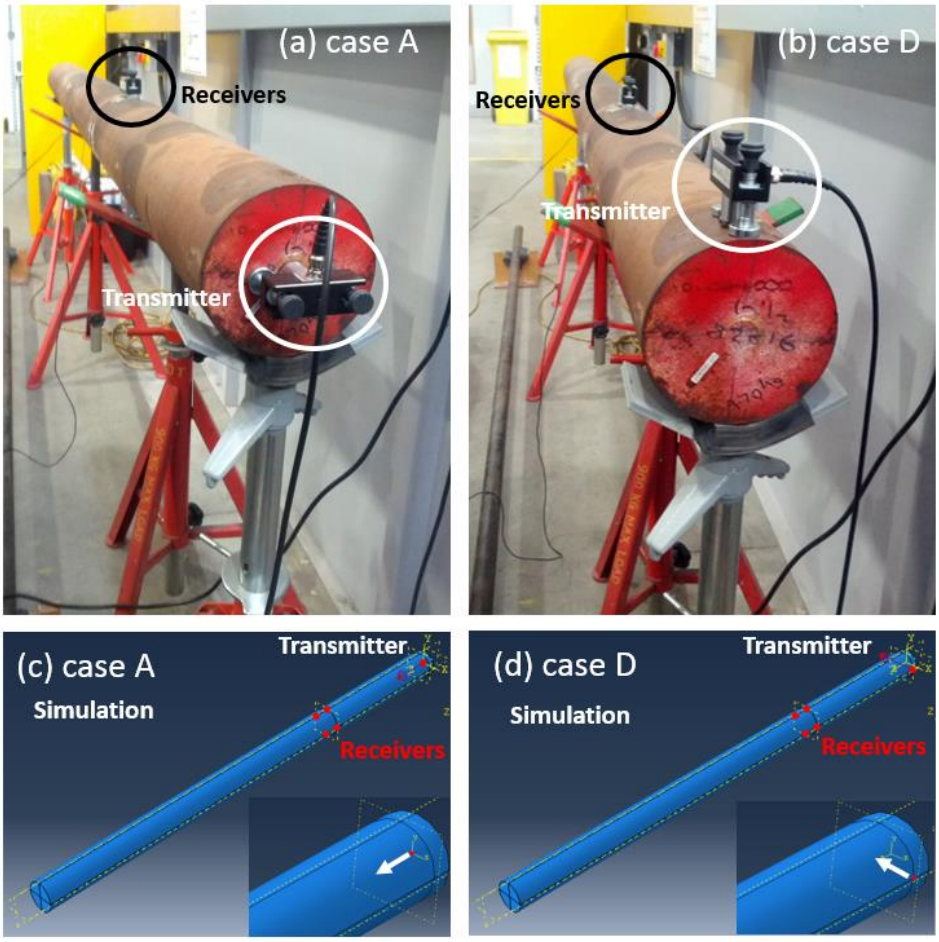

Figure 7-21 Experimental set-up and simulation case for bar of large diameter

Two receiver sensors were used to measure the accelerations at 0.9 m from the excitation source and every 90 degrees around the surface of the bar in the radial, circumferential and axial directions. The same compression sensor and shear sensor with amplifier AEP4 as used in the experiments described in chapter six were used as receivers (Figure 6-22). The preamplifier type AEP4 is a general preamplifier supporting single sensor. This preamplifier is wide-band, with a frequency response from 5 kHz to 1 MHz, and has a 40 dB gain. The compression sensor was used to record the radial direction on the surface, and the shear sensor was used to record the circumferential and axial direction on the surface. The test was repeated 12 times to record the 12 degrees of freedom, because only two sensors were available to record every 90 degrees in the radial, circumferential and axial direction. The receiver channels were synchronised as in chapter six to be sure that the 12 receiver signals are triggered at the same time. The receiver sensor has a frequency response range from 20 kHz to 90 kHz [109]. Figure 7-22 shows the frequency response of a similar sensor used for different preloads in a test carried out by Arun et al. [109]. In this thesis the magnetic holder used, it is able to apply a force of 50N in the similar sensor used during the experimental work. It is observed a linear behaviour in a frequency range from 20 to 70 kHz.

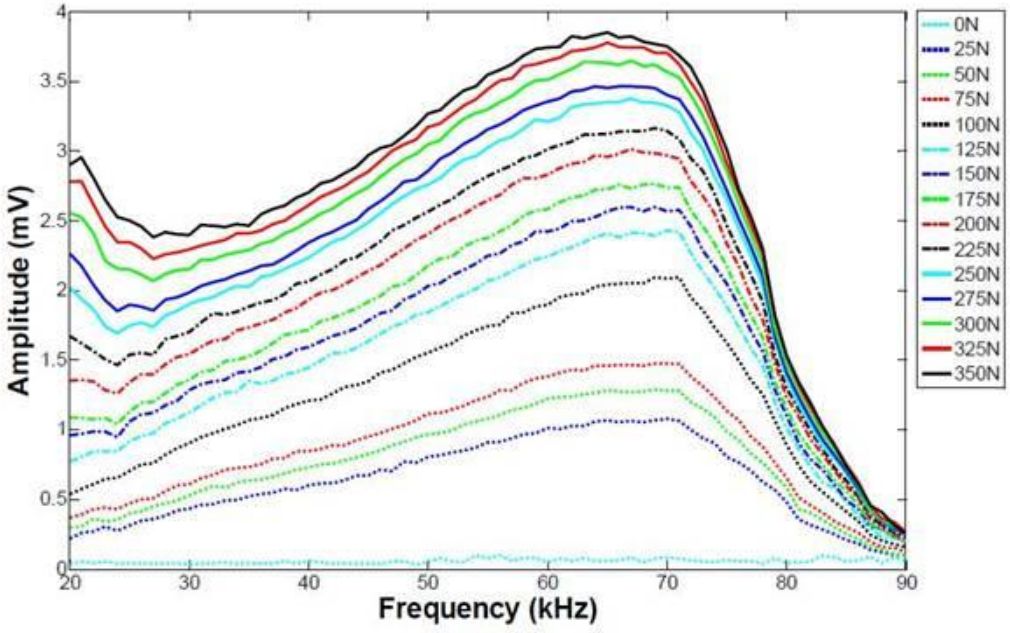

Figure 7-22 Frequency response of receiver sensor for different static preloads carried out by Arun et al. [109]

Figure 7-23 shows the experimental and simulation set-up for case E and case F on the mooring link. Case E was carried out to exactly match with the experiment, where the transverse point load was applied at the straight part of the chain. For Case F, the transverse point load was considered at the bend of the chain. The chain has the same dimensions as the FEA model (160

mm diameter). The chain was resting on two wooden supports and isolated with rubber material as was the case with the cylindrical bar, in order to isolate it. Figure 7-23(a) shows the magnetic clamp used to attach the compression transducer and apply the pulse at the outer surface in the straight part of the chain. Moreover, Figure 7-23(a) shows the receivers at 0.9 m along the curvature length from the excitation. Figure 7-23(c) presents the simulation scenario for case E to match with the experiment. Then, Figure 7-23 (b) presents the case F set-up where a transverse load is applied at the outer surface of one bend in the chain. In addition, Figure 7-23(d) shows the simulation receivers at 0.4 m along the curvature length from the excitation. The same excitation function of a 5-cycle Hann-windowed pulse at 30 kHz central frequency was applied (Figure 7-20). The same VS30-SIC-46dB compression piezo-electric AE sensor with integrated preamplifier was used as transmitter. As before, the receiver signals were synchronised and the test was repeated 12 times for each case to obtain the radial, circumferential and axial components. It should be noted that the Hilbert transform was applied only to the axial component nodal acceleration before the wave decomposition.

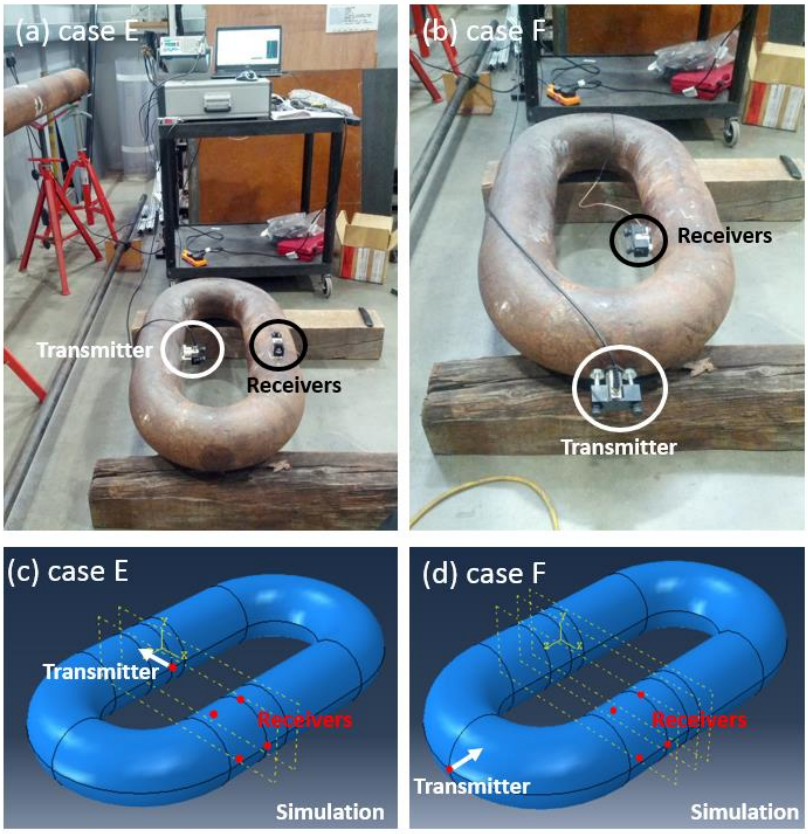

Figure 7-23 Experimental set-up and simulation case for chain link of large diameter

7.6.2 Experimental results of wave decomposition in case A for bar of large diameter

Figure 7-24 presents the wave decomposition for case A (axial excitation). The wave decomposition was done, applying the Hilbert transform to the nodal acceleration of axial component to get that the three components (radial, circumferential and axial) can be in phase. There is good agreement in the wave decomposition between the experiment and simulation FEM model results for L(0,1) and L(0,2). For instance, for a load in the centre of the end face with an excitation in the axial direction, both the experiment and the model find the longitudinal L(0,1) to have the highest contribution. In the experimental results for case A, there is some contribution of flexural waves which cannot be observed in the FEM model. Again as in the previous experiment, this is thought to be because the transmitter excites a small pulse in parallel direction on the surface and is not capable of transmitting a pure compressional pulse. Figure 7-25 shows the envelope of each wave decomposition for a better visualization, where good agreement is observed in the enveloped pulse for L(0,1) and L(0,2).

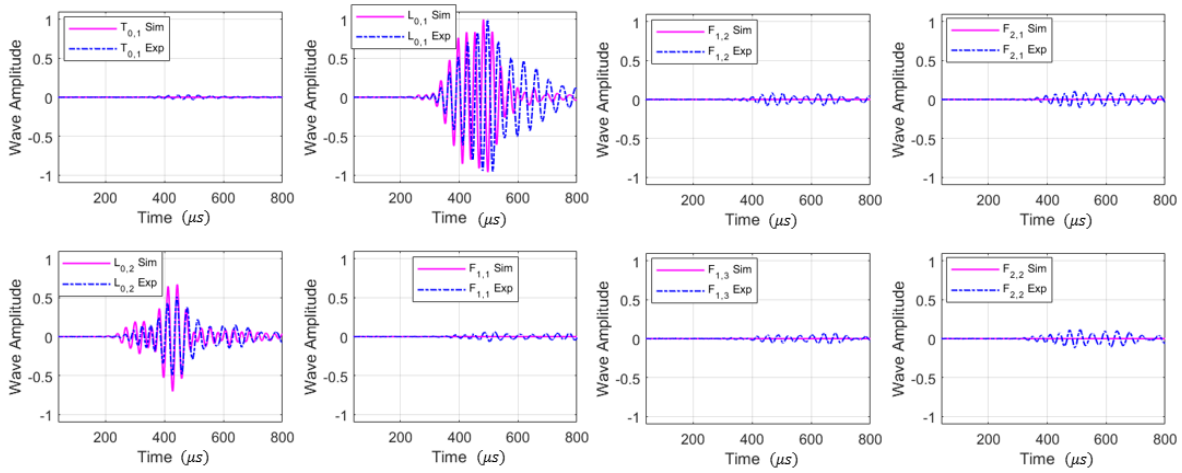

Figure 7-24 Wave decomposition for simulation and experiment in case A (using all components)

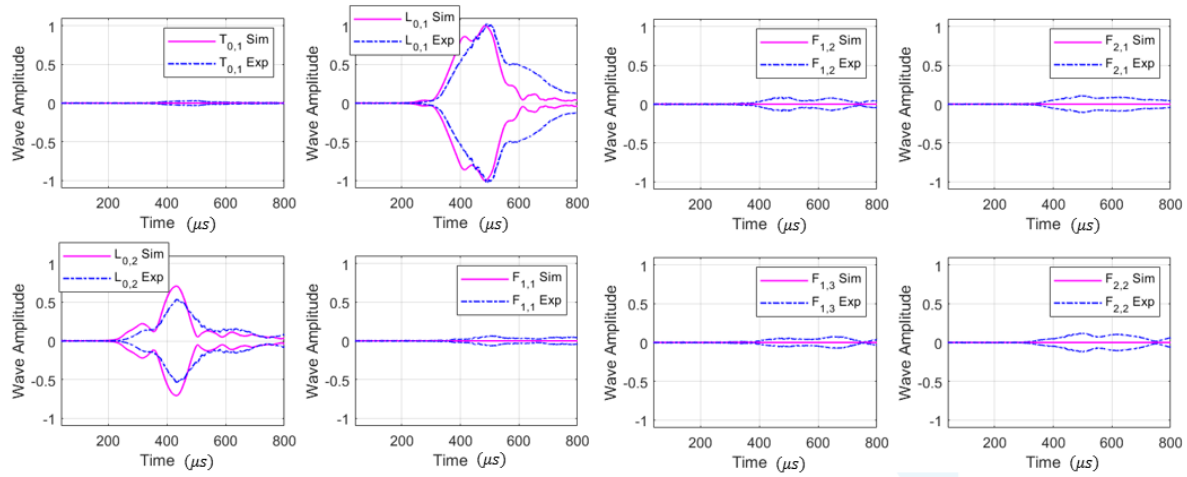

Figure 7-25 Envelope of wave decomposition for simulation and experiment in case A (using all components)

7.6.3 Experimental results of wave decomposition in case D for bar of large diameter

Figure 7-26 shows the wave decomposition for case D, when the excitation is applied in transverse direction at the outer surface. Only flexural waves were expected from the transverse excitation. However, it can be observed that longitudinal waves L(0,1) and L(0,2) are excited in experiment and simulation. It is inferred that the free end face produces longitudinal wave conversion. In general, all the waves are arriving at a similar time and have similar wave amplitude between simulation and experiment. It should be noted that the wave decomposition is normalized using the maximum amplitude of the wave with the highest contribution. Figure 7-27 shows the envelope of each wave decomposition for better visualization between the waves. For instance, the flexural F(2,1), F(2,2) and F(1,3) wave form envelopes show good agreement between simulation and experiment. In addition, the longitudinal wave form L(0,1) has good agreement between simulation and experiment. However, the waves form envelopes for L(0,2), F(1,1) and F(1,2) present some disagreement between simulation and experiment. The highest wave contribution is observed at F(1,2) for simulation and in F(1,3) for experiment. It is noted, that now using the radial, circumferential and Hilbert transform in axial component, the wave decomposition is able to identify the contribution of individual waves with similar harmonic order around the surface, instead of the family of waves like the method presented by Hayashi and Catton et al. [57], [59]. For example, with using this Hilbert transform in the axial component, it is possible to obtain the contribution of F(1,1), F(1,2), F(1,3) F(2,1) and F(2,2). Before, without Hilbert transform, it was not possible to obtain the contribution of each wave. It should be noted that the number of excited waves increases, when the bar diameter and excitation frequency increase. Finally, in the experiment, the transmitter is not purely compressional, so a contribution due to shear in the circumferential direction can excite a very small T(0,1) wave as well.

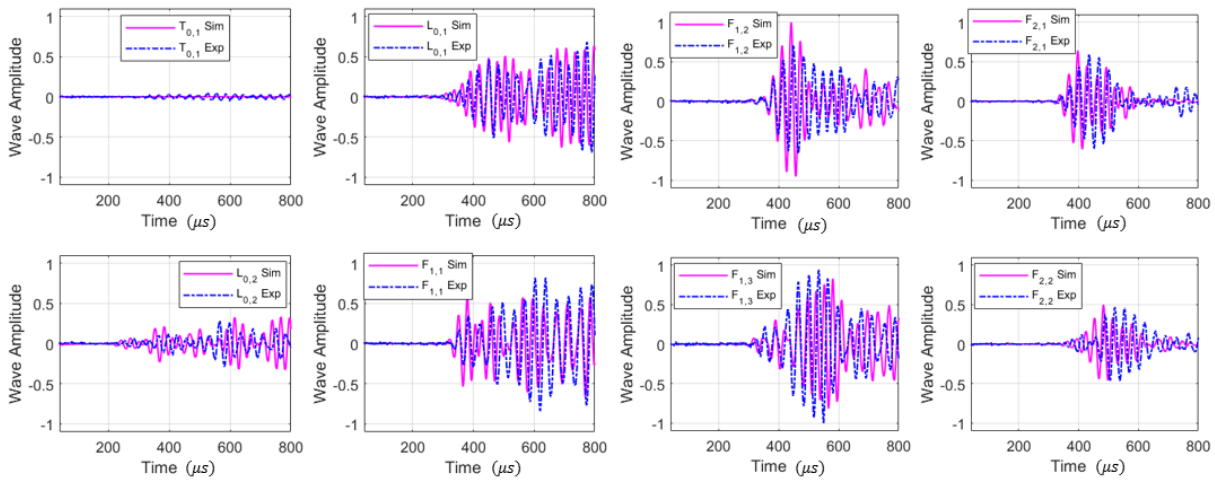

Figure 7-26 Wave decomposition for simulation and experiment in case D (using all components)

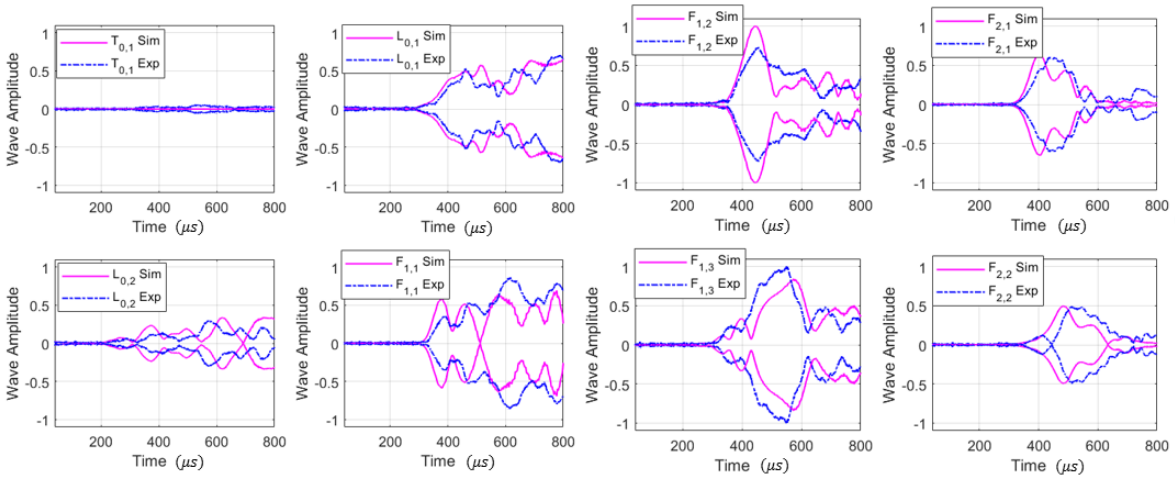

Figure 7-27 Envelope of wave decomposition for simulation and experiment in case D (using all components)

7.6.4 Experimental results of wave decomposition in case E for chain link of large diameter

Figure 7-28 shows the wave decomposition comparison for case E, when the transverse excitation is applied at the outer surface in straight part of chain. Figure 7-29 shows the envelope of each wave decomposition for simulation and experiment. L(0,1) L(0,2) and F(1,1) show good agreement in the wave forms and the wave amplitudes. However, F(1,2) and F(1,3) presents a large discrepancy in the wave amplitude and wave form. In addition, F(2,1) and F(2,2) have a discrepancy between simulation and experiments. The discrepancy could be due to the imperfections on the surface and slight reductions in diameter of the chain. These types of imperfections could produce two pulse like in F(1,2). The link used for the testing has been in-service in an offshore oil installation. In this case, F(1,2) is the highest wave amplitude in both simulation and experiment.

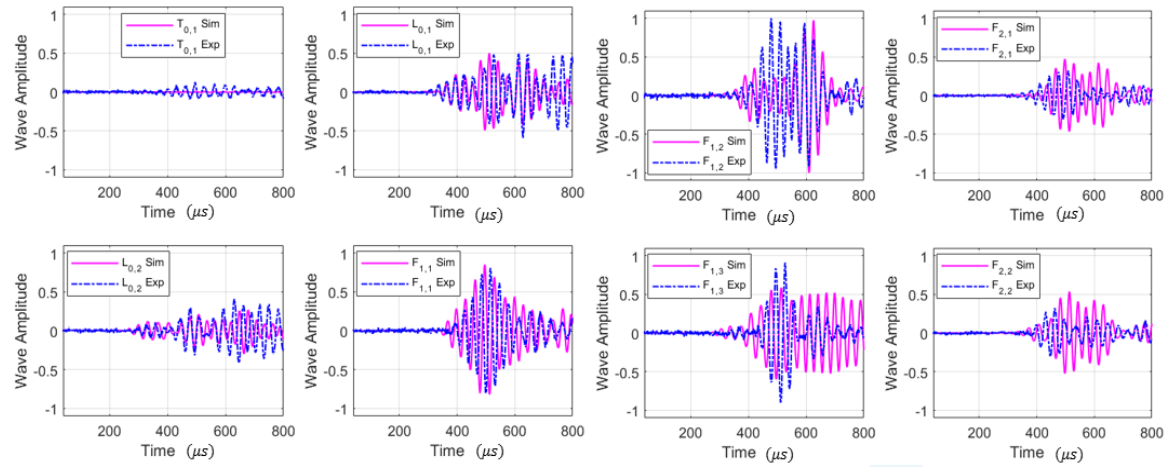

Figure 7-28 Wave decomposition for simulation and experiment in case E (using all components)

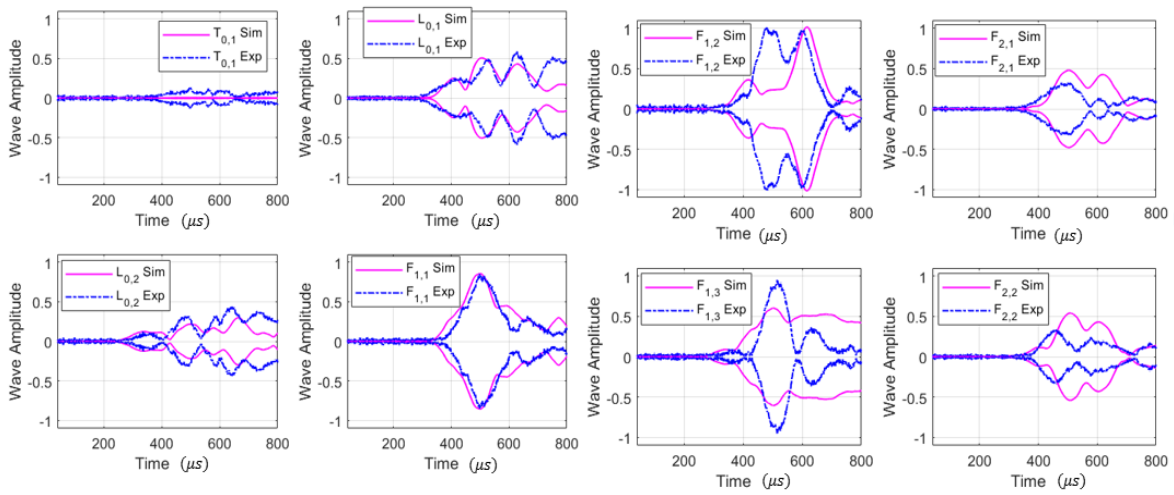

Figure 7-29 Envelope of wave decomposition for simulation and experiment in case E (using all components)

7.6.5 Experimental results of wave decomposition in case F for chain link of large diameter

Figure 7-30 shows the wave decomposition for case F, when the excitation is applied at the bend of the chain. Figure 7-31 shows the envelope of each wave decomposition for simulation and experiment. In this case F, as the receivers distance is shorter than case D, it can be observed that the waves arrive at around 200 μs instead of 400 μs. In addition, better agreement is observed between simulation and experiments for F(1,2), F(1,3), F(2,1), F(2,2). This could be because for shorter distances from exciter and receiver, lower dispersion is obtained. In addition, the better agreement could be because the wave propagation is only around half bend. For case F, F(1,3) is the highest wave amplitude in experiment and simulation. This knowledge could be used to deduce information about the location of the source of wave excitation. It should be noted that Acoustic Emission testing is a passive technique and has only receivers for detecting AE cracks. This means that this wave decomposition could estimate the possible crack location. However, experimental work with Pencil Lead Break (PLB) to simulate AE from a crack should be carried out to validate it.

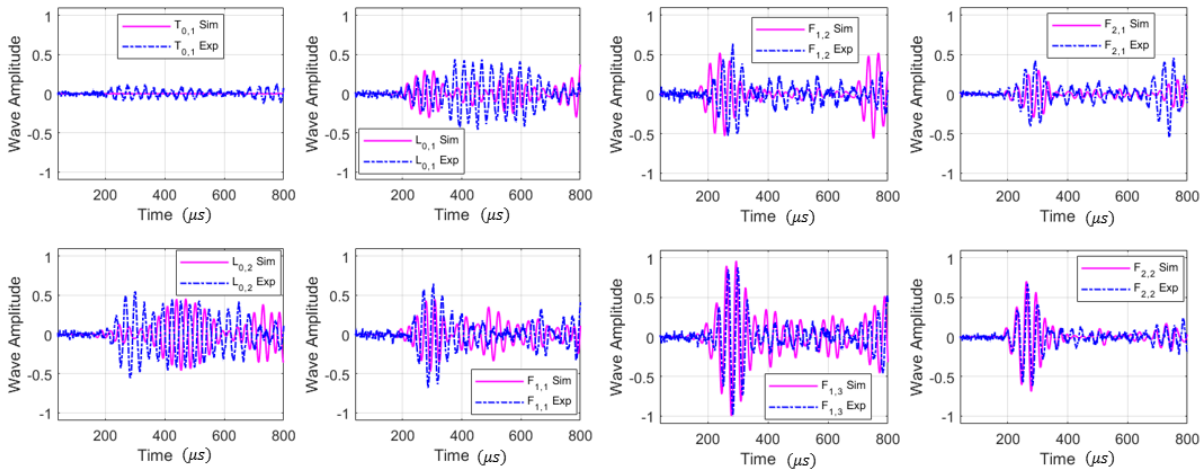

Figure 7-30 Wave decomposition for simulation and experiment in case F (using all components)

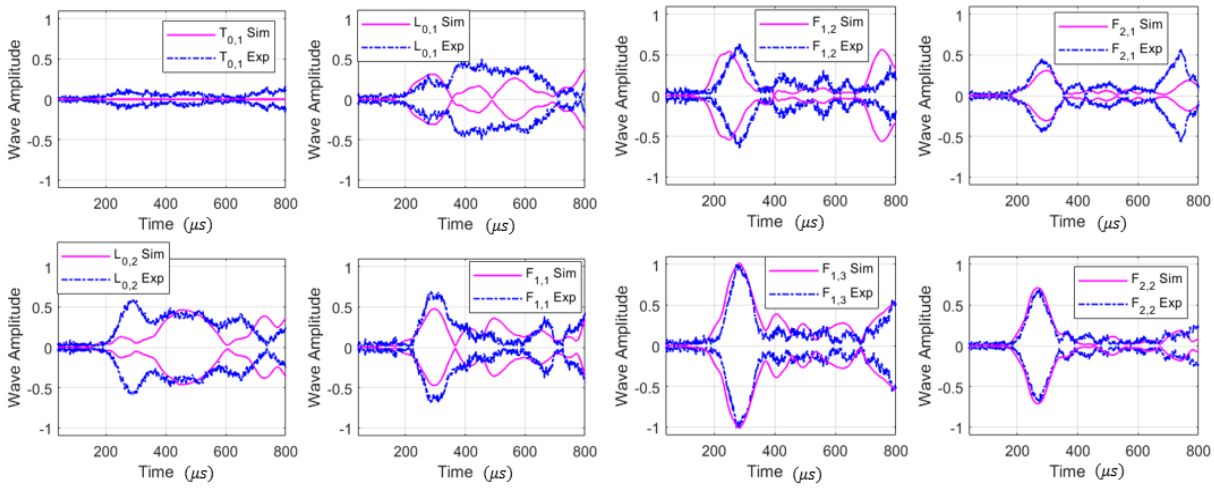

Figure 7-31 Envelope of wave decomposition for simulation and experiment in case F (using all components)

7.6.6 Discrepancies between simulation and experiments

Some discrepancies were observed between the simulations and the experiments. For example, in simulation of axial excitation, flexural waves are not excited. However, in the experiments, some contribution of flexural waves were obtained, the simple reason is that the exciter is not pure compression, this means that the transducer could excite the Hann-Window pulse in normal direction to the surface but with a slightly excitation in parallel surface as well. Another difference observed between simulations and experiments is that the amplitude in some waves are different. It should be considered that the simulation considered the receivers as broadband sensors with the same gain. However, in the experiments, the receiver sensors can be broadband sensor but with linear frequency gain as Figure 7-22. In addition, the two different sensors used to do the wave decomposition during the experiments can be a reason for discrepancy with simulation. One sensor is compressional and the other shear, this mean that the sensors are

complex systems and difficult to manufacture to obtain the same frequency response. Slight differences in construction between two nominally identical sensors can cause a different characteristic frequency response, whereby different amplitudes are received over a frequency range. Moreover, an extra reason of the discrepancy between simulation and experiment can be the variation in coupling conditions between the transducer and the specimen. The ability of transducer to vibrate the surface of a specimen is dependent on the contact area and the normal force. The contact area should be uniform for transducers and for all sensors. However, it is possible that some way not lie perfectly perpendicular to the surface. This may lead to contact along line instead of over an area, greatly reducing the traction. In addition, the force applied to each receiver may also vary if it is not perpendicular to the specimen surface. For example, to record the measurements with only two sensors. It was necessary to repeat the test twelve time to be able to obtain the signals every 90 degrees in radial, circumferential and axial direction. This means that operator error can add noise to the measurements. No matter how advanced is the equipment, one must always be aware that its operator is fallible and make mistake.

On the other hand, the material properties can be other reason of the discrepancy between simulations and experiments. In simulation, the material was selected as steel, which has some specific properties like density, Elastic Young's modulus and Poisson's ratio. However, in the experiments, the material was also steel but the chain is not within the elastic region because the chain was used in offshore field, and a proof loading was applied to the chain before it can be in service, getting that the chain can reach plastic region to increase its service life. Ideally, a measurements of material properties should be conducted before any test are carried out on a specimen. Finally, the last reason of the discrepancies is the variation in the specimen geometry. In simulation is considered to have a perfect geometry. However, when laboratory specimen are used following similar dimensions like simulation, it is likely that there will be a variation or irregularity in geometry. Specimen geometry is a key variable in the propagation of guided waves, and so small changes such as these can cause significant, unpredictable effects. For example, the link is not a perfect geometry because as the chain was in service, some reduced diameter can be observed in the bends, which were generated due to the surface contact between links. A new chain or rod with a very fine surface finish is likely to behave differently from a heavily used chain, as the surface roughness will cause more scatter.

7.7 The propagation of simulated acoustic emission waves

The acoustic emissions (AEs) caused by fatigue phenomena concentrated in particular locations of the link, are carried out by a number of elastic waves. The AEs caused by moving dislocations are complex dynamic phenomena, which are associated with cracks, loading cycles and fatigue load in a rod or chain. The generation of realistic AEs waves requires the application of cyclic loads in laboratory or industrial environment to induce cracks in a chain. As an alternative, the pencil lead break (PLB) has been used to excited AEs waves as possible crack source [48]. It is a robust and generalizable way to assess the propagation of simulated AEs. The application of the PLB technique to a structure, corresponds to the application of a concentrated transient load, which is presented in Figure 7-32. Figure 7-32 shows the time and frequency pulse of a transient load to excite the propagation of simulated AEs. The excitation is a Gaussian pulse function with a width pulse around 10 μs, which is defined in chapter four. The bandwidth of the transient pulse is very wide and extends over 200 kHz.

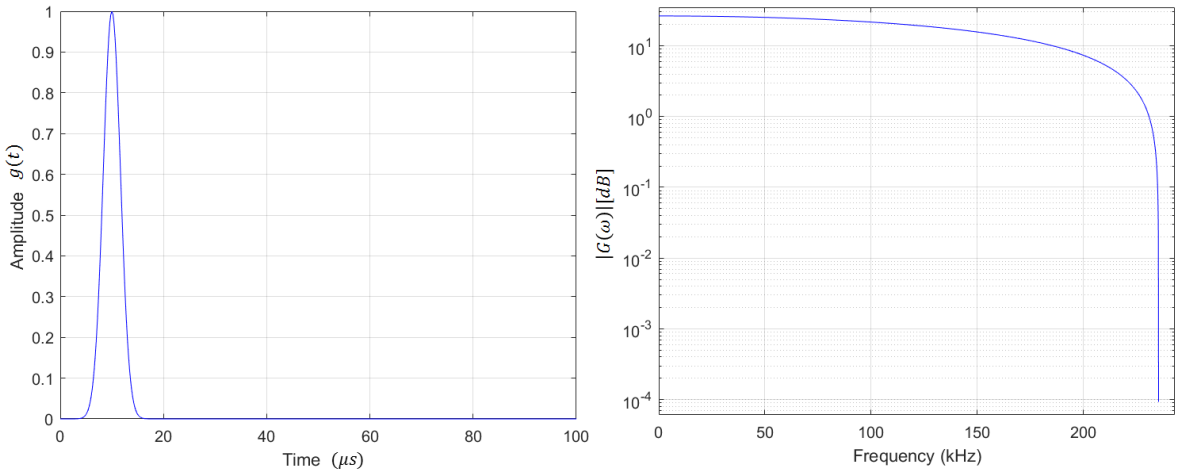

Figure 7-32 Transient pulse to excite AE propagation: Excitation pulse (left), Excitation spectrum (right)

Figure 7-33 presents the four cases of study to simulate AEs waves in a rod and chain. Applying a concentrated load to a certain point of the rod and chain is considered. The case A is the axial excitation in the rod, the case B is the transverse excitation in the rod. According to Bastid et al. [14] the cracks are generated in the bend part of the chain. Therefore, the point load was considered in the bend part of the chain for extrados (case F) and intrados (case G) excitation.

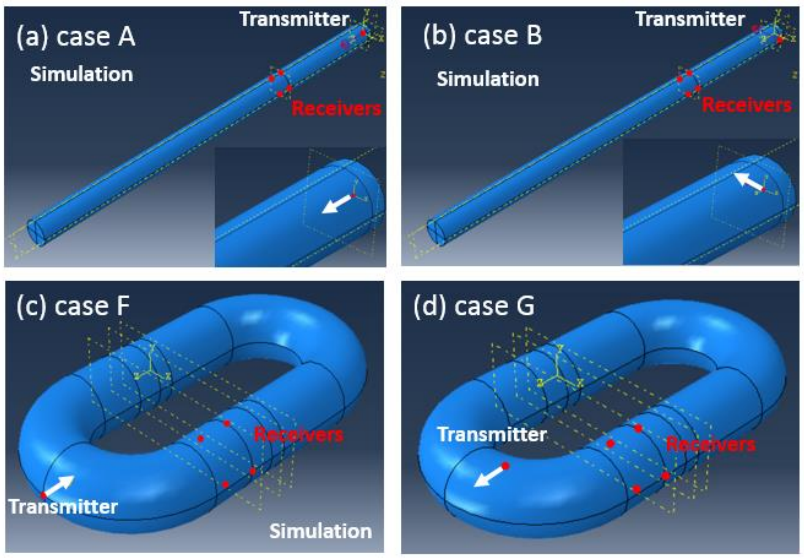

Figure 7-33 Simulation cases to excite AE propagation in a rod and chain link

Figure 7-34 shows the wave decomposition respond from the transient load in a rod. It should be noted that for case A, only the longitudinal waves L(0,1) and L(0,2) are excited as it was expected. For case B, only the flexural waves F(1,2), F(1,2) and F(1,3) of one harmonic are excited because the excitation is done at the centre of the rod.

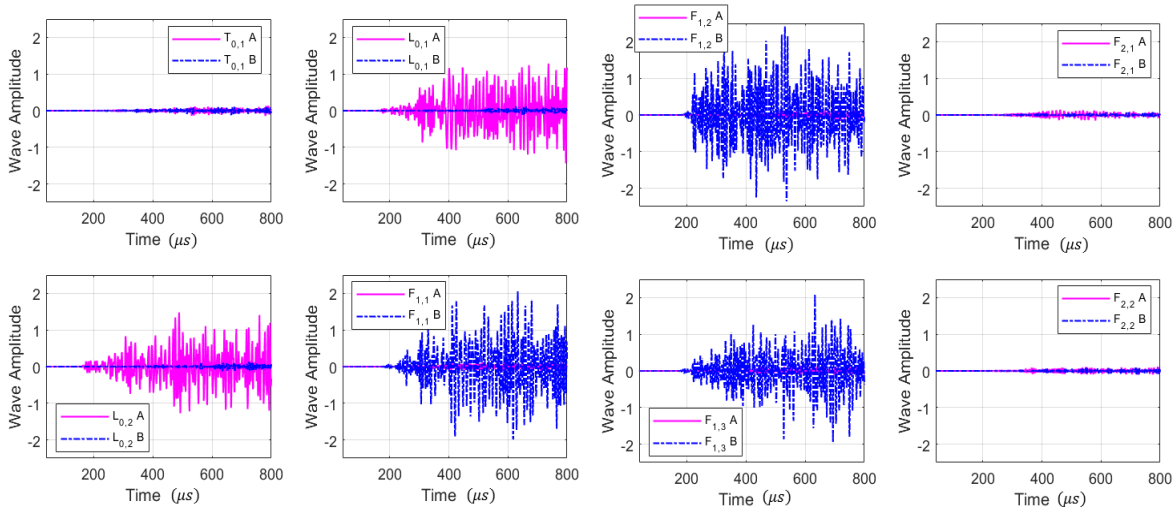

Figure 7-34 Wave decomposition for simulation cases A and B in the rod (using all components)

Figure 7-35 shows the wave decomposition in a chain, when the transient load is applied at the bend. Comparing the wave decomposition between the rod and chain, it can be observed that for the chain, all the waves are excited. It is hard to identify the wave amplitude of the highest contribution. However, it can be estimated that the highest wave amplitude between 200 μs and 300 μs could be in F(1,2) and F(1,3) when the excitation is applied in the extrados of the bend (case F). This comparison between rod and chain shows that the chain is a complex structure to

identity the wave amplitude of the highest contribution. However, the wave decomposition in time domain could be helpful to reduce the reflections and obtain the AE features in each wave.

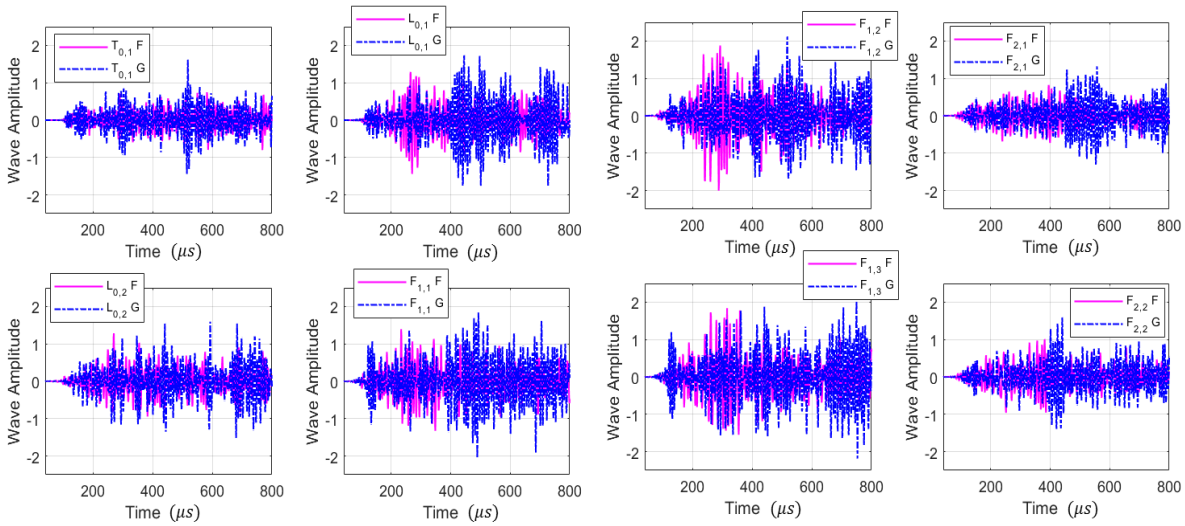

Figure 7-35 Wave decomposition for simulation cases F and G in the chain (using all components)

Unfortunately, it was not possible to do experimental work for this wave decomposition to represent a crack or AE source (PLB) excitation. The main reason is that the PLB test cannot be repeated twelve times such as previous test, where the Hann-window was excited every time. In this case, it is necessary to record the twelve signals (radial, circumferential and axial every 90 degrees) at the same time because the same pencil lead break cannot be excited twelve time exactly. Therefore, for future work, it should be considered to use three axes sensors with similar frequency response, which can provide the twelve measurements at the same time. However, now at day, suppliers can produce only three axes accelerometer for a frequency up to 10 kHz. This means that it is difficult to find three axes sensors working in high frequency. There is only normal surface uniaxial sensors working in high frequency like the ones used in chapter six. However, using only radial component, it is not possible to know the contribution of each individual wave during the wave decomposition. In addition, it should be noted that this wave decomposition methodology can be implemented only in laboratory to carry out wave decomposition study to know the impact of the bent in a link. It is unpractical to install sensors in each link of the mooring line because the additional weight of the sensors could have an impact in the mooring line and it will have a high cost in field.

7.8 Conclusions

A new wave decomposition methodology in the time domain was presented for a cylindrical steel bar, bent bar and a mooring link of large diameter. The wave decomposition was done in specimens of large diameter because this research project is looking to have an impact in the industry, where the mooring chain of large diameter are used by offshore industry. Moreover, the wave decomposition in time domain is the best option to reduce the multiple reflections from bends so that only the first incident waves can be considered. The following conclusions were drawn:

- A comparison of wave decomposition between straight bar, bent bar and link was carried out. It was observed that the complex geometry with bends have a high impact in dispersion and mode conversion waves.
- For axial excitation case, the longitudinal waves were excited only in the straight bar, where the highest contribution was obtained from L(0,1). However, in the bent bar time shifts, wave conversions and dispersion were observed. In fact, it was for the link, that the scattering was the highest. The main reason of this scattering is that longitudinal waves, were converted to flexural waves in the bent bar and chain.
- For transversal excitation case, similar behaviour of wave mode conversion was obtained in bent bar and a chain. However for this case, the flexural waves were converted to longitudinal waves. It can be considered that without any knowledge of this, there is greater potential for false interpretation of inspection results beyond bend. However, it is still possible to obtain the highest contribution in flexural wave for transversal excitation.
- A method has been suggested, which can be used to predict the behaviour of guided waves beyond bends. The wave decomposition was successfully validated against experiments, where good agreements were obtained between simulations and experimental works for most cases. The discrepancies observed are most likely due to variations in transducer coupling and the geometry of the bar and the chain.
- Experimentally validated finite modelling has been used to show that although the incident wave mode can be made to pass through a bar bend and a chain, mode conversion occurs and the wave modes are often altered.

It has been shown that the wave decomposition methodology in the time domain has the potential to get excitation localisation in a link, where the individual wave with the highest contribution is obtained according to the excitation location. Therefore, opening up the possibility of using wave decomposition to detect flaws in a link and implement this methodology for structural health monitoring on mooring chain.

Chapter 8: Conclusions and future work

8.1 Conclusions

The implementation of Acoustic Emission Technique (AET) has been investigated for structural health monitoring in different structures for many years. However, few researchers have used AET for structural health monitoring of a link. The main reason is the complex geometry in a chain, and the difficulty in separating the elastic waves in the superposition of AE signals. In the literature, researchers have tended to the AE features to monitor crack growth in different specimens, where only the main AE features in an AE signal, such as cumulative energy and cumulative counts have been used to measure crack growth. However, in the literature review the researches have been done in small specimens over short test terms, where the AE signals from cracks are mixed with noise signals, and the interpretation of crack growth can be misunderstood.

That being the case, in this thesis, a long term chain tensile test was carried out to monitor Stress Corrosion Cracking (SCC). During this long term test, it can be concluded that all the AE features have the potential to be used to monitor different stages of SCC. For example, two groups with similar curve trends are found, the first group is integrated by the cumulative AE features of rise time, hits and peak amplitudes. The second group, with similar curve trends, is formed by the cumulative of energy, counts and durations of the AE signals. It should be noted that the trend curves of the two groups was observed only for 45 dB and 55 dB filters. However, the 65 dB filter shows that the first group (cumulative: hits, rise time, peak amplitude) can be used to know when the crack is growing fast or slowly, and the noise level of the environment can be discriminated easily due to the high number of events generated during the SCC propagation. To the contrary, the second group (cumulative: count, duration and energy) of the 65 dB filter, can be used to show the time of crack extensions. Moreover, plotting energy of each event instead of cumulative energy, similar behaviour of crack extension is obtained in 45 dB and 65 dB filters. It can be concluded that for future chain tensile tests, it is enough to have a 65 dB filter to monitor SCC. From the chain tensile test evidence it is, in essence, achievable to monitor SCC growth with acoustic emission technique. Moreover, this study proved that AE is a powerful tool for continuous monitoring.

On the other hand, coming back to the complex geometry of the chain, it should be noted that the AE monitoring was carried out in the straight part of the chain. However, the cracks are often produced in the bend of the chain. At the beginning of this research work, the initial aim was to identify the type of elastic waves that may transmit AE from cracks in a chain. However, the crack

or Pencil Lead Break (PLB) sources used to simulate cracks, excite a broadband spectrum, in which a high order number of waves is excited. This makes, more complex to understand the physics behind the AE propagation from crack. Therefore, to provide insight into the application of the AE technique, research was carried out to analyse and understand the physics of excited waves in a bar, bar with a bend and chain.

To understand the effect of the bends in a chain on the waves, first a harmonic analysis was carried out. An approach to do wave decomposition in frequency domain was introduced. It was shown that in a straight bar of radius 80 mm, the fundamental theory was not suit to understanding the contribution of the wave at a frequency up to 10 kHz. Instead, finite element analysis was necessary to know the contribution of multiple waves in high frequency. Using perfectly matched layers to avoid reflection, it was possible to obtain the contribution of the longitudinal incident waves during axial excitation, and the contribution of the flexural incident wave during transverse excitation in a bar. However, in a bar with bend, during axial excitation, wave oscillation and wave modes conversion were obtained, where axisymmetric waves were converted to antisymmetric waves, but the highest wave amplitude contribution is still in the axisymmetric wave. To the contrary during transverse excitation, the antisymmetric waves were converted to axisymmetric waves, but the highest wave contribution is kept in the converted wave in the frequency range up to 30 kHz.

In the real world, the boundary conditions of a structure should be considered. Therefore, the wave decomposition in a full chain without PML was considered. However, during axial and transversal excitation in the straight part of the chain, many resonance peaks of the wave amplitudes were obtained, due to the multiple reflections from the bends and the superposition of incident and reflected waves. For that reason, a wave decomposition in time domain was carried out to reduce the reflections. However, first the wave decomposition was carried out in a long rod of smaller diameter than the large diameter like the chain. The transient Gaussian modulated sinusoidal excitation was considered instead of harmonic excitation to narrow the excitation frequency and reduce the number of excited waves. The wave decomposition method in time domain was able to identify the wave with the highest contribution in each scenario of loading condition. Only the longitudinal wave was excited during axial excitation, and only torsional waves for rotation excitation. However, the flexural wave F(1,2) have the highest wave amplitude for transverse excitation at the centre of the free end face, and F(1,1) for the case of transverse excitation on the outer surface of the rod. Considering the three components (radial, circumferential and axial), the wave decomposition method has the potential to identify whether the excitation source is internal or external in the rod, providing information about location excitation. This method is able to get the highest contribution arising from axial, shear or bending

forces. Moreover, the minimum number of sensors to capture the contribution of each wave of n order should be 2^n, this was confirmed with simulation and experimental work. In addition, using only radial component, the wave decomposition can get the superposition of the family waves to describe what type of excitation is applied in-plane or out-of-plane, but it cannot provide information about excitation location. Similar behaviour can be obtained during PLB using only radial component as the experiments shown, where the AE features can be extracted to be plotted as cumulative, and describe whether the excitation is due to tensile or bending forces, potentially providing information about the type of excited wave for structural health monitoring of cylindrical bar.

It is important to note that to have an impact in the industry, the wave decomposition was carried out in long bar, bend bar and chain of large diameter, where the number of excited wave is higher than in small diameter. Thanks to the Hilbert transform in the axial component, it was possible to get the wave contribution of each wave with higher order. The ultimate aim is to apply the wave decomposition on the chain to reduce the reflections from the bends. During the wave decomposition comparison between the bar, bent bar and chain, it was concluded that the bends have a high impact in the arrival time of the pulse, dispersion and mode conversion wave. For axial excitation, only longitudinal waves were excited in straight bar, but in the bent bar and chain, axisymmetric waves were converted to antisymmetric waves and vice versa. Moreover, the wave decomposition method was validated with experimental work. Good agreements were obtained between simulation and experimental work in the straight bar, and few discrepancies in the chain. It should be noted that this method can estimate the wave decomposition for only a specific frequency, and no broadband frequency. The method can still be a good approach to extract the contribution of each wave during broadband excitation from cracks source or PLB in laboratory tests. However, it should be noted that to obtain the contribution of individual wave, it is mandatory to use three axes sensors with similar frequency response. Now at day, there is not three axes sensors available, which can work in high frequency. In fact, it could be impractical to attach twelve sensors on a mooring chain. Therefore, it is recommended to start using this methodology for laboratory test. Later, for future work, it is open to explore the possibility to implement this methodology for structural health monitoring on mooring chains. However, at this moment, for crack growth monitoring in the field, it is recommended to use only one compressional sensor in each chain to monitor cracks growth in a mooring line.

8.2 Future work

Using wave decomposition to detect flaws in a chain and implement this methodology for structural health monitoring on a mooring chain, suggestions for further research are proposed.

(i) Wave decomposition for broadband frequency excitation

So far, the wave decomposition in time domain was estimated for only a specific frequency. However, the spectrum from a crack or PLB transient pulse can be broadband (see Figure 7-32). In fact, the spectrum excitation of the Gaussian modulated sinusoidal used in previous chapters, is observed between 10 kHz and 50 kHz, as shown in Figure 8-1. Therefore, a wave decomposition in a range of the frequency should be done every delta frequency.

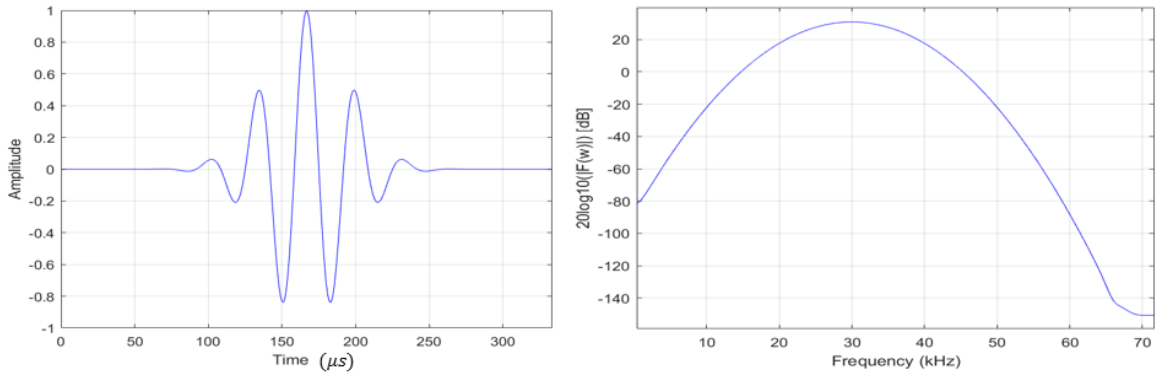

Figure 8-1 Gaussian modulated sinusoidal function (left) and its spectrum (right)

As a focus for future work equation 8.1 is presented, where the nodal acceleration matrix $\mathbf{N}(\omega)$ is obtained, applying a Fast Fourier transform to the transient time response of nodal accelerations of the matrix $\mathbf{N}(t)$. The wave mode shape $\mathbf{Q}(\omega)$ matrix and its pseudo inverse can be calculated every delta frequency to obtain the wave amplitudes $\mathbf{A}(\omega)$. Then, an inverse Fourier transform can be implemented in the wave amplitude vector to get the time response.

$$[\mathbf{A}(\omega)] = [\mathbf{Q}(\omega)]^{+}[\mathbf{N}(\omega)] \tag{8.1}$$

Figure 8-2 and 8-3 show the wave decomposition for a bar and a bent bar, using the proposed equation with a delta frequency of 1 kHz. The comparison between straight bar and bent bar can

be observed at z=0 m (waves go in) and z=0.9 m (waves go out), where the z-axis is along the axis of the rod and bent rod. However, future analysis interpretation and experimental work should be carried out to validate this approach.

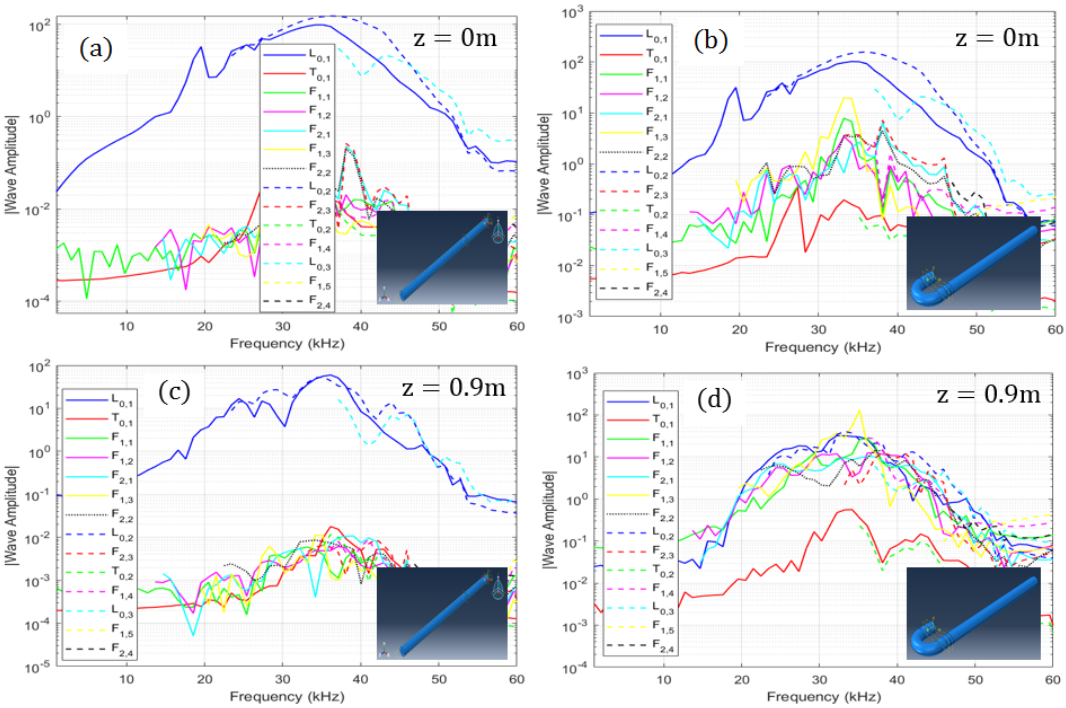

Figure 8-2 Wave decomposition in frequency domain for cases A (axial excitation): (a) Waves in a rod at 0 m, (b) Waves in a bent rod at 0 m, (c) Waves in a rod at 0.9 m, (d) Waves in a bent rod at 0.9 m

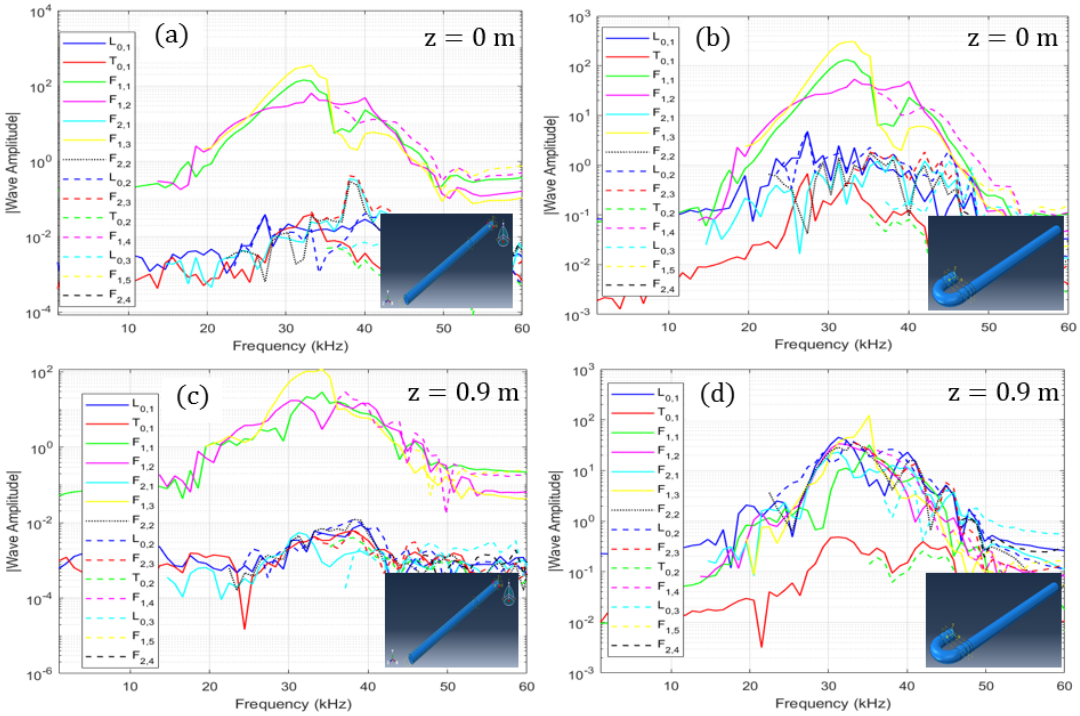

Figure 8-3 Wave decomposition in frequency domain for cases B (transversal excitation): (a) Waves in a rod at 0m, (b) Waves in a bent rod at 0 m, (c) Waves in a rod at 0.9 m, (d) Waves in a bent rod at 0.9 m

(ii) Reflection and transmission coefficients in a chain

Transmission and reflection coefficients can be one way to characterise the bend in a chain. This wave decomposition methodology can be a starting point for obtaining them. The transmission $T_{I,S}$ and reflection $R_{I,S}$ coefficients require a knowledge of the scattered wave amplitude in positive and negative direction after the bend. In addition, it is necessary to Figure out a way to excite only one incident wave instead of exciting all waves at the same time.

$$T_{I,S} = \frac{A_S{}^{+}}{A_I} \qquad R_{I,S} = \frac{A_S{}^{-}}{A_I} \tag{8.2}$$

However, a transmission ration T_R coefficient could be estimated from each incident wave in a frequency range with this wave decomposition method, knowing the wave amplitude of each incident wave A_I and the wave amplitude of the scattered waves A_S after the bend.

$$T_R = \frac{A_S}{A_I} \tag{8.3}$$

Figure 8-4 shows the transmission ratio coefficient for axial excitation, where the ratio is calculated for incident wave L(0,1) and L(0,2) for a bar and a bent bar. However, future analysis interpretation should be done to validate this results.

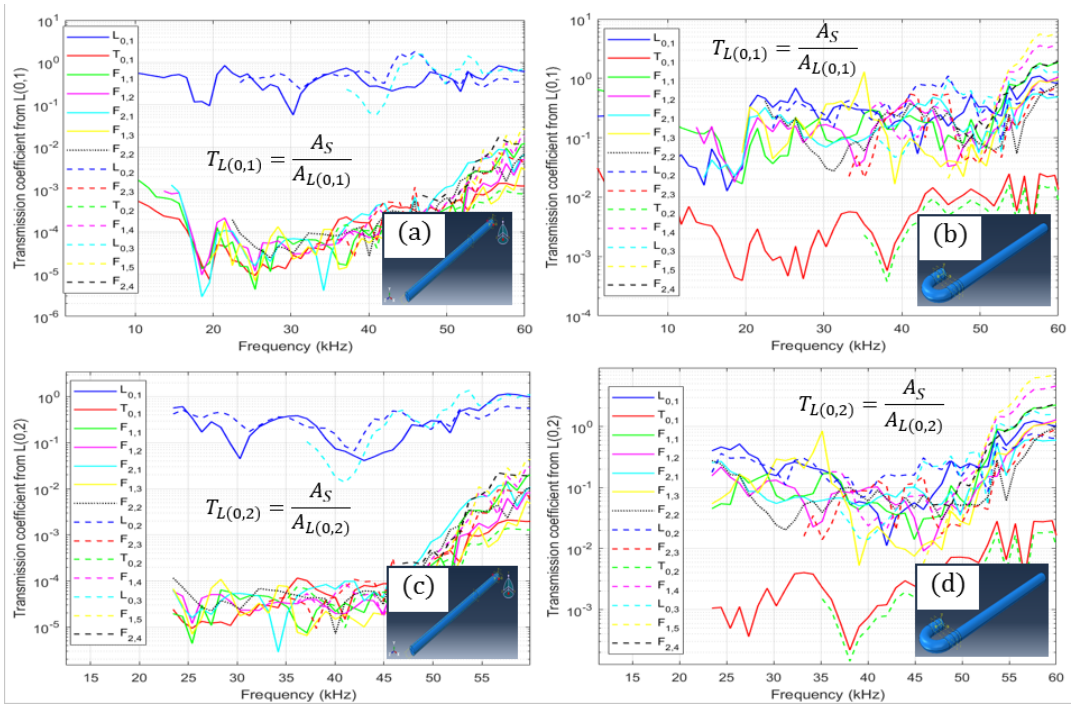

Figure 8-4 Transmission ratio coefficient for cases A (axial excitation): (a) $T_{L(0,1)}$ in a rod, (b) $T_{L(0,1)}$ in a bent rod, (c) $T_{L(0,2)}$ in a rod, (d) $T_{L(0,2)}$ in a bent rod

(iii) Wave decomposition in multiple links

The wave decomposition method in time and frequency domain should be implemented in multiple links to research what types of waves are transmitted between the links and to know the attenuation and possible wave modes conversion. Moreover, further modelling and experimental work should be considered to obtain the wave responses from more realistic crack sources or PLB.

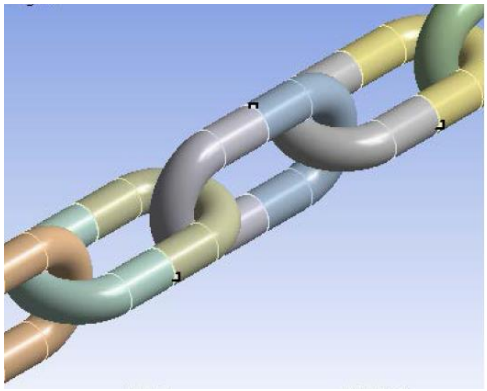

Figure 8-5 Multiple links [110]

(iv) Fatigue test using Acoustic Emission Technique

Mooring chain lines are subject to environmental forces such as ocean waves and currents. These types of load can produce a fatigue damage in one or more links. Acoustic emission waves are generated not only from cracks, but also from other sources, such as friction between the links, impact and environmental noise. These extra sources add noise affecting a good interpretation of signals from fatigue cracks. Therefore, for better representation of a mooring line, AET during a fatigue test, using a rig similar to the one in Figure 8.5 should be implemented to research whether the noise signals can be discriminated as they were in the long term static tensile test carried out in this thesis.

Figure 8-6 Fatigue chain tensile test

References

[1] Offshore Standard Report DNVGL-OS-E302, “Offshore Mooring Chain,” Oslo, Norway, 2015.

[2] Noble Denton Europe Limited for the Health and Safety, “Research report of floating production system, JIP FPS mooring integrity,” Bootle, U.K., 2006.

[3] I. Ridge, P. Smedley, and R. Hobbs, “Effects of twist on chain strength and fatigue performance: small scale test results,” in *In ASME 2011 30th International Conference on Ocean, Offshore and Arctic Engineering*, 2011, pp. 183–189.

[4] M. Dissanayake *et al.*, “Automated Application of Full Matrix Capture to Assess the Structural Integrity of Mooring Chains,” *IEEE Access J.*, vol. 6, pp. 75560–75571, 2018.

[5] A. Lee, F. B. Stanley, E. VanDerHorn, and G. Wang, “Structural Health Monitoring on Mooring Chain using Acoustic Emission Testing,” in *Proceeding of the PRADS2013, CECO*, 2013.

[6] F. G. Rivera, G. Edwards, E. Eren, and S. Soua, “Acoustic emission technique to monitor crack growth in a mooring chain,” *J. Appl. Acoust.*, vol. 139, pp. 156–164, 2018.

[7] Y. W. Kai-Tung Ma, Yong Luo, Thomas Kwan, “Mooring System Engineering for Offshore Structures,” Y. W. Kai-Tung Ma, Yong Luo, Thomas Kwan, Ed. Gulf Professional Publishing, 2019, pp. 19–39.

[8] D. Fontaine, E.; Kilner, A.; Carra, C.; Washington, “Industry Survey of Past Failures, Pre-emptive Replacements and Reported Degradations for Mooring Systems of Floating Production Units,” in *Offshore Technology Conference*, 2014.

[9] T. M. Roberts and M. Talebzadeh, “Acoustic emission monitoring of fatigue crack propagation,” *J. Constr. Steel Res.*, vol. 59, no. 6, pp. 695–712, 2003.

[10] C. T. Jin and Z.-H. Sun, *Fractures mechanics*. Academic Press, 2012.

[11] J. W. Frank Fahy, *Advanced Applications in Acoustics, Noise and Vibration*. London: Spon Press, 2004.

[12] H. Towsyfyan, A. Biguri, R. Boardman, and T. Blumensath, “Successes and challenges in non-destructive testing of aircraft composite structures,” *Chinese J. Aeronaut.*, pp. 1–21, 2019.

References

[13] Vallen Systeme GmbH, “Vallen AMSY-6 Handbook, System Description.,” Germany, 2015.

[14] P. Bastid and S. D. Smith, “Numerical analysis of contact stresses between mooirng chain links and potential consequences for fatigue damage,” in *OMAE 2013 TWI Ltd*, 2013.

[15] Offshore Standard Report DNVGL-OS-E301, “Position Mooring,” Oslo, Norway, 2015.

[16] Z. Han, H. Luo, C. Sun, J. Li, M. Papaelias, and C. Davis, “Acoustic emission study of fatigue crack propagation in extruded AZ31 magnesium alloy,” *J. Mater. Sci. Eng. A*, vol. 597, pp. 270–278, 2014.

[17] H. Chang, E. Han, J. Q. Wang, and W. KE, “Acoustic emission study of corrosion fatigue crack propagation mechanism for LY12CZ and 7075-T6 aluminium alloys,” *J. Mater. Sci.*, vol. 40, pp. 5669–5674, 2005.

[18] A. Lee, G. Wang, S. Ternowchek, and F. B. Stanley, “Structural Health Monitoring on Mooring on Ships Using Acoustic Emission Testing,” in *Proceeding of the PRADS2013, CECO*, 2013.

[19] R. M. Sanderson, D. A. Hutchins, D. R. Billson, and P. J. Mudge, “The investigation of guided wave propagation around a pipe bend using an analytical modeling approach,” *J. Acoust. Soc. Am.*, vol. 133, no. 3, pp. 1404–1414, 2013.

[20] T. H. Courtney, *Mechanical behavior of materials*, Second Edi. Waveland Press, INC, 2005.

[21] V. M. Karbhari, *Non-Destructive Evaluation of Polymer Matrix Composites*. University of Texas at Arlington, USA: Woodhead Publising Limited, 2013.

[22] R. B. Thompson, “NDE Simulations: Critical tools in the integration of NDE and SHM,” in *Proceedings of SPIE, Vol. 7294*, 2009, p. 729402.

[23] D.S.Forsyth, “Corrosion Control in the Aerospace Industry,” S. Benavides, Ed. Austin, USA: Woodhead Publishing Series in Metals and Surface Engineering, 2009, pp. 111–130.

[24] Z. D. Wang, Y. Gu, and Y. S. Wang, “A review of three magnetic NDT technologies,” *J. Magn. Magn. Mater.*, vol. 324, pp. 382–388, 2012.

[25] A. Mazzinghi, A. Freni, and L. Capineri, “A microwave non-destructive testing method for controlling polymeric coating of metal layers in industrial products,” *NDT E Int.*, vol. 102, no. November 2018, pp. 207–217, 2019.

[26] M. Seleznev, A. Weidner, H. Biermann, and A. Vinogradov, “Novel method for in situ

damage monitoring during ultrasonic fatigue testing by the advanced acoustic emission technique," *Int. J. Fatigue*, vol. 142, no. July 2020, p. 105918, 2021.

[27] J. Xu, X. Wu, and E. H. Han, "Acoustic emission during pitting corrosion of 304 stainless steel," *J. Corros. Sci.*, vol. 53, no. 4, pp. 1537–1546, 2011.

[28] R. K. Miller, *Nondestructive Testing Handbook*. Columbus, OH: American Society for Nondestructive Testing, 1987.

[29] M. Chai, J. Zhang, Z. Zhang, Q. Duan, and G. Cheng, "Acoustic emission studies for characterization of fatigue crack growth in 316LN stainless steel and welds," *J. Appl. Acoust.*, vol. 126, pp. 101–113, 2017.

[30] V. Smanio, M. Fregonese, T. Cassagne, B. Normand, and F. Ropital, "Acoustic Emission Monitoring of Wet H2S Cracking of Linepipe Steels," *J. Corros.*, vol. 67, no. 6, pp. 1–12, 2011.

[31] W. Hwang, S. Bae, J. Kim, S. Kang, N. Kwag, and B. Lee, "Acoustic emission characteristics of stress corrosion cracks in a type 304 stainless steel tube," *J. Nucl. Eng. Technol.*, vol. 47, no. 4, pp. 454–460, 2015.

[32] W. Mao and I. Towhata, "Monitoring of single-particle fragmentation process under static loading using acoustic emission," *J. Appl. Acoust.*, vol. 94, pp. 39–45, 2015.

[33] M. N. Bassim, "Detection of Fatigue Crack propagation with acoustic emission," *J. NDT E Int.*, vol. 25, no. 6, pp. 287–289, 2012.

[34] Z. Han, H. Luo, J. Cao, and H. Wang, "Acoustic emission during fatigue crack propagation in a micro-alloyed steel and welds," *J. Mater. Sci. Eng. A*, vol. 528, no. 25–26, pp. 7751–7756, 2011.

[35] S. Yuyama, T. Kishi, and Y. Hisamatsu, "AE analysis during corrosion, stress corrosion cracking and corrosion fatigue processes," *J. Acoust. Emiss.*, vol. 2, no. 1–2, pp. 71–93, 1983.

[36] J. L. Rose, *Ultrasonic Waves in Solid Media*. Cambridge, UK: Cambridge University Press, 1999.

[37] Z. Nazarchuk, V. Skalskyi, and O. Serhiyenko, *Acoustic Emission Methodology and Aplication*. Springer, 2017.

[38] F. Seco and A. R. Jimenez, "Modelling the generation and propagation of ultrasonic signals

in cylindrical waveguides," in *Ultrasonics waves*, Intech Open Access, 2012, pp. 1–28.

[39] G. Valsamos, F. Casadei, and G. Solomos, "A numerical study of wave dispersion curves in cylindrical rods with circular cross-section," *J. Appl. Comput. Mech.*, vol. 7, pp. 99–114, 2013.

[40] D. C. Gazis, "Three-Dimensional Investigation of the Propagation of Waves in Hollow Circular Cylinders. I. Analytical Foundation," *J. Acoust. Soc. Am.*, vol. 31, no. 5, pp. 568–573, 2005.

[41] K. F. Graff, *Wave Motion in Elastic Solids*. Dover, 1991.

[42] A. Demma, "Mode conversion of longitudinal and torsional guided modes due to pipe bends," in *AIP Conference Proceeedings 557,172*, 2003, vol. 172, no. June 2001, pp. 172–179.

[43] A. Demma, "Guided waves in curved pipes," in *AIP Conference Proceedings 615*, 2003, vol. 157, no. May 2002, pp. 157–164.

[44] A. Demma, P. Cawley, M. Lowe, and B. Pavlakovic, "The effects of bends on the propagation of guided waves in pipes," *J. Press. Vessel Technol.*, vol. 127, pp. 328–335, 2005.

[45] K. Abbasi, N. H. Motlagh, M. R. Neamatollahi, and H. Hashizume, "Detection of axial crack in the bend region of a pipe by high frequency electromagnetic waves," *Int. J. Press. Vessel. Pip.*, vol. 86, no. 11, pp. 764–768, 2009.

[46] B. Verma, T. K. Mishra, K. Balasubramaniam, and P. Rajagopal, "Interaction of low-frequency axisymmetric ultrasonic guided waves with bends in pipes of arbitrary bend angle and general bend radius," *J. Ultrason.*, vol. 54, no. 3, pp. 801–808, 2014.

[47] T. Yamamoto, T. Furukawa, and H. Nishino, "Efficient defect detections of elbow pipes using propagation characteristics of guided waves," in *AIP Conference Proceedings*, 2014, vol. 1581 33, no. February, pp. 373–379.

[48] G. R. S. Markus, "Investigation of pencil lead breaks as acoustic emission sources," *J. Acoust. Emiss.*, vol. 29, pp. 184–196, 2011.

[49] G. Zarini, "Propagation and sensing of acoustic emissions in main load-bearing aircraft structures," PhD Thesis, The University of Southampton, 2015.

[50] R. N. Thurston, "Elastic waves in rods and clad rods," *J. Acoust. Soc. Am.*, vol. 64, no. 1, pp.

1–37, 2005.

[51] J. Zemanek, “An Experimental and Theoretical Investigation of Elastic Wave Propagation in a Cylinder,” *J. Acoust. Soc. Am.*, vol. 51, no. 1B, pp. 265–283, 2005.

[52] M. V. Lysak, “Development of the Theory of Acoustic Emission by Propagation Cracks in Term of Fracture Mechanics,” *J. Eng. Fract. Mech.*, vol. III, no. 55, pp. 443–452, 1996.

[53] A. Puckett, “Axially symmetric wave propagation in thick cylindrical waveguides,” PhD Thesis, The University of Maine, 2004.

[54] D. Alleyne, “Rayleigh and Lamb waves and their excitation,” PhD Thesis, Imperial College, 1987.

[55] D. Alleyne and P. Cawley, “A two-dimensional Fourier transform method for the measurement of propagating multimodes signals,” *J. Acoust. Soc. Am.*, vol. 89, no. 3, pp. 1159–1168, 1991.

[56] S. K. Pedram, A. Haig, K. T. P. S. Lowe, L. Gan, and P. Mudge, “Spllit-Spectrum Signal Processing for Reduction of the Effect of Dispersive Wave Modes in Long-range Ultrasonic Testing,” in *International Congress on Ultrasonics*, 2015.

[57] P. P. Catton, “Long range ultrasonic guided waves for the quantitative inspection of pipes lines,” PhD Thesis, Brunel University, 2009.

[58] T. Hayashi, K. Kawashima, Z. Sun, and J. L. Rose, “Analysis of flexural mode focusing by a semianalytical finite element method,” *J. Acoust. Soc. Am.*, vol. 113, no. 3, pp. 1241–1248, 2003.

[59] T. Hayashi and M. Murase, “Mode extraction technique for guided waves in a pipe,” *J. Nondestruct. Test. Eval.*, vol. 20, no. 1, pp. 63–75, 2005.

[60] S. Fateri, S. L. Premesh, E. Bhavin, and N. V. Boulgouris, “Investigation of ultrasonic gudied waves interacting with piezoelectric transducers,” *IEEE Sens. J.*, vol. 15, no. 8, pp. 4319–4328, 2015.

[61] P. Lowe, S. Fateri, R. Sanderson, and B. N. V, “Finite element modelling of interaction of ultrasonic guided waves with coupled piezoelectric transducers,” *Insight-Non-Destruct Test. Cond. Monit.*, vol. 56, no. 9, pp. 505–509, 2014.

[62] B. Hosten and M. Castings, “Finite Elements Methods for Modeling the Guided Waves Propagation in Structures with Weak Interfaces,” *J. Acoust. Soc. Am.*, vol. 117, pp. 1108–

1132, 2005.

[63] R. Sanderson and J. Gao, “The effect of pipe bend radii on guided wave propagation in small diameters pipes,” in *TWI Ltd*, 2010.

[64] R. M. Sanderson and S. D. Smith, “The application of finite element modelling to guided testing system,” *Rev. Quant. Nondestruct. Eval.*, vol. 22, pp. 256–263, 2003.

[65] R. Sanderson and P. Catton, “The reflection of guided waves from multiple flaws in pipes,” *J. Nondestruct. Eval.*, vol. 32, pp. 384–397, 2013.

[66] R. Sanderson and S. Smith, “The application of finite element modelling to guided ultrasonic waves in rails,” in *Insight-Non-Destruct Testing and Condition Monitoring*, 2002, pp. 359–363.

[67] H. Jia, M. Jing, and J. Rose, “Guided wave propagation in single and double layer hollow cylinder embedded in infinite media,” *J. Acoust. Soc. Am.*, vol. 129, no. 2, pp. 691–700, 2011.

[68] V. Damljanovic and R. L. Weaver, “Propagating and evanescent elastic wave in cylindrical waveguides of arbitrary cross section,” *J. Acoust. Soc. Am.*, vol. 115, no. 4, pp. 1572–1581, 2004.

[69] F. Karpfinger, B. Gurevich, and A. Bakulin, “Modeling of wave dispersion along cylindrical structures using the spectral method,” *J. Acoust. Soc. Am.*, vol. 124, no. 2, pp. 859–865, 2008.

[70] B. Pavlakovic and M. Lowe, “Disperse: A general purpose approach to calculating the longitudinal and flexural modes of multi-layered, embedded, transverserly isotropic cylinders.” Annual Review of Progress in Quantitative Nondestructive Evaluation, pp. 239–246, 1999.

[71] P. Bocchini, A. Marcani, and E. Viola, “Graphical user interface for guided acoustuc waves,” *J. Comput. Civ. Eng.*, vol. 25, no. 3, pp. 202–210, 2011.

[72] Y.-H. Zhang, N. Zettlemoyer, and P. J. Tuppy, “Fatigue crack growth rates of mooring chains steels,” in *Proceeding of the ASME 2012 31st International Conference on Ocean*, 2012.

[73] I. Bashir, J. Walsh, P. R. Thies, S. D. Weller, P. Blondel, and L. Johanning, “Underwater acoustic emission monitoring – Experimental investigations and acoustic signature recognition of synthetic mooring ropes,” *J. Appl. Acoust.*, vol. 121, pp. 95–103, 2017.

[74] T. Shiotani, “Evaluation of long-term stability for rock slope by means of acoustic emission technique,” *J. NDT E Int.*, vol. 39, no. 3, pp. 217–228, 2006.

[75] K. B. Kim, D. J. Yoon, J. C. Jeong, and S. S. Lee, “Determining the stress intensity factor of a material with an artificial neural network from acoustic emission measurements,” *J. NDT E Int.*, vol. 37, no. 6, pp. 423–429, 2004.

[76] F. Mansfeld and P. J. Stocker, “Acoustic Emission From Corroding Electrodes,” *J. Corros.*, vol. 35, no. 12, pp. 541–544, 1979.

[77] H. Guo, “A Simple Algorithm for Fitting a Gaussian Function [DSP Tips and Tricks],” *IEEE Signal Process. Mag.*, vol. 28, no. 5, pp. 134–137, 2011.

[78] E. W. Grafarend, *Linear and Nonlinear Models: Fixed effects, random effects and mixed models*. 2006.

[79] F. Pukelsheim, “The three sigma rule,” in *JSTOR: American Statistician*, 1994, pp. 48:88-91.

[80] H. Lais, P. S. Lowe, T. H. Gan, L. C. Wrobel, and J. Kanfoud, “Characterization of the use of low frequency ultrasonic guided waves to detect fouling deposition in pipelines,” *J. Sensors*, vol. 18, no. 7, pp. 2122–2134, 2018.

[81] W. Lowe, “Advances in Resolution and sensitivity of Ultrasonic Guided Waves for Quantitative Inspection of Pipelines,” PhD Thesis, Brunel University London, 2016.

[82] T. P. Waters, “A chirp excitation for focussing flexural waves,” *J. Sound Vib.*, vol. 439, pp. 113–128, 2019.

[83] X. Q. Wang and R. M. C. So, “Various standing waves in a Timoshenko beam,” *J. Sound Vib.*, vol. 280, pp. 311–328, 2005.

[84] X. Q. Wang and R. M. C. So, “Timoshenko beam theory : A perspective based on the wave-mechanics approach,” *J. Wave Motion*, vol. 57, pp. 64–87, 2015.

[85] A. E. H. Love, *A threatise on the Mathematical Theory of Elasticity*. Cambridge, UK, 1927.

[86] S. P. Timoshenko, *Strength of Materials*, 2bd edn. New York, 1941.

[87] S. P. Timoshenko, “On the correction for shear of the differential equation for transverse vibrations of prismatic bars,” *Phil. Mag.*, vol. 41, no. 6, p. 744, 1921.

[88] *Vibration Problems in Engineering*, 2nd edn. New York, 1937.

[89] L. S. D. Morley, “Elastic waves in a naturally curved rod,” *J. Mech. Appl. Math*, vol. XIV, pp. 156–172, 1961.

[90] G. Herrmann and I. Mirsky, *Three-dimensional and shell theory analysis of axially symmetric motions of cylinders*. New York: Columbia University. Department of Civil Engineering and Engineering Mechanics. Institute of Air Flight Structures. Technical note ; Contract AF 18(600)-1247, no. 1., 1955.

[91] Y.-W. M. Xian-Fang Li, Bao-lin Wang, “Effects of a surrounding elastic medium on flexural waves propagating in carbon nanotubes via nonlocal elasticity,” *J. Appl. Phys.*, vol. 074309, no. November 2007, pp. 1–9, 2008.

[92] G. Liu and J. Qu, “Transient wave propagation in a circular annulus, Journal of Acoustical Society of America,” *J. Acoust. Soc. Am.*, vol. 104, pp. 1210–1220, 1998.

[93] G. Liu and J. Qu, “Guided circumferential waves in a circular annulus,” *J. Appl. Mech.*, vol. 65, pp. 424–430, 1998.

[94] C. Aristegui, P. Cawley, and M. Lowe, “Reflection and mode conversion of guided waves at bends in pipes,” in *Review of Progress in Quantitative NDE 2000*, 2000.

[95] M. G. Silk and K. F. Bainton, “The propagation in metal tubing of ultrasonic wave modes equivalent to Lamb waves,” *J. Ultrason.*, vol. 17, no. 1, pp. 11–19, 1979.

[96] J. Mu and J. L. Rose, “Guided wave propagation and mode differebtiation in hollow cylinder with viscoelastic coating,” *J. Acoust. Soc. Am.*, vol. 124, no. 2, pp. 866–874, 2008.

[97] J. P. Bérenger, “A Perfectly Matched Layer for the Absorption of Electromagnetic Waves,” *J. Comput. Phys.*, vol. 114, pp. 185–200, 1994.

[98] M. Zampolli, N. Malm, and A. Tesei, “Improved Perfectly Matched Layers for Acoustic Radiation and Scattering Problems,” *Proc. COMSOL Conf. 2008 Hann. Improv.*, 2008.

[99] M. Morvaridi and M. Brun, “International Journal of Solids and Structures Perfectly matched layers for flexural waves : An exact analytical model,” *Int. J. Solids Struct.*, vol. 102–103, pp. 1–9, 2016.

[100] O. C. Zienkiewicz, C. Emson, and P. Bettess, “A Novel Boundary Infinite Element,” *J. Numer. Methods Eng.*, vol. 19, pp. 393–404, 1983.

[101] I. M. Perez and P. Bastid, “Prediction of residual stresses in mooring chains and its impact on fatigue life,” in *OMAE 2017 Trondheim*, 2017.

[102] Y. N. Al-Nassar, S. K. Datta, and A. H. Shah, “Scattering of Lamb waves by a normal rectangular strip weldment,” *J. Ultrason.*, vol. 29, pp. 125–132, 1991.

[103] B. Romuald, A. Sylvain, T. Jean-hugh, P. Charles, F. Didier, and B.-M. Laurence, “Experimental modal decomposition of acoustic field in cavitation tunnel with square duct section,” in *173rd Meeting of Acoustical Society of America and 8th Forum Acusticum*, 2017.

[104] J. R. Buck, M. M. Daniel, and A. C. Singer, *Computer Explorations in Signals and Systems Using MATLAB®*, 2nd Editio. Upper Saddle River, NJ: Prentice Hall, 2002.

[105] P. Stoica and R. Moses, *Spectral Analysis of Signals*. Upper Saddle River, NJ: Prentice Hall, 2005.

[106] N. N. Hsu and F. R. Breckenridge, “Characterization and Calibration of Acoustic Emission Sensors,” *J. Mater. Eval.*, vol. 39, pp. 60–68, 1981.

[107] N. Ferguson and T. Waters, “Lecture notes of Advance Vibration, Structural Vibration, Wave propagation, Wave reflection and transmission,” 2015.

[108] E. Titchmarsh, *Introduction to the theory of Fourier integrals*, 2nd ed. Oxford: Oxford University: Clarendon Press, 1986.

[109] B. Arun, “The mechanical and resonant behaviour of a dry coupled thickness-shear PZT transducer used for guided wave testing in pipe line,” PhD Thesis, Brunel University, 2013.

[110] N.-Z. C. X. Xue, “Fracture mechanics analysis for a mooring system subjected to tension and out-of-plane bending Fracture mechanics analysis for a mooring system subjected to tension and out-of-plane bending,” in *IOP Conference Series: Materials Science and Engineering*, 2017, pp. 276–284.

Appendices

Appendix A

A.1 Numerical analysis of mooring chains in ANSYS

A finite element static analysis was carried out in ANSYS for studless chains, where a profile load of proof load, maximum load and minimum operational load was applied to emulate the numerical analysis result of reference [14]. The purpose with these analysis was to study the residual stresses and stress range distribution in links subjected to operational cycle loading, then using the stresses range result a crack growth model was used to predict the mooring life, only residual stresses due to proof loading were considered in these analysis. The geometry of the modelled studless links are meant to match the dimensions provided by JIF FPS mooring integrity [2]. The cross sectional diameter was set to 124mm and the material behaviour was grade R4, the material was assumed to be elastic-plastic, with linear isotropic work hardening as reference [14], see Table A-1, this grade was chosen because it is commonly used in existing mooring system. The analysis model consists of two parts, each part was made up of one eight of a link, and symmetry conditions were applied on the symmetric planes.

Table A-1 Material's behaviour used in analysis [14]

Structural Steel	*Value*	*Units*	*Region*
Young's Modulus	210	GPa	Elastic
Poisson's Ratio	0.3		Elastic
Tensile Yield	875	MPa	Plastic
Tensile Ultimate	1010	MPa	Plastic

A.1.1 Boundary conditions and loading

Three symmetry planes were defined in accordance to the geometry and loading of the model, each plane of symmetric, except the load surface was assigned symmetric boundary conditions. The displacement of nodes lying on the faces highlighted in the Figure A-1 bottom left, is constrained in the normal direction, the symmetric boundary condition restrained displacement in one direction and prevent rotation about the other directions. The load was applied to the face at the centre of the second link, see Figure A-1. The nodes lying on this face are constrained so that their displacement is the direction of the chain axis is uniform across the face.

The two parts of the chains were connected as shown in Figure A-1. The upper end was fixed while a uniformly distribution tensile load was applied at the lower end. The models were meshed with quadratic 3D solid elements of size 6 mm, in order to refine the mesh, in the region for contacting zone was defined with elements size of 3 mm. The total number of nodes was 255480 and the total number of elements was 59472. Also in this analysis a frictional contact was assumed between the links as reference [14], with a contact coefficient of 0.4. The interaction between the two parts was defined as surface to surface contact in ANSYS. The two parts of chains had identical material properties, the master chain was the chain where the load was applied, and the slave chain was the fixed part at the end.

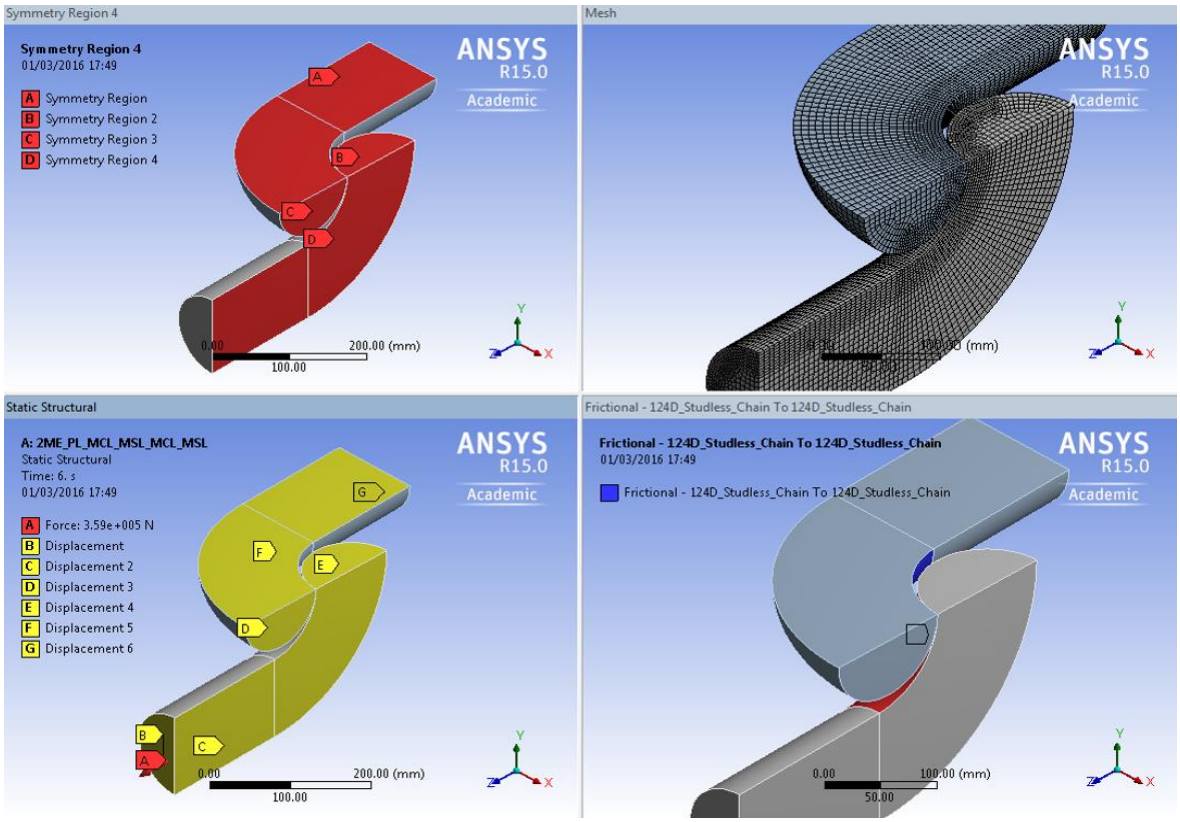

Figure A-1 Boundary conditions of chains analysis

The load profile history was determined following the specification for the chain size and grade according to JIP FPS mooring integrity [2] and emulating the reference [14], in Figure A-2 is shown the loading history steps, where the proof loading (step 1 and 2) applied before that the chains are in service was the 70 % of minimum breaking load (MBL). The model of the link was permanently under tensile loading during service, maximum cyclic load (step 3 and 5) was 20 % of MBL representing the maximum environmental loads applied, and minimum cyclic load (step 4 and 6) or static load was 10 % of MBL mainly caused by the dead weight of the chain, and 0 % of MBL to see the residual stresses before chains are in service.

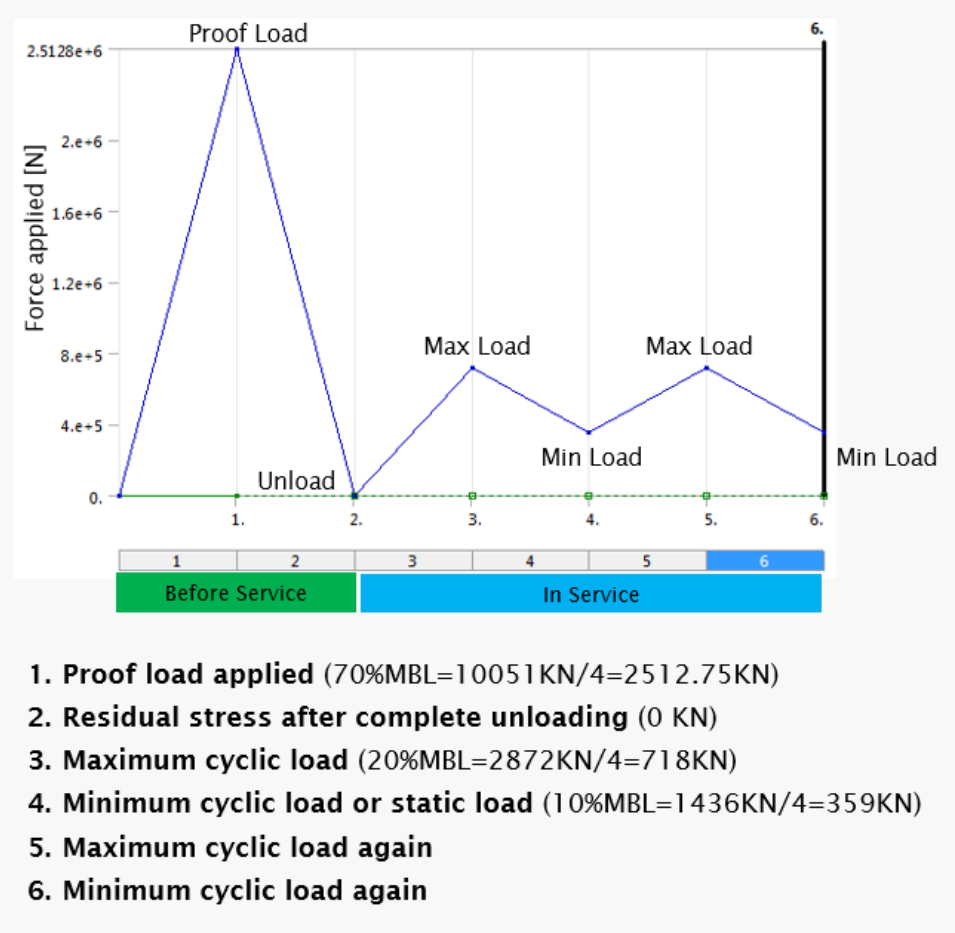

Figure A-2 History of load applied on mooring chains

Figure A-2 shows the steps during the analysis, in step 1 the proof load is applied, in step 2 the proof load is removed, in step 3 the maximum load is applied, in step 4 the minimum load is applied, then again in step 5 the maximum load is applied, and finally in step 6 the minimum load is applied as well. In this analysis the residual stress distribution was considered at the end of step 2, at the end of step 5 the stress distribution of maximum cyclic load was taken, and in step 6 the stress distribution due to minimum cyclic load was obtained. Table A-2 shows the calculations of the loads applied according to the JIP FPS mooring integrity [2].

Table A-2 Calculations of loads applied

Load on chain	*Studless chain* $\boldsymbol{D}$*=124* mm
MBL R4	$0.0274\,D^2\,(44-0.08\,D) = 14357.985$ kN
Proof load (70% MBL R4)	10050.589 kN
Max load (20% MBL R4)	2871.597 kN
Min load (10% MBL R4)	1435.798 kN

The residual stresses, von Mises, axial stresses and principal stresses were compared with the reference [14], the results of stress distribution are very similar.

A.1.2 Results of residual stresses distribution

The results from the analysis are presented as von Mises stresses and maximum principal stresses. Von Mises stresses are helpful when using failure criteria to predict failure in ductile materials. However, von Mises yield criterion do not distinguish between tensile stresses and compressive stresses. When it comes to fatigue analysis, the sign of the stress is essential. As a rule, a tensile mean stress reduces fatigue life while a compressive mean stress increases fatigue. The sign of the stress is also key to crack initiation. Unlike von Mises stresses, the principal stresses are denoted as positive or negative.

Figure A-3 shows the Von Mises stress distribution contour plot when the link is at the proof load. As it is shown in the Figure only half part of the shanks is still in the elastic domain and the rest part of the shank is in plastic domain, the red contour are its values above the yield strength of 875 MPa.

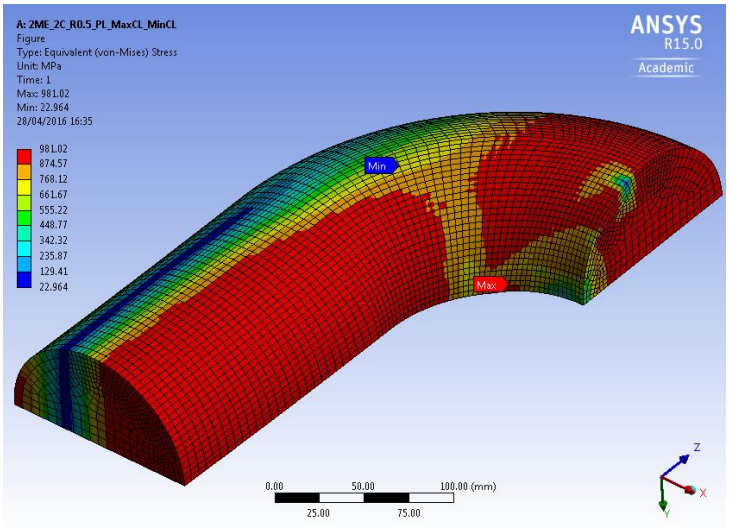

Figure A-3 Von Mises stress contour plot at proof load

Figure A-4 shows the axial residual stresses after complete unloading from proof load. As reference [14] some regions of particular interest are defined. In the same Figure A-4 is observed that in region 1 the axial residual stress is compressive, which will improve the fatigue life. However, region 2 and region 5 axial residual stress is tensile and reach high values, which will decrease the fatigue life or in this region 2 a crack growth could initiate due to the cycling load in service. Also in region 3 the axial residual stresses are tensile but lower than region 2.

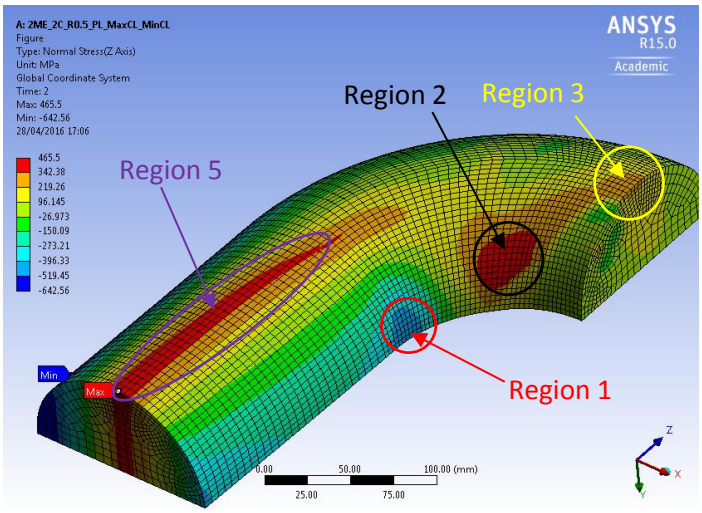

Figure A-4 Axial stress after unloading from proof load

Figure A-5 shows the maximum principal stresses after unloading from the proof load. This shows that region 2, the red area, is increasing until the inner edge of the arch of the zone contact, but region 5 decreases, and a new region 4 near the intrados of contact zone is observed in tensile with the maximum principal stress as shows in Figure A-5, where the residual stresses are tensile.

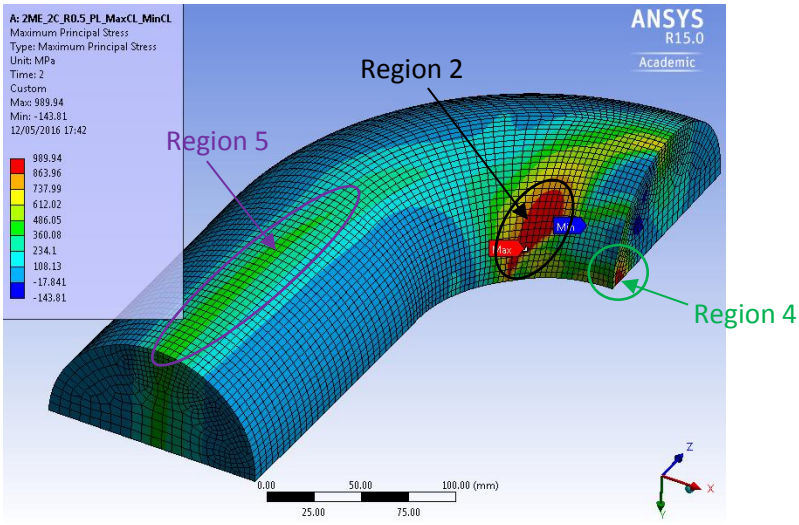

Figure A-5 Maximum principal stresses after unloading from proof load

Region 2 and region 4 of residual stress in tensile are very important to be analysed together with the local stress cycle due to the subsequent cyclic loading of maximum and minimum.

A.1.3 Results of stresses distribution with maximum load and minimum load

Fatigue strength occurs when a material is subjected to repeat loading (maximum load) and unloading (minimum load), fatigue strength is expressed as stress range $\Delta\sigma = \sigma_{max} - \sigma_{min}$. If the loads are above a certain threshold, microscopic cracks will begin to form at the stress concentration. The cyclic stress range is a very important parameter because it is generated from the distribution stress of the maximum load (20 % MBL) and the distribution stress of minimum load (10 % MBL). Figure A-6 shows the maximum principal stresses during maximum load. This plot shows the region 2 in tensile stress result, and also the region 3 is in tensile stress. However, near region 4 the plot is showing compressive stress results.

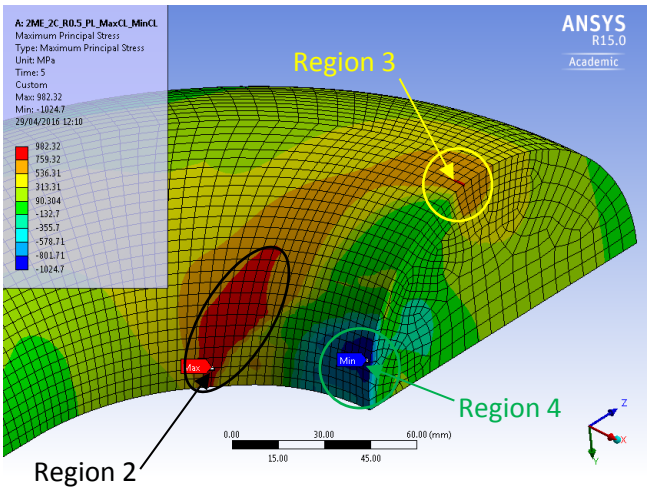

Figure A-6 Maximum principal stresses during maximum load

Figure A-7 shows the maximum principal stresses during minimum load, as it was expected the stress distribution was reduced in some regions like 3 and 4, but in region 2 is still keeping tensile stress. Region 4 is still in compressive stress where this changed from -1024.7 MPa to -681.16 MPa, and one part of region 3 reduced from 982.32 MPa to 788.83 MPa due to the minimum load.

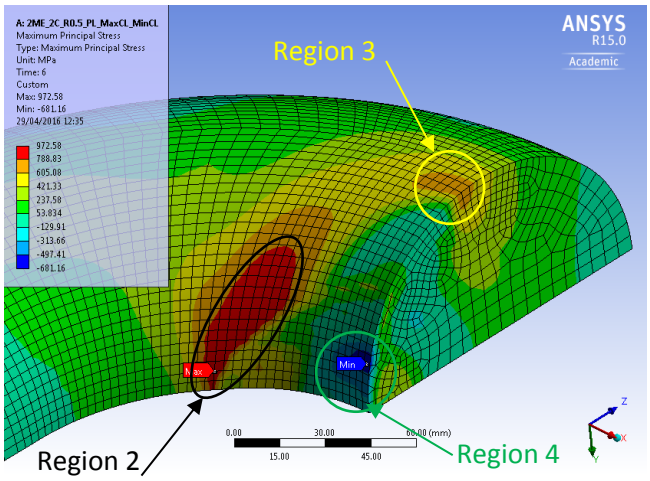

Figure A-7 Maximum principal stresses during minimum load

In graph A-8 is shown the behaviour of the maximum principal tensile stress (maximum stress) and the maximum principal compressive stress (minimum stress) of the full history load applied in the analysis. The maximum principal tensile stress result is not changing a lot after the proof load completed. However the maximum principal compressive stress result is changing during cyclic loading (chains in service operation), it looks that when the maximum load is applied (step 3 and 5) the compressive stress result is lower than when the minimum load is applied (step 4 and 6).

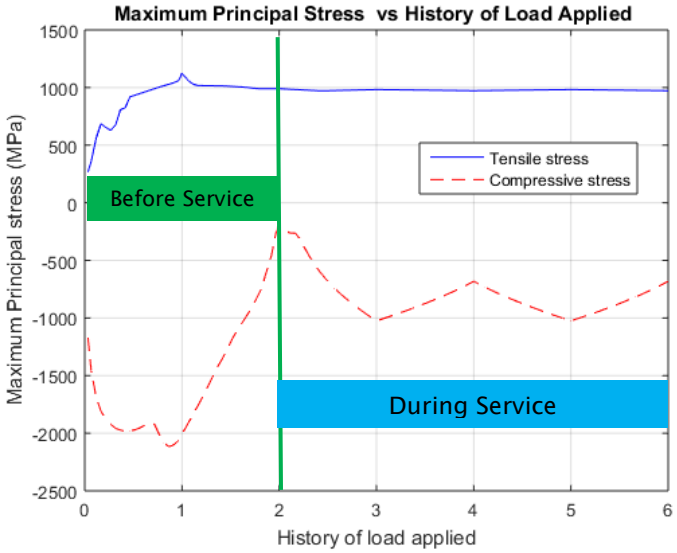

Figure A-8 Maximum principal stress during analysis

Graph A-9 is showing the axial deformation during the analysis. It can be seen that the maximum deformation of 10.7 mm has taken place during the proof load (step 1). This means that the elastic behaviour of the material is almost complete during proof test (step 1 and 2). During the time that the chains are in service, they are in plastic deformation. The deformation is oscillating from 7.1 mm to 7.8 mm, almost 1 mm.

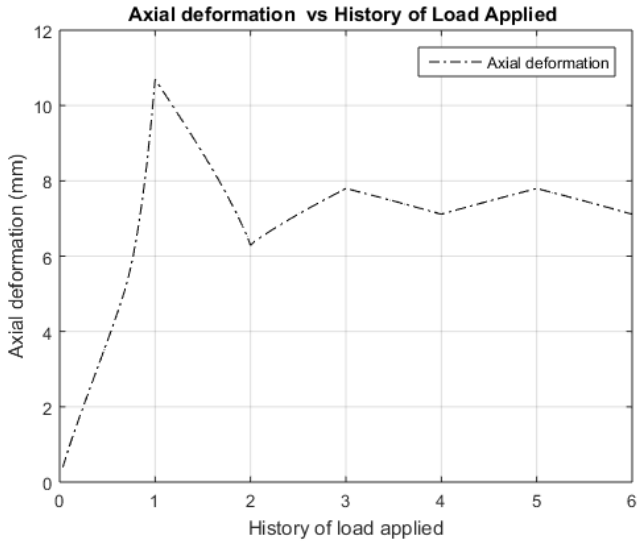

Figure A-9 Axial deformation during analysis

Appendix B

B.1 Free wave propagation in a cylindrical bar

The propagation of elastic harmonic waves in an infinite rod is most convenient to solve this problem using cylindrical coordinate (r, θ, z), where the z-axis is along the axis of the rod. The equation of motion can be written in full as follows, using aspects of Navier's equations in cylindrical coordinate system [36].

$$(\lambda + 2\mu)\frac{\partial \phi}{\partial r} - \frac{2\mu}{r}\frac{\partial \omega_z}{\partial \theta} + 2\mu\frac{\partial \omega_\theta}{\partial z} = \rho\frac{\partial^2 \hat{u}_r}{\partial t^2} \tag{B.1}$$

$$(\lambda + 2\mu)\frac{1}{r}\frac{\partial \phi}{\partial \theta} - \frac{2\mu}{r}\frac{\partial \omega_r}{\partial z} + 2\mu\frac{\partial \omega_z}{\partial r} = \rho\frac{\partial^2 \hat{u}_\theta}{\partial t^2} \tag{B.2}$$

$$(\lambda + 2\mu)\frac{\partial \phi}{\partial z} - \frac{2\mu}{r}\frac{\partial (r\omega_\theta)}{\partial r} + \frac{2\mu}{r}\frac{\partial \omega_r}{\partial \theta} = \rho\frac{\partial^2 \hat{u}_z}{\partial t^2} \tag{B.3}$$

Where λ and μ are the Lame' constants of the isotropic body and ρ denotes its mass density. ϕ is the dilatation in cylindrical coordinates and $\omega_r, \omega_\theta, \omega_z$ represents elements of the rotation tensor. Hence

$$\phi = \frac{1}{r}\frac{\partial (r\hat{u}_r)}{\partial r} + \frac{1}{r}\frac{\partial \hat{u}_\theta}{\partial \theta} + \frac{\partial \hat{u}_z}{\partial z} \tag{B.4}$$

$$2\omega_r = \frac{1}{r}\frac{\partial \hat{u}_z}{\partial \theta} - \frac{\partial \hat{u}_\theta}{\partial z} \tag{B.5}$$

$$2\omega_\theta = \frac{\partial \hat{u}_r}{\partial z} - \frac{\partial \hat{u}_z}{\partial r} \tag{B.6}$$

$$2\omega_z = \frac{1}{r}\left[\frac{\partial (r\hat{u}_\theta)}{\partial r} - \frac{\partial \hat{u}_r}{\partial \theta}\right] \tag{B.7}$$

At the surface of the rod, three stress components vanish [36]. From the stress-deformation relations, they are defined as

$$\sigma_{rr} = \lambda\phi + 2\mu\frac{\partial \hat{u}_r}{\partial r} \tag{B.8}$$

$$\sigma_{r\theta} = \mu\left[\frac{1}{r}\frac{\partial \hat{u}_r}{\partial \theta} + r\frac{\partial}{\partial r}\left(\frac{\hat{u}_\theta}{r}\right)\right] \tag{B.9}$$

$$\sigma_{rz} = \mu\left(\frac{\partial \hat{u}_r}{\partial z} + \frac{\partial \hat{u}_z}{\partial r}\right) \tag{B.10}$$

It is now considered the propagation of harmonic waves along a rod. As follow from equation of motion Graff [41], the general solution for the displacement distribution in cylindrical coordinate has the form:

$$\hat{u}_r = u_r(r)\cos(n\theta)\ \mathrm{e}^{\mathrm{j}(\omega t - kz)} \tag{B.11}$$

$$\hat{u}_\theta = u_\theta(r)\sin(n\theta)\ \mathrm{e}^{\mathrm{j}(\omega t - kz)} \tag{B.12}$$

$$\hat{u}_z = u_z(r)\cos(n\theta)\ \mathrm{e}^{\mathrm{j}(\omega t - kz)} \tag{B.13}$$

, where ω is the radian frequency, k is the wavenumber propagation constant, n is the integer that helps determine the type of mode.

B.1.1 Longitudinal modes in a solid cylindrical bar

Longitudinal wave [36] are axially symmetric, with displacement components in the radial and axial direction. Longitudinal waves corresponds to the case $n = 0$ in equation (B.11)-(B.13).

It is convenient to employ the potentials Γ and Ψ that satisfy the wave equations:

$$\nabla^2\Gamma = \frac{1}{{c_L}^2}\frac{\partial^2\Gamma}{\partial t^2} \tag{B.14}$$

$$\nabla^2\Psi = \frac{1}{{c_T}^2}\frac{\partial^2\Psi}{\partial t^2} \tag{B.15}$$

$${c_L}^2 = \frac{\lambda + 2\mu}{\rho}, {c_T}^2 = \frac{\mu}{\rho}$$

Because of symmetry, the solution with respect to the z-axis is

$$\nabla^2 = \frac{\partial^2}{\partial r^2} + \frac{1}{r}\frac{\partial}{\partial r} + \frac{\partial^2}{\partial z^2} \tag{B.16}$$

The scalar components of the displacement vector $\bar{u} = (\hat{u}_r, 0, \hat{u}_z)$ are given by

$$\hat{u}_r = \frac{\partial\Gamma}{\partial r} + \frac{\partial^2\Psi}{\partial r\partial z} \tag{B.17}$$

$$\hat{u}_z = \frac{\partial\Gamma}{\partial z} - \frac{\partial^2\Psi}{\partial r^2} - \frac{1}{r}\frac{\partial\Psi}{\partial r} \tag{B.18}$$

The stresses are given by Hooke's law as

$$\sigma_{rr} = 2\mu\frac{\partial\hat{u}_r}{\partial r} + \lambda\left(\frac{\hat{u}_r}{r} + \frac{\partial\hat{u}_r}{\partial r} + \frac{\partial\hat{u}_z}{\partial z}\right) \tag{B.19}$$

$$\sigma_{rz} = \mu\left(\frac{\partial \hat{u}_r}{\partial z} + \frac{\partial \hat{u}_z}{\partial r}\right) \tag{B.20}$$

The boundary conditions for the problem are given by

$$\sigma_{rr} = \sigma_{rz} = 0 \qquad at\ r = a \tag{B.21}$$

The harmonic waves propagate in a cylinder along the z-axis. Thus, it is considered solutions of (B.14) and (B.15) to be of the general form

$$\Gamma = G_1(r)\ \mathrm{e}^{\mathrm{j}(\omega t - kz)} \tag{B.22}$$

$$\Psi = G_2(r)\ \mathrm{e}^{\mathrm{j}(\omega t - kz)} \tag{B.23}$$

When (B.22) and (B.23) are substituted into the wave equation (B.14) and (B.15), respectively, it is obtained ordinary differential equations for $G_i(r)$ $(i = 1,2)$:

$$\frac{\mathrm{d}^2 G_i}{\mathrm{d}r^2} + \frac{1}{r}\frac{\mathrm{d}G_i}{\mathrm{d}r} + \left(\frac{\omega^2}{c_i^2} - k^2\right) G_i = 0 \qquad (i = 1,2) \tag{B.24}$$

Define

$$\alpha^2 = \frac{\omega^2}{c_L^2} - k^2 \qquad and \qquad \beta^2 = \frac{\omega^2}{c_T^2} - k^2 \tag{B.25}$$

Equation (B.24) is Bessel's equation, whose solutions are

$$G_1(r) = AJ_0(\alpha r) \tag{C.26}$$

$$G_2(r) = BJ_0(\beta r) \tag{C.27}$$

Substituting (B.26) and (B.27) into (B.22) and (B.23), the solution is

$$\Gamma = AJ_0(\alpha r)\ \mathrm{e}^{\mathrm{j}(\omega t - kz)} \tag{B.28}$$

$$\Psi = BJ_0(\beta r)\ \mathrm{e}^{\mathrm{j}(\omega t - kz)} \tag{B.29}$$

Substituting (B.28) and (B.29) into (B.17) and (B.18), u_r and u_z are obtained.

$$\hat{u}_r = [-A\ \alpha J_1(\alpha r) - B\ k\beta J_1(\beta r)]\ \mathrm{e}^{\mathrm{j}(\omega t - kz)} \tag{B.30}$$

$$\hat{u}_z = \mathrm{j}\ [A\ kJ_0(\alpha r) + B\ \beta J_0(\beta r)]\ \mathrm{e}^{\mathrm{j}(\omega t - kz)} \tag{B.31}$$

At the cylindrical surface $(r = a)$, the stresses must be zero. Substituting (B.30) and (B.31) into (B.19) and (B.20), and setting the resulting expression for $\sigma_{rr} = \sigma_{rz} = 0$ at $(r = a)$, the characteristic equation of waveguide can be obtained, and its roots determine the longitudinal

modes. They are also known as the Pochhammer frequency equations for longitudinal modes. Once these roots are known, the amplitudes of the coefficients A and B are determined by solving a homogeneous system equations. With A and B determined, the displacement u_r, u_z are known.

B.1.2 Torsional waves in a solid cylindrical bar

Torsional waves results when u_r and u_z vanish. From the equation of motion, it follows that u_θ must be independent of θ. For torsional waves [36], the equation of motion is

$$\frac{\partial^2 \hat{u}_\theta}{\partial r^2} + \frac{1}{r}\frac{\partial \hat{u}_\theta}{\partial r} - \frac{\hat{u}_\theta}{r^2} + \frac{\partial \hat{u}_\theta}{\partial z^2} = \frac{1}{c_T^2}\frac{\partial^2 \hat{u}_\theta}{\partial t^2} \tag{B.32}$$

It is considered harmonic waves of the form

$$\hat{u}_\theta = u_\theta(r)\ \ \mathrm{e}^{\mathrm{j}(\omega t - kz)} \tag{B.33}$$

Substituting (B.33) into (B.32) and solving the differential equation for the unknown function $u_\theta(r)$, it is obtained

$$\hat{u}_\theta = \frac{1}{\beta} B J_1(\beta r)\ \mathrm{e}^{\mathrm{j}(\omega t - kz)} \tag{B.34}$$

, where *B* is arbitrary.

The three boundary conditions for the problem are

$$\sigma_{rr} = \sigma_{rz} = \sigma_{r\theta} = 0 \qquad at\ r = a \tag{B.35}$$

For torsional wave only the condition

$$\sigma_{r\theta} = 0 \qquad at\ r = a \tag{B.36}$$

is nontrivial. This condition yields the dispersion frequency transcendental equation, whose roots are obtained. For the first root $\beta \to 0$, where the lowest torsional mode displacement is

$$\hat{u}_\theta = \frac{1}{2} B r\ \mathrm{e}^{\mathrm{j}(\omega t - kz)} \tag{B.37}$$

In the lowest mode, the amplitude of $\hat{u}_\theta$ is proportional to the radius, and both $\hat{u}_r$ and $\hat{u}_z$ are zero. The motion corresponding to this solution is a rotation of each cross-section of the cylinder as a whole about its centre. Note that, since $\beta = 0$ implies that the phase velocity equals c_T, the lowest torsional mode is not dispersive but the higher modes are dispersive.

On the other hand, flexural waves [36] depend on the circumferential angle θ through the trigonometric functions shown in equations (B.11)-(B.13). From the flexural modes, the family defined by $n = 1$ is the fundamental wave mode most important, it is obtained

$$\hat{u}_r = u_r(r)\cos(\theta)\ \mathrm{e}^{\mathrm{j}(\omega t - kz)} \tag{B.38}$$

$$\hat{u}_\theta = u_\theta(r)\sin(\theta)\ \mathrm{e}^{\mathrm{j}(\omega t - kz)} \tag{B.39}$$

$$\hat{u}_z = u_z(r)\cos(\theta)\ \mathrm{e}^{\mathrm{j}(\omega t - kz)} \tag{B.40}$$

Substituting these equations (B.38)-(B.40) into (B.1)-(B.3), it is found the system of three differential equations containing $u_r(r)$, $u_\theta(r)$, $u_z(r)$. To determine the frequency equations, the displacement (B.38)-(B.40) must be substituted into the stress expressions, and $\sigma_{rr} = \sigma_{rz} = \sigma_{r\theta} = 0, \text{at}\, r = a$. This leads to a system of three homogeneous equations for A, B and C. The requirement that the determinant of the coefficients must vanish yields the frequency equations [41], more details are provided in next section.

B.1.3 Flexural waves in a solid cylindrical bar (Pochhammer-Chree theory)

Pochhammer-Chree theory deals with wave propagation in structures of cylindrical geometry like rods and tubes, which behave as wave guides. Waveguide behaviour occurs in axially long prismatic structure and is characterized by the existence of discrete propagation modes and dispersion. The solution of the wave equations in a cylindrical material are readily found by the use of potentials and the technique of separation of variables. The equation are solved by the Singular Value Decomposition (SVD) method to find the mode's amplitude [38]. The solution of the wave equations follows largely the treatment given by Gazis et al. [40] for wave propagation in an infinite hollow cylinder, and also work of Zemanek et al. [51] and Thurston et al. [50] for solid cylinders. The starting point is the following general equation B.41 for the displacement distribution vector $\hat{u}$.

$$\hat{\mathbf{u}}(r,\theta,z) = \tilde{\mathbf{u}}(r,\theta)\,\mathrm{e}^{-\mathrm{j}kz} = \mathbf{u}(r)\,\mathrm{e}^{\mathrm{j}n\theta}\mathrm{e}^{-\mathrm{j}kz} \tag{B.41}$$

where the cylindrical system is used with coordinates (r,θ,z), harmonic time variation $\mathrm{e}^{\mathrm{j}\omega t}$ is assumed, and ω is the angular frequency, k is the wavenumber and integer n is a separation constant called the circumferential order, which determines the symmetry of the solution in the circumferential direction. Well known references can be consulted for further information, for example, Graff et al. [41] and Rose et al. [36].

The radially dependent part of the wave mode shape vector $u(r)$ for a rod is expressed in matrix form according to Seco et al. [38], Zemanek et al. [51] and Thurston et al. [50]:

$$\mathbf{u}(r) = \begin{bmatrix} u_r(r) \\ u_\theta(r) \\ u_z(r) \end{bmatrix} = \mathbf{D}^u(r) \cdot A_{coeff} = \begin{bmatrix} D_{11}^u & D_{12}^u & D_{13}^u \\ D_{21}^u & D_{22}^u & D_{23}^u \\ D_{31}^u & D_{32}^u & D_{33}^u \end{bmatrix} \begin{bmatrix} A \\ B \\ C \end{bmatrix} \tag{B.42}$$

The coefficients of matrix $\mathbf{D}^u(r)$ are given explicitly in table B-1, which depends on Bessel functions, the longitudinal speed c_L and the transverse speed c_T of the solid in infinite media. Where ${c_L}^2 = \frac{(1-\upsilon)}{(1+\upsilon)(1-2\upsilon)}$, and ${c_T}^2 = \frac{1}{2(1+\upsilon)}$, υ is the Poisson's ratio. The Bessel functions describe the radial part of the modes of vibration of a circular cross section [36]. The amplitude coefficients vector $A_{coeff} = [A \quad B \quad C]^T$ consists of longitudinal (*A*), shear vertical (*B*) and shear horizontal (*C*) deformation components. The unknown coefficients *A*, *B* and *C* are determined by application of the boundary conditions. They specify that the traction part of the stress tensor σ_t is null at the cylindrical outer surface of the rod [36], [38], [40], [51], so.

$$\sigma_t = [\sigma_{rr}, \sigma_{r\theta}, \sigma_{rz}]^T = 0 \tag{B.43}$$

where $\sigma_{rr}, \sigma_{r\theta}, \sigma_{rz}$ are the components of outer surface stress, which leads to the following matrix determinant equation.

$$\det[\mathbf{D}^{\sigma t}] = \det \begin{bmatrix} \sigma_{rr} \\ \sigma_{r\theta} \\ \sigma_{rz} \end{bmatrix} = \det \begin{bmatrix} D_{11}^\sigma & D_{12}^\sigma & D_{13}^\sigma \\ D_{21}^\sigma & D_{22}^\sigma & D_{23}^\sigma \\ D_{31}^\sigma & D_{32}^\sigma & D_{33}^\sigma \end{bmatrix} = \begin{bmatrix} 0 \\ 0 \\ 0 \end{bmatrix} \tag{B.44}$$

The coefficients of the stress tensor matrix $\mathbf{D}^{\sigma t}$ are given in table C-2. Equation B.44 is called the frequency or characteristic equation of the waveguide, and its roots (ω, k) determine the proper modes supported by it. Once these roots are known, the vector of amplitude coefficients, A_{coeff} are determined by solving the following homogenous system of equations.

$$\mathbf{D}^{\sigma t}(\omega, k) \cdot A_{coeff} = 0 \tag{B.45}$$

Since matrix $\mathbf{D}^{\sigma t}(\omega, k)$ is singular at the mode's frequency wavenumber roots, a robust method like the singular value decomposition (SVD) for computing the amplitude can be implemented [38]. Knowing the amplitude coefficients A_{coeff}, the displacement distribution of the wave mode shape vector in equation B.42 is obtained $\mathbf{u}(r) = [u_r(r) \quad u_\theta(r) \quad u_z(r)]^T$.

Appendix B

Table B-1 Coefficients of matrix $D^u(r)$. [38]

$D_{11}^u = \frac{n}{r}Z_n(\alpha r) - \lambda_1 \alpha Z_{n+1}(\alpha r)$	$D_{12}^u = kZ_{n+1}(\beta r)$	$D_{13}^u = \frac{n}{r}Z_n(\beta r)$
$D_{21}^u = \mathrm{j}\frac{n}{r}Z_n(\alpha r)$	$D_{22}^u = -\mathrm{j}kZ_{n+1}(\beta r)$	$D_{23}^u = \mathrm{j}\frac{n}{r}Z_n(\beta r) - \mathrm{j}\lambda_2 \beta Z_{n+1}(\beta r)$
$D_{31}^u = \mathrm{j}kZ_n(\alpha r)$	$D_{32}^u = \mathrm{j}\beta Z_n(\beta r)$	$D_{33}^u = 0$

Table B-2 Coefficients of the stress matrix $D^{\sigma t}$. [38]

$D_{11}^\sigma = \left((k^2-\beta^2)r^2 + 2(n-1)\right) Z_n(\alpha r) + 2\lambda_1 \alpha r Z_{n+1}(\alpha r)$	$D_{12}^\sigma = 2\beta k r^2 Z_n(\beta r) -2(n+1)\, kr\, Z_{n+1}(\beta r)$	$D_{13}^\sigma = 2n(n-1)Z_n(\beta r) -2n\lambda_2 \beta r\, Z_{n+1}(\beta r)$
$D_{21}^\sigma = 2\mathrm{j}nkrZ_n(\alpha r) -2\mathrm{j}\lambda_1 k\alpha r^2 Z_{n+1}(\alpha r)$	$D_{22}^\sigma = \mathrm{j}n\beta r Z_n(\beta r) -\mathrm{j}(\beta^2 - r^2)r^2 Z_{n+1}(\beta r)$	$D_{23}^\sigma = \mathrm{j}nkrZ_n(\beta r)$
$D_{31}^\sigma = 2\mathrm{j}n(n-1)Z_n(\alpha r) -2\mathrm{j}n\lambda_1 \alpha r Z_{n+1}(\alpha r)$	$D_{32}^\sigma = -\mathrm{j}\beta k r^2 Z_n(\beta r) +2\mathrm{j}kr(n+1)Z_{n+1}(\beta r)$	$D_{33}^\sigma = \mathrm{j}(2n(n-1) - \beta^2 r^2) Z_n(\beta r) + 2\mathrm{j}\lambda_2 \beta r Z_{n+1}(\beta r)$

Table B-3 Choice of Bessel functions in the solutions of the Pochhammer-Chree' equations [38]

Wavenumber	*Frequency range*	*Coefficients*	*Bessel functions*
Real	$\frac{\omega}{\mathrm{k}} < c_L, c_T$	$\alpha^2, \beta^2 < 0$ $\lambda_1, \lambda_2 = -1$	$Z_n(\alpha r) = I_n(\alpha r)$ $Z_n(\beta r) = I_n(\beta r)$
Real	$c_T < \frac{\omega}{\mathrm{k}} < c_L$	$\alpha^2 < 0, \beta^2 > 0$ $\lambda_1 = -1, \lambda_2 = 1$	$Z_n(\alpha r) = I_n(\alpha r)$ $Z_n(\beta r) = J_n(\beta r)$
Real	$\frac{\omega}{\mathrm{k}} > c_L, c_T$	$\alpha^2, \beta^2 > 0$ $\lambda_1, \lambda_2 = 1$	$Z_n(\alpha r) = J_n(\alpha r)$ $Z_n(\beta r) = J_n(\beta r)$
Imaginary	any	$\alpha^2, \beta^2 > 0$ $\lambda_1, \lambda_2 = 1$	$Z_n(\alpha r) = J_n(\alpha r)$ $Z_n(\beta r) = J_n(\beta r)$
Complex	any	$\alpha^2, \beta^2 complex$ $\lambda_1, \lambda_2 = 1$	$Z_n(\alpha r) = J_n(\alpha r)$ $Z_n(\beta r) = J_n(\beta r)$

In table B-1 and table B-2 $\alpha^2 = \frac{\omega^2}{c_L^2} - k^2$ and $\beta^2 = \frac{\omega^2}{c_T^2} - k^2$, where the longitudinal speed c_L and transverse speed c_T of the solid in infinite media [36]. Function Z_n is the independent solution of the Bessel's different equations with complex arguments, where Z_n can be the Bessel's function J_n or the modified Bessel's function I_n. The possible choice of the Bessel function for Z_n depends

on the solution of the Pochhammer-Chree's equations and on the stability of frequency range under consideration, as table B-3 shows. To cope with the fact that the recurrence relationships between Bessel's ordinary functions are different from those of the modified functions, signs λ_1 and λ_2 are introduces, following the scheme of table B-3 [38].

The work described in this appendix B has resulted in some routines written in Matlab environment by Seco et al. [38], which were used to plot the dispersion curves and the wave mode shape.